



HAL
open science

Control of shape and mechanical properties of flexible micro-helices and their deformation in viscous flows

Lucas Prévost

► **To cite this version:**

Lucas Prévost. Control of shape and mechanical properties of flexible micro-helices and their deformation in viscous flows. General Physics [physics.gen-ph]. Université Paris Cité, 2021. English. NNT : 2021UNIP7141 . tel-03850859

HAL Id: tel-03850859

<https://theses.hal.science/tel-03850859>

Submitted on 14 Nov 2022

HAL is a multi-disciplinary open access archive for the deposit and dissemination of scientific research documents, whether they are published or not. The documents may come from teaching and research institutions in France or abroad, or from public or private research centers.

L'archive ouverte pluridisciplinaire **HAL**, est destinée au dépôt et à la diffusion de documents scientifiques de niveau recherche, publiés ou non, émanant des établissements d'enseignement et de recherche français ou étrangers, des laboratoires publics ou privés.



ESPCI PARIS
EDUCATION SCIENCE INNOVATION

Université de Paris



École doctorale n° 564 : Physique en Île-de-France (EDPIF)

Thèse de Doctorat

pour obtenir le grade de docteur délivré par

Université de Paris

Spécialité doctorale “Physique”

présentée et soutenue publiquement par

Lucas PRÉVOST

le 17 décembre 2021

Control of shape and mechanical properties of flexible micro-helices and their deformation in viscous flows

Dirigé par : **Olivia DU ROURE & ANKE LINDNER**

Jury

M. Pedro Reis,	Professeur, EPFL	Rapporteur
M. Clément De Loubens,	Chargé de recherche, CNRS	Rapporteur
Mme Élise Lorenceau,	Directrice de recherche, CNRS	Examinatrice
M. Henry Fu,	Professeur, University of Utah	Examineur
M. Lucio Isa,	Professeur, ETH Zurich	Examineur
Mme Olivia du Roure,	Directrice de recherche, CNRS	Directrice de thèse
Mme Anke Lindner,	Professeur, Université de Paris	Directrice de thèse
M. Alfred Crosby,	Professeur, University of Massachusetts	Invité

ESPCI Paris

Laboratoire de Physique et Mécanique des Milieux Hétérogènes (PMMH)

UMR7636 CNRS, ESPCI Paris, PSL Research University, Sorbonne Université, Université de Paris, Paris, France



Abstract

The study of the mechanical properties of flexible helical structures and of their interactions with flows is of importance for both fundamental science and technological applications. Better comprehension of the physics of flexible helices is critical to understand the swimming behavior of microorganisms and may lead to better design of flow micro-sensors, micro-swimmers for targeted cargo delivery or nanosprings actuators. In this work, micro-fabrication techniques, optical microscopy, cantilever measurements, microfluidic systems and shape reconstruction by image analysis are combined to build a fully integrated experimental set-up. This set-up allows investigation of the physics of flexible helices, from the characterization of their mechanical properties to the study of their interactions with flows.

For the first time, fabrication of highly flexible micron-sized helices with full shape control is reported. Building upon a spontaneous formation technique of helical ribbons, we demonstrate that the creep properties of materials can be leveraged to shape helical ribbons into any desired geometry. The mechanical properties of helical ribbons are then characterized by measuring the force-extension relationship. Taking advantage of the newly achieved control on the helix geometry, influence of the helical pitch on the mechanical response is quantified. Experimental results are found to agree qualitatively and quantitatively with existing models of inextensible elastic strips. Finally, the deformation of helical ribbons in viscous axial flows is studied and influence of the helical pitch is for the first time investigated experimentally. An effective stiffening is highlighted as the pitch increases, which is unexplained by existing models. A new analytical framework is developed and experimental results are found to be well described by a combination of an inextensible elastic strip model and of slender-body theory to model the hydrodynamic forces. Overall the methods and results reported in this work pave the way for a better understanding of the physics of flexible helices. The presented helical ribbons constitute an ideal model system to explore the complex interactions between flexible helical structures and viscous flows.

Keywords: fluid-structure interaction, helical ribbon, flexible helix, micro-fabrication, viscous flow, microfluidic



Résumé

De nombreux systèmes naturels ou artificiels sont de forme hélicoïdale et sont hautement déformables : double-hélice de l'ADN, vrille végétale ou structure hélice alpha dans les protéines. L'étude des propriétés mécaniques de telles structures et de leurs comportements en écoulement est critique à de nombreux égards. Une meilleure connaissance de ses effets participerait à mieux comprendre la propulsion des micro-organismes et mènerait à de nombreuses innovations technologiques : micro-capteurs de débit, nageurs artificiels ou nano-ressorts pouvant servir de capteur de force ou d'actionneur. Dans cette thèse, diverses techniques de micro-fabrication, de micro-fluidique, de microscopie optique et de mesure de force par poutre cantilever sont combinées. Elles permettent de mener plusieurs expériences rigoureusement contrôlées explorant la physique des hélices flexibles. Un dispositif expérimental complet est conçu, intégrant la fabrication de micro-hélices flexibles, la caractérisation de leurs propriétés mécaniques et l'étude des interactions fluide-structure.

Une méthode de fabrication de rubans hélicoïdaux micrométriques hautement déformables est mise au point, permettant pour la première fois un contrôle complet de tous les paramètres géométriques. En nous basant sur une technique de formation spontanée de rubans hélicoïdaux, nous démontrons que les propriétés de fluage des matériaux peuvent être exploitées pour modifier à volonté la géométrie de la structure. Les propriétés mécaniques sont ensuite caractérisées par la mesure de la loi force-extension. Tirant parti du contrôle nouvellement accru de la géométrie, l'influence du pas de l'hélice sur la réponse mécanique est quantifiée. Les résultats expérimentaux concordent qualitativement et quantitativement avec les modèles existants de rubans élastiques inextensibles. Enfin, l'extension de rubans hélicoïdaux soumis à un écoulement axial visqueux est étudiée. Pour la première fois expérimentalement, l'influence du pas de l'hélice est quantifiée. Une rigidification effective de l'hélice est observée lorsque le pas augmente, phénomène qui n'est pas décrit par les modèles existants. Une nouvelle approche analytique est développée. Il apparaît que le comportement expérimental est bien décrit par une combinaison d'un modèle de ruban élastique inextensible et de "slender-body theory" pour la modélisation des forces visqueuses. L'ensemble des méthodes et résultats présenté ici ouvre la voie à une meilleure compréhension de la physique des hélices flexibles. Le dispositif expérimental permet notamment une étude approfondie des interactions entre de telles structures et des écoulements complexes.

Mots-clés : interaction fluid-structure, ruban hélicoïdal, hélice flexible, micro-fabrication, écoulement visqueux, micro-fluidique



Remerciements & Acknowledgments

À mes deux directrices de thèse, Olivia du Roure et Anke Lindner, pour toute la confiance qu'elles m'ont accordée pendant ces 4 années et pour m'avoir offert les meilleures conditions possibles pour mon travail.

To the members of my jury, Élise Lorenceau, Henry Fu, Lucio Isa and in particular to the two reviewers, Clément de Loubens and Pedro Reis, for their careful reading of my manuscript and their relevant questions and remarks.

To our collaborators and friends in UMass, Dylan Barber, Al Crosby and Todd Emrick, for all their help and for sharing their invaluable expertise in material science and chemistry. To the members of the Crosby group, Konane and Cynthia, for the warm welcome in Amherst.

À Sylvain Patinet et Christophe Josserand pour leur participation à mon comité de thèse et les précieuses idées qu'ils ont fait émerger.

Au laboratoire PMMH et à tous ses membres pour son excellence scientifique et pour le joyeux esprit de partage et de collaboration qui y règne. Je remercie particulièrement ses directeurs successifs, Philippe Petitjeans et Damien Vandembroucq, qui ont su cultiver cet esprit au fil des ans ainsi que les administratrices, Frédérique Auger et Claudette Barez, pour leur efficacité et leur sourire.

À l'IPGG et aux ingénieurs de la plateforme microfluidique pour leur appui crucial et leurs conseils.

Aux anciens doctorants et post-doctorants du groupe, Jean, Charles, Francesca, Yanan, Lucie et Martyna, pour toute l'expérience et les compétences qu'ils ont partagées avec moi et leur accueil. Je remercie tout particulièrement Marine Daïeff d'avoir exploré la première ce sujet de thèse, malgré les nombreuses difficultés expérimentales. Je souhaite beaucoup de réussite aux nouveaux doctorants du groupe, Zhibo, Lars, Guillaume et Andrea.

À tous mes collègues et amis du laboratoire, avec qui j'ai partagé au quotidien ces années de recherche. Je remercie Charles, Manon, Chloé et Baptiste d'avoir fait vivre la communauté des doctorants avec moi.

Aux membres successifs de la Grotte, Jeanne, les deux Matthias, Armand, Pierre-Brice, Amaury, Olivier et Pierre-Ewen, pour leur bonne humeur et leurs nombreuses blagues douteuses. J'adresse une pensée émue à Matthias Lerbinger.

À tous mes amis d'hier et d'aujourd'hui, qui m'ont accompagné au fil des ans.

À mes soeurs, ma mère, mon père et toute ma famille pour tous les moments partagés.

À Alice enfin, pour tout son soutien et son aide dans les hauts et les bas, du début jusqu'à la fin, et à qui je dois tant.



Glossary

Symbols

Re Reynolds number

η liquid viscosity

$\dot{\epsilon}$ extension rate

$\dot{\gamma}$ shear rate

U flow velocity

R helix radius

p helix pitch

L total filament length

α helix pitch angle

H helix axial length

N number of turns in helix

s contour position

t time

B filament bending modulus

C filament twisting modulus

E Young's modulus

μ shear modulus

ν Poisson's ratio

w ribbon width

t ribbon thickness

γ liquid surface tension

T temperature

ξ_2 drag coefficient along the ribbon width

ξ_3 drag coefficient along the ribbon length

$\rho = \xi_3/\xi_2$ drag coefficient ratio

M_w molecular weight

Acronyms

PMMA poly(methyl methacrylate)

PDMAEMA poly(dimethylaminoethyl methacrylate)

PAA polyacrylic acid

PSS polystyrene sulfonate

RFT resistive-force theory

SBT slender-body theory



Table of Contents

Abstract	3
Résumé	5
Glossary	9
Table of Contents	11
1 Introduction	13
1.1 Fluid-Structure Interactions	15
1.2 Helices and Chiral Objects in the Micro-World	20
1.3 Methods of Study	24
1.4 References	29
2 Fabrication of Flexible Micro-Helices and Experimental Apparatus	37
2.1 Principle of the Helix Fabrication	38
2.2 Experimental Protocol: from Ribbons to Helices	40
2.3 Factors for Optimal Helix Fabrication	45
2.4 General Experimental Set-Up	48
2.5 References	51
3 Control of the Helical Pitch	53
3.1 Principles of the Method	54
3.2 Mechanics of Deformed Helical Ribbons	55
3.3 Uniform Stress: the Stretching Treatment	57
3.4 Towards More Complex Shapes	61
3.5 Discussion of the Physical Phenomenon	63
3.6 References	68
4 Mechanical Characterization of Helical Ribbons	73
4.1 Experimental Protocol and Methods	74
4.2 Experimental Results	77
4.3 References	82
5 Deformation of Helical Ribbons in Viscous Axial Flows	85
5.1 Experimental Protocol and Methods	86
5.2 Experimental Results	89
5.3 Shape Analysis of the Deformed Helices	92
5.4 References	97

6	Theoretical Analysis and Numerical Simulations	99
6.1	General Framework and Constitutive Relations	100
6.2	Helices in Viscous Axial Flows: the Weak Flow Limit	103
6.3	RFT-Based Numerical Simulations	108
6.4	End-Loaded Helices	112
6.5	References	115
	Appendix A	117
	Appendix B	117
7	Discussion of the Experimental Results	119
7.1	RFT-Based Analytical Model	120
7.2	Towards Slender-Body Theory	124
7.3	References	132
8	Conclusion and Perspectives	135
8.1	General Conclusion	136
8.2	Future Works and Perspectives	137
8.3	References	139
9	Résumé Substantiel	141
9.1	Introduction	141
9.2	Contenu	142
9.3	Conclusion	146
9.4	Références	146
	List of Figures	149
	List of Tables	151
	Appendix I: "Programmed Wrapping and Assembly of Droplets with Mesoscale Polymers"	151
	Appendix II: Supporting Information for "Programmed Wrapping and Assembly of Droplets with Mesoscale Polymers"	161

Chapter 1

Introduction

Contents

1.1 Fluid-Structure Interactions	15
1.1.1 Viscous Flows	16
1.1.2 Decomposition of the General Problem	17
1.1.3 Objects in Uniform Viscous Flows	18
1.1.4 Objects in Shear Flows	19
1.2 Helices and Chiral Objects in the Micro-World	20
1.2.1 Motivations	20
1.2.2 Helices in Viscous Flows	21
1.3 Methods of Study	24
1.3.1 Theoretical and Numerical Tools	24
1.3.2 Experimental Approaches	25
1.3.3 Strategies for Micro-Helix Fabrication	26
1.4 References	29

General Introduction

Helical structures play a crucial role in many chemical, biological and mechanical contexts. Nature offers many examples, spanning several orders of magnitude in length, including double-stranded DNA, alpha helix structures in proteins or plant tendrils. Helical structures are of special importance for the propulsion of microorganisms, as many propel themselves by rotating flexible helically-shaped flagella [1]. Finally, many technologies rely on helical structures, including metallic nanosprings [2, 3], artificial micro-swimmers [4], or flow sensors [5, 6]. The study of the mechanics of helical structures and of their interactions with flows is thus of importance for both fundamental science and technological applications.

For helices and more generally for chiral objects in flows, a coupling exists between translational and rotational motions. Chiral particles in flows typically drift across streamlines in a direction that depends on their handedness [7–9]. This phenomenon has been used to separate objects of opposite chirality, a process crucial in food or pharmaceutical industries. Influence of the chirality has been investigated in various situations, such as particle sedimentation [10] or particle transport in shear flows [8, 11]. Bacteria and artificial micro-swimmers are typically constituted of one or multiple helical flagella attached to a non-chiral body. For these systems, the chirality-induced drift force creates a torque that can reorient the swimmer [12]. Across these studies, a key finding is that for helical objects, magnitude of the chiral effects is mainly controlled by the helical pitch *i.e.* the distance between two consecutive loops. A zero pitch helix corresponds to a ring, which is not chiral, and an infinite pitch helix to a straight rod, which is again not chiral. Therefore, chirality effects are maximized for a finite non-zero pitch.

But most of these studies only consider rigid particles, although most natural and artificial structures motivating them are highly flexible. For flexible helices, additional degrees of liberty are added, such as axial elongation/compression or buckling. A very complex coupling is thus created between translational motion, rotational motion and deformation. For example, deformation may vary the helical pitch, which will in turn modulate the magnitude of the chiral effects. Only a small number of studies have investigated this coupling between chirality and flexibility, most of them analytical or numerical [13–17].

On the experimental side, two approaches, at different length scales, have been explored. On the one hand, working at the macro-scale allows easy fabrication of flexible helices with controlled properties. Control of flows is however complex and free transport of helices is unpractical, as it requires the channel length to be much greater than the typical helix size. This approach is thus especially adapted to still fluid situations [14, 15]. On the other hand, working at the micro-scale allows easy flow control through microfluidic techniques and arbitrary channel size can be reached, allowing free transport. But the fabrication and characterization of flexible helices at the micro-scale are a challenge. Indeed, very few methods exist for the fabrication of micron-sized flexible helices with tunable geometry. Notably, control of the helical pitch, which is crucial in setting the magnitude of chiral effects, is very rarely achieved. These shortcomings in experimental methods hamper progress in the study of the coupling between chirality and flexibility.

Within this context, this work aims at developing a fully integrated experimental set-up, from the fabrication of flexible micron-sized helices to the characterization of their mechanical properties and to the study of their interactions with flows. Strong emphasis is put on control of the helix shape and mechanical properties. The developed platform

builds upon the spontaneous formation of highly flexible micron-sized helical ribbons evidenced by Crosby et al. [18–20]. Our work was conducted in close collaboration with Dylan M. Barber and Alfred J. Crosby from the University of Massachusetts, Amherst, USA. Anirban Jana and Andrea de la Sen contributed to this work during their Master research internship. Most of the work reported here is experimental but is complemented by analytical and numerical approaches, in which some assistance has been provided by Lyndon Koens from Macquarie University, Sidney, Australia.

In the following chapter, we present the state of the art and start in section 1.1 with a general introduction of fluid-structure interaction problems. In section 1.2 we review in details the studies dedicated to helical structures and introduce in section 1.3 the analytical, numerical and experimental tools leveraged for these studies. We discuss the various fabrication methods for flexible micron-sized helices.

The rest of this manuscript is organized as follows. In chapter 2 we describe the general experimental set-up and the experimental techniques used throughout the study. We detail the fabrication method of helical ribbons on which we rely and underline that control of the helical pitch is not achieved. In chapter 3 we address this issue by implementing an in-situ pitch modification process. We thus demonstrate a fabrication method for flexible helices with full shape control. In chapter 4 we characterize the mechanical properties of flexible helical ribbons by measuring the force-extension relationship. Leveraging the newly achieved control of the pitch angle, we examine for the first time experimentally influence of this parameter on the mechanical properties of helical ribbons. In chapter 5 we investigate experimentally the deformation of flexible helical ribbons subjected to viscous axial flows and quantify for the first time the influence of the pitch angle. We thus demonstrate applicability of our experimental platform to study the complex interactions between flexible helices and flows. Highlighting the insufficiencies of previous analytical derivations, we develop in chapter 6 a new analytical framework to understand the deformation of helical ribbons in flows. In chapter 7 we compare the analytical findings to our experimental results and discuss various models for estimating the viscous forces acting on helical structures. Overall the methods and results presented in this work pave the way for a better understanding of the mechanics of flexible helices and of the interplay between flexibility and chirality. Future possible works are highlighted in chapter 8.

1.1 Fluid-Structure Interactions

Fluid-structure interactions describe a very wide range of physical situations where deformable or movable objects and fluids interact. These problems arise everywhere around us, from the effects of wind on kilometer-tall skyscrapers to the flagellar beating of micron-sized sperm cells. Nature provides numerous examples: gliding of birds in hot air current, collective swimming of fish schools or blood flow in deformable vessels. Fluid-structure interactions are a crucial consideration in the design of many engineering systems: wind turbines, planes or bridges for example.

Fluid-structure interactions are, by definition, multi-phase problems and coupling exists between the dynamics of the solid and of the fluid phase. Flow of the fluid exerts forces that deform and/or move the solid structure, and in return, motion or deformation of the structure disturbs the flow field. As a result of this coupling, fluid-structure interaction problems are often very intricate and typically do not exhibit analytical solutions: they

have to be analyzed through experimental or numerical means. In recent years, following the development of new experimental techniques and the improvement of computational capacities, increasingly complex problems can be tackled. Complexity can originate from the structure, for example as a result of non-symmetrical or highly deformable objects. Complexity can also originate from the fluid flow, either from the fluid itself through non-linear or non-local properties for example, or from the flow. In this case, complexity usually rises for disordered or turbulent flows.

1.1.1 Viscous Flows

Behavior of the fluid can be characterized by the dimensionless Reynolds number Re , which helps predict flow patterns. The Reynolds number is a property of the flow and is defined as the ratio of inertial forces to viscous forces

$$Re = \frac{\rho L v}{\eta} \quad (1.1.1)$$

with ρ fluid density, η dynamic viscosity of the fluid, v typical flow velocity and L characteristic flow length scale. At low Reynolds number $Re \ll 1$, viscous forces dominate and flows tend to be laminar. As viscous forces are linear with flow velocity, forces exerted by low Reynolds number flows scale linearly with flow velocity. In contrast, at high Reynolds number $Re \gg 1$, inertial effects dominate and flows tend to be turbulent. Forces exerted by high Reynolds number flows tend to scale quadratically with flow velocity.

In this work, we focus on low Reynolds number flows, also called viscous flows. Low Reynolds number flows are typically flows of highly viscous fluids, such as lava or honey, or flows at the micro-scale. Indeed, as the typical length L and speed v are decreased, $Re \ll 1$ can be achieved even for low viscosity fluids, such as water for which $\eta = 1 \times 10^{-3} \text{ Pa} \cdot \text{s}$. Thus, sub-millimetric objects or particles in liquids are typically displaced and deformed by viscous flows. Notably, most microorganisms, such as bacteria, or other biological objects, such as cells, move and live at low Reynolds number. Examples include transport and deformation of red blood cells in vessels, which happens for $Re \approx 10^{-3} - 10^{-1}$ depending on the size of the vessel [21]; swimming of human sperm cells, which happens at $Re \approx 10^{-2}$ [22]; or swimming of bacteria, which happens at $Re \approx 10^{-5} - 10^{-4}$ [1].

In the common case of incompressible Newtonian fluids, the dynamics of viscous flows are described by the Stokes equations, which correspond to the inertial-free limit of the Navier-Stokes equations

$$-\vec{\nabla} p + \eta \nabla^2 \vec{u} + \vec{f} = \vec{0} \quad (1.1.2)$$

$$\vec{\nabla} \cdot \vec{u} = 0 \quad (1.1.3)$$

with p hydrodynamic pressure, \vec{u} flow field and \vec{f} external volumic forces. Specifying the boundary conditions is necessary to fully solve the Stokes equations. This is typically here that motion and/or deformation of objects come into play. In general, a no-slip condition is used at the surface of the object, which assumes that the fluid has zero velocity relative to the surface. The Stokes equations are linear, meaning that a linear combination of solutions is also a solution, and time-reversible, meaning that a time-reversed solution to the Stokes equation is also a solution.

1.1.2 Decomposition of the General Problem

A general fluid-structure interaction problem consists of an object immersed in an external flow field \vec{u}^∞ . In the vicinity of the particle, a Taylor series expansion can be performed

$$\vec{u}^\infty(\vec{r}) = \vec{u}^\infty(\vec{0}) + \nabla \vec{u}^\infty(\vec{0}) \cdot \vec{r} + \dots \quad (1.1.4)$$

where we have taken $\vec{r} = \vec{0}$ center of mass of the object, the flow field being expressed in the reference frame associated to the object. As the Stokes equations are linear, a fluid-structure interaction problem at low Reynolds number can be decomposed into smaller and simpler problems, following the decomposition of the flow field. Total response of the system is the sum of the responses to each term appearing in eq. (1.1.4). In most cases, the typical length scale over which the flow varies is much larger than the object size and second order terms and highest can be neglected. More complicated problems arise in the case of objects in highly confined geometries where highest order terms must be considered [23–27] or in quickly evolving flows, oscillatory flows [28–30] for example.

The zeroth order term, given by $\vec{u}^\infty(\vec{0})$, is naturally a uniform flow. The first order term is given by $\nabla \vec{u}^\infty(\vec{0}) \cdot \vec{r}$. For a uniaxial flow, in the x direction for example *i.e.* $\vec{u}^\infty = u^\infty \vec{e}_x$, this expression rewrites

$$\nabla \vec{u}^\infty(\vec{0}) \cdot \vec{r} = \frac{\partial u^\infty}{\partial x}(0)x \vec{e}_x + \frac{\partial u^\infty}{\partial y}(0)y \vec{e}_y + \frac{\partial u^\infty}{\partial z}(0)z \vec{e}_z \quad (1.1.5)$$

expressed in the Cartesian coordinate system $\{x, y, z\}$. Again, because of the linearity of the Stokes equation, each term can be considered individually. The term along the x direction corresponds to an extensional or compressional flow, depending on the sign of the extension rate $\dot{\epsilon} = \frac{\partial u^\infty}{\partial x}$. As incompressibility of the fluid imposes $\vec{\nabla} \cdot \vec{u} = 0$, which rewrites $\frac{\partial u^\infty}{\partial x} = 0$ in the case of a uniaxial flow, an extensional or compressional uniaxial flow cannot exist. A common implementation of extensional/compressional flows is the planar elongation flow, depicted in fig. 1.1 (a). Uniaxial extension is then achieved on the $(y = 0)$ -line and uniaxial compression is achieved on the $(x = 0)$ -line.

The two terms along the y and z directions are similar and both correspond to a shear flow, with shearing direction perpendicular to the flow direction. Magnitude of the shearing

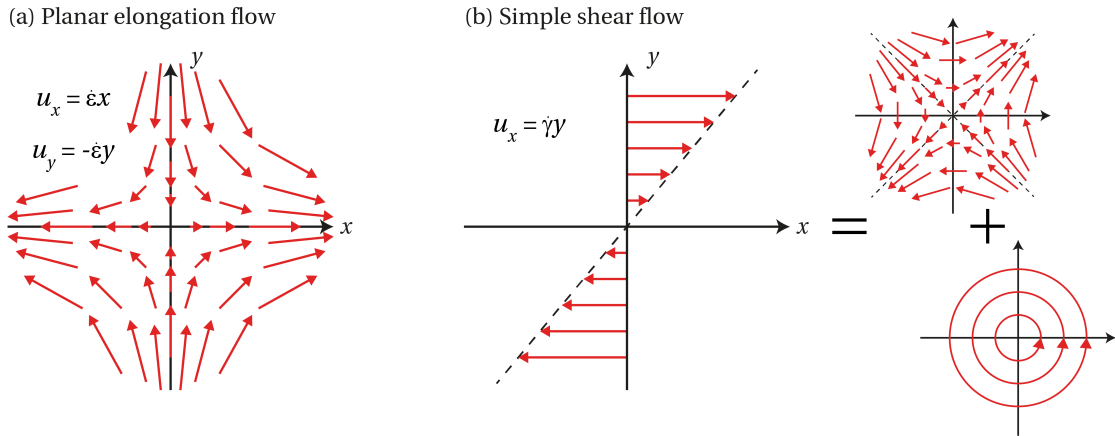


FIGURE 1.1 – Velocity field for (a) a planar elongation flow with extension rate $\dot{\epsilon}$ and (b) a shear flow with shear rate $\dot{\gamma}$, itself decomposed into a tilted planar elongation flow and a rotational flow.

is given by the shear rate $\dot{\gamma} = \frac{\partial u^\infty}{\partial y}$. We illustrate such situation in fig. 1.1 (b). Shear flows themselves can be decomposed into the sum of a rotational flow and of a planar elongation flow oriented at 45° relative to the flow direction

$$\vec{u} = \dot{\gamma} y \vec{e}_x = \underbrace{\frac{1}{2} \dot{\gamma} (y \vec{e}_x - x \vec{e}_y)}_{\text{Rotational flow}} + \underbrace{\frac{1}{2} \dot{\gamma} (y \vec{e}_x + x \vec{e}_y)}_{\text{Planar elongation flow}} \quad (1.1.6)$$

Overall, three elementary fluid-structure interaction problems appear at low Reynolds number: interaction with uniform flows, interaction with shear flows and interaction with extensional flows. We now detail some fundamental results for objects in uniform flows and shear flows.

1.1.3 Objects in Uniform Viscous Flows

Earliest studies of fluid-structure interactions at low Reynolds number have investigated the forces exerted by uniform viscous flows on various objects, and the reciprocal disturbance in the flow field. The classical work of Stokes has established the drag force exerted by uniform viscous flows on hard spheres [31]. With a sphere radius a and a flow velocity U , the drag force is given by $F = 6\pi\eta aU$. As underlined previously, the force varies linearly with the flow velocity and also varies linearly with the particle size. Oberbeck tackled a similar problem for hard spheroidal particles [32]. Expression of the drag force is then much more complex and is notably not linear with particle size. Furthermore, the drag force depends on the particle orientation with respect to the flow direction.

Linearity with the particle size is however recovered in the case of elongated spheroids *i.e.* when one of the two dimensions is much larger than the other. In this case, the drag force is roughly twice as strong when the largest dimension is oriented perpendicularly to the flow direction than when it is parallel to the flow direction. In details, with length l (large dimension) and radius a (small dimension), the perpendicular force is given by

$$F_\perp \approx \frac{8\pi\eta l U}{\ln(2l/a)} \approx 2F_\parallel \quad (1.1.7)$$

The total drag force in the general case is recovered by decomposing the velocity \vec{U} into two components, one parallel to the length direction and the other perpendicular. Again, due to the linearity of the Stokes equations, the total response is the sum of the responses to each component

$$\vec{F} = \frac{4\pi\eta l}{\ln(2l/a)} (\vec{U} \cdot \vec{e}_\parallel) \vec{e}_\parallel + \frac{8\pi\eta l}{\ln(2l/a)} \left[\vec{U} - (\vec{U} \cdot \vec{e}_\parallel) \vec{e}_\parallel \right] \quad (1.1.8)$$

with \vec{e}_\parallel unit vector oriented along the object length. As a result of the force anisotropy, the total drag force exerted by viscous flows on rigid elongated spheroids is in general not oriented in the velocity direction. These results are preserved for all axisymmetric elongated objects [33]. Recent works extended these results in the case of rigid elongated ellipsoids [34]. These findings are key in modeling the viscous forces acting on complex or flexible fibers, which is discussed in section 1.3.1.

1.1.4 Objects in Shear Flows

The dynamics of particles in shear flows was first studied by Jeffery, who derived the motion of rigid spheroids in shear flows [35]. Jeffery found that rigid spheroids perform closed periodic rotation with typical time scale $\dot{\gamma}^{-1}$, the period being set by the aspect ratio of the object. Qualitatively, elongated particles rotate with a longer period and in an unsteady fashion: they spend a long time aligned with the flow but quickly flip from one aligned position to the next, which corresponds to a 180° change in orientation. Less elongated particles rotate with a shorter period and in a smoother manner, the limiting case being the sphere, which rotates at uniform speed. The precise rotational motion is determined within an infinity of solutions, called 'Jeffery orbits', by the initial orientation of the particle. This motion is driven by the rotational component of shear flows, while the extensional component has little impact on rigid objects. It was later shown by Bretherton [36] that these findings are also valid for all rigid axisymmetric particles, provided an effective aspect ratio is substituted to the particle actual aspect ratio.

Jeffery orbits also arise for more complex particles. For Brownian particles in shear flows *i.e.* objects small enough to be affected by thermal noise, particle orientation may diffuse from one Jeffery orbit to another, creating a statistical distribution of orientations [37, 38]. This orientation distribution plays a key role in setting the rheological properties of particle suspensions [39, 40]. For non-axisymmetric particles in shear flows, a doubly periodic motion is observed: at short time particles approximately follow Jeffery orbits, but at long time the trajectory evolves. This longer time scale evolution may be periodic, quasi-periodic or chaotic, depending on the particle shape and initial orientation [41, 42].

For deformable objects in shear flows, influence of the extensional component becomes significant. Objects are compressed in one direction and stretched in the other. Combined with the rotational component, a complex interplay is created between deformation and rotation: objects are successively compressed and stretched as they rotate. The deformation behavior is then typically set by a dimensionless number which compares the viscous forcing to the restorative force. This restorative force can be surface tension in the case of droplets and bubbles [43] or thermal entropy in the case of polymers [44, 45]. For polymers, entropy favors coiled configurations, hence when viscous stretching forces increase and eventually overcome entropy, a coil-stretch transition is observed. These microscopic effects are again crucial in setting the rheological properties of polymer suspensions, leading to rod climbing effects for example [46]. More complex dynamics occur for biological capsules and vesicles in shear flows. These objects are typically self-assembled bilayers of lipids, which can freely rearrange at the surface. The restorative force is then a complex combination of elasticity, surface tension and viscosity [47]. As a result, a rich variety of phenomenon is observed for capsules and vesicles in shear flows: tank-treading, Jeffery-like tumbling or shape oscillations [48–52].

Finally, in the case of flexible filaments, the restorative force is elasticity and more precisely elastic bending. Very long objects can indeed be considered inextensible and their deformations are dominated by bending effects. Flexible filaments in shear flows may undergo buckling as a result of the compressive viscous forces. This straight-to-buckled transition happening under compressive forces can be compared to the coil-stretch transition happening for polymer molecules under stretching forces. As the viscous forces increase, a variety of buckling modes is observed [53, 54]. For very strong compressive viscous forces, buckling into three-dimensional helical shapes can even be observed [55].

Combined with the rotational component, a 'snaking' motion of the filament emerges: a 'U-turn' curvature wave initiates at one end and propagates towards the other end [56, 57].

The case of flexible filaments in shear flows is of notable interest to biology. Several crucial biological processes, such as intracellular motion or microorganism locomotion, indeed involve interactions of flexible filaments with viscous flows. A notable example among these biological filaments is the case of helically-shaped filaments, which we detail in the next section.

1.2 Helices and Chiral Objects in the Micro-World

Before moving forward, the basic parameters of helices are specified. A helical shape is completely defined by its helical radius R , helical pitch p and total contour length L . For the helical axis aligned along the z direction, the filament centerline is given by

$$\vec{r} = \left\{ R \cos \frac{2\pi z}{p}, \delta R \sin \frac{2\pi z}{p}, z \right\} \quad (1.2.1)$$

expressed in the Cartesian coordinate system $\{x, y, z\}$ and with δ chirality index: $\delta = +1$ for right-handed helices and $\delta = -1$ for left-handed helices. Definition of the pitch angle α varies within the literature but it is defined in this work as the angle between a circumferential line and the filament tangent. The pitch angle is expressed as a function of the rescaled helical pitch by $\tan \alpha = p/2\pi R$. $\alpha = 0^\circ$ corresponds to a zero pitch helix *i.e.* a ring and $\alpha = 90^\circ$ to a straight rod. Finally, the axial length $H = L \sin \alpha$ is the filament length projected on the helical axis. Helix geometrical parameters are illustrated in fig. 1.2 (a) for a helical ribbon.

1.2.1 Motivations

Micron-sized helical structures indeed play a crucial role in several biological contexts, the most noteworthy being microorganism locomotion. This stems from the fact that, as viscous flows are time-reversible, reciprocal motion, such as the back and forth of a rigid oar or the opening and closing of a scallop hinge, cannot generate thrust in viscous environments [58, 59]. Microorganisms have thus evolved a variety of propelling mechanisms, which all rely on non-reciprocal motions, such as beating of flexible filaments or rotation of helical flagella [1].

Figure 1.2 shows several examples of microscopic helices for locomotion. We show in fig. 1.2 (b) images of a tethered *E. coli* bacteria, reproduced from Turner et al. [60]. *E. coli* bacteria propel themselves in viscous media by rotating a bundle of helical flagella. As shown, the helical flagella of bacteria such as *E. coli* are very flexible and can undergo significant changes in morphology. These morphological transformations enabled by flexibility are exploited for the bundling and synchronization of multiple flagella [61, 62], bacterial reorientation [60, 63] or swimming in crowded environments [64]. The bending modulus of *E. coli* flagella has been experimentally measured at $B \sim 1 - 4 \times 10^{-24} \text{ Pa} \cdot \text{m}^4$ [65, 66], which corresponds to a persistence length of $l_p = B/k_B T \sim 10^{-3} \text{ m}$. Given typical flagella length of $L \sim 10 - 20 \mu\text{m}$, flagella of *E. coli* can be deformed by forces $\sim 50 - 100$ times stronger than thermal fluctuations. Generally for bacterial flagella, bending moduli range within $B \sim 10^{-24} - 10^{-22} \text{ Pa} \cdot \text{m}^4$ [67]. We show in fig. 1.2 (c) image of a spirochete bacteria, reproduced from Wolgemuth [68]. For spirochetes, the entire bacterial body is

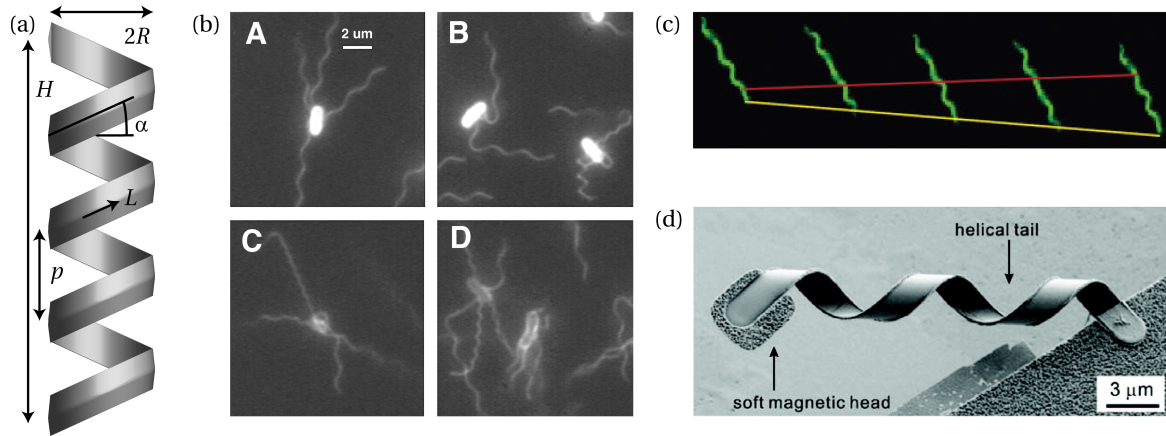


FIGURE 1.2 – Examples of microscopic helices for locomotion. (a) Helix geometrical parameters. (b) Tethered *E. coli* bacteria, reproduced from [60]. (c) Swimming of *B. burgdorferi* spirochete bacteria. Yellow and red lines show a traveling wave undulation, reproduced from [68]. (d) Electron microscopy image of a fabricated flagellated micro-robot, reproduced from [69].

helical, and they propel themselves by rotations and/or undulations of the full body [68]. Flexibility of the helical structure is thus key in achieving locomotion. Such locomotion strategies are exploited to fabricate self-propelled micro-robots [4]. We show in fig. 1.2 (d) image of a flagellated micro-robot, reproduced from Zhang et al. [69].

Helical structures also arise in other biological and chemical contexts. Examples include double-stranded DNA or the alpha helix motif, a common secondary structure of proteins. Moreover, many molecules, despite not being helically shaped, are chiral. This property, shared with helices, significantly influences their physical and mechanical behavior. Study of the behavior of helices, and specifically of the chirality-induced effects, may thus lead to a better understanding of the physics of all chiral objects.

Finally, to the difference of polymer molecules that are only stretched in flows and to the difference of elastic filaments that are only compressed in flows, flexible helices can potentially be both compressed and stretched. Furthermore, several modes of deformation are possible for helices, axial compression/extension or buckling for example. We therefore expect a very wide range of behavior for flexible helices in flows. This may lead to interesting or useful properties for suspensions of flexible helices. We now review the literature investigating the physics of helices in viscous flows, with emphasis put on the studies considering flexibility.

1.2.2 Helices in Viscous Flows

We follow the decomposition of fluid-structure interactions at low Reynolds number introduced in section 1.1. We first review the behavior of helices in uniform flows, then in shear flows and finally the behavior of rotating helices in still fluids.

Helices in Uniform Flows

The interactions between helices and uniform viscous flows is naturally a central question. Even in the case of rigid helices, no analytical solution exists for the viscous forces acting on helices and the reciprocal disturbance in flow. Researchers have thus developed several analytical and numerical methods to estimate the viscous forces acting on helices,

which are detailed in the next section. The work of Rodenborn et al. reviewed these different methods and compared the respective estimations to experimental measurements [70]. The basic scaling for the total drag force D acting on helix immersed in a flow with velocity U is $D \sim \eta UL$. Rodenborn et al. showed that greater precision can be achieved with a logarithmic correction $D \sim \eta UL / \ln(L/R)$.

In the case of flexible helices, these viscous forces naturally deform the helix. The deformation of flexible helices in uniform axial flows (uniaxial flows oriented parallelly to the helical axis) has notably been addressed. The restorative force is elastic bending, which scales as $F \sim B/R^2$ with B bending modulus of the filament. Equilibrium gives the helix deformation, expressed as the change in axial length

$$\frac{\Delta H}{L} \sim \frac{R^2}{B} \eta UL \quad (1.2.2)$$

The work of Kim et al. and the work of Katsamba et al., both relying on the same analytical framework, validated this scaling [13, 71]. Both works also investigated the influence of the helical pitch on the extension of helices in axial flows. They found vanishing influence of the helical pitch in the limit of long helices *i.e.* $L \gg R$. This condition may seem restrictive but, as L/R is given by the geometrical relation $L/R = 2\pi N / \cos \alpha$ with N number of turns, even for a 3-turn helix $L/R \gtrsim 20$.

Leveraging the relation between the axial extension in flow and the filament modulus, Hoshikawa et al. subjected helically-shaped bacterial flagella to viscous axial flows and measured the bending modulus of these biological structures [72]. They further confirmed the linear relationship between the axial extension ΔH and the flow velocity U . Much later, Pham et al. studied experimentally the deformation of micro-fabricated flexible helices in axial viscous flows [73]. Using helices of various radii and lengths, the geometrical scaling $\Delta H \propto R^2 L^2$ was confirmed. They however highlighted that, as the velocity is increased, the relation $\Delta H(U)$ becomes non-linear. The observed non-linear effects are accurately described by a finite extensibility correction, which accounts for the fact that helix extension is limited by the total filament length L . Non-linear effects typically occur for $\Delta H/L \gtrsim 0.1$. Using a similar experimental system, these results were confirmed by Daieff et al [74]. The finite extensibility effect was highlighted again by Li et al. [6] using metallic micro-springs, and confirmed that maximum extension is reached when the helix is fully uncoiled. Again however, influence of the helical pitch on the extension was not studied.

Finally, this problem was tackled numerically by Jawed et al. [15], who similarly found a finite extensibility effect. They showed that the non-linear $\Delta H(U)$ relationship can be characterized by an exponential saturation $\Delta H \propto (1 - e^{-U/U_c})$ with U_c typical velocity needed to stretch the helix. These results are discussed in more details in section 7.2 .

Helices in Shear Flows

For helical structures in shear flows, a coupling exists between rotational and translational motion. In addition to Jeffery-like tumbling, rigid helices in shear flows experience a lateral drift out of the shear plane (plane formed by the flow direction and the shearing direction) [75]. The direction of drift is determined by the handedness of the helix. The lateral drift of helices was observed experimentally by Marcos et al. using as experimental system the helical body of spirochete bacteria [8]. Based on these findings, separation by shear flows of helical or chiral objects depending on their handedness has been demons-

trated [7–9]. This chiral sorting process is of interest to the pharmaceutical industry to separate chiral molecules from their enantiomers (molecule having opposite handedness).

The dynamics of flexible helices in shear flows was studied numerically by Li et al. [17]. For rather stiff helices or weak shearing, a periodic Jeffery-like tumbling motion accompanied by an oscillatory axial extension/compression is found. The overall helix shape is thus preserved and lateral drift is observed, whose magnitude is mainly set by the rescaled helical pitch p/R . As a zero pitch helix corresponds to a ring, which is not chiral, and an infinite pitch helix to a straight rod, again not chiral, we indeed expect chiral effects to be maximized for a finite non-zero pitch. The drift velocity is here maximized for $p/R \sim 8$. For softer helices or strong shearing, a destabilization mechanism is observed: the tumbling motion becomes chaotic, and the helical shape is highly deformed. As a consequence, the drift velocity decreases as the helix gets softer until complete suppression for the softest conditions. This study highlights a complex interplay between chirality and flexibility in the behavior of flexible helices in shear flows. To our knowledge, no experimental work has been reported yet on this topic.

Rotating Helices

A sizable literature is dedicated to the study of helical flagella rotating in viscous fluids, this case being of special relevance for the propulsion of microorganisms [1, 4, 76]. As these studies overwhelmingly consider rigid helices, we will not detail them. We however highlight that a key finding across multiple studies is that the rescaled helical pitch p/R is again crucial in setting the propulsion behavior. This is consistent with the fact that the propelling phenomenon ultimately originates from the helix chirality. As such, these effects are expected to be maximized for a finite non-zero pitch. For a rigid helical flagellum rotating in a Newtonian fluid, Rodenborn et al. found experimentally and numerically a maximum propulsive thrust for a rescaled helical pitch $p/R \sim 6$ [70]. For a rigid helical flagellum rotating in a viscoelastic fluid, Liu et al. found experimentally a maximum swimming speed for $p/R \sim 5$ [77] while a very similar value was found numerically by Leshansky for a rigid helical flagellum rotating in a viscous fluid laden with hard spheres [78].

A few studies investigated the influence of the flexibility on the propulsion behavior. Jawed et al. quantified experimentally and numerically the propulsive thrust for a flexible helix rotating in a Newtonian fluid and described a buckling instability that occurs above a critical rotation velocity [14]. They hypothesized that this destabilization mechanism may be leveraged by microorganisms to change orientation. Katsamba et al. tackled a similar problem analytically [71]. They again found an optimal pitch value for propulsion and highlighted an interplay between flexibility and propulsion.

Overall, review of the literature has evidenced the complex coupling between flexibility and chirality at play in the fluid-structure interactions between flexible helices and viscous flows. Better comprehension of this coupling is critical to understand the swimming behavior of microorganisms and may lead to better design of micro-swimmers or flow micro-sensors. We have highlighted the significant influence of the rescaled helical pitch p/R on the chirality-induced effects. But despite significant analytical and numerical progress, experimental studies remain scarce. For example, influence of the helical pitch on the extension of helices in flows has not been addressed experimentally. And no experimental study has been reported for the behavior of flexible helices in shear flows. We attribute this

scarcity to a lack of adapted experimental methods. Specifically, very few methods exist for the controlled fabrication of flexible helices at the micro-scale. This is detailed in the next section, along with the numerical and analytical methods.

1.3 Methods of Study

1.3.1 Theoretical and Numerical Tools

When studying analytically or numerically the behavior of flexible filaments in viscous flows, two distinct questions naturally arise: the modeling of the filament mechanics and the modeling of the flow behavior.

For the mechanics of flexible filaments, the common approach is to approximate the filament to a one-dimensional elastic rod. The mechanical behavior is then governed by the classical Kirchhoff rod equations [79]. The material stress and strain and the external forcing are averaged over the cross-section of the filament, and filament dynamics are thus solely parametrized by the arc-length of the centerline s and time t . The mechanical properties of the filament are described by three moduli, associated to filament bending in the two possible directions and to filament torsion. These moduli are determined by the filament cross-sectional shape and by the material Young's modulus E and Poisson's ratio ν . We implement such a method in chapter 6 where more details can be found.

Resistive-Force Theory

For the modeling of the flow behavior, several approaches have been developed. The simplest approach, which is also the only one with an analytical formulation, is resistive-force theory (RFT). Within RFT, the disturbance in the external flow field created by the filament is neglected. The question is thus reduced to the calculation of the viscous forces exerted on the structure by the undisturbed external flow field. The basic idea is then to consider the filament, whose configuration can be highly complex, as a linear collection of straight elongated objects. The hydrodynamic interactions between each portion of the filament are neglected. The viscous forces acting on each of these portions can thus be approximated to the forces acting on an isolated elongated object, for which an approximate expression is possible. This expression is given by eq. (1.1.8) and is usually rewritten as a force per unit length

$$\vec{f} = \lim_{\Delta s \rightarrow 0} \frac{\vec{F}}{\Delta s} = \xi_{\parallel} (\vec{U} \cdot \vec{t}) \vec{t} + \xi_{\perp} \left[\vec{U} - (\vec{U} \cdot \vec{t}) \vec{t} \right] \quad (1.3.1)$$

with Δs length of a portion and \vec{t} tangent unit vector. ξ_{\parallel} and ξ_{\perp} are drag coefficients, taken as constant for all portions. Expression of these coefficients is given from eq. (1.1.7)

$$\xi_{\perp} \approx \frac{8\pi\eta}{\ln(2l/a)} \approx 2\xi_{\parallel} \quad (1.3.2)$$

The relevant value for the parameter l , which is in eq. (1.1.7) the length of the object, has been subject to debate. In the case of helical structure, Lighthill suggested to use $l = 0.09\Lambda$ with Λ helical wavelength *i.e.* the filament contour length corresponding to one helical loop [80]. Because of its analytical formulation, RFT is widely used to estimate the viscous forces acting on elongated filaments and usually provides good qualitative

understanding. This approach is used in the already mentioned works of Kim et al. and of Katsamba et al. [13, 71] to estimate the viscous forces acting on a flexible helix. But errors can get significant when the different portions of the structure are close-by and that hydrodynamics interactions become significant. This is the case for highly curved or three-dimensional structures. For rigid helices, Rodenborn et al. [70] found that RFT yields a very poor estimation of the viscous forces.

Slender-Body Theory and Other Methods

A more complex and accurate approach is slender-body theory (SBT), which takes into account the hydrodynamic interactions. The so-called local SBT consists in calculating the flow field created by a moving filament as the flow field created by a discrete collection of point forces placed along the filament centerline. At this stage, the magnitude of the point forces are unknown, which corresponds to $3N$ unknown quantities with N number of point forces. Due to the linearity of the Stokes equations, the total flow field is simply calculated as the sum of the flow contribution from each point force. As a no-slip condition is enforced at solid boundaries, the velocity of the fluid at the filament position is known: it is simply the velocity of the filament. By equating the calculated flow field to the known velocities at each position of the point forces, $3N$ equations are obtained. By inverting the system, the magnitude of the point forces can be obtained. Thus, both the disturbance in flow created by the filament and the forces acting on the filament can be calculated. A more elaborate method, called non-local SBT, adds a discrete collection of force dipoles along the filament centerline. Naturally, this approach is numerical and no analytical formulation exists. In the case of rigid helices, and in contrast to RFT, Rodenborn et al. [70] found excellent agreement between SBT predictions and experimental measurements.

Several other approaches have been developed, notably when the filament cannot be considered slender. One of them is the so-called Multi-Particle Collision Dynamics method (MPC) [81]. This numerical approach models the fluid as a collection of point particles, each defined by its velocity and position. The algorithm consists of alternating streaming and collision steps. In the streaming step, the particles simply move ballistically. In the collision step, the particles are sorted into collision groups based on proximity and interchange momentum with all the other particles within the group. MPC accurately captures hydrodynamic interactions and potential Brownian fluctuations. This method is used in the already mentioned study of Li et al. to simulate the behavior of flexible helices in shear flows [17].

1.3.2 Experimental Approaches

On the experimental side, two approaches, at different length scales, have been explored. On the one hand, working at the macro-scale allows easy fabrication and characterization of flexible helices. However, it requires a highly viscous fluid to fall into the viscous regime and in significant quantity. Control of background flow is complex, and transport of helices is unpractical, as it requires the channel length to be much greater than the typical helix size. Furthermore, obtaining high values of shear rate or extension rate is very difficult. For example, considering glycerol as the fluid, which is a common choice for macro-scale viscous flows, we have $\eta \sim 1 \text{ Pa} \cdot \text{s}$ and $\rho \sim 10^3 \text{ kg} \cdot \text{m}^{-3}$. To satisfy $\text{Re} \ll 1$, we must therefore satisfy $Lv \ll 10^{-3} \text{ m}^2 \cdot \text{s}^{-1}$. For a centimetric object $L \sim 10^{-2} \text{ m}$, this imposes

$v \ll 10^{-1} \text{ m} \cdot \text{s}^{-1}$. Hence, even in a highly confined geometry *i.e.* with centimetric confining length, we can reach at most $\dot{\gamma} \sim 1 \text{ s}^{-1}$. This approach is thus especially adapted to still fluid situations and was followed by Jawed et al. to study the rotation of flexible helices in still fluids [14, 16].

On the other hand, working at the micro-scale allows easy flow control through micro-fluidic techniques and any fluid can be used, including water and water-based suspensions. Recent advances in micro-fabrication have enabled precise control of small-scale flows in microfluidic devices: various flow fields can be obtained through control of the channel geometry [82]. Arbitrary channel size can be reached, which allows free transport. Furthermore, very high values of shear rate or extension rate can be obtained. Considering water as the fluid, we have $\eta \sim 10^{-3} \text{ Pa} \cdot \text{s}$ and $\rho \sim 10^3 \text{ kg} \cdot \text{m}^{-3}$. For a micron-sized object $L \sim 10 \mu\text{m}$, falling into the viscous regime requires $v \ll 10^{-1} \text{ m} \cdot \text{s}^{-1}$. Hence, even for a weakly confined flow, of typical confining length $\sim 100 \mu\text{m}$, the shear rate value can easily reach $\dot{\gamma} \sim 100 \text{ s}^{-1}$. The micro-scale approach was followed by all the works that studied experimentally the behavior of flexible helices in moving fluids [6, 72–74]. But the fabrication and characterization of flexible helices at the micro-scale are a challenge. Indeed, very few methods exist for the fabrication of micron-sized flexible helices with tunable geometry.

1.3.3 Strategies for Micro-Helix Fabrication

Firstly, helically-shaped biological structures can be used. For example, Marcos et al. used spirochete bacteria to evidence the lateral drift of flexible helices in shear flows [8]. But the mechanical and geometrical properties are then biologically determined and thus hardly tunable, which prevents any parametric study. Micro-fabricated model systems are preferable as they allow more control.

Numerous methods have been reported for the fabrication of micron-sized helices, using either direct fabrication or spontaneous helix formation. A quantity of methods have also been proposed for sub-micron helices [83] but such objects require electron microscopy for imaging, which considerably complexifies experiments. Direct fabrication methods rely on complex manufacturing techniques, such as 3D-printing [84, 85] or electro-spinning [86]. For the spontaneous formation methods, a wide variety of mechanisms have been exploited: bilayer or trilayer systems [87–90], differential swelling [91, 92], material anisotropy [6, 93, 94], molecular chirality [95, 96], mechanical frustration [97] or surface tension [20].

The direct fabrication methods usually allow full shape control but result in rigid structures. Meanwhile, several of the spontaneous formation methods result in flexible structures [6, 20, 92, 94, 97] but lack control of the helix shape. The characteristics of these methods are synthesized in table 1.1 and the obtained helices are shown in fig. 1.3. For some of these structures, the flexibility is apparent but has not been precisely quantified. For reference, we recall the typical bending modulus of bacterial flagella $B \sim 10^{-24} - 10^{-22} \text{ Pa} \cdot \text{m}^4$ [67].

Zastavker et al. reported self-assembly of helical ribbons from a multi-component solution containing bile salt, a fatty acid and a steroid analog of cholesterol [94]. Images of the obtained helical ribbons are shown in fig. 1.3 (a). The helical radius can be varied within $R = 5 - 50 \mu\text{m}$ by tuning the solution composition. However, these helical ribbons can only adopt three different values for the pitch angle $\alpha = 11^\circ, 41^\circ, 54^\circ$. Flexibility of these structures was demonstrated and quantified by the latter work of Smith et al. [98],

Study	Filament	Mechanism	Radius	Flexibility	Shape control
[94]	Ribbon	Self-assembly	$R = 5 - 50 \mu\text{m}$	$B \sim 10^{-18} - 10^{-17} \text{ Pa} \cdot \text{m}^4$	Only 3 possible pitch angles $\alpha = 11^\circ, 41^\circ, 54^\circ$
[20]	Ribbon	Surface tension	$R = 2 - 100 \mu\text{m}$	$B \sim 10^{-21} - 10^{-18} \text{ Pa} \cdot \text{m}^4$	No control on pitch angle
[6]	Ribbon	Strain anisotropy	$R = 5 - 30 \mu\text{m}$	$B \sim 10^{-17} - 10^{-16} \text{ Pa} \cdot \text{m}^4$	Full shape control
[92]	Ribbon	Differential swelling	$R = 2 - 8 \mu\text{m}$	Not measured	Inter-dependency between radius and pitch angle
[97]	Hollow tube	Self-assembly	$R = 0.2 - 2 \mu\text{m}$	Not measured	Full shape control

TABLE 1.1 – Synthesis of the available fabrication methods for micron-sized flexible helices. For two studies, filament flexibility is apparent but has not been precisely quantified. Full shape control means that all geometrical parameters *i.e.* radius, pitch and length, are independently tunable.

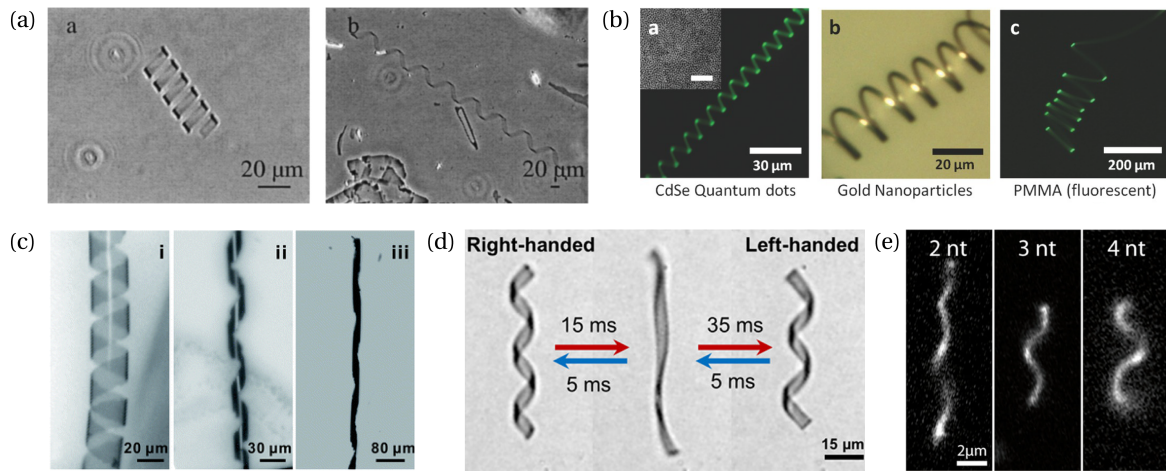


FIGURE 1.3 – Various micro-fabricated flexible helices. (a) Self-assembled cholesteric helical ribbons obtained by Zastavker et al. [94] with (left) low pitch helical ribbon $\alpha = 11^\circ$ and (right) high pitch helical ribbon $\alpha = 54^\circ$. (b) Helical ribbons of various materials obtained by Pham et al. [20]. (c) Titanium-made helical ribbons of various pitch angles $\alpha = 20^\circ, 50^\circ, 70^\circ$ obtained by Li et al. [6]. (d) Dynamic handedness reversal of a hydrogel helical ribbon triggered by temperature change, obtained by Zhang et al. [92]. (e) Helical DNA tile tubes with various pitch angles, obtained by Maier et al. [97].

obtaining a bending modulus of $B \sim 10^{-18} - 10^{-17} \text{ Pa} \cdot \text{m}^4$ *i.e.* stiffer than typical bacterial flagella.

Pham et al. reported a self-coiling mechanism from two-dimensional ribbons driven by surface tension [20]. When the ribbons are immersed in a fluid, they self-coil into a helical shape. The helical radius is tunable at will and various materials can be used, as illustrated in fig. 1.3 (b). However, although slightly different values can be obtained for the helical pitch depending on the material, control of the pitch is not achieved. The bending modulus varies depending on the ribbon width and thickness and ranges within $B \sim 10^{-21} - 10^{-18} \text{ Pa} \cdot \text{m}^4$ *i.e.* close to the typical values for bacterial flagella. Applicability of this fabrication method to investigate fluid-structure interaction problems has already been demonstrated, in combination with microfluidic flow control techniques [73, 74]. In this work we adopt this method to produce flexible helices. More details on this method and on the fabrication process are given in chapter 2.

Li et al. obtained helical ribbons by deposition of anisotropic titanium nanomembranes cut into ribbons [6]. Typical helical ribbons are shown in fig. 1.3 (c). Interestingly, full shape control is reported, which would allow parametric study of the fluid-structure interactions. And applicability of this system for fluid-structure interactions studies has already been demonstrated. However, the bending modulus was estimated at $B \sim 10^{-17} \text{ Pa} \cdot \text{m}^4$ *i.e.* significantly stiffer than bacterial flagella. As a result, strong stress must be applied to deform these structures. Furthermore, the helices ribbons are soldered to the substrate, thus preventing study of the behavior in shear flows or in extensional flows.

Zhang et al. reported buckling of gold-coated hydrogel ribbons into helices as a result of differential swelling [92]. The radius and pitch can be varied but are co-dependent, as shown in fig. 1.3 (d). It is apparent that these helical ribbons are flexible, since morphological changes are possible, but the bending modulus was not quantified. Finally, Maier et al. reported self-assembly of micron-sized helical DNA nanotubes, achieved by selectively adding or deleting base pair in the DNA filaments [97]. Full shape control is demonstrated but helical radii do not exceed $2 \mu\text{m}$. High flexibility is expected given that the filament diameter is nanometric, but the bending modulus was not quantified.

Overall, most of the presented methods result in ribbon-like filaments with only the work of Maier et al. producing circular filaments. This comes in contrast with biological helices, for which the filament is usually cylindrical. This difference in filament cross-section may induce some variations in behavior between fabricated helical ribbons and biological helices. So far, the experimental studies relying on micro-fabricated helical ribbons as model systems have neglected these differences [73, 74, 99]. The fabrication method proposed by Maier et al. would allow fabrication of helically-shaped cylindrical filaments but integrability within a microfluidic set-up has not been demonstrated yet.



In this chapter, we have introduced fluid-structure interaction problems and reviewed some fundamental results. We have underlined the interest of studying the interactions between flexible helices and viscous flows. The state of the art of this topic was discussed and we highlighted the crucial coupling between chirality and flexibility. Influence of the chirality is mainly set by the rescaled helical pitch p/R (equivalent to the pitch angle α) while influence of the flexibility is set by the filament bending modulus. Accurate characterization and control of these parameters is thus crucial. Within an analytical or numerical approach, this is easily achieved but within an experimental approach at the micro-scale, fabrication of flexible helices with controlled geometrical and mechanical parameters is a challenge. We reviewed the existing fabrication methods and found that no method results in flexible helices with full shape and flexibility control.

In this work, we experimentally investigate the mechanics of flexible helices and their behavior in viscous flows. We rely on the fabrication method of helical ribbons developed by Pham et al. [20], combined with microfluidic flow control techniques. The obtained helices are highly flexible and control of the radius and length is already achieved. In the next chapter, we detail the experimental methods as well as the rest of the experimental set-up.

1.4 References

- [1] Eric Lauga and Thomas R Powers. The hydrodynamics of swimming microorganisms. *Reports on Progress in Physics*, 72(9):096601, 2009. [14](#), [16](#), [20](#), [23](#)
- [2] Gaoshan Huang and Yongfeng Mei. Helices in micro-world: Materials, properties, and applications. *Journal of Materiomics*, 1(4):296–306, 2015. [14](#)
- [3] Lichun Liu, Liqiu Zhang, Sang Min Kim, and Sungho Park. Helical metallic micro-and nanostructures: fabrication and application. *Nanoscale*, 6(16):9355–9365, 2014. [14](#)
- [4] Bradley J Nelson, Ioannis K Kaliakatsos, and Jake J Abbott. Microrobots for minimally invasive medicine. *Annual review of biomedical engineering*, 12:55–85, 2010. [14](#), [21](#), [23](#)
- [5] Rafaele Attia, Daniel C Pregibon, Patrick S Doyle, Jean-Louis Viovy, and Denis Bartolo. Soft microflow sensors. *Lab on a Chip*, 9(9):1213–1218, 2009. [14](#)
- [6] Weiming Li, Gaoshan Huang, Jiao Wang, Ying Yu, Xiaojing Wu, Xugao Cui, and Yongfeng Mei. Superelastic metal microsprings as fluidic sensors and actuators. *Lab on a Chip*, 12(13):2322–2328, 2012. [14](#), [22](#), [26](#), [27](#), [28](#)
- [7] Masato Makino and Masao Doi. Migration of twisted ribbon-like particles in simple shear flow. *Physics of Fluids*, 17(10):103605, 2005. [14](#), [23](#)
- [8] Marcos, Henry C Fu, Thomas R Powers, Roman Stocker, et al. Separation of microscale chiral objects by shear flow. *Physical review letters*, 102(15):158103, 2009. [14](#), [22](#), [26](#)
- [9] Marcin Kostur, Michael Schindler, Peter Talkner, and Peter Hänggi. Chiral separation in microflows. *Physical review letters*, 96(1):014502, 2006. [14](#), [23](#)
- [10] Martina Palusa, Joost De Graaf, Aidan Brown, and Alexander Morozov. Sedimentation of a rigid helix in viscous media. *Physical Review Fluids*, 3(12):124301, 2018. [14](#)
- [11] Qi-Yi Zhang. Chirality-specific lift forces of helix under shear flows: Helix perpendicular to shear plane. *Chirality*, 29(2):97–102, 2017. [14](#)
- [12] Arnold JTM Mathijssen, Nuris Figueroa-Morales, Gaspard Junot, Éric Clément, Anke Lindner, and Andreas Zöttl. Oscillatory surface rheotaxis of swimming e. coli bacteria. *Nature communications*, 10(1):1–12, 2019. [14](#)
- [13] MunJu Kim and Thomas R Powers. Deformation of a helical filament by flow and electric or magnetic fields. *Physical Review E*, 71(2):021914, 2005. [14](#), [22](#), [25](#)
- [14] Mohammad K Jawed, Noor K Khouri, Fang Da, Eitan Grinspun, and Pedro M Reis. Propulsion and instability of a flexible helical rod rotating in a viscous fluid. *Physical review letters*, 115(16):168101, 2015. [14](#), [23](#), [26](#)
- [15] Mohammad K Jawed and Pedro M Reis. Deformation of a soft helical filament in an axial flow at low reynolds number. *Soft matter*, 12(6):1898–1905, 2016. [14](#), [22](#)
- [16] MK Jawed and Pedro M Reis. Dynamics of a flexible helical filament rotating in a viscous fluid near a rigid boundary. *Physical Review Fluids*, 2(3):034101, 2017. [26](#)

- [17] Run Li, Gerhard Gompper, and Marisol Ripoll. Tumbling and vorticity drift of flexible helicoidal polymers in shear flow. *Macromolecules*, 54(2):812–823, 2021. [14](#), [23](#), [25](#)
- [18] Hyun Suk Kim, Cheol Hee Lee, PK Sudeep, Todd Emrick, and Alfred J Crosby. Nanoparticle stripes, grids, and ribbons produced by flow coating. *Advanced Materials*, 22(41):4600–4604, 2010. [15](#)
- [19] Dong Yun Lee, Jonathan T Pham, Jimmy Lawrence, Cheol Hee Lee, Cassandra Parkos, Todd Emrick, and Alfred J Crosby. Macroscopic nanoparticle ribbons and fabrics. *Advanced materials*, 25(9):1248–1253, 2013.
- [20] Jonathan T Pham, Jimmy Lawrence, Dong Yun Lee, Gregory M Grason, Todd Emrick, and Alfred J Crosby. Highly stretchable nanoparticle helices through geometric asymmetry and surface forces. *Advanced Materials*, 25(46):6703–6708, 2013. [15](#), [26](#), [27](#), [28](#)
- [21] HL Goldsmith, Jean Marlow, and Frank Campbell MacIntosh. Flow behaviour of erythrocytes-i. rotation and deformation in dilute suspensions. *Proceedings of the Royal Society of London. Series B. Biological Sciences*, 182(1068):351–384, 1972. [16](#)
- [22] Christopher Brennen and Howard Winet. Fluid mechanics of propulsion by cilia and flagella. *Annual Review of Fluid Mechanics*, 9(1):339–398, 1977. [16](#)
- [23] Raghunath Chelakkot, Roland G Winkler, and Gerhard Gompper. Migration of semiflexible polymers in microcapillary flow. *EPL (Europhysics Letters)*, 91(1):14001, 2010. [17](#)
- [24] S Reddig and H Stark. Cross-streamline migration of a semiflexible polymer in a pressure driven flow. *The Journal of chemical physics*, 135(16):10B620, 2011.
- [25] Dagmar Steinhauser, Sarah Koster, and Thomas Pfohl. Mobility gradient induces cross-streamline migration of semiflexible polymers. *ACS Macro Letters*, 1(5):541–545, 2012.
- [26] Alexander Farutin and Chaouqi Misbah. Symmetry breaking and cross-streamline migration of three-dimensional vesicles in an axial poiseuille flow. *Physical review E*, 89(4):042709, 2014.
- [27] Gerrit Danker, Petia M Vlahovska, and Chaouqi Misbah. Vesicles in poiseuille flow. *Physical review letters*, 102(14):148102, 2009. [17](#)
- [28] Sylwia Pawłowska, Paweł Nakielski, Filippo Pierini, Izabela K Piechocka, Krzysztof Zembrzycki, and Tomasz A Kowalewski. Lateral migration of electrospun hydrogel nanofilaments in an oscillatory flow. *PloS one*, 12(11):e0187815, 2017. [17](#)
- [29] Kaustav Chaudhury, Shubhadeep Mandal, and Suman Chakraborty. Droplet migration characteristics in confined oscillatory microflows. *Physical Review E*, 93(2):023106, 2016.
- [30] Y-L Chen, MD Graham, JJ De Pablo, K Jo, and DC Schwartz. Dna molecules in microfluidic oscillatory flow. *Macromolecules*, 38(15):6680–6687, 2005. [17](#)

- [31] GG Stokes. On the effect of internal friction of fluids on the motion of pendulums. *Trans. Camb. phil. Soc.*, 9(8):106, 1850. [18](#)
- [32] Anton Oberbeck. Ueber stationäre flüssigkeitsbewegungen mit berücksichtigung der inneren reibung. In *Journal für die reine und angewandte Mathematik Band 81*, pages 62–80. De Gruyter, 2021. [18](#)
- [33] RG Cox. The motion of long slender bodies in a viscous fluid part 1. general theory. *Journal of Fluid mechanics*, 44(4):791–810, 1970. [18](#)
- [34] Lyndon Koens and Eric Lauga. Analytical solutions to slender-ribbon theory. *Physical Review Fluids*, 2(8):084101, 2017. [18](#)
- [35] George Barker Jeffery. The motion of ellipsoidal particles immersed in a viscous fluid. *Proceedings of the Royal Society of London. Series A, Containing papers of a mathematical and physical character*, 102(715):161–179, 1922. [19](#)
- [36] Francis P Bretherton. The motion of rigid particles in a shear flow at low reynolds number. *Journal of Fluid Mechanics*, 14(2):284–304, 1962. [19](#)
- [37] LG Leal and EJ Hinch. The effect of weak brownian rotations on particles in shear flow. *Journal of Fluid Mechanics*, 46(4):685–703, 1971. [19](#)
- [38] EJ Hinch and LG Leal. Constitutive equations in suspension mechanics. part 2. approximate forms for a suspension of rigid particles affected by brownian rotations. *Journal of Fluid Mechanics*, 76(1):187–208, 1976. [19](#)
- [39] S Mueller, EW Llewellyn, and HM Mader. The rheology of suspensions of solid particles. *Proceedings of the Royal Society A: Mathematical, Physical and Engineering Sciences*, 466(2116):1201–1228, 2010. [19](#)
- [40] Robert L Powell. Rheology of suspensions of rodlike particles. *Journal of statistical physics*, 62(5):1073–1094, 1991. [19](#)
- [41] EJ Hinch and LG Leal. Rotation of small non-axisymmetric particles in a simple shear flow. *Journal of Fluid Mechanics*, 92(3):591–607, 1979. [19](#)
- [42] J Einarsson, BM Mihiretie, A Laas, S Ankardal, JR Angilella, D Hanstorp, and B Mehlig. Tumbling of asymmetric microrods in a microchannel flow. *Physics of Fluids*, 28(1):013302, 2016. [19](#)
- [43] JM Rallison. The deformation of small viscous drops and bubbles in shear flows. *Annual review of fluid mechanics*, 16(1):45–66, 1984. [19](#)
- [44] Thomas T Perkins, Douglas E Smith, and Steven Chu. Single polymer dynamics in an elongational flow. *Science*, 276(5321):2016–2021, 1997. [19](#)
- [45] Douglas E Smith, Hazen P Babcock, and Steven Chu. Single-polymer dynamics in steady shear flow. *Science*, 283(5408):1724–1727, 1999. [19](#)
- [46] Robert Byron Bird, Robert Calvin Armstrong, and Ole Hassager. Dynamics of polymeric liquids. vol. 1: Fluid mechanics. 1987. [19](#)

- [47] D Barthes-Biesel. Role of interfacial properties on the motion and deformation of capsules in shear flow. *Physica A: Statistical Mechanics and its Applications*, 172(1-2): 103–124, 1991. [19](#)
- [48] Manouk Abkarian and Annie Viallat. Vesicles and red blood cells in shear flow. *Soft Matter*, 4(4):653–657, 2008. [19](#)
- [49] Vasiliiy Kantsler and Victor Steinberg. Transition to tumbling and two regimes of tumbling motion of a vesicle in shear flow. *Physical review letters*, 96(3):036001, 2006.
- [50] Chaouqi Misbah. Vacillating breathing and tumbling of vesicles under shear flow. *Physical review letters*, 96(2):028104, 2006.
- [51] Manouk Abkarian, Magalie Faivre, and Annie Viallat. Swinging of red blood cells under shear flow. *Physical review letters*, 98(18):188302, 2007.
- [52] Clément de Loubens, Julien Deschamps, Florence Edwards-Lévy, and Marc Leonetti. Tank-treading of microcapsules in shear flow. *Journal of Fluid Mechanics*, 789:750–767, 2016. [19](#)
- [53] Vasily Kantsler and Raymond E Goldstein. Fluctuations, dynamics, and the stretch-coil transition of single actin filaments in extensional flows. *Physical review letters*, 108(3):038103, 2012. [19](#)
- [54] N Quennouz, Michael Shelley, O Du Roure, and A Lindner. Transport and buckling dynamics of an elastic fibre in a viscous cellular flow. *Journal of Fluid Mechanics*, 769: 387–402, 2015. [19](#)
- [55] Brato Chakrabarti, Yanan Liu, John LaGrone, Ricardo Cortez, Lisa Fauci, Olivia Du Roure, David Saintillan, and Anke Lindner. Flexible filaments buckle into helical shapes in strong compressional flows. *Nature Physics*, 16(6):689–694, 2020. [19](#)
- [56] Markus Harasim, Bernhard Wunderlich, Orit Peleg, Martin Kröger, and Andreas R Bausch. Direct observation of the dynamics of semiflexible polymers in shear flow. *Physical review letters*, 110(10):108302, 2013. [20](#)
- [57] Yanan Liu, Brato Chakrabarti, David Saintillan, Anke Lindner, and Olivia Du Roure. Morphological transitions of elastic filaments in shear flow. *Proceedings of the National Academy of Sciences*, 115(38):9438–9443, 2018. [20](#)
- [58] Edward M Purcell. Life at low reynolds number. *American journal of physics*, 45(1): 3–11, 1977. [20](#)
- [59] Kenta Ishimoto and Michio Yamada. A coordinate-based proof of the scallop theorem. *SIAM Journal on Applied Mathematics*, 72(5):1686–1694, 2012. [20](#)
- [60] Linda Turner, William S Ryu, and Howard C Berg. Real-time imaging of fluorescent flagellar filaments. *Journal of bacteriology*, 182(10):2793–2801, 2000. [20](#), [21](#)
- [61] MunJu Kim, James C Bird, Annemarie J Van Parys, Kenneth S Breuer, and Thomas R Powers. A macroscopic scale model of bacterial flagellar bundling. *Proceedings of the National Academy of Sciences*, 100(26):15481–15485, 2003. [20](#)

- [62] Shang Yik Reigh, Roland G Winkler, and Gerhard Gompper. Synchronization and bundling of anchored bacterial flagella. *Soft Matter*, 8(16):4363–4372, 2012. [20](#)
- [63] Robert M Macnab and May Kihara Ornston. Normal-to-curly flagellar transitions and their role in bacterial tumbling. stabilization of an alternative quaternary structure by mechanical force. *Journal of molecular biology*, 112(1):1–30, 1977. [20](#)
- [64] Marco J Kühn, Felix K Schmidt, Bruno Eckhardt, and Kai M Thormann. Bacteria exploit a polymorphic instability of the flagellar filament to escape from traps. *Proceedings of the National Academy of Sciences*, 114(24):6340–6345, 2017. [20](#)
- [65] S Fujime, M Maruyama, and S Asakura. Flexural rigidity of bacterial flagella studied by quasielastic scattering of laser light. *Journal of molecular biology*, 68(2):347–359, 1972. [20](#)
- [66] Nicholas C Darnton and Howard C Berg. Force-extension measurements on bacterial flagella: triggering polymorphic transformations. *Biophysical journal*, 92(6):2230–2236, 2007. [20](#)
- [67] Shlomo Trachtenberg and Ilan Hammel. The rigidity of bacterial flagellar filaments and its relation to filament polymorphism. *Journal of structural biology*, 109(1):18–27, 1992. [20](#), [26](#)
- [68] Charles W Wolgemuth. Flagellar motility of the pathogenic spirochetes. In *Seminars in cell & developmental biology*, volume 46, pages 104–112. Elsevier, 2015. [20](#), [21](#)
- [69] Li Zhang, Jake J Abbott, Lixin Dong, Kathrin E Peyer, Bradley E Kratochvil, Haixin Zhang, Christos Bergeles, and Bradley J Nelson. Characterizing the swimming properties of artificial bacterial flagella. *Nano letters*, 9(10):3663–3667, 2009. [21](#)
- [70] Bruce Rodenborn, Chih-Hung Chen, Harry L Swinney, Bin Liu, and HP Zhang. Propulsion of microorganisms by a helical flagellum. *Proceedings of the National Academy of Sciences*, 110(5):E338–E347, 2013. [22](#), [23](#), [25](#)
- [71] Panayiota Katsamba and Eric Lauga. Propulsion by stiff elastic filaments in viscous fluids. *Physical Review E*, 99(5):053107, 2019. [22](#), [23](#), [25](#)
- [72] Hiroshi Hoshikawa and Ritsu Kamiya. Elastic properties of bacterial flagellar filaments: II. determination of the modulus of rigidity. *Biophysical chemistry*, 22(3):159–166, 1985. [22](#), [26](#)
- [73] Jonathan T Pham, Alexander Morozov, Alfred J Crosby, Anke Lindner, and Olivia du Roure. Deformation and shape of flexible, microscale helices in viscous flow. *Physical Review E*, 92(1):011004, 2015. [22](#), [27](#), [28](#)
- [74] Marine Daieff. *Deformation and shape of flexible, microscale helices in viscous flows*. PhD thesis, Sorbonne Paris Cité, 2018. [22](#), [26](#), [27](#), [28](#)
- [75] Y-J Kim and WJ Rae. Separation of screw-sensed particles in a homogeneous shear field. *International journal of multiphase flow*, 17(6):717–744, 1991. [22](#)

- [76] Jens Elgeti, Roland G Winkler, and Gerhard Gompper. Physics of microswimmers—single particle motion and collective behavior: a review. *Reports on progress in physics*, 78(5):056601, 2015. [23](#)
- [77] Bin Liu, Thomas R Powers, and Kenneth S Breuer. Force-free swimming of a model helical flagellum in viscoelastic fluids. *Proceedings of the National Academy of Sciences*, 108(49):19516–19520, 2011. [23](#)
- [78] AM Leshansky. Enhanced low-reynolds-number propulsion in heterogeneous viscous environments. *Physical Review E*, 80(5):051911, 2009. [23](#)
- [79] Ellis Harold Dill. Kirchhoff’s theory of rods. *Archive for History of Exact Sciences*, pages 1–23, 1992. [24](#)
- [80] James Lighthill. Flagellar hydrodynamics. *SIAM review*, 18(2):161–230, 1976. [24](#)
- [81] G Gompper, T Ihle, DM Kroll, and RG Winkler. Multi-particle collision dynamics: A particle-based mesoscale simulation approach to the hydrodynamics of complex fluids. *Advanced computer simulation approaches for soft matter sciences III*, pages 1–87, 2009. [25](#)
- [82] Danielle J Mai, Christopher Brockman, and Charles M Schroeder. Microfluidic systems for single dna dynamics. *Soft matter*, 8(41):10560–10572, 2012. [26](#)
- [83] Zheng Ren and Pu-Xian Gao. A review of helical nanostructures: growth theories, synthesis strategies and properties. *Nanoscale*, 6(16):9366–9400, 2014. [26](#)
- [84] Soichiro Tottori, Li Zhang, Famin Qiu, Krzysztof K Krawczyk, Alfredo Franco-Obregón, and Bradley J Nelson. Magnetic helical micromachines: fabrication, controlled swimming, and cargo transport. *Advanced materials*, 24(6):811–816, 2012. [26](#)
- [85] Haojian Lu, Panbing Wang, Rong Tan, Xiong Yang, and Yajing Shen. Nanorobotic system for precise in situ three-dimensional manufacture of helical microstructures. *IEEE Robotics and Automation Letters*, 3(4):2846–2853, 2018. [26](#)
- [86] PES Silva, F Vistulo de Abreu, and MH Godinho. Shaping helical electrospun filaments: a review. *Soft Matter*, 13(38):6678–6688, 2017. [26](#)
- [87] Li Zhang, Jake J Abbott, Lixin Dong, Bradley E Kratochvil, Dominik Bell, and Bradley J Nelson. Artificial bacterial flagella: Fabrication and magnetic control. *Applied Physics Letters*, 94(6):064107, 2009. [26](#)
- [88] Minghuang Huang, Carl Boone, Michelle Roberts, Don E Savage, Max G Lagally, Nakul Shaji, Hua Qin, Robert Blick, John A Nairn, and Feng Liu. Nanomechanical architecture of strained bilayer thin films: from design principles to experimental fabrication. *Advanced Materials*, 17(23):2860–2864, 2005.
- [89] Joonwoo Jeong, Yigil Cho, Su Yeon Lee, Xingting Gong, Randall D Kamien, Shu Yang, and Arjun G Yodh. Topography-guided buckling of swollen polymer bilayer films into three-dimensional structures. *Soft matter*, 13(5):956–962, 2017.
- [90] Jia Liu, Jiangshui Huang, Tianxiang Su, Katia Bertoldi, and David R Clarke. Structural transition from helices to hemihelices. *PloS one*, 9(4), 2014. [26](#)

- [91] Stéphane Douezan, Matthieu Wyart, Françoise Brochard-Wyart, and Damien Cuvelier. Curling instability induced by swelling. *Soft Matter*, 7(4):1506–1511, 2011. [26](#)
- [92] Hang Zhang, Ahmed Mourran, and Martin Moller. Dynamic switching of helical microgel ribbons. *Nano letters*, 17(3):2010–2014, 2017. [26](#), [27](#), [28](#)
- [93] Xiaojiao Yu, Lina Zhang, Nan Hu, Hannah Grover, Shicheng Huang, Dong Wang, and Zi Chen. Shape formation of helical ribbons induced by material anisotropy. *Applied Physics Letters*, 110(9):091901, 2017. [26](#)
- [94] Yevgeniya V Zastavker, Neer Asherie, Aleksey Lomakin, Jayanti Pande, Joanne M Donovan, Joel M Schnur, and George B Benedek. Self-assembly of helical ribbons. *Proceedings of the National Academy of Sciences*, 96(14):7883–7887, 1999. [26](#), [27](#)
- [95] Yeo-Wan Chiang, Rong-Ming Ho, Christian Burger, and Hirokazu Hasegawa. Helical assemblies from chiral block copolymers. *Soft Matter*, 7(21):9797–9803, 2011. [26](#)
- [96] Supitchaya Iamsaard, Sarah J AShoff, Benjamin Matt, Tibor Kudernac, Jeroen JLM Cornelissen, Stephen P Fletcher, and Nathalie Katsonis. Conversion of light into macroscopic helical motion. *Nature chemistry*, 6(3):229–235, 2014. [26](#)
- [97] Alexander Mario Maier, Wooli Bae, Daniel Schiffels, Johannes Friedrich Emmerig, Maximilian Schiff, and Tim Liedl. Self-assembled dna tubes forming helices of controlled diameter and chirality. *ACS nano*, 11(2):1301–1306, 2017. [26](#), [27](#), [28](#)
- [98] Brice Smith, Yevgeniya V Zastavker, and George B Benedek. Tension-induced straightening transition of self-assembled helical ribbons. *Physical review letters*, 87(27):278101, 2001. [26](#)
- [99] Jonathan T Pham, Jimmy Lawrence, Gregory M Grason, Todd Emrick, and Alfred J Crosby. Stretching of assembled nanoparticle helical springs. *Physical Chemistry Chemical Physics*, 16(22):10261–10266, 2014. [28](#)

Chapter 2

Fabrication of Flexible Micro-Helices and Experimental Apparatus

Contents

2.1 Principle of the Helix Fabrication	38
2.2 Experimental Protocol: from Ribbons to Helices	40
2.2.1 Preparation of the Slides and Spin-Coating	40
2.2.2 The Flow-coating Method	41
2.2.3 Control of Ribbon Properties	42
2.2.4 Control of the Helix Geometry	44
2.3 Factors for Optimal Helix Fabrication	45
2.3.1 Ribbon Fabrication Issues	45
2.3.2 Ribbon Detachment Issues	46
2.3.3 Ribbon Coiling Issues	47
2.4 General Experimental Set-Up	48
2.5 References	51

In this chapter, we describe the experimental methods and techniques leading to the formation of micron-sized helical ribbons, the characterization of their mechanical properties and the study of their behavior in flows. Most preparation and fabrication steps are performed at the PMMH laboratory or at the IPGG micro-fabrication platform. Notably, the fabrication set-up for helical ribbons was adapted and installed at the PMMH laboratory. In previous works [1], the fabrication was performed by the Crosby group at the University of Massachusetts, Amherst, USA. This gives us much more control on the fabrication settings, as well as a quicker and more efficient feed-back loop to optimize the obtained helices.

The chapter is organized as follows. In section 2.1 we introduce the principles of the helix fabrication method and explain the underlying physical phenomenon. In section 2.2 we describe the helix fabrication set-up and the successive experimental steps followed to obtain helical ribbons. We discuss control of the helix properties, geometrical and mechanical. We then identify in section 2.3 the key parameters that ensure optimal ribbon fabrication and helix formation. Finally, in section 2.4 we describe the experimental apparatus.

2.1 Principle of the Helix Fabrication

The fabrication method relies on the spontaneous coiling of ribbons exhibiting flat triangular cross-sections. This phenomenon was highlighted and explained by several works from the Crosby group at UMass [2-4]. Ribbons are prepared through an evaporative assembly technique. They display, as a result of the fabrication process, a flat triangular cross-section of width w (typically few micrometers) and thickness $t \ll w$ (typically tens of nanometers), as depicted in fig. 2.1 (a). Upon release of the ribbons into a liquid, they spontaneously coil into a helical geometry. We show in fig. 2.1 (b) a chronophotography of the coiling process for a ribbon in water. The driving force of the coiling is the reduction of the surface area induced by bending, and hence of the surface free energy associated with the ribbon/liquid interface. This bending-induced energy decrease is made possible by the asymmetry of the ribbons' cross-section.

Indeed, for a triangular cross-section, the center of area X_{ca} and the center of perimeter X_{cp} do not coincide in general. They only coincide in the case of an equilateral triangle, which is far from our experimental conditions. We set $y = 0$ at the base of the triangle, the center of area then corresponds to

$$y_{ca} = \frac{1}{A} \iint y \, dA = \frac{2}{wt} \int_0^t yw \left(1 - \frac{y}{t}\right) dy = \frac{t}{3} \quad (2.1.1)$$

while the center of perimeter corresponds to

$$y_{cp} = \frac{1}{P} \oint y \, dP = \frac{1}{P} \int_0^t \frac{y}{t} \sqrt{4t^2 + w^2} \, dy = \frac{t}{2} \left(1 - \frac{w}{P}\right) \quad (2.1.2)$$

with the perimeter $P = w + \sqrt{w^2 + 4t^2}$ and area $A = wt/2$. For flat triangular cross-sections, we have $t \ll w$ so $y_{cp} \approx 1/4 < y_{ca}$: there is more perimeter below the center of area than above the center of area. We consider bending of the ribbon around the width direction, as represented in fig. 2.1 (c). The intersection of the neutral axis of deformation with the cross-section is the center of area. The material above the neutral axis is stretched while the

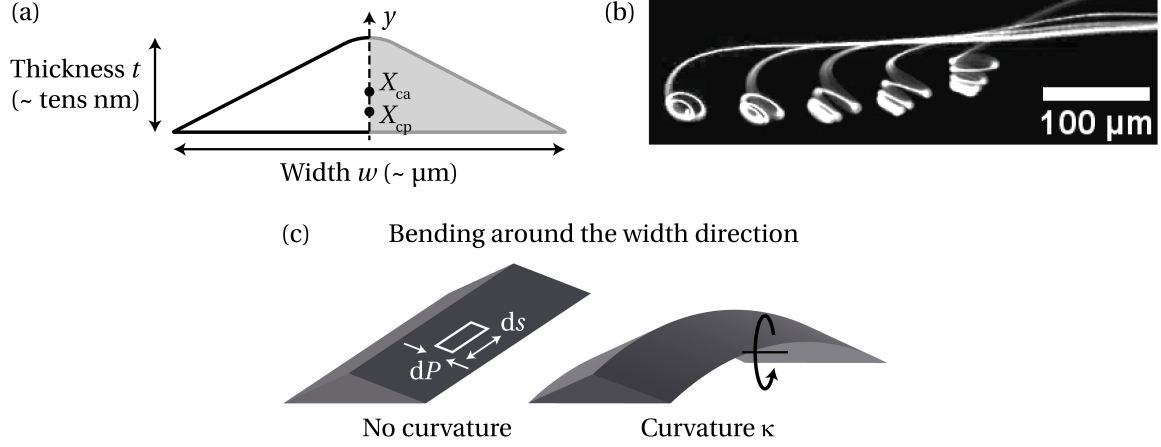


FIGURE 2.1 – (a) Schematic of a triangular cross-section with thickness t and width w . The ratio t/w is not at scale with typical experimental values. X_{ca} and X_{cp} indicate respectively the position of the center of area and of the center of perimeter. (b) Chronophotography of a ribbon, made with poly(methyl methacrylate) (PMMA), coiling in water. The time step between pictures is 2 seconds. (c) Schematic illustrating the bending mode around the width direction, for a triangular ribbon. We draw on the non-curved configuration an element of the ribbon surface, characterized by its length ds and contribution to the cross-section perimeter dP .

material below the neutral axis is compressed. Naturally, this corresponds to an increase in the surface area above the neutral axis and a decrease in the surface area below the neutral axis. For symmetrical cross-sections, these changes in area would compensate: no net change in area would be obtained. But for asymmetrical cross-sections, because more perimeter is situated below the neutral axis than above, a net change in area is obtained.

In more details, we denote \vec{n} the vector normal to the neutral axis and κ the curvature of the neutral axis. We consider an element of the ribbon surface of length ds and contribution dP to the total cross-section perimeter. We draw in fig. 2.1 (c) such an element. We denote \vec{X} its position. The change of area of this surface element induced by a change of curvature $\Delta\kappa$ is given by

$$dA = \Delta\kappa \vec{n} \cdot (\vec{X} - \vec{X}_{ca}) ds dP \quad (2.1.3)$$

with \vec{X}_{ca} position of the center of area. Integrating over the perimeter gives

$$dA = \Delta\kappa P \vec{n} \cdot (\vec{X}_{cp} - \vec{X}_{ca}) ds \quad (2.1.4)$$

with \vec{X}_{cp} position of the center of perimeter. In the case of a flat triangular cross-section, the surface area change per unit length is simply given by

$$\frac{dA}{ds} = -\Delta\kappa P \frac{t}{12} = -\Delta\kappa \frac{tw}{6} \quad (2.1.5)$$

We do obtain that bending of the ribbon decreases the total surface area. This decrease in the surface area is associated with a decrease in the surface free energy. It is apparent from eq. (2.1.4) that this phenomenon is a consequence of the cross-section asymmetry, allowing $\vec{X}_{cp} \neq \vec{X}_{ca}$.

Ribbon equilibrium is given by balance with the elastic energy cost associated to bending. The elastic energy cost per unit length associated with a change of curvature $\Delta\kappa$ is

$$\frac{dU}{ds} = B\Delta\kappa^2 \quad (2.1.6)$$

with $B = EI$ ribbon bending modulus, $B = (1/36)Ewt^3$ for triangular cross-sections. Minimization of the total energy per unit length $\frac{dE}{ds} = B\Delta\kappa^2 - G\Delta\kappa\frac{tw}{6}$ yields a preferred curvature

$$\kappa_0 = \frac{1}{12} \frac{Gtw}{B} = 3 \frac{G}{Et^2} \quad (2.1.7)$$

where G is the liquid/ribbon interfacial tension. The quantity G/E is the elasto-capillary length of the material. In most cases we will have $G \sim \gamma$ surface tension of the liquid. This law and the scaling $\kappa_0 \propto 1/t^2$ was predicted and experimentally confirmed by the work of Pham et al. [3]. Interestingly, the mechanism for helix formation is not specific to a material but stems only from the cross-section geometry.

Flat triangular ribbons hence exhibit a preferred curvature, but there is no energetic incentive to twisting the ribbons. The preferred ribbon torsion is thus zero, favoring tightly coiled helices. As shown in fig. 2.1 (b), the helix shape does converge towards a tight configuration. A non-zero pitch is observed nonetheless due to ribbon non-intersection: the pitch is determined by ribbon self-contact. The pitch is thus of the order of the ribbon width w . The resulting object is a uniform tightly packed helical ribbon.

2.2 Experimental Protocol: from Ribbons to Helices

The evaporative assembly technique that produces these flat triangular ribbons is called the flow-coating method. Here, we describe the successive steps involved, following the method established by Lee et al. [2].

2.2.1 Preparation of the Slides and Spin-Coating

Firstly, we prepare glass slides coated with a sacrificial layer. In the overwhelming majority of cases, ribbons will be released in water or in water-based solutions. Thus, the sacrificial layer is usually water dissoluble. The preparation of the coated slides goes as follows. Commercially bought glass slides, of size $24 \text{ mm} \times 40 \text{ mm} \times 170 \mu\text{m}$, are carefully cleaned. The glass slides are sonicated for 15 minutes in three successive solutions: water and soap, then water, and finally isopropanol. The glass slides are then dried using an air gun and introduced in an oxygen plasma cleaner during a few minutes. This step further cleans the surface and enhances the hydrophilicity of the surface. This improves the affinity between the glass surface and the sacrificial layer that will be coated onto it.

To deposit a thin and homogeneous sacrificial layer, we use a spin-coating method. The material chosen for the sacrificial layer is suspended in a solvent. Depending on the ribbon material, we use either a $25 \text{ mg} \cdot \text{mL}^{-1}$ solution of polyacrylic acid (PAA, $M_w = 1800$, Sigma-Aldrich) in pure water or a $20 \text{ mg} \cdot \text{mL}^{-1}$ solution of polystyrene sulfonate (PSS, $M_w = 70 \times 10^3$, Sigma-Aldrich) in pure water. The solution is applied onto the cleaned and hydrophilized glass surface by spin-coating (using the spin-coater POLOS Spin150i). For PAA, slides are spun at 3000 rpm (rotation per minute) for 30s, which creates a homogeneous $\sim 25 \text{ nm}$ thick layer. For PSS, slides are spun at 500 rpm for 10s, then at 2000 rpm for 40s, which creates a homogeneous $\sim 50 \text{ nm}$ thick layer. Once the spin-coating is done, the glass slides are ready for flow-coating. Ribbon can also be prepared on mica slides. In this case, due to the hydrophilic properties of mica, no sacrificial layer is required. Commercially bought mica slides are simply cleaved and are ready for flow-coating. The

freshly cleaved mica slides need to be flow-coated immediately, as they catch dust very easily.

2.2.2 The Flow-coating Method

The flow-coating method is inspired by the coffee-ring effect, which we illustrate in fig. 2.2 (a). The coffee-ring effect is the phenomenon of particle accumulation along the perimeter of a drying droplet of suspension, at the triple-line of contact. The pattern originates from the outward flow induced by differential solvent evaporation: the liquid evaporating at the pinned edge is replenished by flow from the bulk. The flow-coating method leverages this phenomenon to fabricate ribbons.

The material of interest is suspended in a highly volatile solvent (usually toluene). We denote c the suspension concentration. The materials we work with are poly(methyl methacrylate) (PMMA, $M_w = 120 \times 10^3$, Sigma-Aldrich) and modified poly(dimethylaminoethyl methacrylate) (PDMAEMA). The suspension concentration c for PMMA was varied but typical value is $c = 1 \text{ mg} \cdot \text{mL}^{-1}$. To the PMMA solution, we add a fluorescent dye (Coumarin 153, Sigma-Aldrich) to afford fluorescence of the samples, with typical concentration $1 - 5 \mu\text{g} \cdot \text{mL}^{-1}$. PMMA ribbons are prepared on a PAA sacrificial layer or on mica. The PDMAEMA was prepared by Dylan Barber at UMass by free radical copolymerization of dimethylaminoethyl methacrylate (DMAEMA) with 5 mol% of benzophenone methacrylate (BPMA) and 1 mol% of fluorescein-o-methacrylate (FMA). Addition of BPMA enables

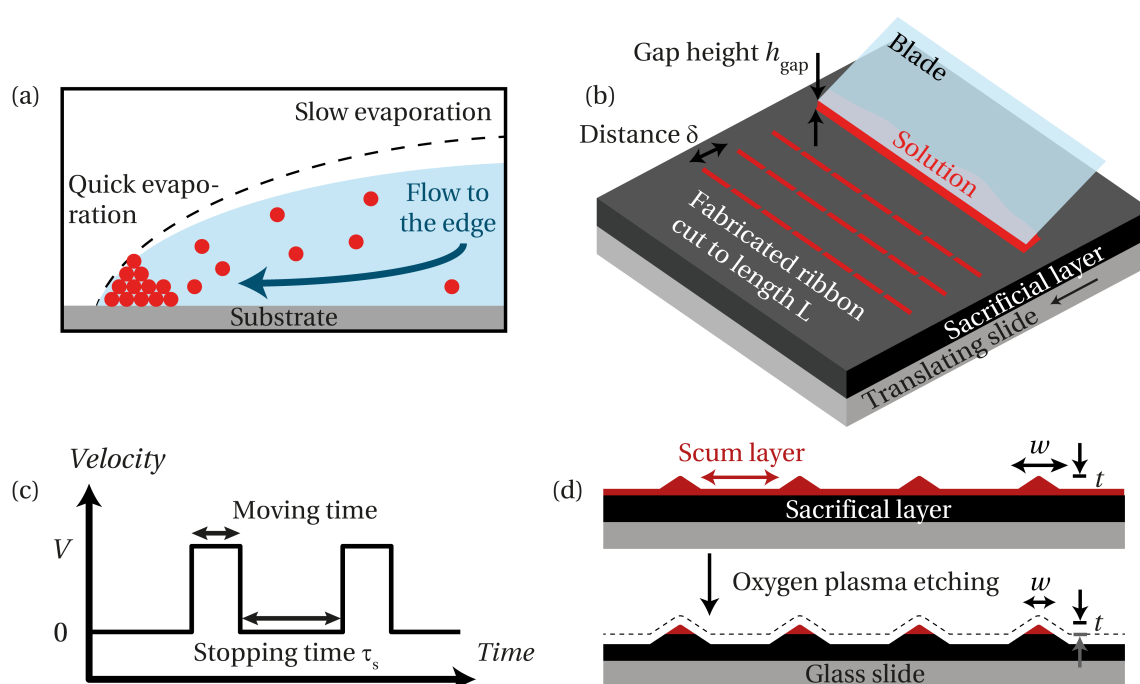


FIGURE 2.2 – (a) Schematic of the coffee-ring effect in the case of a suspension of particles (represented here by red disks). The differential evaporation drives the particles to the triple-line of contact. (b) Experimental apparatus for the flow-coating method. The blade is positioned as to form an angle relative to the substrate and so that the bottom edge of the blade is parallel to the substrate, at a distance h_{gap} . The solution is loaded in the wedge. (c) Typical stop-and-go motion prescribed to the stage mounted with the coated glass slide. The moving time is set by the inter-ribbon distance δ and the moving speed V . (d) Oxygen plasma etching to remove the inter-ribbon scum layer. Typical thickness of the scum layer is $\sim 5 \text{ nm}$. The treatment modifies the thickness and width of the ribbons.

pH response while addition of FMA contributes fluorescence. More details on the polymer preparation can be found in the publication [5]. The suspension concentration c for PDMAEMA ribbons is typically $c = 16 \text{ mg} \cdot \text{mL}^{-1}$. PDMAEMA ribbons are prepared on a PSS sacrificial layer.

Figure 2.2 (b) illustrates the experimental apparatus used for flow-coating. A centimetric rigid straight blade sits at an angle relative to the substrate and the bottom edge of the blade is set parallel to the substrate, at a height h_{gap} . $5 \mu\text{L}$ of solution is loaded in the wedge between the blade and the substrate. Due to capillary forces, the droplet is pinned under the blade and the triple-line of contact on the substrate arranges into a straight line. Hence, the accumulation of particles driven at the edge spontaneously creates a straight ribbon. Finally, the substrate performs a stop-and-go motion prescribed through a motorized stage: between intermittent stopping times τ_s , the stage translates of a fixed distance δ at a fixed velocity V . We show in fig. 2.2 (c) the typical velocity profile applied during the stop-and-go motion of the stage. As the stage moves, the meniscus is stretched by the relative motion of the blade. The contact angle eventually goes below the critical receding angle, at which point the contact line slips and translates from the same distance δ . This stop-and-go motion thus leads to well-aligned stripes of the chosen material. We typically fabricate 10 to 15 ribbons on a given slide, as to increase the total number of helices that would form.

During the stop-and-go motion, the moving time is much smaller than the stopping time. Despite this, some particles are still deposited during the stage translation, *i.e.* between the ribbons. This forms a very thin layer of particles between each ribbon termed the 'scum layer', as illustrated in fig. 2.2 (d). The scum layer links the ribbons together and thus prevents ribbon coiling upon release from the substrate. In order to get rid of the scum-layer, the ribbons are etched by exposure to oxygen plasma after the flow-coating. This technique is very similar to the reactive ion etching method (RIE), which was used in previous works [1]. Oxygen plasma etching is isotropic while RIE provides a more directional etching (downwards usually). Although this difference is essential for some applications like semiconductor engineering, it is not crucial for us. The oxygen plasma etching is further used to control the ribbon thickness and we will describe the method in details in the next section. Once the scum-layer is removed, the samples are ready for experiments. We show in fig. 2.3 various examples of fully formed helices, once the ribbons have coiled. The obtained helices span a very wide range of size, radii ranging from a few microns to more than 50 microns. PDMAEMA ribbons are fabricated much thicker and forms bigger helices than PMMA ribbons. PDMAEMA helices tend to exhibit a non-vanishing pitch *i.e.* $p \neq w$ but the reason for this remains unclear.

2.2.3 Control of Ribbon Properties

The flow-coating is a highly versatile method to fabricate helical ribbons. As the coiling phenomenon is not material related, any material can be used in principle, as long as it can be suspended in a volatile solvent. We work with PMMA and modified PDMAEMA, but Cd-Se quantum dots and gold nano-particles have also been used [3]. Thus, a wide range of material properties can be achieved. The material properties (Young's modulus E and Poisson's ratio ν) naturally dictate the mechanical properties of the ribbon. The geometrical dimensions of the ribbon, thickness t and width w , are controlled by the flow-coating settings. Together with the mechanical properties, they set the ribbon bending

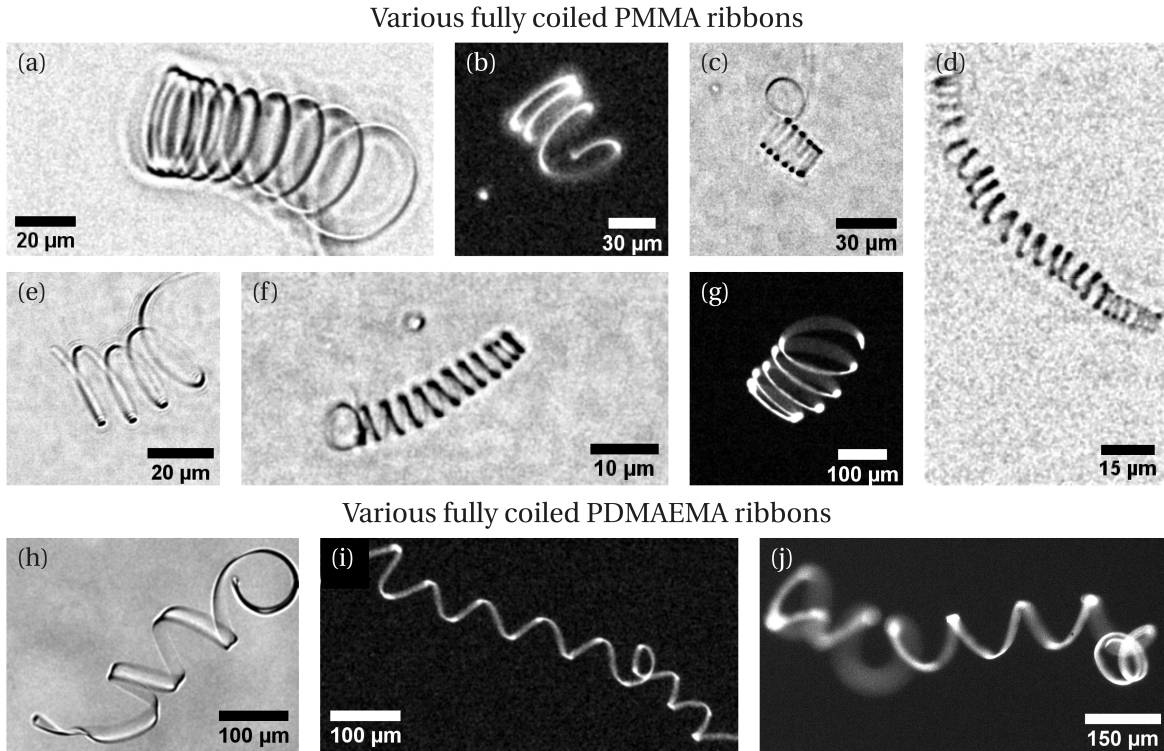


FIGURE 2.3 – Various examples of fully formed helical ribbons, made (a) to (g) from PMMA ribbons or (h) to (j) from PDMAEMA ribbons. Helices span a wide range of radius $R_0 = 5 - 70\mu\text{m}$ and length $L = 0.2 - 3\text{mm}$. Images with a dark background are taken using fluorescence microscopy and images with a light background are taken using phase-contrast bright-field microscopy.

modulus $B = Ewt^3/36$ and twisting modulus $C = \mu wt^3/12$ [6] with $\mu = \frac{E}{2(1+\nu)}$ shear modulus. From these equations, it is apparent that the ribbon thickness is the most crucial parameter for determining the ribbon moduli.

Please note that fabrication and processing of the PDMAEMA ribbons were done by Dylan Barber at UMass. We focus specifically in this section on the processing of PMMA ribbons, giving typical values for this material only. However, the methods that we implement would be identical to characterize and control PDMAEMA ribbons. We recall that typical concentration for PMMA and toluene solutions is $c = 1\text{ mg}\cdot\text{mL}^{-1}$ and that PMMA ribbons are prepared on a PAA sacrificial layer.

The work of Choudhary et al. [7] has established the precise influence of the flow-coating settings, notably the stopping time τ_s and the gap distance h_{gap} , on the ribbon geometrical properties. These results were established for both PMMA ribbons and Cd-Se quantum dots so we can assume they hold true also for PDMAEMA ribbons. They found that $t \propto \tau_s^{(3/5)}$ and $t \propto h_{\text{gap}}^{(1/3)}$. The influence of the concentration was not addressed, but we can reasonably expect that the obtained thickness would increase with solution concentration. The translating velocity V was also found to have a weak influence on the thickness. These findings enable better control of the ribbon dimensions. However, some fabrication settings are difficult to control, the gap height h_{gap} in particular. Precise control of this parameter would require mounting the flow-coating apparatus with a camera, thus complexifying the set-up. We rely on these findings only to control qualitatively the ribbon dimensions: decreasing gap height, stopping time or suspension concentration to decrease the ribbon thickness and width and inversely.

To control precisely the ribbon dimensions, we rather measure the dimensions and use oxygen plasma etching to decrease the thickness and width. Typical thickness after flow-coating lies in the range 30–150 nm so measurements cannot be performed with a standard optical microscope. Measurements are performed with an optical profilometer, which uses a differential interferometry technique (Veeco Wyko NT9100 Optical Profilometer). One should note that the profilometer only measures the height difference between the ribbon and the flat surface around it. Therefore, the measured height difference does not include the scum layer thickness, as illustrated in fig. 2.2 (d). The total ribbon thickness is thus the addition of the measured height and of the scum layer thickness. For a translating speed of $V = 5 \text{ mm} \cdot \text{s}^{-1}$ and concentration $c = 1 \text{ mg} \cdot \text{mL}^{-1}$, typical scum layer thickness is $\sim 5 \text{ nm}$. To estimate the scum layer thickness, we prepare ribbons on bare glass. We then scratch the surface with a blade and as glass is much more resistant than the scum layer, only the PMMA scum layer is scratched. Measuring the depth of the scratch, using the optical profiler, gives the thickness of the scum layer. Once the ribbon thickness is known, the exposure time to oxygen plasma etching is set to obtain the desired thickness. Knowledge of the etching rate, *i.e.* the etching depth per unit time, is naturally also needed. Although some values have been tabulated in the literature [8], the etching rate is highly dependent on the etched material and on the machine used and precise etching parameters. The etching rate therefore needs to be calibrated.

Very critically, in the presence of a sacrificial layer, the ribbon thickness can no longer be measured after etching was performed. This issue is illustrated in fig. 2.2 (d). Indeed, as the sacrificial layer is also etched by the oxygen plasma treatment, there is no stable point of reference conserved during the etching treatment. The thickness measured after etching includes both the ribbon of interest and some sacrificial layer, which will dissolve upon release. Hence, the final ribbon thickness before experiments is not measured but rather computed from the initial thickness, the exposure time to plasma and the etching rate. Unfortunately, this entails a not so good accuracy in determining the ribbon thickness prior to experiments.

This sacrificial layer-related problem needs nonetheless to be circumvented in order to calibrate the etching rate. We proceed simply by preparing ribbons on bare glass. As glass is not affected by the plasma treatment, the glass surface serves as a point of reference for the thickness measurements. We can thus track the ribbon thickness before and after the plasma treatment. Relating the thickness change to the treatment duration gives the etching rate. Another method is to prepare thick ribbons on a sacrificial layer. A preliminary etching is done as to completely remove both the scum layer and the sacrificial layer between the ribbons. This is ensured by making a scratch with a blade on the substrate. Again, only the sacrificial layer and the scum layer are scratched and not the glass. Therefore, as the scum layer and sacrificial layer are completely etched, the scratch disappears. Once the sacrificial layer is fully etched, the bare glass is exposed and serves again as the point of reference. For PMMA ribbons processed with a Plasma Diener Pico set with an oxygen pressure of $P = (0.40 \pm 0.02) \text{ mbar}$ at 90% power, we obtain for both methods an etching rate of $(0.58 \pm 0.02) \text{ nm} \cdot \text{s}^{-1}$.

2.2.4 Control of the Helix Geometry

The ribbon properties and notably its thickness are also critical in determining the helix geometry. As described by eq. (2.1.7), the preferred ribbon curvature is determined

by the ribbon thickness and by the elasto-capillary length of the material G/E . The ribbon curvature κ_0 is itself linked to the helix radius and pitch angle by the relation $\kappa_0 = \cos^2 \alpha / R$. As we have $\alpha \sim 0$, the helix radius is directly determined by the ribbon thickness $R = \frac{Et^2}{3G}$. For a given material, the elasto-capillary length is fixed but the helix radius can be tuned through control of the ribbon thickness, which was described in the previous section. However, this means that the ribbon bending modulus and the helix radius are codependent and cannot be freely tuned independently: decreasing the ribbon thickness decreases the ribbon modulus as well as the helix radius and inversely. The work of Pham et al. [9] has proposed an empirical relationship between the bending modulus and the helical radius $B = B_0 \exp(\beta R)$ with $B_0 = (2.6 \pm 1.1) \text{ N} \cdot \text{m}^2$ and $\beta = (3.5 \pm 0.5) \times 10^5 \text{ m}^{-1}$.

The helix total length L is directly given by the ribbon length. Immediately after the flow-coating, the ribbon length is the minimum of the glass slide width and the blade length. But the length can be very easily tuned by cutting the ribbons prior to experiments. This is achieved using either a razor blade or a CO_2 laser cutter for a more controlled cut.

Finally, as mentioned previously, the preferred ribbon torsion is zero. As the preferred ribbon torsion τ_0 is linked to the helix radius and pitch angle by the relation $\tau_0 = \cos \alpha \sin \alpha / R$, we indeed have vanishing pitch angle $\alpha \sim 0$ and vanishing pitch $p \sim 0$. Due to ribbon non-intersection we observe $p \sim w$. This is problematic, firstly because a very tight helix is analogous to a hollow tube, which is not a chiral object. In section 1.2 we have underlined the importance of the chirality in the behavior of flexible helices in flows. Secondly because this means that we do not have control of the pitch or pitch angle. Control of the helix geometry is thus incomplete, both radius and length can be freely and independently tuned but the pitch angle cannot. We describe in chapter 3 the method that we have developed to achieve control of this parameter, resulting in a fully controllable helical ribbon.

2.3 Factors for Optimal Helix Fabrication

We recently adapted and installed at the PMMH laboratory the flow-coating apparatus. Consequently, at the beginning of this work, the fabrication process was not completely mastered and controlled. Several experimental issues were observed and had to be overcome. We hence acquired a good knowledge on the factors participating in an optimal ribbon fabrication and helix formation. This work was done in collaboration with Andrea de la Sen during her Master research internship. Once again, this analysis was performed solely for PMMA ribbons.

2.3.1 Ribbon Fabrication Issues

Firstly, in some case, the flow-coating process would not create straight ribbons but rather pearled-like ribbons, with highly heterogeneous thickness along the ribbon length. Upon immersion in liquid and release of the ribbons, these pearled ribbons would not coil into a helix but break up into smaller straight ribbons. A similar problem is observed for ribbons that would arrange into a wavy pattern, with again highly heterogeneous thickness. This problem would typically not affect all the ribbons on a given substrate, only the ones deposited last. The ones being fabricated first would form straight ribbons as expected. This suggests that this problem is related to the duration of the fabrication

process, perhaps through a destabilization of the contact line. To test this hypothesis, we modify the flow-coating stopping time τ_s . Decreasing the stopping time significantly reduces this phenomenon, with complete suppression for $\tau_s = 500$ ms. We thus set this as the default value for the stopping time. We also notice that reducing the gap height h_{gap} seems to decrease occurrence of this phenomenon. But as precise quantification of the gap height is difficult, this hypothesis is not confirmed.

2.3.2 Ribbon Detachment Issues

Secondly, in some cases, the sacrificial layer would not correctly dissolve upon immersion in fluid and hence the ribbon would not lift-off and would remain stuck to the substrate. In order to understand this phenomenon, we test the integrity and the functionality of the sacrificial layer at different steps of the process. First we prepare the sacrificial layer without any ribbon. To test the integrity of the sacrificial layer, the substrate is scratched with a blade. As the slide is immersed, the scratch disappears from the substrate, showing good functionality of the layer. We then prepare ribbons on a sacrificial layer but do not apply the plasma etching treatment (meant to remove the scum layer). Upon immersion, we observe full lift-off of the ribbons, linked together by the inter-ribbon scum layer. Again, the sacrificial layer works as intended. Finally, we prepare ribbons on a sacrificial layer and etch the ribbons with varying times of exposure. We find that there is a critical exposure time to plasma over which the functionality of the sacrificial layer is altered and ribbons do not detach. Below this value, no significant problems are observed. This critical exposure time depends on the sacrificial layer thickness, which is controlled by the spinning speed imposed during spin-coating. For all spinning speeds, slides are spun for 30 s. For spinning speeds below 1000 rpm, centrifugal forces are too weak to coat uniformly the glass slide. Table 2.1 gives the results.

Spinning speed	Sacrificial layer thickness	Critical exposure time
1000 rpm	(46 ± 5) nm	(1.7 ± 0.3) min
1500 rpm	(37 ± 5) nm	(1.3 ± 0.2) min
2000 rpm	(31 ± 5) nm	(1.1 ± 0.1) min
2500 rpm	(24 ± 5) nm	(0.9 ± 0.1) min
3000 rpm	(20 ± 5) nm	(0.7 ± 0.1) min

TABLE 2.1 – Critical exposure time to oxygen plasma treatment over which the functionality of the sacrificial layer is altered, for varying sacrificial layer thickness. The sacrificial layer thickness is controlled by the spinning speed. Below the critical exposure time, no significant problems are observed for the sacrificial layer: all ribbons lift-off as intended upon immersion.

As shown in table 2.1, the critical exposure time decreases as the sacrificial layer gets thinner. As a matter of fact, the critical exposure time roughly corresponds to the time needed for complete etching of the sacrificial layer. This is tested again by scratching the substrate before etching and tracking disappearance of the scratch. It remains however unclear why the complete removal of the sacrificial layer would prevent ribbon lift-off, since some sacrificial layer is expected to remain below the ribbon. So keeping the exposure time to plasma below this critical value is a solution to the ribbon detachment problem. However, this solution caps the exposure time and thus imposes a lower limit to the obtainable ribbon thickness. The ribbon thickness can also be decreased by decreasing

the concentration c of the PMMA and toluene solution or by decreasing the stopping time τ_s . But default values for these parameters are already fairly low *i.e.* $c = 1 \text{ mg} \cdot \text{mL}^{-1}$ and $\tau_s = 500 \text{ ms}$, which limits further decrease.

2.3.3 Ribbon Coiling Issues

Finally, in some cases, ribbons would detach as expected but would not coil into a helical shape. Various shapes were observed, fig. 2.4 gives some examples of unsuccessfully coiled PMMA ribbons. Commonly in these cases, ribbons would adopt two-dimensional wavy shapes, constituted of alternating portions of circles, as illustrated in fig. 2.4 (a) & (b). Sometimes, the coiling process seems to have started but did not complete, leaving a single loop followed by a wavy pattern, as illustrated in fig. 2.4 (c). We hypothesize that the issue stems from the PMMA and toluene solution, rather than from the flow-coating method, which has been shown to work very consistently in the past. Furthermore, as these coiling issues appeared after several months of experiments, the problem could lie on the aging of the solution and/or of the components. Specifically, newly bought toluene is anhydrous while the solubility of water in toluene is 0.3 mol% [10]. Similarly, PMMA is initially anhydrous but can absorb up to $\sim 2 \text{ wt}\%$ of water, which has been shown to affect its mechanical properties [11, 12]. So we hypothesize that toluene, PMMA or PMMA and toluene solutions could hydrate over time through ambient humidity, thus affecting the functionality of the solution.

At first the role of the toluene was investigated. In order to explore the aging hypothesis, we prepare three different solutions: a first one with months old toluene stored in standard conditions in the laboratory (simply covered with a stripe of parafilm); a second one with newly bought toluene; and a third one for which molecular sieves were immersed into the toluene to induce further desiccation. For all three solutions the same batch of PMMA is used. We produce several samples with each solution: no significant differences are found between them, and the coiling issues persist. We thus conclude that aging of the toluene does not participate in the frustration of helix formation.

We similarly explore the role of PMMA. Three solutions are prepared: a first one with months old PMMA stored in standard conditions in the laboratory; a second one with PMMA stored in vacuum; and a third one with newly bought PMMA. For all three of these solutions, the same batch of toluene is used. Again, several samples are prepared with

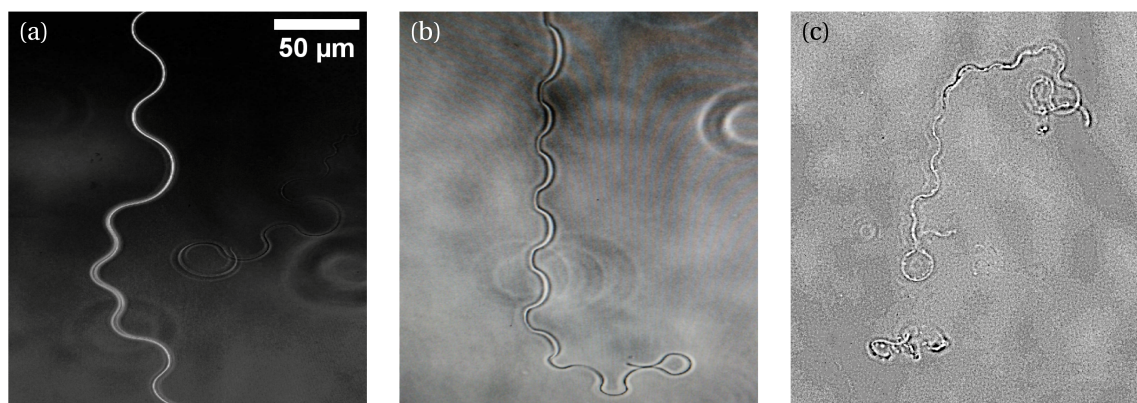


FIGURE 2.4 – Unsuccessfully coiled PMMA ribbons after lift-off from the substrate. Images are taken using phase-contrast bright-field microscopy.

each solution. Interestingly, for the two last solutions *i.e.* in cases where we expect that the anhydrous quality of the PMMA was preserved, some helices do successfully coil. But the coiling issue is only partly suppressed. So hydration of the PMMA does negatively affect the optimal coiling of helices. This problem can be mitigated by storing PMMA in vacuum.

Finally, we investigate the role of the fluorescent dye (Coumarin 153). We simply prepare a PMMA and toluene solution without the addition of the dye. In this case, coiling issues are completely suppressed: all helices coil successfully. This is surprising given the very low amount of dye typically used in solutions (dye concentration $\sim 1-5 \mu\text{g} \cdot \text{mL}^{-1}$). We conclude that the main factor frustrating helix formation is the aging of the fluorescent dye. A simple fix is thus to remove the fluorescent dye from the solution, at the cost of non-fluorescent helices. But as helices can be imaged by phase-contrast bright-field microscopy (as shown in fig. 2.3), fluorescence is not a critical feature. Surprisingly, removing the fluorescent dye also solved the detachment issues exposed in section 2.3.2: any etching time can be applied while preserving the functionality of the sacrificial layer. This indicates that aged Coumarin 153 also modifies the interactions between the ribbons and the sacrificial layer underneath. We expect that using newly bought dye or vacuum-stored dye would also solve the coiling issues but this hypothesis was not tested.

In conclusion, we optimize the ribbon fabrication method for ribbon lift-off and helix coiling. The flow-coating stopping time is set at $\tau_s = 500$ ms and the fluorescent dye is removed from the PMMA and toluene solutions. Both PMMA and toluene are stored in vacuum prior to solution preparation. The solutions are then also stored in vacuum prior to their use for flow-coating.

2.4 General Experimental Set-Up

The ribbons are released into a pool of liquid, usually water, connected to a microfluidic channel. Figure 2.5 (a) illustrates schematically the experimental set-up and fig. 2.5 (d) shows a picture of the set-up. The channel is printed in polydimethylsiloxane (PDMS, Sylgard 184, Corning) using standard soft lithography techniques. Dimensions of the channel vary depending on the intended experiment and will be detailed in the relevant chapters. Its inlet and outlet are respectively connected to the pool and to a syringe. Flow rates in the microchannel are controlled by a syringe pump (NeMESYS, Cetoni). Two micro-manipulators (TransferMan, Eppendorf) mounted each with an open glass capillary connected to a syringe allow capture and release of the helices by pumping or expelling liquid. This allows precise manipulation of the helices in all directions. One of the open glass capillaries can be replaced by a carbon fiber cantilever for force measurements. The tip of each capillary is coated with bovine serum albumin (BSA) by immersion in a 2 wt% water and BSA solution for 15 min. This decreases the non-specific contact forces between the capillaries and the helices, allowing helix release. The tip of the cantilever is not treated as to afford adhesion with helices. The whole set-up is mounted on an inverted optical microscope (Zeiss Axio Observer) connected to a numerical camera (Hamamatsu Orcaflash LT 4.0). When using fluorescent microscopy, a UV-source is used (HXP 120 lamp, Zeiss) combined with a filter set matching the Coumarin 153 excitation bandwidth (filter set 40, Zeiss). UV light influx is controlled by a shutter (Shutter Uniblitz V25).

Upon release in the pool, the ribbons quickly adopt a tight helical configuration. A helix is selected, and one of its ends is caught and clamped by the first capillary, which we

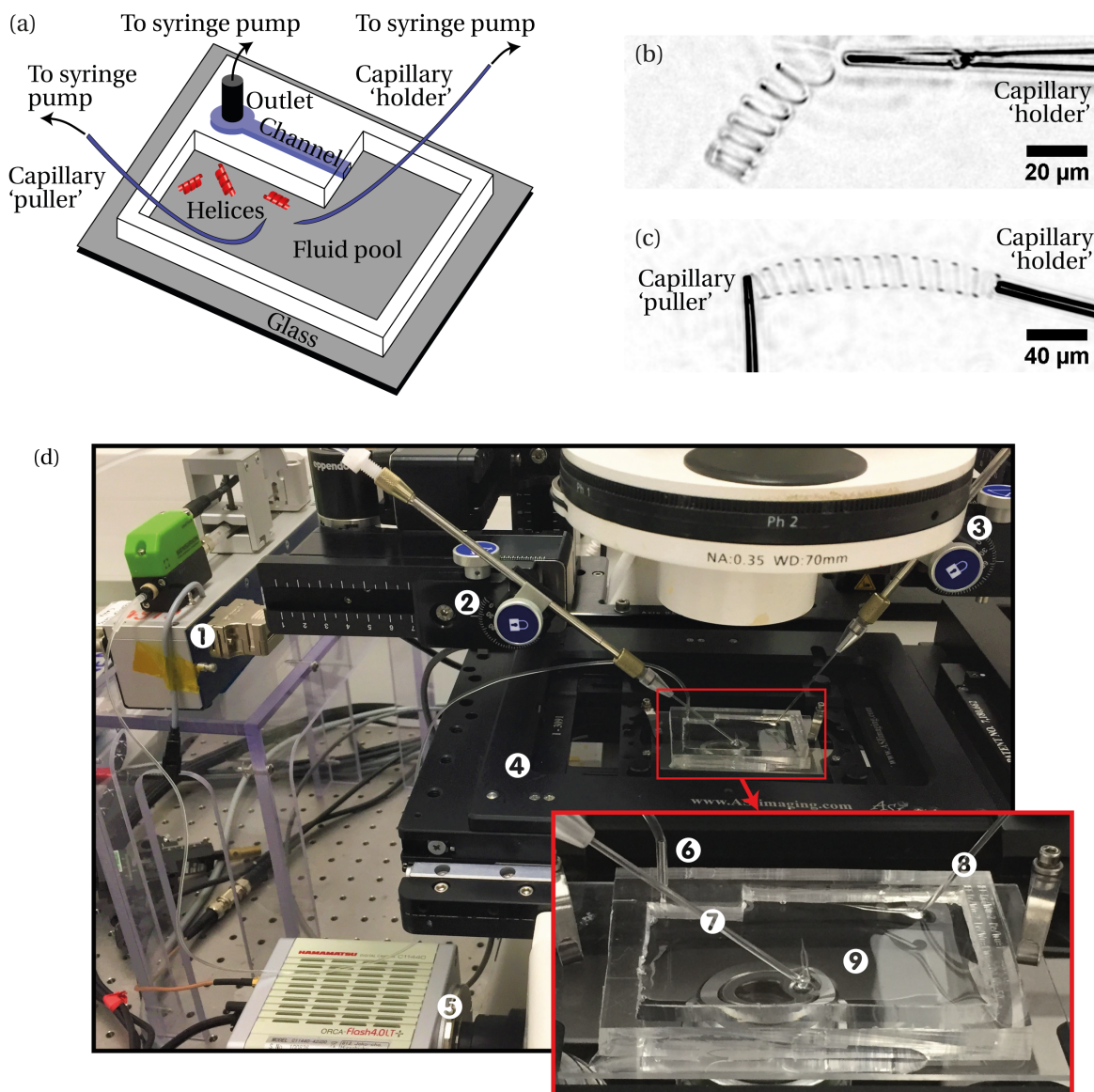


FIGURE 2.5 – (a) Schematic of the experimental set-up. The capillary puller can be replaced by a carbon fiber cantilever to conduct force measurements. The whole set-up is mounted on an inverted microscope equipped with a numerical camera for imaging. (b) PMMA helix clamped at one end, using the holder capillary. (c) PMMA helix clamped at both ends, using both open glass capillaries. (d) Picture of the experimental set-up with ① syringe pump for control of the flow in the channel, ② & ③ two micro-manipulators, ④ motorized stage, ⑤ digital camera, ⑥ outlet of the channel connected to a syringe, ⑦ & ⑧ respectively puller and holder capillary and ⑨ fluid pool connected to the PDMS microchannel.

call the holder, by pumping liquid into the capillary. Figure 2.5 (b) shows an example of a PMMA helix clamped at its right end by the holder. We can then approach the second capillary, which we call the puller, or the carbon fiber cantilever in order to manipulate the helix or to conduct force measurements. Figure 2.5 (c) shows a PMMA helix clamped at both ends, using the holder and the puller. The helix can also be positioned inside the microfluidic channel, in order to conduct flow experiments. All experiments are conducted at room temperature $T = 22^\circ\text{C}$.

Open Glass Capillary

The glass capillaries are prepared from standard glass tubes with 1 mm outside diameter and 0.58 mm inner diameter, using a micropipette puller system (P-1000 Flaming/Brown, Sutter). This creates a very thin closed tip, of typical diameter $\sim 1.5\ \mu\text{m}$. The closed tip is then melted to open the capillary, using a heated glass bead (MF-830 Microforge, Narishige International). The final tip diameter of the open glass capillary ranges within 5 – 20 μm .

Carbon Fiber Cantilever

The cantilever is cut from a circular carbon fiber to $L \sim 1\ \text{cm}$ in length and glued to the end of a glass tube. The cantilever radius is $r = 4\ \mu\text{m}$. The glass tube is mounted on one of the micro-manipulators, in place of the puller capillary. To calibrate the stiffness modulus B of the cantilever, the cantilever is dragged perpendicularly to the cantilever direction and at constant velocity v in still water. This is equivalent to immersing the cantilever in a uniform flow with flow velocity v . The tip deflection δ is measured from the experimental images. The imposed flow velocity is at most $v \sim 6\ \text{mm} \cdot \text{s}^{-1}$ so the Reynolds number is at most $\text{Re} \sim 2 \times 10^{-2}$, r being the relevant dimension of the flow. The flow is thus viscous. We model the viscous hydrodynamic forces as a uniform distributed load, with f the force per unit length. We use resistive-force theory to estimate the load $f = \xi_{\perp} v$ with $\xi_{\perp} = \frac{8\pi\eta}{\ln(2L/r)}$, η being the fluid viscosity. In this case, the tip deflection is given by $\delta = \frac{\xi_{\perp} v L^4}{8B}$. Table 2.2 gives the experimental results with data plotted in fig. 2.6 .

Dragging speed	Tip deflection
$0.50\ \text{mm} \cdot \text{s}^{-1}$	$8.0\ \mu\text{m}$
$0.99\ \text{mm} \cdot \text{s}^{-1}$	$15.4\ \mu\text{m}$
$1.98\ \text{mm} \cdot \text{s}^{-1}$	$31.7\ \mu\text{m}$
$2.96\ \text{mm} \cdot \text{s}^{-1}$	$48.0\ \mu\text{m}$
$3.95\ \text{mm} \cdot \text{s}^{-1}$	$64.8\ \mu\text{m}$
$4.94\ \text{mm} \cdot \text{s}^{-1}$	$82.2\ \mu\text{m}$
$5.94\ \text{mm} \cdot \text{s}^{-1}$	$101.5\ \mu\text{m}$

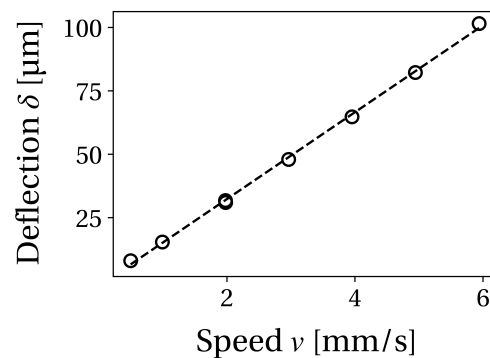


TABLE 2.2 – Experimental results for the calibration of the cantilever stiffness

FIGURE 2.6 – Cantilever tip deflection δ as a function of dragging speed v

As shown, the obtained results are accurately fitted by a linear relationship (correlation coefficient 0.999), which confirms the viscous nature of the flow. From these results we calculate $B = (1.55 \pm 0.02) \times 10^{-11}\ \text{Pa} \cdot \text{m}^4$. As $B = E\pi r^4/4$ for a cylindrical fiber, this corresponds to a Young's modulus $E = (77.3 \pm 1.1)\ \text{GPa}$ for the carbon fiber, consistent with typical

values. For the case of an end-load with force F , the tip deflection is $\delta = FL^3/3B$. With typical cantilever length $L \sim 1$ cm, a deflection of $\sim 10\mu\text{m}$ is associated with an end-load $\sim 4 \times 10^{-10}$ N. Thus, sub-nanonewton forces can be measured with the cantilever.



In this chapter, we have introduced the various experimental methods and techniques that we will use throughout this work, and the general experimental apparatus was described. We have detailed the fabrication process of flexible micron-sized helical ribbons. We have highlighted that the helical radius is set by the ribbon thickness t and by the material elasto-capillary length γ/E

$$R = \frac{Et^2}{3\gamma} \quad (2.4.1)$$

Control of the ribbon thickness is achieved through oxygen plasma etching prior to experiments, which in turn affords control of the helical radius. Total filament length L is tuned by simple cutting of the samples. Control of the pitch angle is however missing, and helices tend to arrange into tightly coiled geometries, with thus very weak chirality. In the next chapter, we address this issue by implementing an in-situ pitch modification process.

Several experimental issues were observed, affecting detrimentally ribbon fabrication and the self-coiling phenomenon. These issues appear to be related to aging of the chemical compounds, PMMA and fluorescent dye specifically, through hydration by ambient humidity. These issues are mitigated by storing components in vacuum prior to their use. Removal of the fluorescent dye also participate in lessening these effects.

2.5 References

- [1] Marine Daieff. *Deformation and shape of flexible, microscale helices in viscous flows*. PhD thesis, Sorbonne Paris Cité, 2018. [38](#), [42](#)
- [2] Dong Yun Lee, Jonathan T Pham, Jimmy Lawrence, Cheol Hee Lee, Cassandra Parkos, Todd Emrick, and Alfred J Crosby. Macroscopic nanoparticle ribbons and fabrics. *Advanced materials*, 25(9):1248–1253, 2013. [38](#), [40](#)
- [3] Jonathan T Pham, Jimmy Lawrence, Dong Yun Lee, Gregory M Grason, Todd Emrick, and Alfred J Crosby. Highly stretchable nanoparticle helices through geometric asymmetry and surface forces. *Advanced Materials*, 25(46):6703–6708, 2013. [40](#), [42](#)
- [4] Jonathan T Pham, Jimmy Lawrence, Gregory M Grason, Todd Emrick, and Alfred J Crosby. Stretching of assembled nanoparticle helical springs. *Physical Chemistry Chemical Physics*, 16(22):10261–10266, 2014. [38](#)
- [5] Dylan M Barber, Zhefei Yang, Lucas Prévost, Olivia Du Roure, Anke Lindner, Todd Emrick, and Alfred J Crosby. Programmed wrapping and assembly of droplets with mesoscale polymers. *Advanced Functional Materials*, 30(36):2002704, 2020. [42](#)
- [6] N. A. Gloumakoff and Yi-Yuan Yu. Torsion of Bars With Isosceles Triangular and Diamond Sections. *Journal of Applied Mechanics*, 31(2):332–334, 06 1964. [43](#)

- [7] Satyan Choudhary and Alfred J Crosby. Controlled processing of polymer nanoribbons: Enabling microhelix transformations. *Journal of Polymer Science Part B: Polymer Physics*, 57(18):1270–1278, 2019. [43](#)
- [8] N Vourdas, AG Boudouvis, and E Gogolides. Plasma etch rate measurements of thin pmma films and correlation with the glass transition temperature. In *Journal of Physics: Conference Series*, volume 10, page 099. IOP Publishing, 2005. [44](#)
- [9] Jonathan T Pham, Alexander Morozov, Alfred J Crosby, Anke Lindner, and Olivia du Roure. Deformation and shape of flexible, microscale helices in viscous flow. *Physical Review E*, 92(1):011004, 2015. [45](#)
- [10] Céline Marche, Corinne Ferronato, Jean-Charles De Hemptinne, and Jacques Jose. Apparatus for the determination of water solubility in hydrocarbon: Toluene and alkylcyclohexanes (c6 to c8) from 30 c to 180 c. *Journal of Chemical & Engineering Data*, 51(2):355–359, 2006. [47](#)
- [11] RP Kusy, JQ Whitley, and S Kalachandra. Mechanical properties and interrelationships of poly (methyl methacrylate) following hydration over saturated salts. *Polymer*, 42(6): 2585–2595, 2001. [47](#)
- [12] AMS Hamouda. The influence of humidity on the deformation and fracture behaviour of pmma. *Journal of materials processing technology*, 124(1-2):238–243, 2002. [47](#)

Chapter 3

Control of the Helical Pitch

Contents

3.1 Principles of the Method	54
3.2 Mechanics of Deformed Helical Ribbons	55
3.3 Uniform Stress: the Stretching Treatment	57
3.3.1 Method and Observations	57
3.3.2 Characterization of the Stretching Treatment	57
3.3.3 Other Materials	60
3.4 Towards More Complex Shapes	61
3.4.1 Piecewise Uniform Stress: the Double-Helix	61
3.4.2 Non-Uniform Stress: the Flow Treatment	62
3.5 Discussion of the Physical Phenomenon	63
3.5.1 Yield Behavior of Confined Polymers	64
3.5.2 Creeping Behavior of Confined Polymers	65
3.6 References	68

In the previous chapter we have described the flow-coating method to produce flexible helical ribbons. As we mentioned, several materials can be used, allowing a wide range of material properties. Furthermore, both the total filament length L and the helical radius R can be freely and independently tuned. The length is tuned by cutting the ribbons prior to experiments to the desired value. The helical radius is controlled by the ribbon thickness, which can be tuned by modifying the flow-coating settings or by plasma etching the samples prior to experiments. However, the helical pitch p and pitch angle α are not controlled and cannot be tuned. Control of the helix geometry is incomplete.

In this chapter, we address this issue by implementing an in-situ pitch modification process. The overall helix fabrication method is now a two-step process: the first step is the flow-coating and helix coiling and the second step is the newly developed pitch tuning process. The full workflow is illustrated in fig. 3.2. Our method triggers irreversible deformation in the material to shape helices into the desired geometry. Depending on the desired final geometry, different methods can be applied. Several materials are tested: PMMA, PDMAEMA and Cd-Se quantum dots, demonstrating the method's versatility. The chapter is organized as follows. In section 3.1 we explain the general principles of the method. In section 3.2 we introduce several mechanical concepts necessary to better describe and understand the method. We study in more details the mechanics of deformed helices in chapters 4 and 6. Section 3.3 describes and characterizes specifically the method resulting in a uniform non-zero pitch. We describe in section 3.4 how more complicated shapes can be obtained. Finally in section 3.5 we discuss these experimental findings and identify the physical phenomenon at play.

3.1 Principles of the Method

We observe that when stress is exerted on a helical ribbon, some deformation persists in the structure even after the stress is relaxed. These observations were made since the first works making use of these helical ribbons. In their 2013 work [1], Pham et al. submitted quantum dot helical ribbons to a series of axial viscous flows, by dragging helices at constant velocity in still water. We reproduce in fig. 3.1 (a) the force-extension curves that they obtained. Hysteresis of the deformation is clearly visible, especially at high strain:

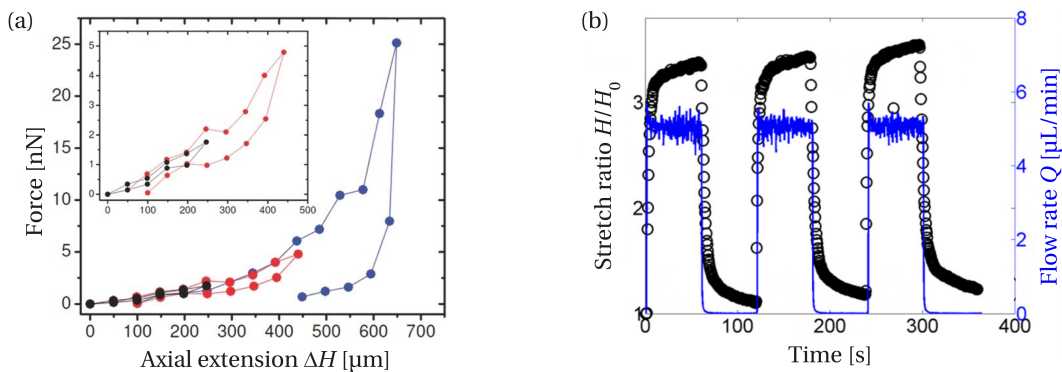


FIGURE 3.1 – (a) Force-extension curves for a quantum dot helical ribbon submitted to a series of three flow steps at increasing velocity, reproduced from [1]. The force is the total drag force induced by the flow and is measured using a cantilever. Inset zooms on the two small strain curves. (b) Stretch ratio H/H_0 for a PMMA helical ribbon submitted to a series of three identical flow steps, reproduced from [2].

when the force is relaxed, the initial axial length is not recovered. Similar observations were made in their 2015 work [2] for PMMA helical ribbons similarly submitted to viscous axial flows. We reproduce in fig. 3.1 (b) the stretch ratio H/H_0 as a function of time while a series of three identical flow steps is applied. H_0 is the initial axial length of the helix. As the helical ribbon is extended by the imposed flow, it never reaches equilibrium. Furthermore, when the flow is stopped, the initial axial length is not recovered *i.e.* $H/H_0 > 1$: the resting axial length has slightly increased as a result of the flow step. These observations were confirmed by the work of Daieff et al. [3] again for PMMA helices in viscous flows.

We show that this phenomenon can be leveraged to tune the helical pitch. The process is executed in-situ, after release and coiling of the ribbons. For all methods, a helix is selected and one of its end is caught and clamped by the holder capillary. This helix end remains clamped throughout the whole experiment. The process consists in creating a persistent stress in the material by extending the helix for a long period of time, typically several minutes. The helix is then allowed to relax to equilibrium. Different stress profiles can be applied to locally control the final helix geometry, as shown in fig. 3.2 (a) to fig. 3.2 (c): uniform stress, piecewise uniform stress or non-uniform stress.

Uniform stress is achieved by end-loading the whole helix, as shown in fig. 3.2 (a). Piecewise uniform stress is achieved by end-loading only a fraction of the helix, as shown in fig. 3.2 (b). Finally a gradient stress profile is realized by immersing the helix in an axial viscous flow, as shown in fig. 3.2 (c). Each stress profile is associated to a different change in geometry. These pitch control methods cannot be used to decrease the pitch since inward forces buckle the helix instead of compressing it. But as helices display vanishing pitch in their initial state, arbitrary values for the helical pitch can be reached nevertheless.

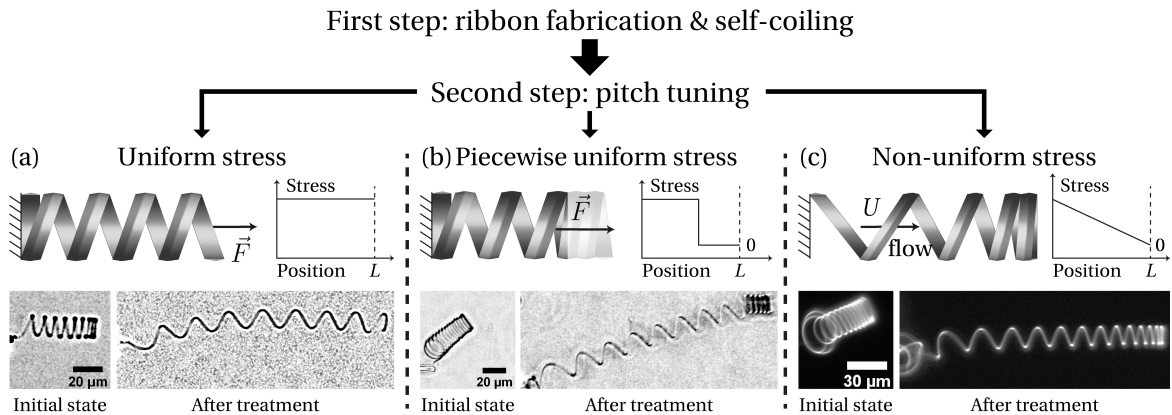


FIGURE 3.2 – Fabrication work-flow: firstly ribbons are fabricated and coiled into helices; secondly, the pitch is encoded. (a) to (c): different methods for pitch tuning, depending on the stress applied, either (a) uniform stress, (b) piecewise uniform stress or (c) non-uniform stress. For each method we show a schematic of the method, a representation of the stress profile along the filament and corresponding before/after experimental images. For all experimental images, no stress is applied: the helix is at equilibrium. Images are taken using phase-contrast bright-field microscopy (light background) or fluorescent microscopy (dark background).

3.2 Mechanics of Deformed Helical Ribbons

The helical structure is highly slender ($R/t \sim 300 - 1000$) so deformation of helical ribbons is dominated by bending and twisting of the filament, filament elongation being

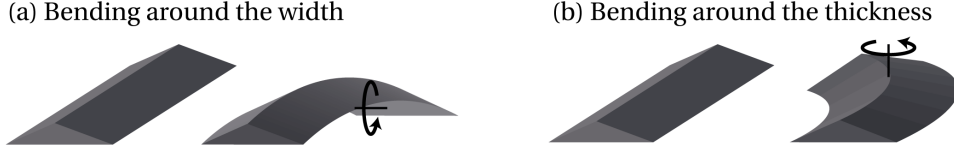


FIGURE 3.3 – Schematic of the two modes of ribbon bending. (a) Bending around the width, the corresponding bending modulus is B . (b) Bending around the thickness, the corresponding bending modulus is A .

negligible. The corresponding material moduli are B bending modulus and C twisting modulus. The bending modulus B corresponds to bending of the ribbon around the width direction, as illustrated in fig. 3.3 (a). Both scale similarly $C \sim B \sim Ewt^3$ but are not equal. More precisely, for a flat triangular cross-section, we have $B = \frac{1}{36}Ewt^3$ and $C = \frac{1}{12}\mu wt^3$ with μ shear modulus [4]. We finally introduce the stresses corresponding to material bending and torsion, respectively the local bending stress σ_{bend} and the local torsional shear τ_{shear} . As the helix is deformed, their maximum values on the cross-section are respectively: $\sigma_{\text{bend}} = \frac{2}{3}Et\Delta\kappa$ and $\tau_{\text{shear}} = \mu t\Delta\tau$ [4]. $\Delta\kappa$ is the local change in material curvature and $\Delta\tau$ is the local change in material torsion, both calculated between the deformed state of the helix and the reference state.

The second bending modulus A scales symmetrically $A \sim Ew^3t$. The bending modulus A corresponds to bending of the ribbon around the thickness direction, as illustrated in fig. 3.3 (b). The filament being a flat ribbon ($t \ll w$), A is much higher than B and C . The elastic energy cost associated to bending around the thickness direction is hence much higher than for the two other modes of deformation: bending around the thickness direction can be neglected. In this case, the material frame coincides with the Frenet frame of the centerline [5, 6]. The material curvature and material torsion can thus be computed as the Frenet curvature and Frenet torsion of the centerline. Therefore, $\Delta\kappa$ and $\Delta\tau$ can be calculated as the local change of Frenet curvature and the local change of Frenet torsion between the deformed state and the reference state. The exact value for the Frenet curvature or torsion depends in a complex way of the precise geometry of the helix. For a uniform helix (uniform radius and angle), the Frenet curvature is $\kappa = \cos^2 \alpha / R$ and the Frenet torsion is $\tau = \cos \alpha \sin \alpha / R$. So we can establish that changes in curvature or torsion both scale as $\Delta\kappa \sim \Delta\tau \sim 1/R$. And thus, the bending stress and the torsional shear scale similarly $\sigma_{\text{bend}} \sim \tau_{\text{shear}} \sim E(t/R)$.

Specific to the cases of end-loading and partial end-loading, illustrated in fig. 3.2 (a) & (b), we introduce the axial force F , force necessary to increase the axial length by ΔH . The work of Love [7] has established that the tension force scales as $F \sim (C/R^2) \times (\Delta H/L)$. Thus the tensile stress σ_{tens} scales as $\sigma_{\text{tens}} \sim F/wt \sim E(t/R)^2$. Given that $t \ll R$, we have $\sigma_{\text{tens}} \ll \sigma_{\text{bend}}, \tau_{\text{shear}}$: bending and twisting effects are indeed dominant while the filament can be considered inextensible. The exact value of the tension force depends in a complex way on the helix geometry. For weak forces or equivalently for small deformations, Starostin et al. [8] obtained analytically

$$F = \frac{C}{R^2} \frac{\Delta H}{L} \frac{1}{\cos^2 \alpha (\cos^2 \alpha + (C/B) \sin^2 \alpha)} \quad (3.2.1)$$

3.3 Uniform Stress: the Stretching Treatment

3.3.1 Method and Observations

The uniform stress method, termed 'stretching treatment', is done in three steps depicted in fig. 3.4 (a). First the free end of the helix is grabbed by the puller capillary. We then impose to the helix a fixed axial extension ΔH_{imp} for several minutes by displacing the puller. Finally, the free end is released from the puller by expelling liquid out of the capillary and the helix is let to relax. As a result from this process, we observe a permanent increase in the helical pitch and thus in the axial length (comparison between top and bottom images of fig. 3.4 (a)). The resulting change in axial length is noted ΔH_{res} .

We show in fig. 3.4 (b) the changes in geometry resulting from several successive stretching treatments, applied to a PMMA helical ribbon. The helix mean pitch angle gradually increases from 8° to 48° . Around twenty stretching treatments were performed during this experiment, but we only show a selection of experimental images in fig. 3.4 (b). Three stretching treatments were performed between each image. The corresponding pitch angle distributions along the filament length are shown in fig. 3.4 (c). The increase in pitch angle is uniform along the length, which tends to minimize initial heterogeneities in the pitch angle distribution. This uniform increase is consistent with the fact that, for an end-loading, the elastic stress and the elastic deformation are uniform along the filament length.

For the same experiment, the temporal evolution of the helix mean pitch angle following the successive stretching treatment is plotted in fig. 3.4 (d). This time the full evolution of the helix is shown, after each stretching treatment is performed. The data points corresponding to the images shown in fig. 3.4 (b) are highlighted. As shown, the pitch angle can only increase throughout the experiment and does so as a consequence of the stretching treatments. We can therefore use the helix mean pitch angle to track progress of a given experiment. The pitch angle is preferable to the pitch because the pitch angle is expressed as the rescaled pitch p/R : this allows easier comparison between different helices, exhibiting different sizes.

Figure 3.4 (e) & (f) show respectively the evolution of the helix axial length H and helix radius R as a function of mean pitch angle, the angle being used to track progress of the experiment. The evolution of H is accurately fitted by the expected geometrical relation $H = L \sin \alpha$, meaning that the total filament length L is kept constant throughout the experiment. This was expected considering the high slenderness of the filament: uniaxial elongation of the ribbon is negligible (see section 3.2 for more details). However, we note that the helical radius R evolves slightly as a side effect of the treatment. The radius change is negligible until $\sim 30^\circ$ pitch angle but then increases up to $\sim 25\%$ of its initial value. This change in helical radius causes a change in the number of turns, which is visible in fig. 3.4 (b).

3.3.2 Characterization of the Stretching Treatment

To describe more accurately and characterize the stretching treatment, we measure the resulting increase in axial length ΔH_{res} as a function of imposed axial elongation ΔH_{imp} for several PMMA helices. The duration of the treatment Δt is kept constant for a given helix but varies from helix to helix. We also characterize the process for the other materials

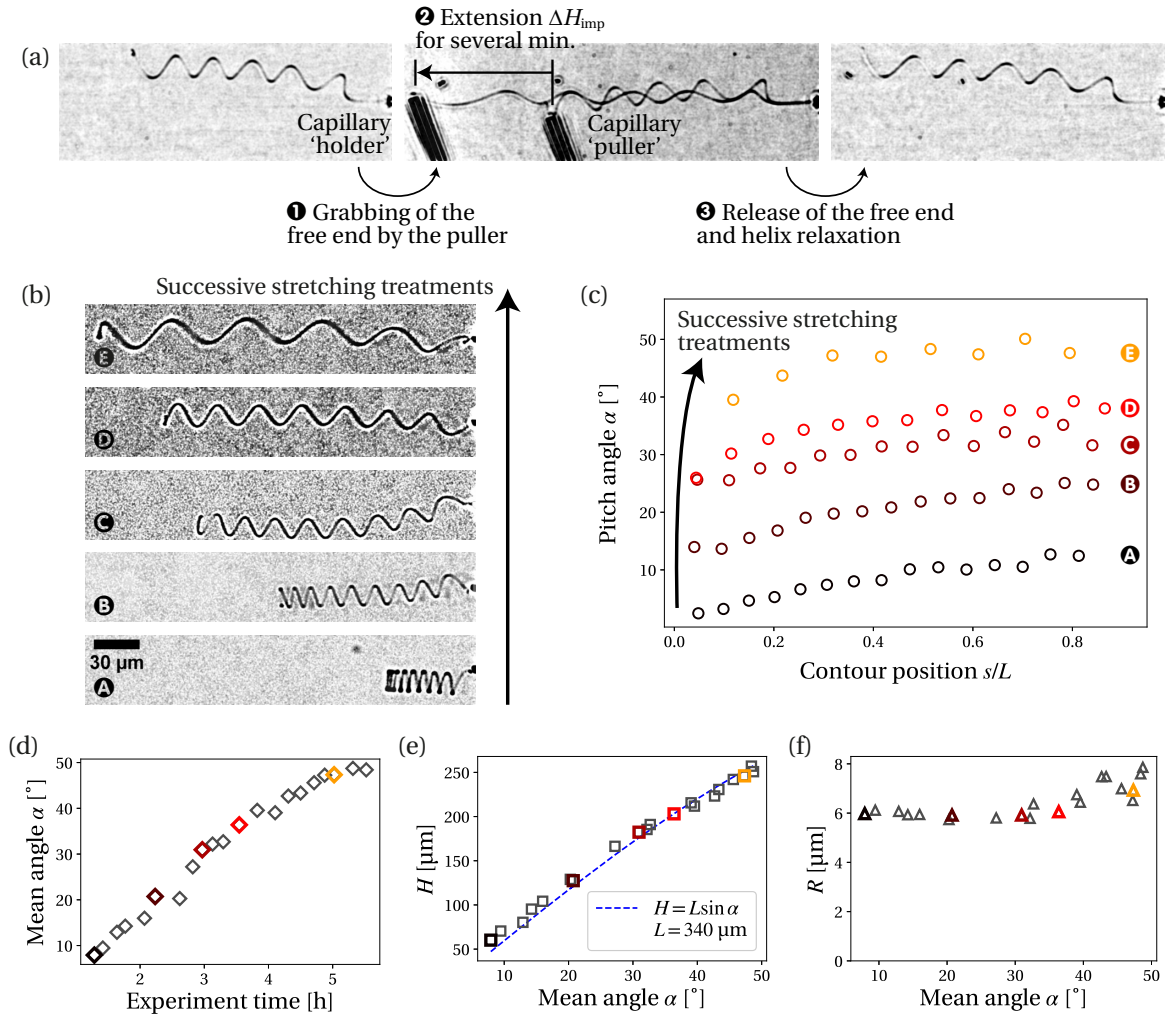


FIGURE 3.4 – (a) Experimental images illustrating the uniform pitch increase process through end-loading, termed stretching treatment. The helix right end is clamped by the holder capillary. The left end is grabbed by pumping liquid into the puller capillary. By displacing the puller capillary, an axial extension ΔH_{imp} is imposed to the helix. After several minutes, the left end is released by expelling liquid out of the puller capillary. The resulting increase in axial length is denoted ΔH_{res} . Images are taken using phase-contrast bright-field microscopy. (b) One PMMA helix after several successive stretching treatments, the first image corresponds to the initial state of the helix. (c) Corresponding pitch angle distribution along the filament length. (d) Temporal evolution of the helix mean pitch angle as the experiment progresses. (e) Axial length H as a function of mean helix pitch angle following the successive stretching treatments, fitted (one fitting parameter) by the expected geometrical relation $H = L \sin \alpha$. (f) Evolution of the helical radius R as a function of mean helix pitch angle.

(PDMAEMA and quantum dots), but in less details, in section 3.3.3.

Results are presented in fig. 3.5 (a). For all tested helices, the resulting increase in axial length is linear with the imposed stretching: $\Delta H_{\text{res}} \propto \Delta H_{\text{imp}}$. The linear relationship is preserved even for the smallest imposed stretching, suggesting that there is no strain or stress threshold to trigger the pitch increase phenomenon. Furthermore the slope of this linear relationship is itself linear with the treatment duration Δt , as shown in inset of fig. 3.5 (a). The resulting increase in axial length is thus both linear with time and with the imposed stretching: $\Delta H_{\text{res}} \propto \Delta H_{\text{imp}} \times \Delta t$. Naturally, we expect the axial length increase to saturate for very long stretch time. Specifically we expect that $\lim_{\Delta t \rightarrow \infty} \Delta H_{\text{res}} = \Delta H_{\text{imp}}$. But this saturation effect is not observed within the range of treatment duration that we

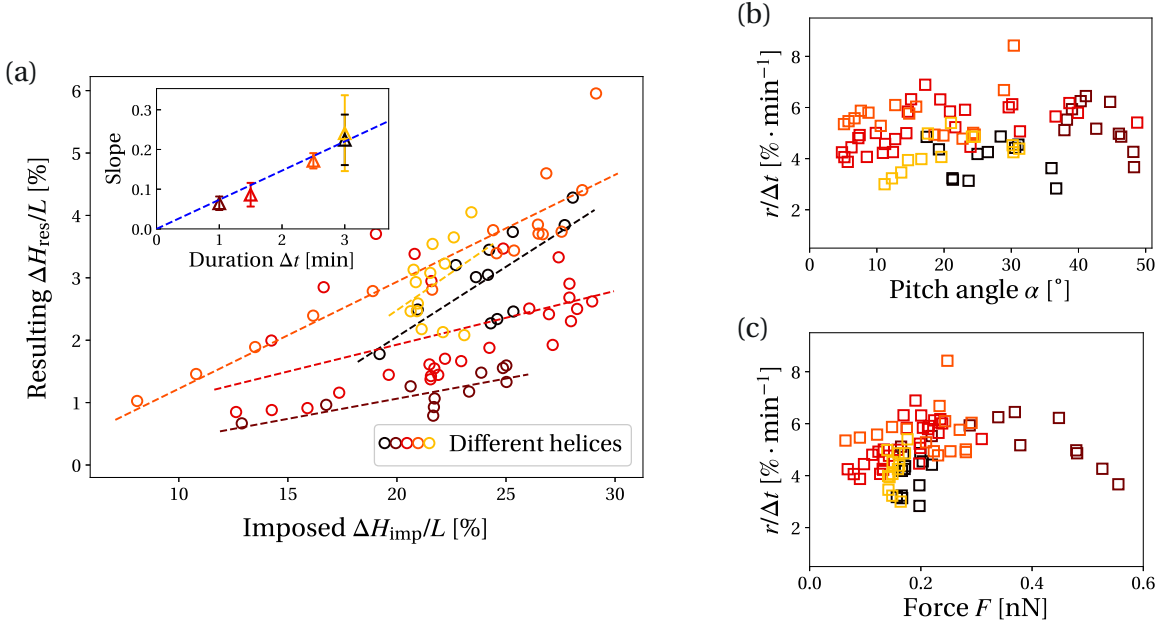


FIGURE 3.5 – Outcome of successive stretching treatments applied to several PMMA helices. (a) Resulting increase in axial length ΔH_{res} as a function of imposed axial stretching ΔH_{imp} , both rescaled by the total length L . Dashed colored lines are linear fitting. Inset shows the slopes of the linear fittings as a function of treatment duration Δt , with linear fitting (blue dashed line). (b) Time-corrected ratio $r/\Delta t$ with $r = \Delta H_{\text{res}}/\Delta H_{\text{imp}}$ as a function of helix pitch angle and (c) as a function of force F applied to stretch the helix.

have tested *i.e.* up to 3 minutes. The ratio $r = \Delta H_{\text{res}}/\Delta H_{\text{imp}}$ divided by the duration time Δt is therefore roughly constant throughout all PMMA helices: $r/\Delta t = (5.0 \pm 1.0) \% \cdot \text{min}^{-1}$. This time-corrected ratio can be interpreted as follows: for each minute of treatment, the helix axial length is permanently increased by $\sim 5\%$ of the imposed stretching. This ratio is characteristic of the material, independently of the helix geometrical parameters. However, the geometrical parameters were varied in a quite narrow range, radii ranging within $5 - 12 \mu\text{m}$ and lengths within $250 - 850 \mu\text{m}$. Hence, a weak influence of the geometrical parameters on the time-corrected ratio cannot be excluded.

We check that this time-corrected ratio does not vary with pitch angle, as shown in fig. 3.5 (b). We recall that the pitch angle tracks progress of a given experiment and acts as a proxy for time and number of applied treatments. The non-correlation with pitch angle means that neither time nor repeated treatments have an influence on the stretching treatment. The history of the system has no influence on its subsequent evolution. We also check that the time-corrected ratio does not vary with the tension force applied, as shown in fig. 3.5 (c). Equation (3.2.1) is used to compute the tension force. The tension force applied during the treatment has no influence on the output of the treatment, only the displacement matters. This highlights the convenience of imposing the displacement during the stretching treatment, rather than imposing the force.

Finally, we calculate the typical stress values (bending stress and torsional shear) imposed during stretching treatments, using the expressions given in section 3.2

$$\sigma_{\text{bend}} = \frac{2}{3} E t \Delta \kappa \quad \text{and} \quad \tau_{\text{shear}} = \mu t \Delta \tau \quad (3.3.1)$$

with $\Delta \kappa$ and $\Delta \tau$ the change in Frenet curvature and Frenet torsion respectively, calculated between the deformed state and the reference state. We calculate these quantities by

approximating both the reference state and the deformed state to a uniform helix (uniform radius and angle). The curvature change and the torsion change can thus be calculated as

$$\Delta\kappa = \frac{\cos^2 \alpha'}{R'} - \frac{\cos^2 \alpha}{R} \quad \text{and} \quad \Delta\tau = \frac{\cos \alpha' \sin \alpha'}{R'} - \frac{\cos \alpha \sin \alpha}{R} \quad (3.3.2)$$

with α' and R' taken respectively as the mean pitch angle and the mean radius in the deformed state. For both stresses, we obtain vanishing values: $\sigma_{\text{bend}}/E = 10^{-4} - 10^{-3}$ and $\tau_{\text{shear}}/\mu = 10^{-4} - 10^{-3}$. Hence, the local material strains are at most 10^{-3} during a stretching treatment.

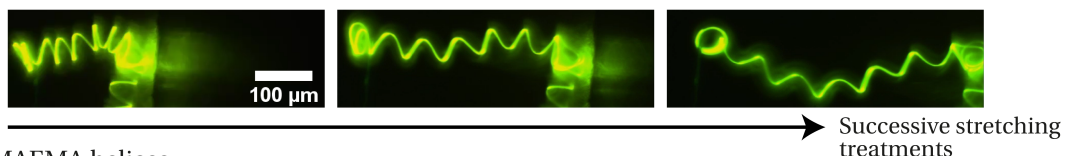
In conclusion, control of the stretching treatment is very convenient: the increase in axial length is directly proportional to the imposed stretching and to the treatment duration. No stress or strain threshold is observed. The effectiveness of the treatment, quantified by the time-corrected ratio $r/\Delta t$ is a property of the material: no influence of the geometrical parameters is found. Furthermore, the time-corrected ratio does not vary with time or repeated stretching treatments. From our experimental data for PMMA helices, we calculate $(r/\Delta t)_{\text{PMMA}} = (5.0 \pm 1.0) \% \cdot \text{min}^{-1}$.

3.3.3 Other Materials

The stretching treatment, yielding uniform pitch increase, gives similar results for the two other tested materials: PDMAEMA and quantum dots. Figure 3.6 (a) shows an example of two successive stretching treatments applied to a quantum dot helix. Fabrication of the quantum dot helices and data collection was performed by John Pham (University of Kentucky). The quantum dot helices consist of highly packed, 8 nm semiconductor Cadmium Selenide (Cd-Se) quantum dots functionalized with chemically reactive undecenylthiol (UDT) ligands. Quantum dots are inherently fluorescent. More details on fabrication and set-up can be found in a previous publication [9].

For quantum dot helices, we similarly obtain a uniform increase in the helical pitch as a result of the stretching treatment. We show in fig. 3.6 (b) the result of one stretching treatment applied to a PDMAEMA helix. Again, uniform pitch increase is observed. For these two materials, a detailed characterization was not conducted. We assume that the findings made for PMMA hold true, notably that the time-corrected ratio is intrinsic to the material. From these two experiments, we estimate the time-corrected ratio for quantum dot helices and for PDMAEMA helices. For quantum dots helices, we found

(a) Cd-Se quantum dot helices



(b) PDMAEMA helices

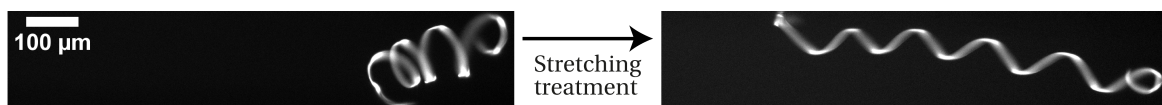


FIGURE 3.6 – Examples of stretching treatments applied to other materials: (a) two successive stretching treatments applied to a quantum dot helix; (b) a single stretching treatment applied to a PDMAEMA helix. Images are taken using fluorescent microscopy.

$(r/\Delta t)_{\text{QD}} \sim 7\% \cdot \text{s}^{-1}$ (notice the change in the time unit). The value of the time-corrected ratio is significantly higher than for PMMA helices. For PDMAEMA helices we estimate the time-corrected ratio to an intermediate value $(r/\Delta t)_{\text{PDMAEMA}} \sim 1\% \cdot \text{s}^{-1}$.

The value of the time-corrected ratio $r/\Delta t$, specific to a material, is highly important. On the one hand, a high value would make the helical ribbons unusable in other contexts as any stress applied to the helix would deform it irreversibly within seconds. On the other hand, a vanishing value would make the stretching treatment very slow and thus inconvenient to conduct. A value of a few percent per minute is desirable. The stretching treatment can be performed in reasonable time (several minutes), and irreversible deformations can be neglected during other experiments, as long as experiment duration does not exceed a few minutes. Overall PMMA helices display the most favorable time-corrected ratio for control of the pitch angle.

3.4 Towards More Complex Shapes

3.4.1 Piecewise Uniform Stress: the Double-Helix

As shown in the previous section, end-loading the helix increases the pitch uniformly along the whole filament. We demonstrated that the increase in axial length is directly proportional to the stretching imposed during the treatment. Consistently with these observations, loading only a fraction of the helix yields a uniform pitch increase only in the loaded part. This partial stretching treatment is similarly conducted in three steps: an arbitrary point of the filament is clamped by the puller capillary, the helix portion between the two capillaries is extended by displacement of the puller and finally the helix is let to relax to equilibrium. The stress applied during the treatment is piecewise uniform. We illustrate this process in fig. 3.7 using a PMMA helix. In this case, we stretch roughly the right half of the helix. This process results in a two-part helix, each part displaying uniform but distinct pitch distribution. We can thus locally control the pitch and pitch angle by selectively applying the stretching treatment to different sections of the helix.

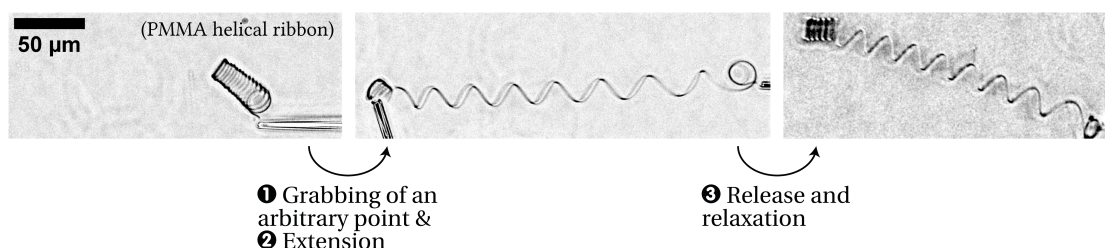


FIGURE 3.7 – Fabrication of a PMMA double-helix by selectively applying the stretching treatment, here only on the right part of the helix. Each part displays a uniform but distinct pitch distribution. Images are taken using phase-contrast bright-field microscopy.

Local control of the helix geometry allows many applications. The double-helix may be used as a model system for a uni-flagellated bacteria: a chiral helically-shaped flexible flagella attached to a non-chiral cylindrical body. Most geometrical properties can be tuned at will: body and flagella length as well as pitch angle of the flagella. This allows detailed parametric exploration of the interactions between uni-flagellated bacteria and viscous flows. The double-helix may also be used as a force sensor with extended measurement range. The pitch angle indeed has a strong influence on the stiffness constant of a helical

ribbon: increasing the pitch angle effectively stiffens the helix. The work of Starostin et al. [8] gives the spring constant k of a helical ribbon

$$k \sim \frac{C}{R^2 L} \frac{1}{\cos^2 \alpha}$$

The double-helix is hence constituted of a softer sensor (small angle part) and a stiffer sensor (high angle part). This effectively increases the measurement range: the small angle part measuring weak forces and the high angle part measuring strong forces. The added measurement range is quantified by the ratio of the spring constants k'/k , with k spring constant of the small angle part and k' spring constant of the high angle part. In the simple case where both parts have same length and radius, the spring constant ratio is simply $k'/k = (\cos \alpha / \cos \alpha')^2 = 1 / \cos^2 \alpha'$ since for the small angle part has vanishing pitch angle *i.e.* $\alpha \sim 0$. In theory, the ratio of the spring constants and thus the added measurement range can be set at will. In practice we can reach up to 70° for the high angle part, which would result in a spring constant ratio of $k'/k \sim 8$. But the ratio can be further increased by decreasing the length and/or radius of the stiffer section.

3.4.2 Non-Uniform Stress: the Flow Treatment

The helix can finally be loaded by a non-uniform stress. We achieve non-uniform stress by immersing the helix in an axial viscous flow. For this method, termed 'flow treatment', the helix is positioned at the center of the microfluidic channel and a flow is applied from the clamped end towards the free end, extending the helix. In this case, we use a simple rectangular channel of height $H = 650 \mu\text{m}$ and width $W = 250 \mu\text{m}$. The flow is parabolic in the channel but as the typical helical radii are small compared to the channel size, we consider that the helix is immersed in a locally uniform flow. After several minutes, the flow is stopped, and the helix relaxes to equilibrium. Figure 3.8 (a) illustrates the different steps of the process. The overall axial length is increased as a result of the flow treatment but this time the pitch distribution is not uniform.

Figure 3.8 (b) shows the result of several successive flow treatments applied to a PMMA helix. The corresponding pitch distributions, plotted in fig. 3.8 (c), are accurately fitted by a linear function of the contour position s/L . The pitch increase is maximum at the clamped end ($s/L = 1$) and zero at the free end ($s/L = 0$). The pitch increase distribution matches the distribution of elastic deformation imposed during the flow treatment, which can be approximated to a linear function of contour position [2]. This confirms that, similarly to the stretching treatment, the local deformation resulting from the flow treatment is directly proportional to the imposed local elastic stretching.

In contrast to the stretching treatment, the flow treatment is force-controlled, since we impose the velocity of the flow and thus the viscous forces acting on the helix. Control of the flow treatment is hence less practical than control of the stretching treatment. Furthermore, precise calculation of the viscous forces acting on the helix is not straightforward, requiring the use of numerical tools such as slender-body theory [10]. Fabrication of helices with controlled geometry using this method is therefore impractical.

However, our experiments show that these helical ribbons can serve as a detailed sensor of the flow history imposed upon the helix. The total length increase tracks the total solution volume moved through the channel and the pitch increase distribution gives information on the local flow geometry. Notably, a uniform flow results in a linear increase

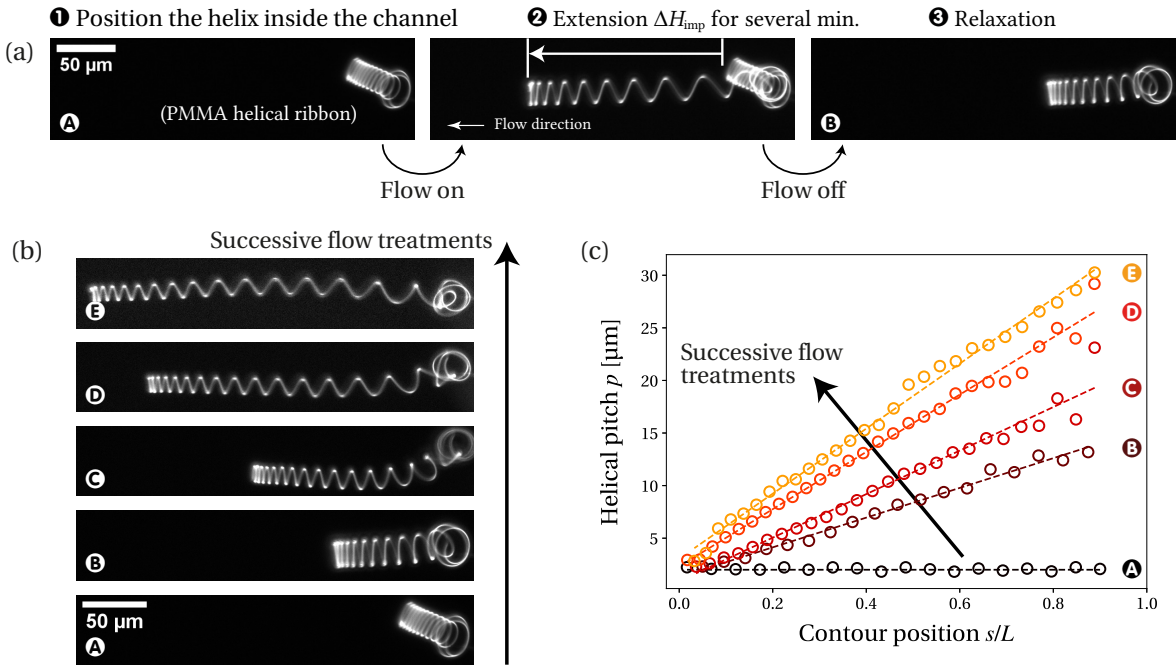


FIGURE 3.8 – (a) Experimental images illustrating the flow treatment. The helix right end is clamped by the holder capillary and the helix is positioned at the center of the microchannel. Flow is applied from the clamped end to the free end. Images are taken using fluorescent microscopy and hence the capillary is not visible. (b) One PMMA helix after several successive flow treatments, the first image corresponds to the initial state of the helix. The images marked **A** and **B** are the same as in (a). (c) Corresponding pitch distribution along the filament length, with linear fit in dashed lines. $s = 0$ corresponds to the free end while $s = L$ corresponds to the clamped end.

of the helical pitch. For non-uniform flows, we expect the pitch increase distribution to simply match the distribution of the elastic stretching imposed by the flow. The different materials can be used to tune the sensitivity of the sensor: quantum dot helices for short times or weak flows or PMMA helices for long times or strong flows.

3.5 Discussion of the Physical Phenomenon

The irreversible deformations that we observe, and on which the methods for shape control rely, happen under persistent stress at a slow rate. They occur at very low strain and stress: typical values calculated for the local strains range within 0.01 – 0.1 % during deformations. These vanishing local strain values are obtained despite significant global displacement: this is a consequence of the high slenderness of the helical structure, specifically that the ribbon thickness is much smaller than the helical radius.

Such sizable irreversible deformations are not expected for bulk materials, especially considering the vanishing strain values. For bulk PMMA under uniaxial tension for example, typical yield stress is $\sigma_{\max} \sim 60$ MPa and typical Young's modulus is ~ 3 GPa, leading to a typical yield strain of $\epsilon_{\max} = \sigma_{\max}/E \sim 2\%$ [11, 12]. For bulk PMMA under shear deformation, values reported for the yield strain are even higher, around 10% [13, 14]. But in recent years, multiple studies have highlighted significant changes in the mechanical properties of polymeric materials in confined geometry compared to bulk. In the following, we review the literature to identify the origin of these deformations.

3.5.1 Yield Behavior of Confined Polymers

Firstly, we focus on the yield behavior of confined polymers. Several authors have reported a decrease in the yield stress for polymers in highly confined geometries [15–17]. This effect could effectively limit the range of the material linear regime, thus leading to an enhanced susceptibility to plastic deformations. Confinement is observed when the typical thickness of the geometry h_F is reduced below the polymer radius, typically given by the chain end-to-end radius R_{ee} . The magnitude of the confinement is then given by the ratio of the film thickness to the polymer radius h_F/R_{ee} . In our case, ribbons are made out of PMMA with $M_w = 120$ kDa, the end-to-end radius is $R_{ee} \approx \sqrt{0.425 \times M_w} = 23$ nm, calculated from the classical literature expression [18, 19]. As typical ribbon thickness is $t \sim 10$ nm, the polymer chains are indeed confined in our experimental conditions.

For PMMA thin films specifically and using a similar molecular weight ($M_w = 104$ kDa), Bay et al. [20] have reported a $\sim 40\%$ decrease in the tensile strength compared to the bulk value, as the film thickness was lowered down to $h_F/R_{ee} \approx 1/2$. The tensile strength is expected to further decrease with the film thickness but experimental data are lacking for $h_F \lesssim R_{ee}/2$. This decrease in yield stress is usually interpreted as a consequence of a loss of interchain entanglements due to the free surface [21–23] and an increased mobility of polymer chains near the free surface [24]. Similar confinement effects are achieved by loading the material with hard nano-particles: confinement is then observed when the inter-particle distance is smaller than the polymer radius [25, 26]. The presence of particles acts in a similar fashion than a free surface and decreases the amount of interchain entanglement. But Bay et al. also observed a decrease in the Young's modulus E as the film thickness was decreased below the typical polymer radius, confirming findings of previous studies [27, 28]. Thus the yield strain may be only weakly affected by the confinement, although this is not examined by the work of Bay et al. Such a phenomenon has been reported for polystyrene (PS) thin films [16], which exhibit an *increase* in yield strain compared to bulk while the yield stress decreases. This is a consequence of a comparatively larger decrease in Young's modulus.

Several differences exist between these studies and our experimental conditions that we must discuss before drawing conclusions. Firstly, the results of Bay et al., much like most of the cited literature, are obtained for polymer thin films submitted to uniaxial tension, while in our experimental conditions, materials are mainly submitted to torsional shear. To our knowledge, no literature is available on the yield behavior of polymeric thin films submitted to torsional shear. But for bulk PMMA, the shear yield strain is higher than the tensile yield strain and so we can expect that it is also the case for PMMA thin films. Hence, this difference probably drives an increase in the yield strain compared to the results of Bay et al. Secondly, the literature only addresses the case of uniformly thick films *i.e.* with rectangular cross-sections. In our experimental conditions, ribbons exhibit a triangular cross-section. This probably results in a lower effective thickness: 25% of the ribbon total mass is situated in regions where the local thickness is below $t/2$. Moreover, the perimeter-to-area ratio is $2/t$ for rectangular cross-sections, while the ratio is $4/t$ for triangular cross-sections. Hence there is more free surface per mass for our ribbons than for uniformly thick films. As both the reduction in thickness and the presence of free surfaces are known to decrease the yield stress, we expect the difference in cross-section to drive a decrease in the yield stress. Finally, in our experimental conditions, the ribbons are submitted to oxygen plasma etching prior to experiments. This treatment probably cuts

some of the polymer chains, effectively decreasing the mean polymer chain length. As a decrease in chain length is associated with a decrease in yield stress for bulk polymers [29], a similar behavior is expected.

Overall, solid experimental evidence point towards a decrease in yield stress for PMMA taken in our experimental conditions compared to bulk. But the magnitude of decrease is fairly limited, usually up to a factor 4. Furthermore decrease in yield stress may originate from a decrease in Young's modulus rather than from a change in yield strain. Therefore, we conclude that PMMA yield strain is not lowered down to a value within our experimental range (0.01 – 0.1 %). The observed irreversible deformations happen within the material linear regime and are not a consequence of yield. This is further confirmed by the overall linearity of the process, both in time and in imposed stretching.

3.5.2 Creeping Behavior of Confined Polymers

If material yield is not the phenomenon at play, material creep probably is. Creep is the tendency of solid materials to slowly flow under stress. Creep can occur in polymeric materials, which typically exhibit a viscoelastic behavior. Such sizable creeping effects are not expected in bulk: the viscosity of polymeric materials diverges at low temperature *i.e.* below the glass-transition temperature T_g . The glass-transition temperature separates a hard and brittle state for $T < T_g$ from a viscous or rubbery state for $T > T_g$. For bulk PMMA, the standard value is $T_g = 115^\circ\text{C}$. Carriere et al. measured the viscosity of bulk PMMA with molecular weight $M_w = 26.9\text{ kDa}$ over a wide range of temperature [30]: at $T = 140^\circ\text{C} > T_g$, they found $\eta = (4.8 \pm 0.2) \times 10^7\text{ Pa}\cdot\text{s}$. Meanwhile, from the time-corrected ratio obtained in section 3.3.2 we estimate an equivalent viscosity for PMMA in our experimental conditions to $\eta \sim 10^7\text{ Pa}\cdot\text{s}$. Estimation of the viscosity is detailed in the next paragraph. We find the same order of magnitude than the results of Carriere et al., which were obtained for ~ 4 times smaller chains and for a temperature above the glass-transition temperature. We plot in fig. 3.9 the full experimental data obtained by Carriere et al., along with an empirical expression from the classical work of Berry et al. [31]. We also plot this empirical expression for the molecular weight matching our experimental conditions. As shown, viscosity of bulk PMMA with $M_w = 120\text{ kDa}$ does not reach $\eta \sim 10^7\text{ Pa}\cdot\text{s}$ until a least

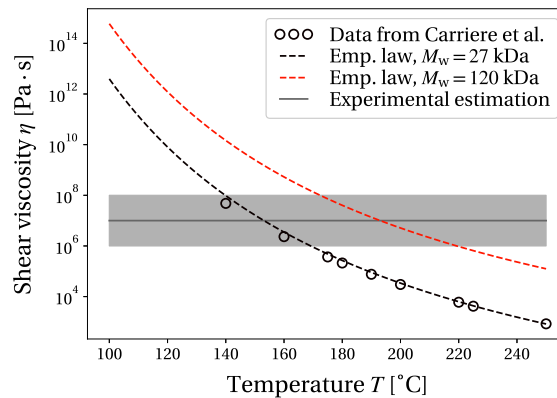


FIGURE 3.9 – Experimental data for the shear viscosity of bulk PMMA obtained by Carriere et al. [30] as a function of temperature, along with the empirical law from Berry et al. [31] for two different molecular weights. The black and red dashed lines correspond respectively to the conditions of Carriere et al. and to our conditions. The gray line represents the estimation $\eta \sim 10^7\text{ Pa}\cdot\text{s}$ for PMMA in our experimental conditions.

$T = 180^\circ\text{C} = T_g + 65^\circ\text{C}$. We recall that experiments are conducted at room temperature $T = 22^\circ\text{C}$. At this temperature, viscosity of bulk PMMA diverges.

To estimate the value of the viscosity, we relate the macroscopic deformation of the helix to the microscopic deformations in the material. As a consequence of the stretching treatment, a permanent increase in axial length ΔH_{res} is observed, which corresponds to a permanent change in pitch angle $\Delta \sin \alpha_{\text{res}} = \Delta H_{\text{res}}/L$. The change in preferred material torsion is the same as the change in Frenet torsion $\Delta \tau = \Delta(\cos \alpha \sin \alpha/R)$. The radius R remains roughly constant and we suppose that the angle remains small so that $\cos \alpha \approx \text{cst} = 1$. Hence, the change in material torsion is $\Delta \tau_{\text{res}} \sim (\Delta H_{\text{res}}/L)/R$. The exact irreversible microscopic deformations in the material resulting from this change in preferred filament torsion are very difficult to model. Keeping in mind that the irreversible deformations are proportional to the local elastic stretching, we model them as the elastic deformation of a straight filament submitted to simple torsion. This situation is illustrated in fig. 3.10 .

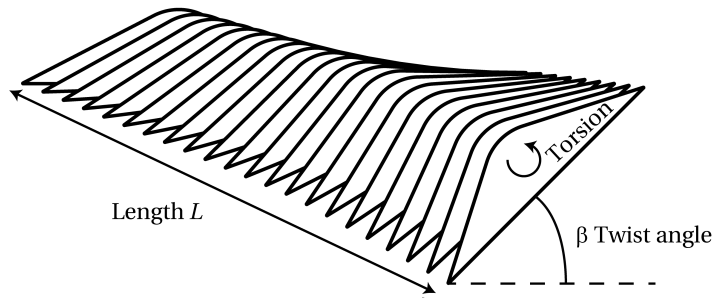


FIGURE 3.10 – Simple torsion of a straight filament of length L with flat triangular cross-section.

The change in filament torsion is naturally $\Delta \tau_{\text{res}}$ so the twist angle β is given by $\beta = L * \Delta \tau_{\text{res}} \sim \Delta H_{\text{res}}/R$. Typical irreversible material deformation resulting from this change in filament torsion is $u \sim \beta t$. Hence, if we denote Δt typical treatment duration, the velocity of the polymer chains is $v \sim u/\Delta t \sim \beta t/\Delta t$. Overall, using the standard definition of the shear viscosity, the torsional shear τ_{shear} is given by

$$\tau_{\text{shear}} = \eta \nabla v \sim \eta \frac{v}{t} \sim \eta \frac{1}{\Delta t} \frac{\Delta H_{\text{res}}}{R} \quad (3.5.1)$$

Comparison with the known value of the torsional shear $\tau_{\text{shear}} = \mu t \Delta \tau_{\text{imp}}$ imposed during the treatment yields

$$\tau_{\text{shear}} \sim \mu t \frac{1}{R} \frac{\Delta H_{\text{imp}}}{L} \sim \eta \frac{1}{\Delta t} \frac{\Delta H_{\text{res}}}{R} \quad (3.5.2)$$

And finally

$$\eta \sim \mu \frac{t}{L} \frac{\Delta H_{\text{imp}}}{\Delta H_{\text{res}}} \Delta t \quad (3.5.3)$$

where we recognize the inverse of the time corrected ratio $\frac{\Delta t}{r} = \frac{\Delta H_{\text{imp}}}{\Delta H_{\text{res}}} \Delta t$. Estimation of the numerical value simply gives

$$\eta \sim 1 \text{ GPa} * \frac{10 \text{ nm}}{1 \text{ mm}} * \frac{1}{5\% \cdot \text{min}^{-1}} \sim 10^7 \text{ Pa} \cdot \text{s} \quad (3.5.4)$$

As mentioned, such sizable creeping effects are not expected in bulk. But similarly to the yield behavior, many authors have reported significant changes in the creep behavior of polymers in confined geometries. The first approach is simply to characterize these

changes by examining the shear viscosity as the film thickness is decreased. Focusing mainly on PS thin films, several authors have reported a decrease in the material viscosity as the polymer chains are confined [32–34]. Experimental data for PMMA are limited, only the work of Li et al. [35] has investigated the viscosity of PMMA thin films. Their work reports a non-divergent viscosity down to $T = 80^\circ\text{C} = T_g - 35^\circ\text{C}$ as the film thickness was decreased to $h_F/R_{ee} \approx 1$. But the viscosity still diverges for $T \lesssim 60^\circ\text{C}$. However, in this study the PMMA thin films are supported on silica, which exhibits strong interactions with PMMA, while in our experimental conditions ribbons are freestanding in water. The polymer/substrate interactions have been shown to influence the creep response: in cases with strong interactions, an increase in viscosity can even be observed [36].

The second approach, followed by most of the literature, examines the confinement-induced changes in the viscoelasticity of polymeric materials as an effective change in the glass-transition temperature. A lower glass-transition temperature shifts the temperature-viscosity curve to the left, decreasing the viscosity for a given temperature. And reciprocally a higher glass-transition temperature shifts the curve to the right. The two approaches are naturally not mutually exclusive. Again, polymer/substrate interactions have been shown to strongly influence the creeping behavior [37] so we focus on results reported for freestanding films. Within this approach, our observations would correspond to a $\sim 170\text{K}$ decrease in the glass-transition temperature. Although such a dramatic decrease in T_g has not been reported yet, for PMMA or for any other material, several studies did report sharp decreases in T_g [38, 39]. This decrease is similarly interpreted as a consequence of a loss of interchain entanglements and an increased chain mobility near free surfaces [40]. Again, similar confinement effects are observed for particle-loaded polymers [41]. The changes in creeping properties and in yield behavior thus originate from the same fundamental mechanisms.

For freestanding PMMA films specifically, Roth et al. reported a $\sim 30\text{K}$ decrease in T_g as the film thickness is lowered to $h_F = 20\text{ nm} \approx 0.8 * R_{ee}$ [42]. Based on their measurements, and following previous theoretical works [43], they proposed an empirical law

$$\Delta T_g(h_F) = -T_g^{\text{bulk}} \left(\frac{a}{h_F} \right)^\delta \quad \text{with } a = 2.9\text{ nm and } \delta = 1.4 \quad (3.5.5)$$

At low molecular weight *i.e.* $M_w < 240\text{kDa}$, M_w was found to have no influence on the parameters a and δ , which replicates findings made for PS thin films [44]. Our PMMA ribbons typically display a thickness of $t \sim 10\text{ nm}$. We take the effective confinement thickness as $t/2 \sim 5\text{ nm}$ to account for the added free surface, compared to films with rectangular cross-section. The empirical expression then predicts a T_g -shift of $\Delta T_g \sim -180\text{K}$, very close to our experimental estimation. But this calculation extrapolates very far out of the tested thickness range: validity of the empirical expression for such a vanishing thickness still has to be demonstrated.

This still suggests that the underlying phenomenon responsible for the strong susceptibility of our system to irreversible deformations is the enhancement of creeping properties for highly confined polymeric materials. This enhancement is evidenced by a sharp decrease in the glass-transition temperature. If this hypothesis is confirmed, our observations would constitute the highest decrease in T_g ever reported. For freestanding polycarbonate thin films, O’Connell et al. [45] reported a 120K decrease in the glass-transition temperature at $h_F = 1\text{ nm}$. For freestanding PS thin films, Pye et al. [46] reported a 85K T_g -decrease

at $h_F = 30$ nm. Finally, we recall that for freestanding PMMA thin films, a T_g -decrease of 30 K at $h_F = 20$ nm was reported by Roth et al. [42].

The fundamental mechanism at play during deformation is thus flow of the polymer chains. The increased susceptibility to creep originates from the loss of interchain entanglements and the increased mobility of chains near free surfaces. Considering this fundamental mechanism, we expect the mechanical properties of the material, notably the Young's modulus, to remain unaffected by the pitch increase processes. As we have shown that the total length L is conserved during treatment and that the helical radius R hardly varies, all helix properties would be conserved during treatment, except for the pitch angle. But to our knowledge, no work has yet investigated potential modulus change resulting from creep in polymeric materials. Thus, change in the material mechanical properties during treatment cannot be fully excluded.



In this chapter, we have presented a set of in-situ methods to locally control the pitch and pitch angle of helical ribbons fabricated from the flow-coating method. All geometrical parameters of the helix are now controllable, as control of the length and radius was already achieved. Furthermore, the geometrical parameters can be tuned independently of one another. We do not expect any change in the material mechanical properties during treatments, although experimental validation would be beneficial. Very few fabrication methods result in flexible helical structures with full shape control [47, 48], and we report for the first time *local* control of the pitch angle. The various methods for pitch modification were tested for three different materials, demonstrating versatility in the material choice: PMMA, modified PDMAEMA and Cd-Se quantum dots. This comes in contrast with the methods cited above for which the material choice is constrained: DNA nanotubes for the work of Maier et al. [48] and metal composites for the work of Li et al. [47].

Our method leverages the enhanced susceptibility of confined materials to creep to shape helices into the desired geometry. The susceptibility of each material to creep was characterized by the time-corrected ratio $r/\Delta t$. PMMA helices were found to display the most favorable ratio, which validates the use of this material in future experiments. PDMAEMA and quantum dot helices were found to be too susceptible to creep.

In the next chapter, we investigate the mechanical properties of helical ribbons. We leverage the newly achieved control of the pitch angle to probe the influence of this parameter. Evolution of the mechanical properties as the angle is modified are tracked. We can thus verify that no change in the material properties is triggered by the pitch increase process.

3.6 References

- [1] Jonathan T Pham, Jimmy Lawrence, Dong Yun Lee, Gregory M Grason, Todd Emrick, and Alfred J Crosby. Highly stretchable nanoparticle helices through geometric asymmetry and surface forces. *Advanced Materials*, 25(46):6703–6708, 2013. [54](#)
- [2] Jonathan T Pham, Alexander Morozov, Alfred J Crosby, Anke Lindner, and Olivia du Roure. Deformation and shape of flexible, microscale helices in viscous flow. *Physical Review E*, 92(1):011004, 2015. [54](#), [55](#), [62](#)

- [3] Marine Daieff. *Deformation and shape of flexible, microscale helices in viscous flows*. PhD thesis, Sorbonne Paris Cité, 2018. [55](#)
- [4] N. A. Gloumakoff and Yi-Yuan Yu. Torsion of Bars With Isosceles Triangular and Diamond Sections. *Journal of Applied Mechanics*, 31(2):332–334, 06 1964. [56](#)
- [5] L Mahadevan and Joseph Bishop Keller. The shape of a möbius band. *Proceedings of the Royal Society of London. Series A: Mathematical and Physical Sciences*, 440(1908): 149–162, 1993. [56](#)
- [6] EL Starostin and GHM Van Der Heijden. The shape of a möbius strip. *Nature materials*, 6(8):563–567, 2007. [56](#)
- [7] Augustus Edward Hough Love. *A treatise on the mathematical theory of elasticity*. Cambridge university press, 1944. [56](#)
- [8] EL Starostin and GHM van der Heijden. Tension-induced multistability in inextensible helical ribbons. *Physical review letters*, 101(8):084301, 2008. [56](#), [62](#)
- [9] Jonathan T Pham, Jimmy Lawrence, Gregory M Grason, Todd Emrick, and Alfred J Crosby. Stretching of assembled nanoparticle helical springs. *Physical Chemistry Chemical Physics*, 16(22):10261–10266, 2014. [60](#)
- [10] Bruce Rodenborn, Chih-Hung Chen, Harry L Swinney, Bin Liu, and HP Zhang. Propulsion of microorganisms by a helical flagellum. *Proceedings of the National Academy of Sciences*, 110(5):E338–E347, 2013. [62](#)
- [11] AMS Hamouda. The influence of humidity on the deformation and fracture behaviour of pmma. *Journal of materials processing technology*, 124(1-2):238–243, 2002. [63](#)
- [12] Josef Jancar, Robert S Hoy, Alan J Lesser, Ema Jancarova, and Jan Zidek. Effect of particle size, temperature, and deformation rate on the plastic flow and strain hardening response of pmma composites. *Macromolecules*, 46(23):9409–9426, 2013. [63](#)
- [13] Kyoungmin Min, Meredith Silberstein, and NR Aluru. Crosslinking pmma: Molecular dynamics investigation of the shear response. *Journal of Polymer Science Part B: Polymer Physics*, 52(6):444–449, 2014. [63](#)
- [14] S Rabinowitz, IM Ward, and JSC Parry. The effect of hydrostatic pressure on the shear yield behaviour of polymers. *Journal of Materials science*, 5(1):29–39, 1970. [63](#)
- [15] Yujie Liu, Yu-Cheng Chen, Shelby Hutchens, Jimmy Lawrence, Todd Emrick, and Alfred J Crosby. Directly measuring the complete stress–strain response of ultrathin polymer films. *Macromolecules*, 48(18):6534–6540, 2015. [64](#)
- [16] Jung-Hyun Lee, Jun Young Chung, and Christopher M Stafford. Effect of confinement on stiffness and fracture of thin amorphous polymer films. *ACS Macro Letters*, 1(1): 122–126, 2012. [64](#)
- [17] Woo Jin Choi, R Konane Bay, and Alfred J Crosby. Tensile properties of ultrathin bisphenol-a polycarbonate films. *Macromolecules*, 52(19):7489–7494, 2019. [64](#)

- [18] Lewis J Fetters, David J Lohse, Scott T Milner, and William W Graessley. Packing length influence in linear polymer melts on the entanglement, critical, and reptation molecular weights. *Macromolecules*, 32(20):6847–6851, 1999. [64](#)
- [19] LJ Fetters, DJ Lohse, D Richter, TA Witten, and A Zirkel. Connection between polymer molecular weight, density, chain dimensions, and melt viscoelastic properties. *Macromolecules*, 27(17):4639–4647, 1994. [64](#)
- [20] R Konane Bay, Klara Zarybnicka, Josef Jancar, and Alfred J Crosby. Mechanical properties of ultrathin polymer nanocomposites. *ACS Applied Polymer Materials*, 2(6):2220–2227, 2020. [64](#)
- [21] Daniel M Sussman. Spatial distribution of entanglements in thin free-standing films. *Physical Review E*, 94(1):012503, 2016. [64](#)
- [22] Daniel M Sussman, Wei-Shao Tung, Karen I Winey, Kenneth S Schweizer, and Robert A Riggleman. Entanglement reduction and anisotropic chain and primitive path conformations in polymer melts under thin film and cylindrical confinement. *Macromolecules*, 47(18):6462–6472, 2014.
- [23] Lun Si, Michael V Massa, Kari Dalnoki-Veress, Hugh R Brown, and Richard AL Jones. Chain entanglement in thin freestanding polymer films. *Physical review letters*, 94(12):127801, 2005. [64](#)
- [24] J Martin, M Krutyeva, M Monkenbusch, A Arbe, J Allgaier, A Radulescu, P Falus, J Maiz, C Mijangos, J Colmenero, et al. Direct observation of confined single chain dynamics by neutron scattering. *Physical review letters*, 104(19):197801, 2010. [64](#)
- [25] Argyrios Karatrantos, Nigel Clarke, Russell J Composto, and Karen I Winey. Entanglements in polymer nanocomposites containing spherical nanoparticles. *Soft Matter*, 12(9):2567–2574, 2016. [64](#)
- [26] Robert A Riggleman, Gregory Toepferwein, George J Papakonstantopoulos, Jean-Louis Barrat, and Juan J de Pablo. Entanglement network in nanoparticle reinforced polymers. *The Journal of chemical physics*, 130(24):244903, 2009. [64](#)
- [27] Christopher M Stafford, Bryan D Vogt, Christopher Harrison, Duangrut Julthongpiput, and Rui Huang. Elastic moduli of ultrathin amorphous polymer films. *Macromolecules*, 39(15):5095–5099, 2006. [64](#)
- [28] Jessica M Torres, Christopher M Stafford, and Bryan D Vogt. Elastic modulus of amorphous polymer thin films: relationship to the glass transition temperature. *Acs Nano*, 3(9):2677–2685, 2009. [64](#)
- [29] John R Martin, Julian F Johnson, and Anthony R Cooper. Mechanical properties of polymers: The influence of molecular weight and molecular weight distribution. *Journal of Macromolecular Science—Reviews in Macromolecular Chemistry*, 8(1):57–199, 1972. [65](#)
- [30] Craig J Carriere, Girma Biresaw, and Robert L Sammler. Temperature dependence of the interfacial tension of ps/pmna, ps/pe, and pmna/pe blends. *Rheologica acta*, 39(5):476–482, 2000. [65](#)

- [31] Guy C Berry and Thomas G Fox. The viscosity of polymers and their concentrated solutions. In *Fortschritte der Hochpolymeren-Forschung*, pages 261–357. Springer, 1968. [65](#)
- [32] Harry D Rowland, William P King, Graham LW Cross, and John B Pethica. Measuring glassy and viscoelastic polymer flow in molecular-scale gaps using a flat punch mechanical probe. *ACS nano*, 2(3):419–428, 2008. [67](#)
- [33] Hugues Bodiguel and Christian Fretigny. Reduced viscosity in thin polymer films. *Physical review letters*, 97(26):266105, 2006.
- [34] Yu Chai, Thomas Salez, Joshua D McGraw, Michael Benzaquen, Kari Dalnoki-Veress, Elie Raphaël, and James A Forrest. A direct quantitative measure of surface mobility in a glassy polymer. *Science*, 343(6174):994–999, 2014. [67](#)
- [35] Ranxing N Li, Fei Chen, Chi-Hang Lam, and Ophelia KC Tsui. Viscosity of pmma on silica: Epitome of systems with strong polymer–substrate interactions. *Macromolecules*, 46(19):7889–7893, 2013. [67](#)
- [36] Jyo Lyn Hor, Haonan Wang, Zahra Fakhraai, and Daeyeon Lee. Effect of physical nanoconfinement on the viscosity of unentangled polymers during capillary rise infiltration. *Macromolecules*, 51(14):5069–5078, 2018. [67](#)
- [37] Ronald P White, Christopher C Price, and Jane EG Lipson. Effect of interfaces on the glass transition of supported and freestanding polymer thin films. *Macromolecules*, 48(12):4132–4141, 2015. [67](#)
- [38] Xiguang Li and Gregory B McKenna. Ultrathin polymer films: Rubbery stiffening, fragility, and t_g reduction. *Macromolecules*, 48(17):6329–6336, 2015. [67](#)
- [39] J Mattsson, JA Forrest, and L Börjesson. Quantifying glass transition behavior in ultrathin free-standing polymer films. *Physical Review E*, 62(4):5187, 2000. [67](#)
- [40] Keewook Paeng and MD Ediger. Molecular motion in free-standing thin films of poly (methyl methacrylate), poly (4-tert-butylstyrene), poly (α -methylstyrene), and poly (2-vinylpyridine). *Macromolecules*, 44(17):7034–7042, 2011. [67](#)
- [41] Amitabh Bansal, Hoichang Yang, Chunzhao Li, Kilwon Cho, Brian C Benicewicz, Sanat K Kumar, and Linda S Schadler. Quantitative equivalence between polymer nanocomposites and thin polymer films. *Nature materials*, 4(9):693–698, 2005. [67](#)
- [42] CB Roth, A Pound, SW Kamp, CA Murray, and JR Dutcher. Molecular-weight dependence of the glass transition temperature of freely-standing poly (methyl methacrylate) films. *The European Physical Journal E*, 20(4):441–448, 2006. [67](#), [68](#)
- [43] Joseph L Keddie, Richard AL Jones, and Rachel A Cory. Size-dependent depression of the glass transition temperature in polymer films. *EPL (Europhysics Letters)*, 27(1):59, 1994. [67](#)
- [44] Christopher J Ellison, Manish K Mundra, and John M Torkelson. Impacts of polystyrene molecular weight and modification to the repeat unit structure on the glass transition- nanoconfinement effect and the cooperativity length scale. *Macromolecules*, 38(5):1767–1778, 2005. [67](#)

- [45] Paul A O'Connell, Jian Wang, T Adeniyi Ishola, and Gregory B McKenna. Exceptional property changes in ultrathin films of polycarbonate: glass temperature, rubbery stiffening, and flow. *Macromolecules*, 45(5):2453–2459, 2012. [67](#)
- [46] Justin E Pye and Connie B Roth. Two simultaneous mechanisms causing glass transition temperature reductions in high molecular weight freestanding polymer films as measured by transmission ellipsometry. *Physical review letters*, 107(23):235701, 2011. [67](#)
- [47] Weiming Li, Gaoshan Huang, Jiao Wang, Ying Yu, Xiaojing Wu, Xugao Cui, and Yongfeng Mei. Superelastic metal microsprints as fluidic sensors and actuators. *Lab on a Chip*, 12(13):2322–2328, 2012. [68](#)
- [48] Alexander Mario Maier, Wooli Bae, Daniel Schiffels, Johannes Friedrich Emmerig, Maximilian Schiff, and Tim Liedl. Self-assembled dna tubes forming helices of controlled diameter and chirality. *ACS nano*, 11(2):1301–1306, 2017. [68](#)

Chapter 4

Mechanical Characterization of Helical Ribbons

Contents

4.1 Experimental Protocol and Methods	74
4.1.1 Establishing the Force-Extension Curve	76
4.1.2 Increasing the Pitch Angle	77
4.2 Experimental Results	77
4.2.1 Force-Extension Curves	77
4.2.2 Measuring the Twisting Modulus of Ribbons	80
4.3 References	82

Helical structures display very interesting mechanical properties. Thanks to their tightly packed geometry, they store a high amount of elastic energy in a small volume. Furthermore, these structures are usually highly slender: in our case helical ribbons are more than 1 order of magnitude larger in total length than radius, and 3 orders of magnitude larger in radius than ribbon thickness. High stretch ratios of the overall geometry can be achieved with comparatively very little material strain and very little force applied. Such structures are widespread at the macro-scale: helical springs can store energy, absorb shocks, measure forces or serve as actuators.

In recent years, considerable efforts have been dedicated to implement such structures at the micro-scale [1, 2]. In regards to these applications, it is critical to accurately characterize the mechanical properties of micro-helices. Mechanical characterization is usually carried out by measuring the force-extension response of the helical structure under an end-loading. At the micro scale, experiments are typically conducted under a microscope to measure deformations and a cantilever is used to measure forces [3–8]. These studies often rely on theoretical derivations to analyze the force-extension relationship and link the overall response to the helix geometry and to the material properties. But few of these studies investigated the case of helical ribbons. Pham et al. [4, 9] followed such an approach to probe the mechanical response of PMMA helical ribbons fabricated using the flow-coating method described in section 2.2. The influence of the pitch angle was not studied, as precise control of this parameter was not achieved yet. The work of Khaykovich et al. [8] has measured experimentally the spring constant of cholesterol helical ribbons. But for these cholesteric helices the pitch angle is always either 11° or 54° , and thus influence of the pitch angle was again not addressed. To our knowledge, only the work of Starostin et al. [10] has addressed the influence of the pitch angle on the mechanical response of helical ribbons. They proposed an analytical model, supported by numerical simulations.

In this chapter, we experimentally characterize the mechanical properties of helical ribbons by measuring the force-extension relationship under an axial end-loading. We leverage the newly developed stretching treatment (described in chapter 3) to investigate the influence of the pitch angle on the helix mechanical response. Experimental results are compared to the theoretical modeling proposed by Starostin et al. Moreover, we check whether the irreversible deformations triggered during the pitch increase process have an effect on material properties. This chapter is organized as follows. In section 4.1 we describe the experimental protocol that we have implemented. Section 4.2 presents the experimental results and how the ribbon modulus is obtained from the experimental data.

4.1 Experimental Protocol and Methods

The general experimental set-up is described in section 2.4. As we conduct force measurements, the puller capillary is replaced by a carbon fiber cantilever and experiments are conducted in the fluid pool. The bending modulus of the carbon fiber cantilever was calibrated at $B_{\text{cant}} = (1.55 \pm 0.02) \times 10^{-11} \text{ Pa} \cdot \text{m}^4$ (see section 2.4 for more details). We recall that when submitted to a force perpendicular to the cantilever direction, the cantilever tip deflection is given by $\delta = FL_{\text{cant}}^3 / 3B_{\text{cant}}$. With typical cantilever length $L_{\text{cant}} \sim 1 \text{ cm}$, sub-nanonewton forces can be measured.

The experimental workflow is illustrated in fig. 4.1. As previously mentioned, samples are released into a pool of water, helices detach from the substrate and self-coil (step 1). A

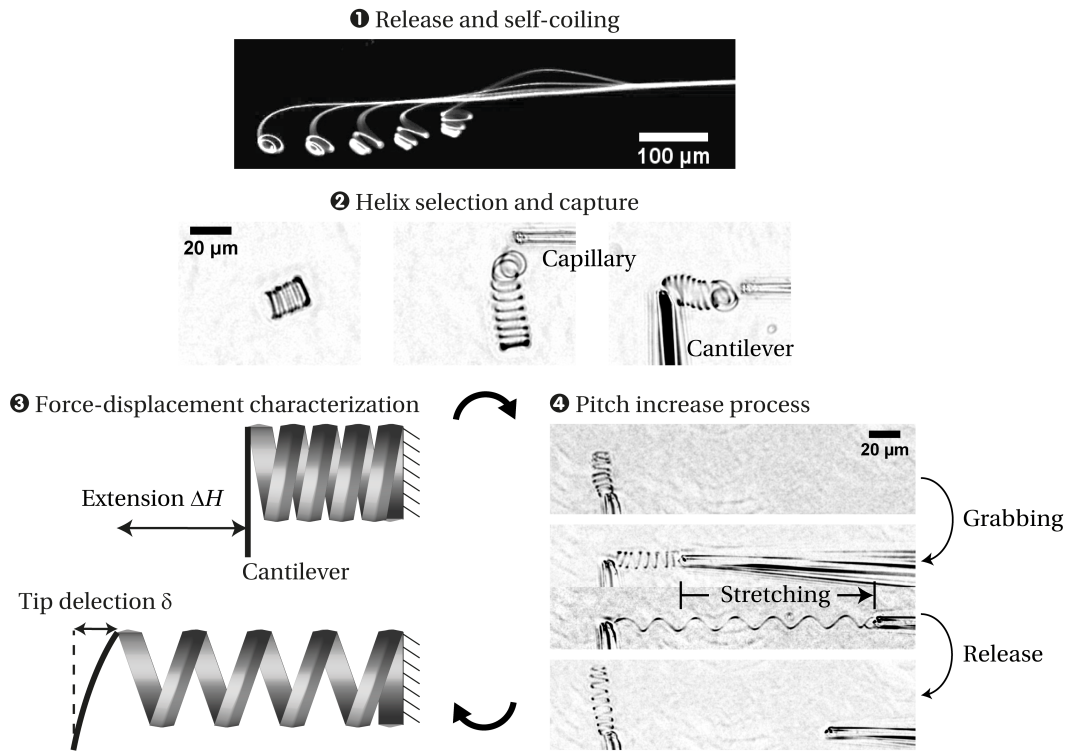


FIGURE 4.1 – Experimental workflow for the mechanical characterization of helical ribbons. Samples are immersed in water: ribbons lift-off following the dissolution of the sacrificial layer and self-coil into a tight helical shape. A helix is selected and captured by the open glass capillary. Contact is made between the tip of the cantilever and the other helix end. The two next steps are repeated until the end of the experiment: firstly establishing the force-extension curve for a given helix geometry and secondly increasing the pitch angle using the stretching treatment method.

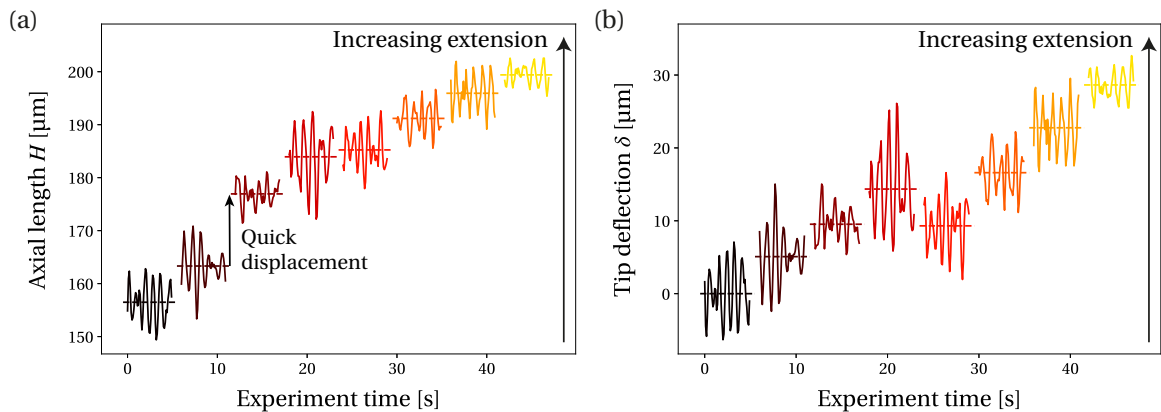


FIGURE 4.2 – Example of a series of measurements made for (a) the helix axial length and (b) the cantilever tip, as steps of increasing extension are imposed to a PMMA helical ribbon, for a given helix geometry. The filament length is $L = 240\mu\text{m}$, the resting pitch angle is $\alpha_0 = 41^\circ$ and the resting radius is $R = 4.0\mu\text{m}$. Significant noise is observed on both the axial length and the tip deflection, which probably originates from ambient flow in the fluid pool. As the helix is held between the cantilever tip and the capillary, fluctuations on ΔH and δ are strongly correlated. Horizontal lines represent the mean value for each condition.

helix is selected and one of its end is caught and clamped by the open glass capillary. The cantilever, mounted on a micro-manipulator, is approached and contact is made between the cantilever tip and the other end of the helix (step 2). Non-specific contact forces allow strong adhesion between the cantilever and the helix. Two steps are then repeated until the end of the experiment: first establishing the force-extension curve (step 3) and then varying the pitch angle using the stretching treatment (step 4), both steps are detailed in the following sections.

4.1.1 Establishing the Force-Extension Curve

Firstly, the force-extension curve is established. A series of increasing elongation steps is imposed to the helix by successively displacing the capillary. As the helix is held at its right end by the capillary, the helix is extended by displacing the capillary to the right. The capillary is quickly displaced from one position to another (typically 6 to 8 positions) and is held still for a few seconds at each position (typically 5 seconds). At each position and for the few seconds the capillary is held still, the geometry of the deformed helix and the cantilever tip displacement are recorded. From the experimental images, we extract the cantilever tip position and the helix axial length. Knowing the reference position of the cantilever tip, the tip deflection is simply obtained. We show in fig. 4.2 (a) a typical series of measurements made for the helix axial length as a function of time, for successive positions of the capillary. Figure 4.2 (b) shows the corresponding tip deflection. As expected, as the axial length is further increased, the cantilever tip is further deflected: the force applied to stretch the helix is recorded by the cantilever.

We observe, as shown in fig. 4.2 (a) & (b), that noise is significant. Noise probably originates from ambient flow in the fluid pool, which, combined to the very long length of the cantilever fiber, creates large fluctuations in the cantilever tip position. As the helix is held between the cantilever tip and the capillary, these fluctuations also impact measurements of the helix axial length. To mitigate the effects of noise, the cantilever tip deflection δ and the helix axial length H are averaged over the 5 seconds recordings. Horizontal lines in fig. 4.2 (a) & (b) represent the averaged values. The tension force F is then simply computed from the tip deflection δ , the cantilever fiber length L_{cant} and the cantilever bending modulus B_{cant} . The cantilever length is measured optically prior to experiments.

Before and after each force-extension curve is established, the helix end clamped by the open glass capillary is released (by expelling liquid out of the capillary) and the axial length is measured. No force is then applied, the helix is thus in its reference configuration. The value for the resting axial length H_0 is taken as the average over these two measurements. Once the resting axial length is known, the axial extension is simply computed $\Delta H = H - H_0$. As stress is necessarily exerted on the helix during force measurements, irreversible deformations are triggered: the resting axial length is increased as a result of the force measurements. Therefore, the geometric parameters of the helix (resting pitch angle notably) may change during the flow cycle. But these effects are mitigated by minimizing the total experiment time, typically below 1 minute. Furthermore, the ribbon material is chosen to be poly(methyl methacrylate) (PMMA), which is the material that minimizes creep among the materials that we have tested. The increase in resting axial length resulting from establishing a given force-extension curve is always below 2% of the total length L . This corresponds to a variation in resting pitch angle of less than 1° , which

we neglect. The helix geometrical parameters (resting axial length, radius and angle) are thus considered constant for a given force-extension curve.

4.1.2 Increasing the Pitch Angle

Secondly, we apply the stretching treatment to uniformly increase the helix resting pitch angle α_0 . The treatment is conducted as described in chapter 3. The helix is grabbed at its two ends, one by the cantilever and one by the capillary, a fixed axial extension is imposed for several minutes by displacing the capillary and the helix is finally let to relax. This treatment results in an irreversible increase in the resting pitch angle. Once the stretching treatment has been performed, the resting axial length H_0 and resting pitch angle α_0 are measured again as to track evolution of the helix geometry.

The force-extension curve is then measured for this new reference geometry before another stretching treatment is performed and so on. At the end of the experiment, the helix is completely stretched to measure the total filament length L . This protocol yields a series of force-extension curves as the reference geometry of a given helix is varied: each force-extension curve corresponds to a different resting pitch angle. As demonstrated in chapter 3 the total filament length is not affected by the stretching treatment and thus remains constant throughout the whole experiment. Similarly to what was observed in chapter 3 the resting radius may vary slightly as a by-product of the successive stretching treatments. But as influence of the radius on the force is well established ($F \propto 1/R^2$), these variations are easily corrected.

4.2 Experimental Results

4.2.1 Force-Extension Curves

We show in fig. 4.3 (a) the measured force F , computed from the cantilever tip deflection δ , as a function of rescaled axial length H/L , for a given PMMA helix as the helix geometry is varied. Each curve on the plot corresponds to a different resting pitch angle. The corresponding resting axial length H_0 for each geometry is represented at the bottom of the plot. The error bars for the force and the axial length are the standard deviations over the 5 seconds-long recordings (see example of a recording in fig. 4.2). Figure 4.3 (b) shows, for the same data, the force F as a function of rescaled axial extension $\Delta H/L$. Some points are obtained for $\Delta H < 0$ to allow measurement of the cantilever reference position. For these points we observe $F \approx 0\text{N}$, which shows that the helix is then not axially compressed but rather buckle out of its axis. For an axial compression, we would indeed expect symmetry of the $F(\Delta H)$ curve. For this example, we observe that the helical ribbon seems to stiffen as the pitch angle is increased. Indeed, for the light-colored curves, which correspond to higher resting pitch angles, a higher force is necessary to extend the helix than for the dark-colored ones. The same observation is repeated for other PMMA helical ribbons. But before we can interpret this stiffening, we must understand how the geometrical and mechanical properties of the helix determine the force-extension response.

As shown in fig. 4.3 (a) the imposed elongation can be significant, the axial length reaching up to 95% of the total length L *i.e.* almost to full elongation. In this high stretch regime, close to full helix extension (corresponding to $H = L$), the force-extension relationship is not linear. Examining the helix deformation only within the linear regime is thus not

relevant. The work of Starostin et al. [10] has examined in the general case the deformation of a helical ribbon submitted to an axial end-loading. The ribbon was modeled as an inextensible elastic strip. Under the assumption that the deformed helix remains a uniform helix (uniform radius and angle), they proposed the following expression for the force

$$F = \frac{C}{R^2} \frac{(\cos \alpha_0 \cos \alpha + \frac{C}{B} \sin \alpha_0 \sin \alpha) \sin(\alpha - \alpha_0)}{(\cos^2 \alpha + \frac{C}{B} \sin^2 \alpha)^2 \cos \alpha} \quad (4.2.1)$$

with $\alpha_0 = \arcsin H_0/L$ resting pitch angle and $\alpha = \arcsin H/L$ pitch angle of the deformed helix (supposedly uniform along the filament length). We recall that $B = EI$ and $C = \mu J$ are respectively the bending and twisting modulus of the ribbon, with I second-moment of area, μ shear modulus and J polar moment of inertia. Because of the multiplicative terme $1/\cos \alpha$, the force diverges as the helix is fully extended (corresponding to $\alpha \rightarrow 90^\circ$), which models the finite extensibility of the helical structure.

In the linear limit $\alpha - \alpha_0 \ll 1$, the expression simplifies

$$F = \frac{C}{R^2} \frac{1}{\cos^2 \alpha_0 (\cos^2 \alpha_0 + \frac{C}{B} \sin^2 \alpha_0)} \frac{\Delta H}{L} \quad (4.2.2)$$

In the case of helices with cylindrical filaments, the classical work of Love [11] found a very similar expression

$$F_{\text{cylinder}} = \frac{C}{R^2} \frac{1}{(\cos^2 \alpha_0 + \frac{C}{B} \sin^2 \alpha_0)} \frac{\Delta H}{L}$$

The general scaling is thus the same but an additional $1/\cos^2 \alpha_0$ is found by Starostin et al. in the case of helical ribbons. This additional term drives an effective stiffening of helical ribbons as the resting pitch angle is increased, which could correspond to our observations. This effect seems thus to be specific to helical ribbons and would not be observed for helices with cylindrical filaments. We now compare the results of Starostin et al. to our experimental measurements.

We take for the ratio C/B its standard value in the case of a flat triangular cross-section $C/B = 3/2(1 + \nu)$. The Poisson's ratio ν for bulk PMMA is usually estimated within the range $\nu = 0.35 - 0.4$. We consider that the Poisson's ratio is not affected by the vanishing thickness of ribbons and we take $\nu = 0.375$. Each force-extension curve is fitted by eq. (4.2.1), with thus a single fitting parameter C/R^2 . In theory, the twisting modulus $C = \frac{1}{12} \mu w t^3$ can be measured prior to experiments by measuring the ribbon thickness t and width w . But in practice and as we discussed in section 2.2.3, accurate measurement of the ribbon thickness prior to experiments is very difficult with our experimental system. Furthermore, determining the material Young's modulus E and shear modulus μ would require further investigation. The bulk values are not relevant, as confined geometries have been shown to influence the Young's modulus. This is discussed in more details in section 3.5.

We show in fig. 4.3 (c) the force-extension curves fitted by the proposed theoretical model. The successive curves are shifted by an arbitrary amount to better distinguish between the different curves. The reference point $\Delta H = 0$ is shown for each curve at the bottom of the plot. For most resting pitch angles, the proposed expression accurately fits the experimental data. Notably, the fitting accurately captures the non-linearity of the force-extension curves. The experimental protocol is repeated for several other PMMA helices (4 in total). We show in fig. 4.4 the fitted force-extension curves for another PMMA helix. Agreement between the experimental data and the proposed model is again very good at all

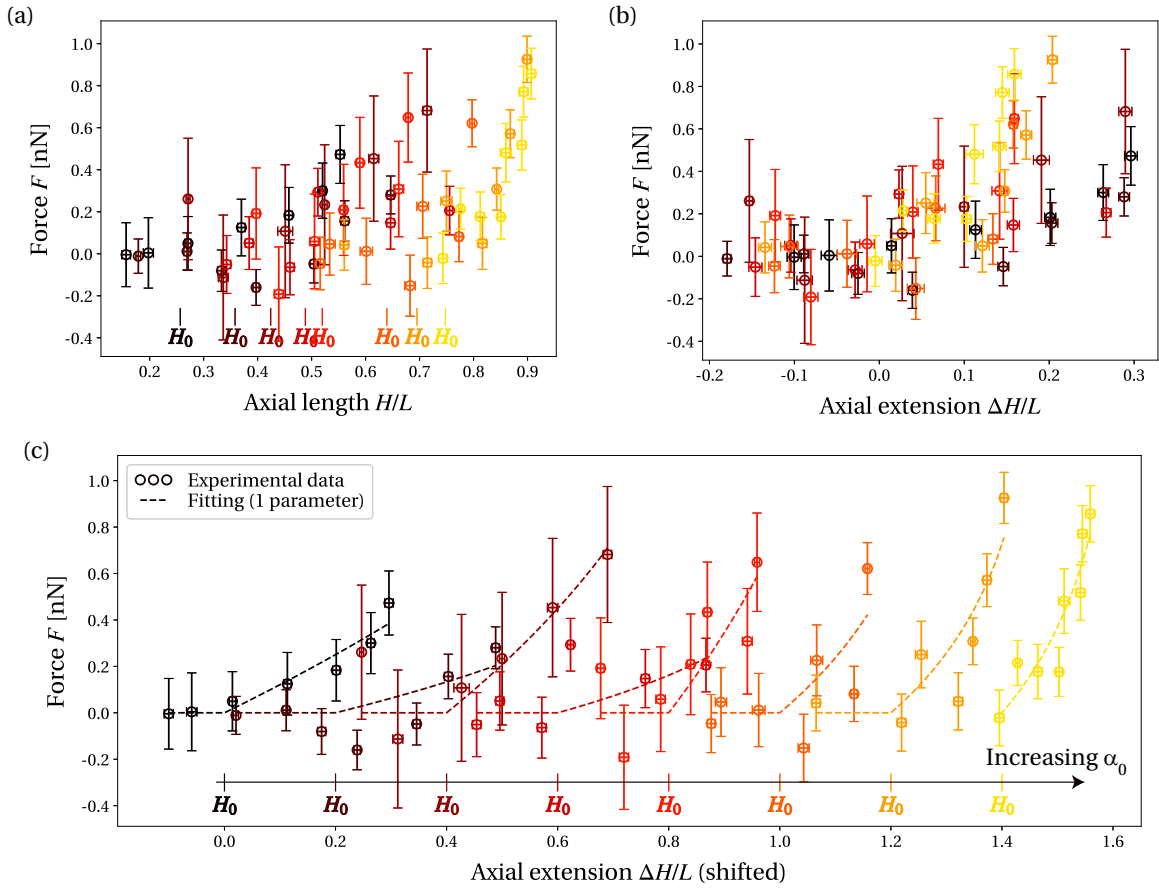


FIGURE 4.3 – Force-extension curves for a PMMA helix under axial end-loading, as the helix geometry is varied using the stretching treatment. Each curve corresponds to a different resting pitch angle α_0 . The total filament length is $L = 670\mu\text{m}$ and the starting helical radius is $R = 12.1\mu\text{m}$. (a) Force F as a function of rescaled axial length H/L . For each curve, the corresponding resting axial length H_0 is represented at the bottom of the plot. The points $H < H_0$ allow measurement of the cantilever reference position. (b) Force F as a function of rescaled axial extension $\Delta H/L$. (c) Force-extension curves fitted with the expression proposed by Starostin et al. (1 fitting parameter). Curves are shifted by an arbitrary amount to better distinguish between the different curves. The reference point $\Delta H = 0$ is shown.

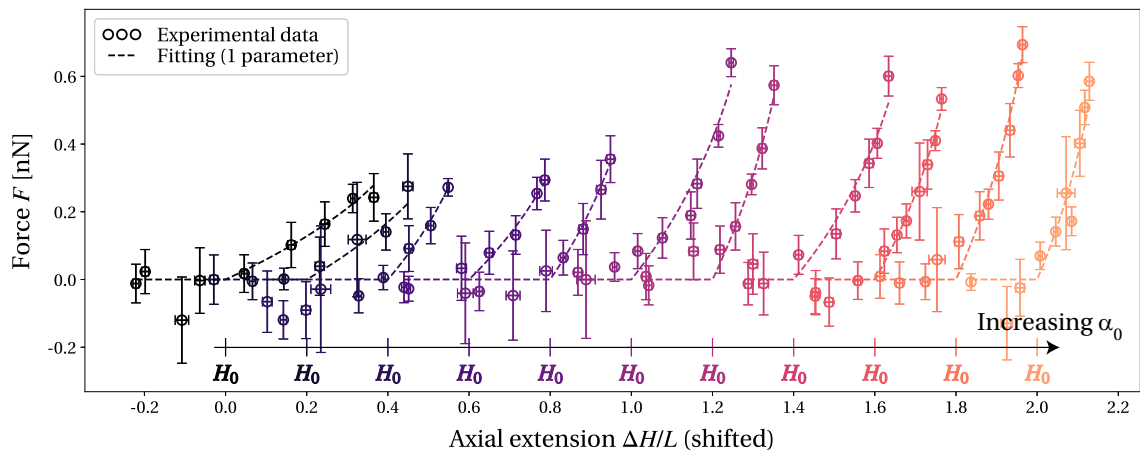


FIGURE 4.4 – Force-extension curves for another PMMA helical ribbon submitted to axial end-loading, as the helix geometry is varied, fitted with the expression proposed by Starostin et al. (1 fitting parameter). Each curve corresponds to a different resting pitch angle α_0 . The total filament length is $L = 480\mu\text{m}$ and the starting helical radius is $R = 5.0\mu\text{m}$. Curves are shifted by an arbitrary amount to better distinguish between the different curves. The reference point $\Delta H = 0$ is shown for each curve.

resting pitch angles. And again, we notice an effective stiffening of the helical ribbon as the resting pitch angle increases. This is evidenced by the initial slopes of the force-extension curves, which get steeper as the resting pitch angle is increased. Our experimental results thus provide strong validation for the relationship $F(\alpha)$ obtained analytically by Starostin et al. Variation of the mechanical response with the resting pitch angle α_0 is discussed in the next section.

This validation comes despite some differences between their assumptions and our experimental conditions. Most importantly, they assumed a force-controlled stretching while in our experiments the stretching is displacement-controlled, the applied force being measured through the cantilever. This entails differences in the boundary conditions. Specifically, in our experimental conditions both ends of the helix are clamped and thus the applied stretching force is not purely axial, a tangential component may also exist. This tangential component is not recorded, as it is applied parallelly to the cantilever axis. Thus, the very good agreement between the predictions of Starostin et al. and our experimental results suggests that boundary conditions have only a weak impact on the overall helix deformation.

4.2.2 Measuring the Twisting Modulus of Ribbons

Once the quantity C/R^2 is obtained from the fitting, the twisting modulus C is computed. The resting radius R is measured for each geometry as to account for possible change in the helical radius induced by the stretching treatment. Hence, fitting of the force-extension curves yields an estimation of the twisting modulus C at each given geometry. We can thus track potential evolution of the mechanical properties of ribbons that may result from the stretching treatment.

We show in fig. 4.5 (a) the successive measurements for the twisting modulus as the resting pitch angle is increased, for all four tested helices. In all four cases and within the experimental errors, no significant change is observed for the twisting modulus. Overall, the resting pitch angle spans a wide range $15 - 70^\circ$. Therefore, we conclude that the twisting modulus C is not affected by the stretching treatment: its value remains constant throughout the experiment. C is expressed from the Young's modulus and from the ribbon cross-sectional geometry $C \sim Ewt^3$. As it is very unlikely that E , w and t would vary while keeping C constant, we conclude that these parameters also remain unaffected by the stretching treatment. Overall, all mechanical properties remain constant. These results further validates the modeling proposed by Starostin et al. The stiffening observed as the resting pitch angle increases is accurately captured by the factor $1/\cos^2 \alpha_0 (\cos^2 \alpha_0 + \frac{C}{B} \sin^2 \alpha_0)$. Conversely, this means that the model proposed by Love for the extension of helically-shaped cylindrical filaments would not describe accurately our experimental measurements. It thus seems that the observed stiffening effect is specific to helical ribbons.

As we mentioned, the work of Pham et al. [9] already studied the mechanical response of PMMA helical ribbons. The twisting modulus C was measured for several PMMA helical ribbons of various radii R . They proposed an empirical relation between C and R , $C = C_0 \exp(\beta R)$ with $C_0 = (2.6 \pm 1.1) \text{ N} \cdot \text{m}^2$ and $\beta = (3.5 \pm 0.5) \times 10^5 \text{ m}^{-1}$. As the pitch angle was not controlled, it is safe to assume that these results were obtained for helices in their initial configuration after coiling *i.e.* with vanishing pitch angles. Influence of the pitch angle on the mechanical response being weak at small angles (the geometrical stiffening factor goes as $\sim 1/\cos^2 \alpha$), this effect is negligible within the work of Pham et al. At small pitch angle

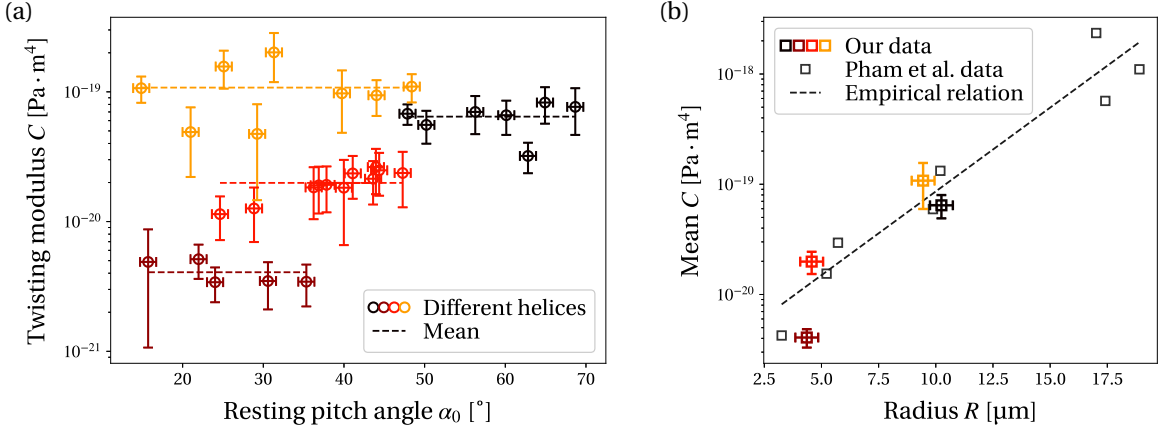


FIGURE 4.5 – (a) Estimation of the twisting modulus C obtained from fitting the force-extension curves as a function of resting pitch angle for 4 different PMMA helical ribbons. Error bars represent numerical errors from the fitting. (b) Twisting modulus C averaged over all resting pitch angles as a function of starting helical radius R . Colored dots show our experimental results while gray dots show the results of Pham et al. (also obtained for PMMA helical ribbons) [9]. The gray dashed line shows the empirical relation proposed by Pham et al.

and in the linear limit, the force-extension relationship simplifies to $F = (C/R^2) * (\Delta H/L)$. Pham et al. mistakenly used a different relation $F = (B/R^2) * (\Delta H/L)$. Their results are thus presented as measurements of the bending modulus B while they actually measured the twisting modulus.

We reproduce in fig. 4.5 (b) the results of Pham et al. along with our results as well as the empirical relation proposed by Pham et al. Our measurements are very consistent with the previous results and agree qualitatively with the proposed empirical relation. We obtain $C \sim 10^{-20} - 10^{-19} \text{ Pa} \cdot \text{m}^4$ for radii within 5 – 10 μm. In details however, some measurements (including results from Pham et al.) deviate quite significantly from the proposed empirical relation, at small radii notably. As we have $R \sim Et^2/\gamma$ and $C \sim Ewt^3$, the following theoretical relation can be proposed $C \sim E * (w/t) * (\gamma R/E)^2$. Thus, a universal relation between C and R would require a constant value for w/t *i.e.* a universal aspect ratio for the cross-section of ribbons.

Precisely, the work of Choudhary et al. [12] has investigated the influence of various parameters on the aspect ratio w/t . They highlighted a significant influence of the gap distance h_{gap} , distance between the blade and the substrate during flow-coating, and of the plasma etching time. For both parameters, a change up to a factor 8 in the aspect ratio was observed. Therefore it is not surprising to observe helices for which the twisting modulus deviates by an order of magnitude away from the empirical relation proposed by Pham et al.



In this chapter, we have experimentally characterized the mechanical properties of helical ribbons by measuring the force-extension relationship. An axial extension was imposed, and the corresponding force was measured using a cantilever beam. Benefiting from the newly achieved control on the pitch angle, influence of this parameter was investigated. At a given reference geometry, the relation $F(\Delta H)$ was found to be non-linear. As the resting pitch angle α_0 was increased, a stiffening of the helical ribbons was

observed. We found that both the non-linear force-extension relation and the effective stiffening are accurately described by the analytical model proposed by Starostin et al. [10]. Equation (4.2.1) gives their analytical results, obtained using an inextensible curved elastic strip model. Our results thus provide strong experimental validation for this expression and for the approach followed by Starostin et al. Comparison with a model previously established for helically-shaped cylindrical filaments [11] suggests that the stiffening effect is specific to helical ribbons.

From the force-extension curves, the filament twisting modulus C was extracted. We tracked potential changes in C as the resting pitch angle was varied. No change was found, confirming that the material mechanical properties are not affected by the irreversible deformations triggered during the pitch increase process. Our measurements for C were compared with previous results from Pham et al., who used the same experimental system [9]. Excellent agreement was found, further validating our results.

We have now established the basic mechanical response of our experimental system, and we have confirmed that the stretching treatment only modifies the pitch angle. We now investigate the fluid-structure interactions between flexible helical ribbons and viscous flows and start by the simple case of a uniform viscous flow.

4.3 References

- [1] Gaoshan Huang and Yongfeng Mei. Helices in micro-world: Materials, properties, and applications. *Journal of Materiomics*, 1(4):296–306, 2015. [74](#)
- [2] Zheng Ren and Pu-Xian Gao. A review of helical nanostructures: growth theories, synthesis strategies and properties. *Nanoscale*, 6(16):9366–9400, 2014. [74](#)
- [3] Brice Smith, Yevgeniya V Zastavker, and George B Benedek. Tension-induced straightening transition of self-assembled helical ribbons. *Physical review letters*, 87(27):278101, 2001. [74](#)
- [4] Jonathan T Pham, Jimmy Lawrence, Gregory M Grason, Todd Emrick, and Alfred J Crosby. Stretching of assembled nanoparticle helical springs. *Physical Chemistry Chemical Physics*, 16(22):10261–10266, 2014. [74](#)
- [5] Dominik J Bell, Lixin Dong, Bradley J Nelson, Matthias Golling, Li Zhang, and Detlev Grützmacher. Fabrication and characterization of three-dimensional ingaas/gaas nanosprings. *Nano Letters*, 6(4):725–729, 2006.
- [6] Xinqi Chen, Sulin Zhang, Dmitriy A Dikin, Weiqiang Ding, Rodney S Ruoff, Lujun Pan, and Yoshikazu Nakayama. Mechanics of a carbon nanocoil. *Nano Letters*, 3(9):1299–1304, 2003.
- [7] Pu Xian Gao, Wenjie Mai, and Zhong Lin Wang. Superelasticity and nanofracture mechanics of zno nanohelices. *Nano letters*, 6(11):2536–2543, 2006.
- [8] Boris Khaykovich, Natalia Kozlova, Wonshik Choi, Aleksey Lomakin, Chintan Hosain, Yongjin Sung, Ramachandra R Dasari, Michael S Feld, and George B Benedek. Thickness–radius relationship and spring constants of cholesterol helical ribbons. *Proceedings of the National Academy of Sciences*, 106(37):15663–15666, 2009. [74](#)

- [9] Jonathan T Pham, Alexander Morozov, Alfred J Crosby, Anke Lindner, and Olivia du Roure. Deformation and shape of flexible, microscale helices in viscous flow. *Physical Review E*, 92(1):011004, 2015. [74](#), [80](#), [81](#), [82](#)
- [10] EL Starostin and GHM van der Heijden. Tension-induced multistability in inextensible helical ribbons. *Physical review letters*, 101(8):084301, 2008. [74](#), [78](#), [82](#)
- [11] Augustus Edward Hough Love. *A treatise on the mathematical theory of elasticity*. Cambridge university press, 1944. [78](#), [82](#)
- [12] Satyan Choudhary and Alfred J Crosby. Controlled processing of polymer nanoribbons: Enabling microhelix transformations. *Journal of Polymer Science Part B: Polymer Physics*, 57(18):1270–1278, 2019. [81](#)

Chapter 5

Deformation of Helical Ribbons in Viscous Axial Flows

Contents

5.1 Experimental Protocol and Methods	86
5.1.1 Experimental Workflow	86
5.1.2 Flow Cycles and Creep Effects in the Material	88
5.2 Experimental Results	89
5.3 Shape Analysis of the Deformed Helices	92
5.3.1 Method for Image Analysis	92
5.3.2 Pitch and Radius Distribution	93
5.3.3 Torsion to Bending Transition	94
5.4 References	97

In the previous chapters, we have described and implemented a general method to obtain highly flexible helical ribbons of arbitrary geometry. All geometrical parameters (radius, length and pitch angle) can be precisely controlled, independently of one another. Furthermore, we have characterized the mechanical properties of helical ribbons under end-point loading. This experimental framework thus constitutes an ideal model system to explore systematically the complex interactions between flexible helical structures and viscous flows. In this chapter, we demonstrate this by investigating experimentally the deformation of clamped PMMA helical ribbons immersed in uniform viscous axial flows.

The position of the problem is fairly simple: a helical ribbon is clamped at one end and is immersed in a uniform viscous flow in the same direction as the helical axis, with flow velocity U . As the flow is applied to the helix, the helix deforms: ΔH is the change in axial length between the deformed situation and the resting situation (no flow). As discussed in chapter 1, multiple studies have already tackled this problem, experimentally [1, 2], numerically [3] or theoretically [4, 5]. We recall that these works have established the scaling for the axial extension: $\Delta H \sim R^2 L^2 (\eta U / B)$. But so far, the influence of the pitch angle on the extension in flow remains obscure. Analytical works have obtained vanishing influence of the pitch angle [4, 5] but these predictions have not been validated experimentally. Leveraging the newly developed stretching treatment to accurately control the pitch angle, we address in detail the influence of this parameter on the deformation in flow.

The chapter is organized as follows. In section 5.1 we describe the experimental protocol that we have implemented to isolate the influence of the pitch angle. Section 5.2 presents the experimental results for the extension of helical ribbons in flow. A significant stiffening of the helical ribbons in flow is found as the pitch angle increases. In section 5.3 we analyze the shape of the flow-deformed helices as to better understand this stiffening effect.

5.1 Experimental Protocol and Methods

5.1.1 Experimental Workflow

The general experimental set-up is described in chapter 2. For the flow experiments, the two open glass capillaries are used (termed holder capillary and puller capillary). Naturally a microfluidic channel is needed: we use a simple rectangular channel of height $H = 650\mu\text{m}$ and width $W = 250\mu\text{m}$. Flow experiments are conducted in a very similar manner than the force characterization experiments: the experimental workflow is illustrated in fig. 5.1. Samples are released into water (with viscosity $\eta = 1.0 \times 10^{-3} \text{ Pa} \cdot \text{s}$) and helices form, from which we select and capture one helix (step 1 & 2 in fig. 5.1). A cycle of two steps is then repeated. Firstly, the helix is clamped and immersed in a uniform viscous axial flow and the induced elastic axial extension ΔH is measured (step 3). This step is called the 'flow cycle'. The flow profile applied during a flow cycle is typically a series of flow steps at increasing velocity, as to also probe the influence of the flow velocity. Secondly, a pitch increase process is applied to the helix, by extending the helix for several minutes (step 4) using the puller capillary. This process results in an increase in the resting pitch angle α_0 . We then repeat these two steps, flow cycle and pitch increase process, until the end of the experiment. Finally, at the end of the experiment, the helix is fully stretched by imposing a very strong flow, as to measure the total length L of the filament. This experimental workflow results in a series of flow-extension curves as the helix geometry is varied.

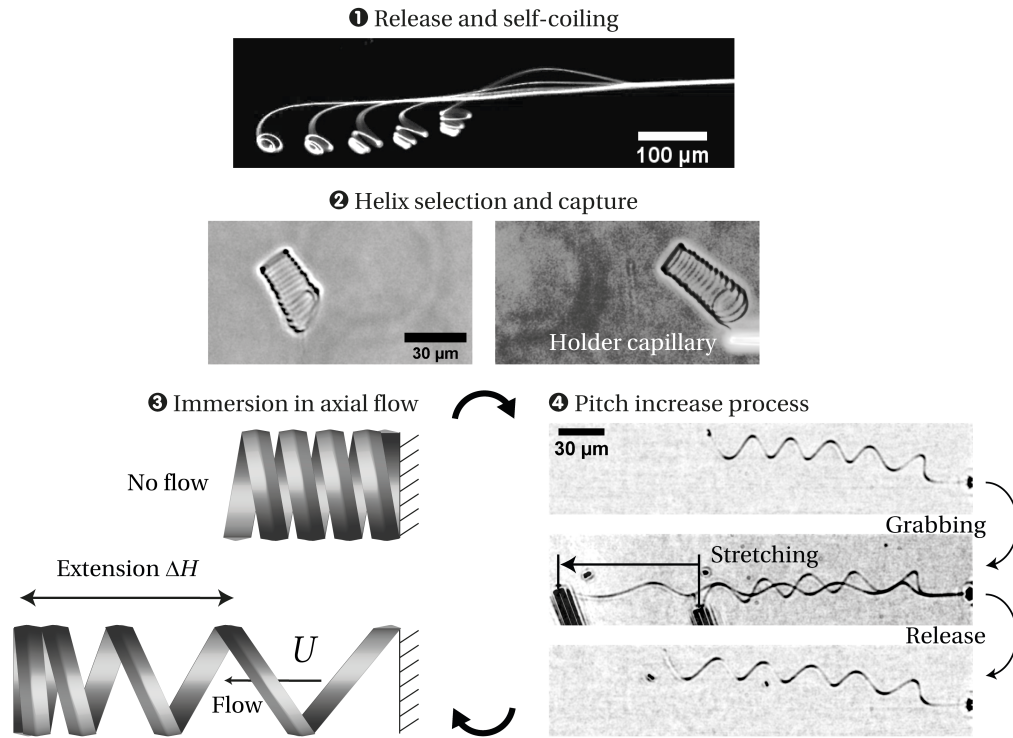


FIGURE 5.1 – Experimental workflow for studying the deformation of clamped helical ribbons in viscous axial flows. Samples are immersed in water: ribbons lift-off following the dissolution of the sacrificial layer and self-coil into a tight helical shape. A helix is selected and captured by the holder capillary. The two next steps are repeated until the end of the experiment: firstly establishing the flow-extension relationship for a given helix geometry and secondly increasing the resting pitch angle using the stretching treatment method.

To conduct the immersion in flow, the helix is positioned at the center of the microfluidic channel. The flow is parabolic in the channel but as typical helical radii ($R \sim 5 - 10 \mu\text{m}$) are small compared to the channel size ($H = 250 \mu\text{m}$), we consider that the helix is immersed in a locally uniform flow. The effect of the flow non-uniformity is further mitigated by placing helices at the center of the channel, where the flow is most uniform. For a given helical ribbon in the microfluidic channel, the velocity U acting on the helix is taken as the average of the flow field velocity over all the positions occupied by the ribbon. The flow field in the channel is computed from the channel dimensions using a derivation from White [6] and the position of the ribbon is measured from the experimental images.

The flow profile imposed onto the object during a flow cycle is kept identical for all flow cycles, as to minimize the number of parameters changing. The filament is highly slender and thus inextensible ($L = \text{cst}$) and we further showed in chapter 4 that the mechanical properties of the helix are not affected during the pitch increase process ($B = \text{cst}$ and $C = \text{cst}$). We do observe small changes in the helical radius R (up to $\sim 25\%$ of its initial value) during the pitch increase process. But as the radius influence is well established ($\Delta H \propto R^2$), these variations can easily be corrected. Therefore, using this experimental protocol, we can unequivocally isolate the influence of the helix pitch angle on the helix extension.

5.1.2 Flow Cycles and Creep Effects in the Material

The material creep properties, leveraged during the pitch increase process, become a problem during a flow cycle. Creeping deformation will indeed add up to the elastic helix response. Furthermore, the geometric parameters of the helix (resting radius and angle) might change during the flow cycle. In order to mitigate these effects, we minimize both the number of flow steps (usually three) and the step duration (less than 10 seconds usually) for a total duration of less than 1 minute for each flow cycle. Furthermore, the ribbon material is chosen to be poly(methyl methacrylate) (PMMA), which is the material that minimizes creep effects among the ones we have tested.

A typical velocity profile imposed during a flow cycle is shown in fig. 5.2 (a), along with the measured helical axial length H , re-scaled by the total filament length L . We further present in fig. 5.2 (b) a zoom onto the first flow step. As underlined previously, we have minimized both the number of steps and the step duration to minimize creep effects during the flow cycle. Overall the duration of this flow cycle is around 40 seconds. Despite these precautions, material creep effects are still visible. Indeed, as seen in fig. 5.2 (a) & fig. 5.2 (b), the helical axial length does not reach an equilibrium state over the duration of one flow step. Furthermore, the value for the axial length is higher at the end than at the beginning of the flow cycle: we observe a $\sim 1\%$ increase in the dimensionless axial length H/L . This corresponds to an increase of $\sim 0.5^\circ$ in resting pitch angle, resulting from the flow cycle. Hence, a small uncontrolled angle increase occurs during the flow cycle, then followed by a large and controlled increase during the pitch increase process. Overall we observe that the increase resulting from flow cycles never exceeds 1° and is negligible compared to the controlled increase. We can thus consider that the geometric parameters (resting radius and angle) are constant during a flow cycle.

But during a single flow step, these creeping effects are fairly visible and prevent a simple measurement of the helix elastic response. In order to quantify the elastic response during a single flow step, we implement an analysis that decouples the elastic and creep components of the axial extension. Assuming constant pulling force and friction, the elastic

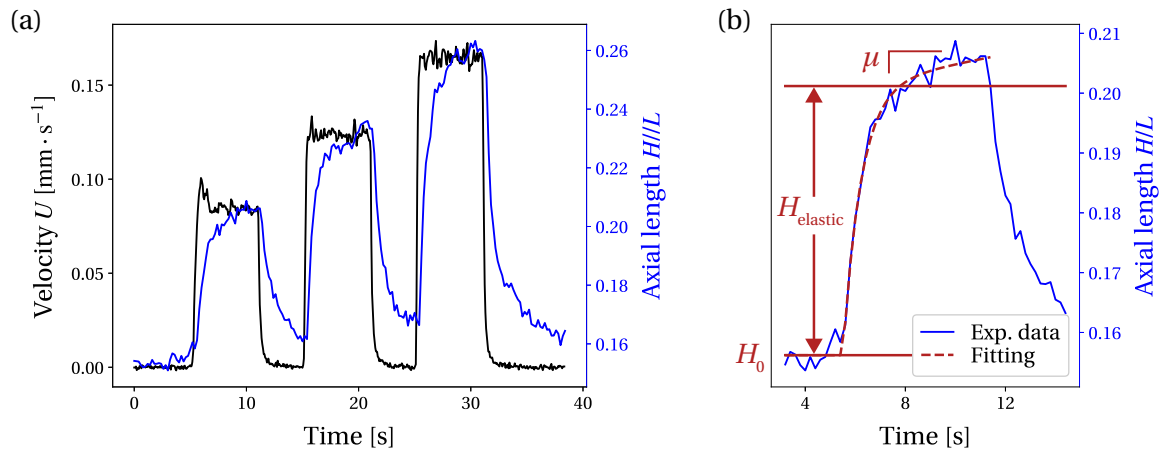


FIGURE 5.2 – (a) Typical velocity profile (in black) imposed during a flow cycle and rescaled axial length H/L (in blue) as a function of time. (b) Zoom onto the first flow step shown in (a): measured axial length H/L fitted by a semi-phenomenological expression to differentiate the helix elastic response from the creep deformation. Three fitting parameters are used: the elastic response H_{elastic} , the response time τ and μ (see eq. (5.1.1) for more details).

component is expressed under the form $H_{\text{elastic}}(1 - e^{-t/\tau})$, where H_{elastic} corresponds to the amplitude of the elastic deformation and τ to the timescale of the helix recovery. We add a phenomenological term, μt , that denotes the susceptibility of the material to creep. The extension curve $H(t)$ is hence fitted by the following semi-phenomenological function

$$H(t) - H_0 = H_{\text{elastic}}(1 - e^{-t/\tau}) + \mu t \quad (5.1.1)$$

H_0 is the resting axial length, which is measured and thus not a fitting parameter.

Experimentally we find the extension timescale τ to be always under 1 s while the creeping timescale H_0/μ is always above 100 s. This significant difference in the timescales allows a clear separation of the elastic deformation from the creeping deformation. As seen in fig. 5.2 (b), agreement with experimental data is good. With this fitting method, we recover the elastic extension $\Delta H = H_{\text{elastic}}$ as well as the helix recovery timescale τ , as a function of the helix geometrical parameters and of the flow velocity U . ΔH sets the magnitude of the elastic extension while τ sets the dynamics of extension and recovery. In the following we focus on the study of ΔH but the study of the elongation dynamics through the timescale τ would be a natural continuation of this work.

5.2 Experimental Results

The results of the experimental investigation are presented in fig. 5.3. First we show in fig. 5.3 (a) the rescaled axial extension $\Delta H/L$ as a function of resting pitch angle α_0 , for a given PMMA helix and for three different flow velocities. The error bars correspond to the numerical errors associated with the fitting procedure. We then show in fig. 5.3 (b) the axial extension normalized by the flow velocity U , for the same data. A good collapse of the data is observed: helix deformation seems to happen within the linear regime *i.e.* $\Delta H \propto U$. Collapse is however not so good at small angles. As it is precisely at small angles that the highest deformations are observed, these discrepancies could be interpreted as non-linear effects, consequence of the helix finite extensibility. But the extension rate $\Delta H/L$ is fairly small throughout the experiment ($\Delta H/L \sim 4 - 8\%$ for the strongest flow), whereas previous studies typically reported non-linear effects for $\Delta H/L \gtrsim 10\%$ [1]. Furthermore, because of the finite extensibility, non-linear effects have been observed to stiffen the helix [1]. And thus we would expect $\Delta H/U$ to decrease with increasing velocity, which is not what is observed here. We rather attribute these discrepancies at small angles to experimental issues.

As mentioned previously, the resting helical radius R may evolve slightly during the experiment, as a consequence of the pitch increase process. We recall the scaling obtained by previous studies $\Delta H \sim (\eta U/B)R^2 L^2$. Therefore, we rescale $\Delta H/U$ by R^2 as to correct the influence of the changes in radius. We further rescale by L^2 (constant for each given helix), as to compare different helices more practically. We hence plot the corrected extension $\Delta H/(UR^2 L^2)$, whose variations only originates from changes in the resting pitch angle, as a function of resting pitch angle in fig. 5.3 (c). The corrected extension $\Delta H/(UR^2 L^2)$ scales as η/B so given typical values of $\eta = 1 \times 10^{-3} \text{ Pa} \cdot \text{s}$ and $B \sim 10^{-20} - 10^{-19} \text{ Pa} \cdot \text{m}^4$, we expect that $\Delta H/(UR^2 L^2) \sim 10^{16} - 10^{17} \text{ s} \cdot \text{m}^{-4}$. This estimation of the order of magnitude is consistent with our observations. In detail, we observe a roughly constant extension at small angles followed by a sharp decrease in extension as the angle increases. The regime change happens for $\alpha_0 \sim 25 - 30^\circ$.

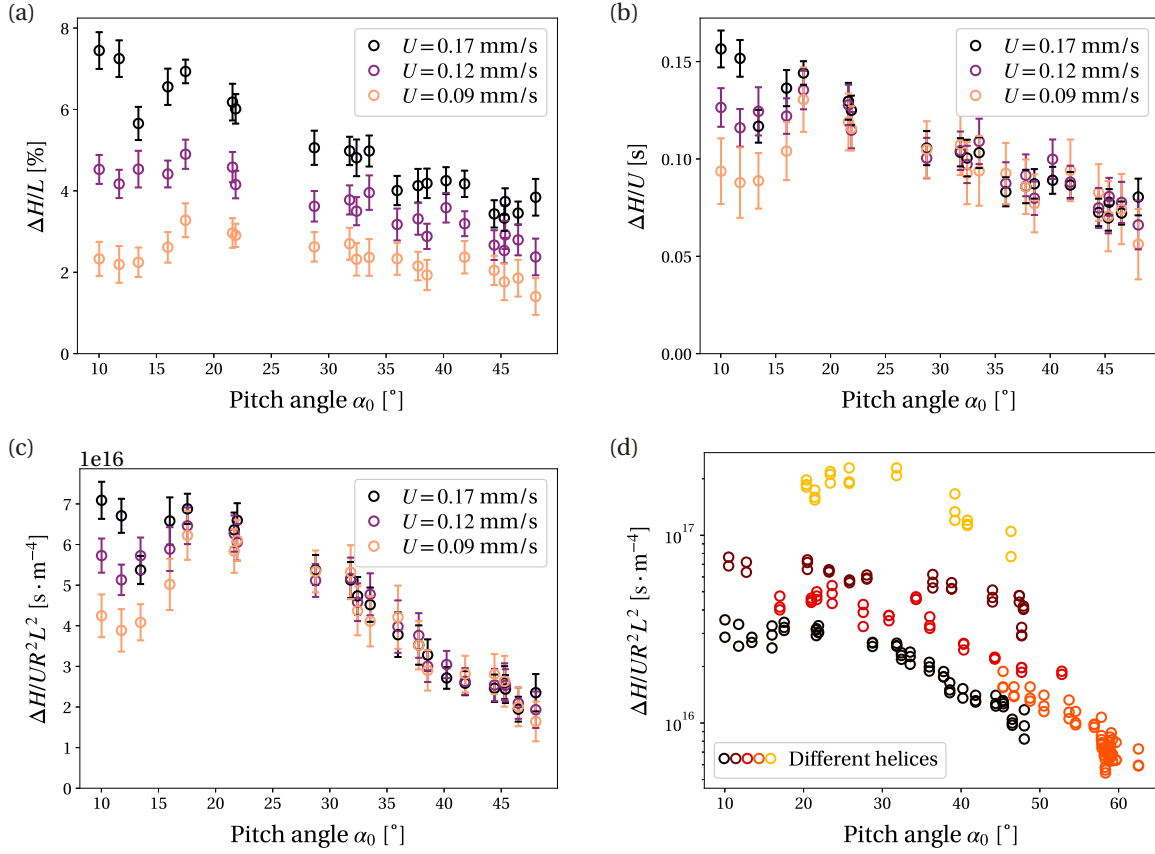


FIGURE 5.3 – Experimental results for the extension in flow of a given PMMA helical ribbon. For this helix, the total filament length is $L = 350\mu\text{m}$ and the initial helical radius is $R = 6.0\mu\text{m}$. (a) Rescaled axial extension $\Delta H/L$ as a function of resting pitch angle α_0 for three different velocities. The error bars correspond to the numerical errors associated with the fitting procedure. (b) Axial extension normalized by the flow velocity $\Delta H/U$ as a function of resting pitch angle α_0 . (c) Normalized axial extension, corrected for radius change, $\Delta H/UR^2L^2$ as a function of resting pitch angle. (d) Corrected axial extension $\Delta H/UR^2L^2$ for all five PMMA helical ribbons that we have tested. Data shown in (a) to (c) correspond to the black dots. Error bars are omitted for clarity of the figure.

This experimental protocol was reproduced for five different PMMA helical ribbons. Helical radii span a range $R = 3 - 12\mu\text{m}$ while lengths span $L = 120 - 650\mu\text{m}$. We show the corrected extension $\Delta H/(UR^2L^2)$ for all five PMMA helical ribbons in fig. 5.3 (d). For all helices, the same behavior is observed: constant extension at small angles until $\alpha_0 \sim 25 - 30^\circ$, followed by a decrease as the angle increases. One exception is the helix represented by the orange dots, for which the starting resting angle was $\sim 40^\circ$. For this helix, we consistently only observe a decrease in corrected extension. The overall value of the corrected extension is naturally different from helix to helix, as it depends on the filament bending modulus B . So to further normalize the data, the bending modulus $B \sim Ewt^3$ needs to be measured for each helical ribbon. But as already discussed in section 2.2.3 accurate measurement of the ribbon dimensions prior to experiments is very difficult with our experimental system.

To circumvent this problem and obtain a master-curve, we normalize the rescaled extension by the value of the extension plateau observed at small angles. The obtained quantity is called the extensibility f and encapsulates the influence of the resting pitch angle on the axial extension in flow. For the helix represented by the orange dots (starting

angle of $\sim 40^\circ$), no plateau is observed. For this helix, the rescaled extension is normalized so that in the region where the curves overlap, the averaged extensibility is matched with the four other helices. We naturally have $f(\alpha_0 = 0^\circ) = 1$ given the definition of f . We also expect $f(\alpha_0 = 90^\circ) = 0$ as this corresponds to a straight rod, which cannot extend. Overall, the axial extension is thus expressed as follows

$$\Delta H = M \frac{\eta U}{B} R^2 L^2 f(\alpha_0) \quad \text{with} \quad f(\alpha_0 = 0) = 1 \quad (5.2.1)$$

with M being a numerical constant. Given the way the extensibility is obtained, *i.e.* by normalizing by the value of the plateau, we cannot access the value of this numerical quantity M . The value of the corrected extension plateau is indeed $M\eta/B$. A combined experiment including both a mechanical characterization to calibrate the filament modulus (as described in chapter 4) and an investigation of the extension in flow would allow access to the value of M .

We present in fig. 5.4 the extensibility f as a function of resting pitch angle for all five tested PMMA helical ribbons. Consistently with the definition of f , we obtain good collapse of the curves at small angles. But we also observe a very good collapse for the remainder of the data, suggesting universality of the extensibility function f . The extensibility is constant at small angles *i.e.* for closed-loop helices (up to $\alpha_0 \sim 25 - 30^\circ$): at small angles, the pitch angle has no influence on the helix extension in flow. This regime is followed by a sharp decrease in extensibility for $\alpha_0 \gtrsim 25 - 30^\circ$. As the pitch angle increases, towards open-loop helices, helical ribbons are less and less deformable by viscous axial flows. The magnitude of this stiffening effect in flow is quite significant: the extensibility decreases by a factor 5 between $\alpha_0 = 10^\circ$ and $\alpha_0 = 60^\circ$.

Naturally, these experimental observations come in stark contrast with analytical results from the literature [4, 5], which predicted vanishing influence of the pitch angle on the extension in flow. In order to understand more precisely this stiffening effect in flow, we now analyze in detail the shape of helices as they are deformed by hydrodynamic viscous forces.

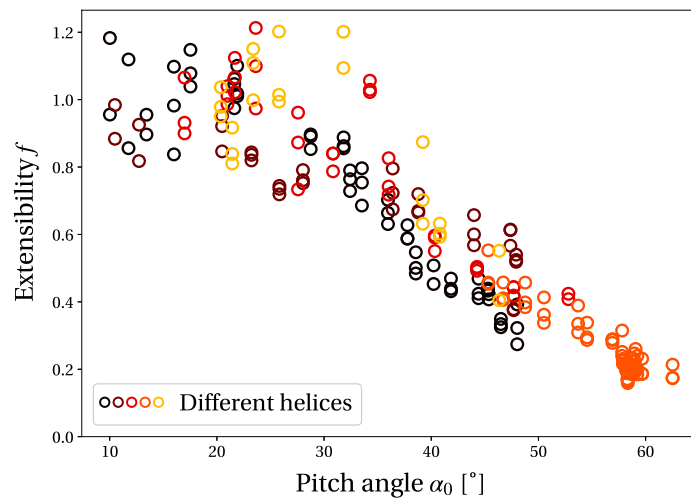


FIGURE 5.4 – Extensibility f , as defined by eq. (5.2.1), as a function of resting pitch angle α_0 for five different PMMA helical ribbons.

5.3 Shape Analysis of the Deformed Helices

So far, we have only used the axial extension ΔH as a measure of the helix deformation. But we have not yet examined distribution of that deformation along the filament length. Qualitatively, we expect high deformation near the clamped end and almost no deformation near the free end. To conduct this investigation, we extract from the experimental images the pitch and radius distribution. This work was done in collaboration with Anirban Jana, during his Master research internship.

5.3.1 Method for Image Analysis

Obtaining the full three-dimensional helix shape from a two-dimensional experimental image is very challenging. Instead, we focus on obtaining the local pitch and local radius at each loop of the helix, as these quantities are easily measured from the 2D shape. This is done in both the reference state and the deformed state as to compute the local changes in pitch and radius induced by the flow. To obtain these quantities, the experimental images are processed in Python using the OpenCV package. Figure 5.5 illustrates the successive steps, starting from the raw experimental image, depicted by fig. 5.5 (a). After removing the background, an enhancement in contrast and noise reduction of the images is performed. Adaptive thresholding is used to segment the experimental images: greyscale images are taken as input and the algorithm outputs binary images representing the segmentation. A threshold is calculated for each pixel, based on the average grey value of the area around this given pixel. If the pixel value is below this calculated threshold, the pixel is set to the background value, otherwise, it assumes the foreground value. Using this approach, an approximation of the two-dimensional filament shape is obtained. Typical binary image is

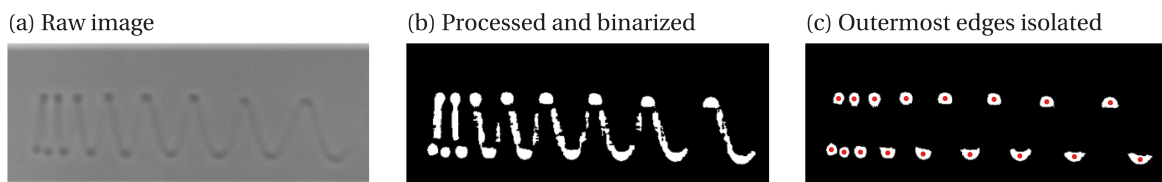


FIGURE 5.5 – Successive image analysis steps to extract the two-dimensional filament shape: (a) starting raw experiment image; (b) processed (noise reduction and contrast enhanced) and binarized image and (c) binarized image with outermost edges isolated. Red points indicate the mean position of each group and correspond to the filament position every half-period.

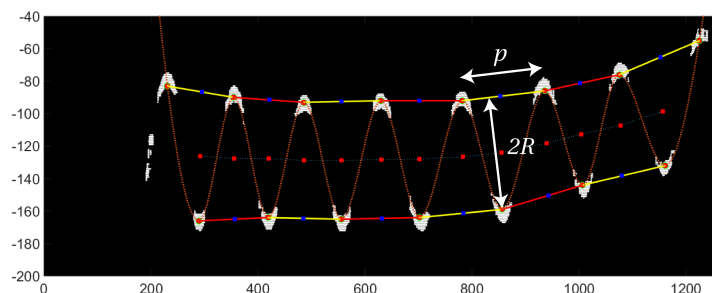


FIGURE 5.6 – Detailed decomposition of the filament two-dimensional shape, yielding measurement of the local pitch p and local radius R , measured for each helix loop.

shown in fig. 5.5 (b). Once the binarization is obtained, we extract the filament position every half period, which corresponds to the outermost edges. This is done by calculating the mean linear axis of the helix, followed by deletion of the points in the vicinity of this line. Once the outermost edges are isolated, the mean position of each is calculated. We represent in fig. 5.5 (c) the isolated groups of points representing the outermost edges and the mean position of each, plotted as red dots.

Hence, the image analysis procedure yields the filament position every half-period. The pitch p and radius R of each loop are then calculated. Figure 5.6 illustrates measurements of p and R once the image analysis process is done. The local pitch for a given loop is taken as the distance between the two points delimiting the loop *i.e.* points situated a period apart. The successive measurements are represented as the yellow and red lines in fig. 5.6. The local radius is calculated as the half-height of the triangle defined by the two points delimiting the loop and the point in-between. We then calculate the local pitch angle α using the geometrical relation $\tan \alpha = p/2\pi R$.

5.3.2 Pitch and Radius Distribution

Figure 5.7 presents the pitch and radius distribution for a given PMMA helical ribbon at a given geometry, as the helix is deformed by a viscous axial flow. Total filament length is $L = 350\mu\text{m}$, helical radius is $R = 6.0\mu\text{m}$ and resting pitch angle is $\alpha_0 = 10^\circ$ *i.e.* corresponding to the small angle regime. The corresponding resting pitch is $p_0 = 2\pi R \tan \alpha_0 = 6.6\mu\text{m}$. We show in fig. 5.7 (a) the change in local pitch Δp , calculated between the deformed state and the reference state, for three different flow velocity U . The change in pitch is plotted as a function of contour position s/L , $s/L = 0$ being the free end and $s/L = 1$ being the clamped end. As shown, the pitch change is not uniformly distributed along the contour length but rather linearly distributed: maximum deformation is measured at the clamped end and almost no deformation is measured at the free end. A previous study by Pham et al. [1] found a similar distribution, directly following from the fact that viscous forces scale linearly with length. Normalizing the pitch change Δp by the flow velocity yields very good collapse of all three curves, as depicted in fig. 5.7 (b), showing linearity of the local helix deformation *i.e.* $\Delta p \propto U$ all along the filament. This is consistent with the linearity of the overall helix deformation, which is quantified by the axial extension ΔH . Figure 5.7 (c) shows the distribution of radius change ΔR along the filament length. Radius change is at most a few percents of the reference value $R = 6\mu\text{m}$: radius change, in this case, is negligible during deformation. Finally, fig. 5.7 (d) shows the pitch angle change distribution $\Delta \alpha$ as a function of contour position. The angle change distribution is also roughly linear along the filament length.

We reproduce this analysis for the same helix but as the geometry was varied using the stretching treatment. The filament length is not affected $L = 350\mu\text{m}$ and the radius has only slightly varied $R = 6.4\mu\text{m}$. But the pitch angle was significantly increased to $\alpha_0 = 50^\circ$ *i.e.* well into the high angle regime. The corresponding resting pitch is $p_0 = 48\mu\text{m}$. Results are shown in fig. 5.8. Similar results are found: the pitch change, shown in fig. 5.8 (a), is linearly distributed. The magnitude of the pitch change is similar to what was found at small angles but as the resting pitch is much higher, the relative deformation is much smaller. The radius change, shown in fig. 5.8 (b), is again small compared to the resting radius and can be neglected. Thus, the deformation is distributed very similarly for small or high angle helices: linearly distributed change in pitch and almost no change in radius.

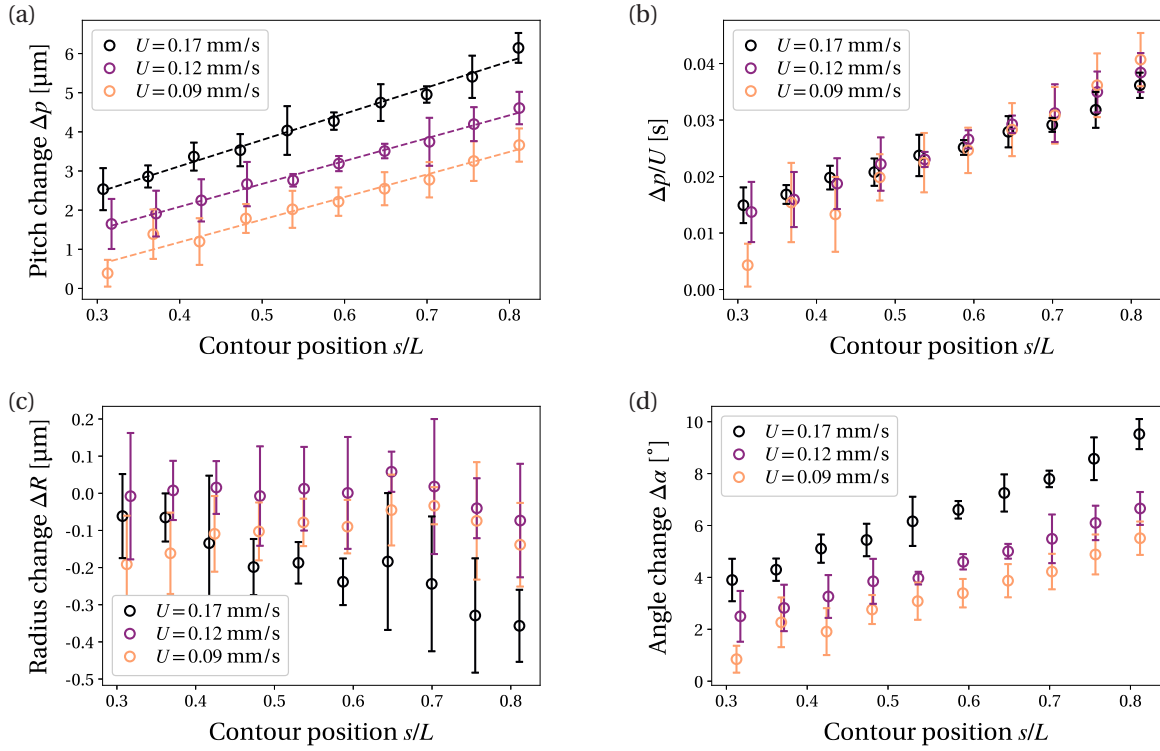


FIGURE 5.7 – Distribution of the flow-induced deformation for a PMMA helical ribbon immersed in a viscous axial flow. The helix geometry is fixed with $L = 350\mu\text{m}$, $R = 6.0\mu\text{m}$, $\alpha_0 = 10^\circ$ and so $p_0 = 6.6\mu\text{m}$. (a) Change in local pitch Δp between the deformed state and the reference state, as a function of contour position s/L , with linear fitting. (b) Flow-induced change in local pitch normalized by the flow velocity $\Delta p/U$ as a function of contour position s/L . (c) Flow-induced change in local radius ΔR as a function of contour position. (d) Flow-induced change in local pitch angle $\Delta\alpha$ as a function of contour position.

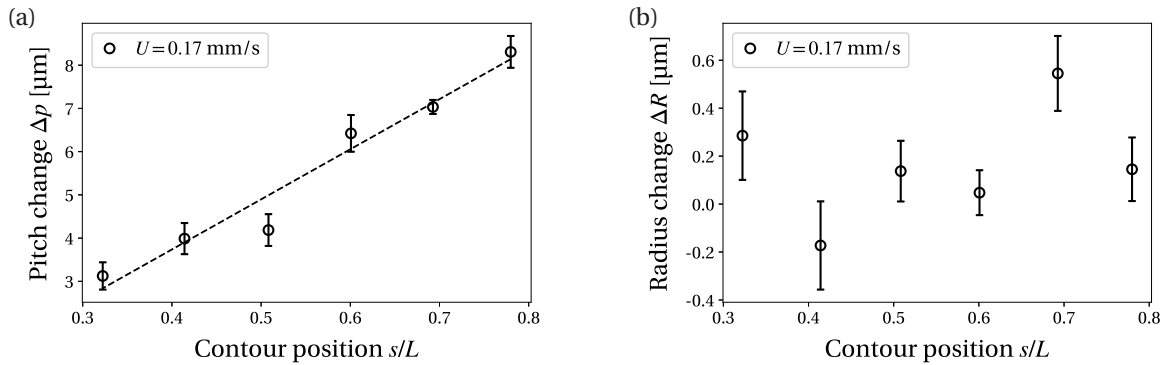


FIGURE 5.8 – Distribution of the flow-induced deformation for the same PMMA helical ribbon as in fig. 5.7 with increased resting pitch angle. The helix geometry $L = 350\mu\text{m}$, $R = 6.4\mu\text{m}$, $\alpha_0 = 50^\circ$ and so $p_0 = 48\mu\text{m}$. (a) Change in local pitch Δp as a function of contour position s/L , with linear fitting. (b) Flow-induced change in local radius ΔR as a function of contour position.

So the stiffening effect in flow observed at high angles cannot be explained by a change in the deformation distribution alone.

5.3.3 Torsion to Bending Transition

Material deformation is very poorly described by the changes in pitch or in radius. Material deformation is rather captured by changes in filament curvature or in filament

torsion, noted respectively $\Delta\kappa$ and $\Delta\tau$. As explained in section 3.2, due to the high anisotropy of the cross-section *i.e.* $w \gg t$, the material frame coincides with the Frenet frame of the filament centerline. And hence $\Delta\kappa$ and $\Delta\tau$ can be computed respectively as the local change in Frenet curvature and in Frenet torsion of the centerline. We approximate each loop to a single-loop helix with uniform radius and pitch angle and so, as we have $\kappa = \cos^2 \alpha / R$ and $\tau = \cos \alpha \sin \alpha / R$ for a uniform helix, we can calculate

$$\Delta\kappa = \Delta \left(\frac{\cos^2 \alpha}{R} \right) = \left[\frac{\cos^2(\alpha_0 + \Delta\alpha)}{R + \Delta R} - \frac{\cos^2 \alpha_0}{R} \right] \quad (5.3.1)$$

$$\Delta\tau = \Delta \left(\frac{\cos \alpha \sin \alpha}{R} \right) = \left[\frac{\cos(\alpha_0 + \Delta\alpha) \sin(\alpha_0 + \Delta\alpha)}{R + \Delta R} - \frac{\cos \alpha_0 \sin \alpha_0}{R} \right] \quad (5.3.2)$$

Thus, knowing the radius and angle distribution, we can compute the change in material curvature and in material torsion for each loop.

Figure 5.9 presents the distribution of curvature change and of torsion change for a given PMMA helical ribbon, for different resting pitch angles (varied using the stretching treatment). Experimental data are the same as in fig. 5.7 and fig. 5.8. Again the change is calculated between the deformed state and the reference state. The pitch angle starts in the small angle regime $\alpha_0 = 10^\circ$ and increases up to $\alpha_0 = 50^\circ$, well into the high angle regime. Data for $\alpha_0 = 10^\circ$ and for $\alpha_0 = 50^\circ$ are the same as in fig. 5.7 and fig. 5.8 but are shown for a single flow velocity ($U = 0.17 \text{ mm} \cdot \text{s}^{-1}$) for clarity. Figure 5.9 (a) shows the distribution of the torsion change $\Delta\tau$ normalized by the reference value τ_0 , as the resting pitch angle is varied. As shown, torsion change is significant at small angles, reaching up to $\Delta\tau \sim \tau_0$, and is linearly distributed along the filament length. As the resting pitch angle increases, magnitude of the torsion change decreases sharply, with almost no change in torsion for $\alpha_0 = 42^\circ$ and $\alpha_0 = 50^\circ$. An inverse evolution is found for the curvature change $\Delta\kappa$, whose distribution is shown in fig. 5.9 (b): curvature change is almost zero at small angles then increases sharply as the resting pitch angle increases. The magnitude of the curvature change remains however limited, reaching up to $\Delta\kappa \sim 0.2 * \kappa_0$. The relative change in curvature at high angles is thus way less than the relative change in torsion at small angles. This seems consistent with the fact that high angles helices are way less deformed than small angle helices.

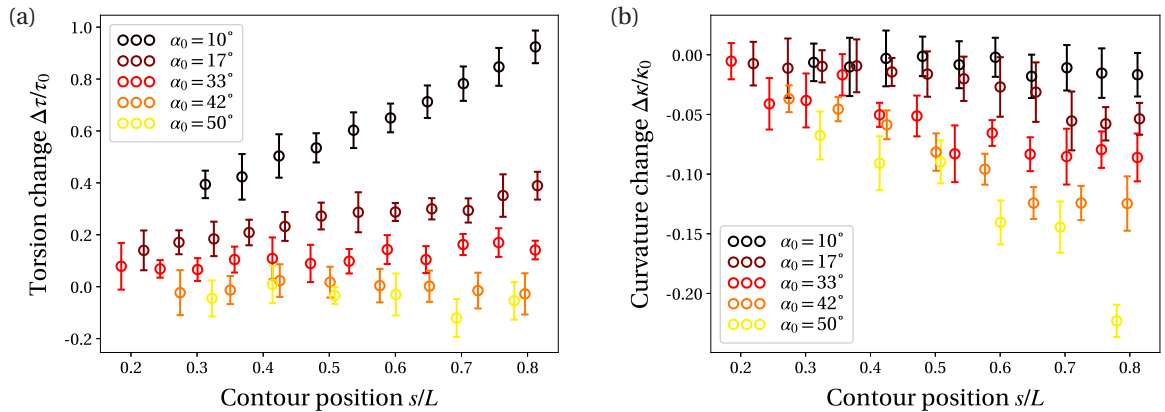


FIGURE 5.9 – Torsion change $\Delta\tau$ and curvature change $\Delta\kappa$ distribution, both rescaled by their reference value τ_0 and κ_0 , for a PMMA helical ribbon deformed by flow with velocity $U = 0.17 \text{ mm} \cdot \text{s}^{-1}$, as the resting pitch angle α_0 is varied.

Overall, deformation of small angle helices is dominated by filament torsion while deformation of high angle helices is dominated by filament bending. These two modes of deformation are each associated to a different modulus, C and B for torsion and bending respectively. The transition between the two regimes happens for $\alpha_0 \sim 20 - 35^\circ$, which matches the angle range for which the stiffening effect in flow is triggered. Such a transition from torsion to bending was already highlighted in previous studies investigating the deformation of helical structures. For example, the work of Starostin et al. [7] has tackled the deformation of helical ribbons under axial end-point forces. This situation was investigated in chapter 4 and we highlighted good agreement between their analytical approach and our experimental results. They found that, in the linear regime, the force necessary to extend the helix by ΔH is

$$F = \frac{C}{R^2} \frac{1}{\cos^2 \alpha_0 \left(\cos^2 \alpha_0 + \frac{C}{B} \sin^2 \alpha_0 \right)} \frac{\Delta H}{L} \quad (5.3.3)$$

At small angles *i.e.* $\alpha_0 \ll 1$, this expression rewrites $F \simeq \frac{C}{R^2} \frac{1}{\cos^4 \alpha_0} \frac{\Delta H}{L}$ while at high angles *i.e.* $\alpha_0 \rightarrow 90^\circ$, the expression rewrites $F \simeq \frac{B}{R^2} \frac{1}{\cos^2 \alpha_0 \sin^2 \alpha_0} \frac{\Delta H}{L}$.

Hence, a transition happens from a regime where C is the relevant modulus *i.e.* dominated by filament torsion to a regime where B is the relevant modulus. Both scale similarly $B \sim C \sim E w t^3$ but have different values, which may drive a change in the extensibility. However, if considering only this torsion-to-bending effect, the transition happens at $\alpha_0 \sim 45^\circ$, which does not match the typical angle range for which the changes in extensibility are observed. Therefore the torsion-to-bending transition alone cannot explain the observed behavior of helical ribbons in flow. The influence of the hydrodynamic viscous forces and how these forces vary with the pitch angle must also be considered.



In this chapter, we have presented experimental results for the extension of helical ribbons immersed in viscous axial flows. Leveraging the newly developed stretching treatment to precisely control the pitch angle, influence of this parameter on the extension in flow was investigated. We introduced the extensibility function f , which encapsulates the influence of the resting pitch angle on the extension. We report constant extensibility at small angles (closed-loop helices) followed by a sharp decrease at high angles (towards open loop helices). Thus, at small angles, the pitch angle has no influence on the deformation while at high angles, increasing the pitch angle leads to a decrease in the extension. The regime change happens around $\alpha_0 \sim 25 - 30^\circ$. The magnitude of this stiffening effect in flow is quite significant: the extensibility decreases by a factor 5 between $\alpha_0 = 10^\circ$ and $\alpha_0 = 60^\circ$. Previously reported analytical results for the deformation of helices in viscous flows fail to describe this effect [4, 5].

We have then analyzed the shape of the flow-deformed helices, highlighting a change in the mode of deformation as the resting pitch angle was increased. At small angles, the filament is mainly twisted while at high angles, the filament is mostly bent. This transition in the mode of deformation and the stiffening effect are reminiscent of the observations made in the previous chapter. But considering only the influence of the ribbon mechanics cannot describe accurately the behavior in flow. Influence of the hydrodynamic viscous

forces must be taken into account. Qualitatively, for small angle helices, the geometry is highly packed and the filament is oriented perpendicularly to the flow direction. As the pitch angles increases, the geometry gets more open and the filament is oriented more parallelly to the flow direction. Given these simultaneous changes in both compactness and filament orientation, it is difficult to estimate how the viscous forces will vary with the resting pitch angle. In the next chapter, we propose a modeling of the viscous forces and investigate the interplay with the torsion-to-bending transition.

5.4 References

- [1] Jonathan T Pham, Alexander Morozov, Alfred J Crosby, Anke Lindner, and Olivia du Roure. Deformation and shape of flexible, microscale helices in viscous flow. *Physical Review E*, 92(1):011004, 2015. [86](#), [89](#), [93](#)
- [2] Marine Daieff. *Deformation and shape of flexible, microscale helices in viscous flows*. PhD thesis, Sorbonne Paris Cité, 2018. [86](#)
- [3] Mohammad K Jawed and Pedro M Reis. Deformation of a soft helical filament in an axial flow at low reynolds number. *Soft matter*, 12(6):1898–1905, 2016. [86](#)
- [4] MunJu Kim and Thomas R Powers. Deformation of a helical filament by flow and electric or magnetic fields. *Physical Review E*, 71(2):021914, 2005. [86](#), [91](#), [96](#)
- [5] Panayiota Katsamba and Eric Lauga. Propulsion by stiff elastic filaments in viscous fluids. *Physical Review E*, 99(5):053107, 2019. [86](#), [91](#), [96](#)
- [6] Frank M White and Joseph Majdalani. *Viscous fluid flow*, volume 3. McGraw-Hill New York, 2006. [87](#)
- [7] EL Starostin and GHM van der Heijden. Tension-induced multistability in inextensible helical ribbons. *Physical review letters*, 101(8):084301, 2008. [96](#)

Chapter 6

Theoretical Analysis and Numerical Simulations

Contents

6.1 General Framework and Constitutive Relations	100
6.1.1 Filament Parametrization	100
6.1.2 Filament Intrinsic Curvature	101
6.1.3 Kirchhoff Rod Equations	102
6.1.4 Helical Reference Configuration	102
6.2 Helices in Viscous Axial Flows: the Weak Flow Limit	103
6.2.1 Force and Stress Solutions	104
6.2.2 Actuation of the Filament Configuration	105
6.2.3 Helical Axial Extension	107
6.3 RFT-Based Numerical Simulations	108
6.3.1 Parametric Set-Up	109
6.3.2 Simulation Results	110
6.4 End-Loaded Helices	112
6.4.1 Helical Axial Extension	112
6.4.2 Discussion and Consequences for the Modeling of Helical Ribbons	114
6.5 References	115
Appendix A	117
Appendix B	117

In this chapter, we implement analytical and numerical tools to better analyze and understand the experimental results, notably the stiffening of helical ribbons observed in the previous chapter. We set up an analytical framework to model the deformation of slender helically-shaped filaments submitted to viscous flows. The viscous forces are modeled using resistive-force theory: forces are simplified by introducing constant local drag coefficients. Although shown to inaccurately estimate the viscous forces acting on a helix [1], RFT is still widely used and usually provides good qualitative understanding.

The filament, of arbitrary cross-section, is modeled as a uni-dimensional rod. Its mechanical properties are hence solely described by the two bending moduli A, B and the twisting modulus C , which are determined by the filament cross-sectional shape and the material mechanical properties. We use the well-known Kirchhoff rod equations [2] to establish the force and moment equilibrium along the filament. This approach is especially relevant in the case of isotropic or near-isotropic filaments *i.e.* for cross-sections such as circles, squares or equilateral triangles. Naturally, this corresponds to isotropic or near-isotropic moduli $A \sim B \sim C$. For anisotropic cross-sections, such as thin ribbons in our case, we extrapolate this approach by simply adjusting the moduli to the geometry of the cross-section. It must however be noted that, in the case of vanishingly thin ribbons, previous works have found Kirchhoff rod equations to fail to describe accurately the ribbon mechanics [3, 4]. In the literature, this problem is typically solved by constructing a uni-dimensional energy functional from an inextensible elastic strip model [5, 6]. Force and moment equations resembling the Kirchhoff rod equations can then be obtained. Such approach is followed by Starostin et al. to establish the deformation of end-loaded helical ribbons [7]. However this approach is beyond the scope of our work. This analytical work was realized with initial insights of Lyndon Koens (Macquarie University, Sidney). Results are derived using the SymPy library for Python.

This chapter is organized as follows. Section 6.1 establishes the general constitutive relations. Section 6.2 specifically investigates the deformation of a helix submitted to a weak axial flow. We find significant differences between our results and previous derivations [8, 9]. In section 6.3 we implement numerical simulations to confirm our analysis. The simulations rely on the same general equations: Kirchhoff rod equations and resistive-force theory. We find very good agreement between our results and the simulations, which validates our derivation. Finally, in section 6.4 we further test our framework by investigating the deformation of end-loaded helices and compare our results with the literature.

6.1 General Framework and Constitutive Relations

6.1.1 Filament Parametrization

We consider an inextensible slender filament of length L , with uniform cross-section of arbitrary shape. We use Kirchhoff rod equations to describe the mechanical behavior of the filament. The material stress and strain and the external forcing are averaged over the cross-section of the filament, and these quantities are thus parametrized solely by the filament contour length s and time t , with $0 \leq s \leq L$. We only address the equilibrium problem and hence drop all time dependency.

The filament 3D shape is given by the position of the centerline $\vec{x}(s)$ and by a unit vector $\vec{d}_1(s)$ normal to the filament centerline, which gives the orientation of the filament body relative to the centerline. We introduce the vector basis attached to the filament body

$\{\vec{d}_1, \vec{d}_2, \vec{d}_3\}$. The vector \vec{d}_3 is the centerline tangent vector so $\vec{d}_3 = \vec{x}'$ where $'$ denotes the derivative with respect to s . The vector $\vec{d}_2 = \vec{d}_3 \wedge \vec{d}_1$ is chosen so that the vector basis is a right-handed orthonormal basis. Since this basis is attached to the body of the filament, it rotates and twists with the material. The twist vector (also called the Darboux vector) of the material $\vec{\kappa} = \{\kappa_1, \kappa_2, \kappa_3\}$, expressed in the vector basis attached to the body, is defined so that

$$\vec{d}_i' = \vec{\kappa} \wedge \vec{d}_i \quad \text{with } i = 1, 2, 3 \quad (6.1.1)$$

κ_1 and κ_2 are the two components of the filament curvature and κ_3 is the filament twist. We finally introduce I_1 and I_2 the second moments of area with respect respectively to \vec{d}_1 and \vec{d}_2 as well as the torsion constant J . The bending moduli are hence given by $A = EI_1$ and $B = EI_2$ with E Young's modulus, and the twisting modulus by $C = \mu J$ with μ shear modulus.

We then introduce the Frenet triad $\{\vec{t}, \vec{n}, \vec{b}\}$ attached to the filament centerline. The vector \vec{t} is the centerline tangent vector so $\vec{t} = \vec{d}_3$. The Frenet curvature κ and the Frenet torsion τ are defined by

$$\vec{t} = \vec{x}', \quad \vec{t}' = \kappa \vec{n}, \quad \vec{b} = \vec{t} \wedge \vec{n}, \quad \vec{b}' = -\tau \vec{n} \quad (6.1.2)$$

To relate the vector basis $\{\vec{d}_1, \vec{d}_2, \vec{d}_3\}$ to the Frenet triad, and following previous approach [10], we introduce the excess twist $\zeta(s)$ as the angle between the Frenet normal vector $\vec{n}(s)$ and the vector $\vec{d}_1(s)$. This leads to

$$\vec{d}_1 = \cos \zeta \vec{n} + \sin \zeta \vec{b}, \quad \vec{d}_2 = -\sin \zeta \vec{n} + \cos \zeta \vec{b} \quad (6.1.3)$$

and

$$\vec{\kappa} = \{\kappa_1, \kappa_2, \kappa_3\} = \{\kappa \sin \zeta, \kappa \cos \zeta, \tau + \zeta'\} \quad (6.1.4)$$

This equation relates the position of the filament centerline, expressed by its Frenet curvature and torsion, to the material strain rates.

6.1.2 Filament Intrinsic Curvature

The intrinsic curvature describes the property of a filament to display a non-vanishing curvature while no stress is applied. The intrinsic curvature is quantified by the reference twist vector $\vec{\kappa}^{(0)}$. In the following, the (0) exponent relate to the reference value of a quantity, when no external constraint is applied. A filament with no intrinsic curvature is therefore straight in its reference configuration. Naturally, a helically-shaped filament must possess an intrinsic curvature. In the general case, the twist vector in the reference state is $\vec{\kappa}^{(0)} = \{\kappa_1^{(0)}, \kappa_2^{(0)}, \kappa_3^{(0)}\}$.

In our experimental conditions, although the preferred state of the material is $\vec{\kappa}^{(e)} = \vec{0}$, an intrinsic curvature is created nonetheless by the effect of surface tension. The elastic energy of the filament in the reference state is thus: $E_b = L \left(A(\kappa_1^{(0)})^2 + B(\kappa_2^{(0)})^2 + C(\kappa_3^{(0)})^2 \right)$. As the reference state is given by total energy minimization (taking into account surface energy) and considering that $A \propto Ew^3 t$ while $B \propto Ewt^3$ with $t \ll w$, we can assume that $\kappa_1^{(0)} = 0$. The argument can be extended to all ribbon-like filaments, as we expect a ribbon to be curved in the direction of the lowest bending modulus.

We also address the case of helically-shaped cylindrical filaments. For a round cross-section, all choices for \vec{d}_1 are equivalent and we therefore chose \vec{d}_1 to align with \vec{n} in the

absence of external forcing. The reference value of the excess twist is then simply given by $\zeta^{(0)} = 0$. Comparison with eq. (6.1.4) yields a similar result than for ribbon-like filaments: $\kappa_1^{(0)} = 0$. In the following, we hence assume $\kappa_1^{(0)} = 0$.

6.1.3 Kirchhoff Rod Equations

The Kirchhoff rod equations are, in the static case

$$\vec{M}' + \vec{d}_3 \wedge \vec{F} = 0 \quad (6.1.5)$$

$$\vec{F}' + \vec{f} = 0 \quad (6.1.6)$$

where \vec{M} is the elastic torque, $\vec{F} = F_1 \vec{d}_1 + F_2 \vec{d}_2 + F_3 \vec{d}_3$ is the elastic stress and $\vec{f} = f_1 \vec{d}_1 + f_2 \vec{d}_2 + f_3 \vec{d}_3$ is the external forcing per unit length. Both are expressed in the vector basis attached to the filament body. In the linear limit of the material (*i.e.* small material strain), we can express the elastic torque

$$\vec{M} = A(\kappa_1 - \kappa_1^{(0)}) \vec{d}_1 + B(\kappa_2 - \kappa_2^{(0)}) \vec{d}_2 + C(\kappa_3 - \kappa_3^{(0)}) \vec{d}_3 \quad (6.1.7)$$

The external forcing results from the viscous drag of the fluid on the filament. In the general case, the filament cross-section does not admit an axis of symmetry, so the classical resistive-force theory with two anisotropic drag coefficients cannot be applied. Instead, following recent developments on the hydrodynamics of slender ribbons [11], we introduce three different drag coefficients and propose the following form for the external forcing (in the static case)

$$\vec{f} = (\xi_1 \vec{d}_1 \otimes \vec{d}_1 + \xi_2 \vec{d}_2 \otimes \vec{d}_2 + \xi_3 \vec{d}_3 \otimes \vec{d}_3) \cdot \vec{U} \quad (6.1.8)$$

where ξ_i is the drag coefficient along the \vec{d}_i direction and \vec{U} is the background flow. Classical resistive-force theory is easily recovered by taking $\xi_1 = \xi_2 = \xi_\perp$ and $\xi_3 = \xi_\parallel$. The expression of the external forcing, which ultimately determines the material stress, depends on the local orientation of the filament. Equation (6.1.4) provides another relation between the filament position (through the Frenet curvature and torsion) and the material stresses. Thus a coupling exists between the mechanical equations and the filament position.

Finally we need to specify the boundary conditions to close the system. At the free end, which we chose to correspond to ($s = 0$), we have

$$\vec{F}(s = 0) = \vec{0} \quad (6.1.9)$$

$$\vec{M}(s = 0) = \vec{0} \quad (6.1.10)$$

6.1.4 Helical Reference Configuration

When no external constraint (*i.e.* $\vec{U} = \vec{0}$) is applied, the filament is in its reference configuration. Solving the Kirchhoff static equations in this case simply yields $\vec{F}(s) = \vec{0}$ and $\vec{M}(s) = \vec{0}$. Comparison with the preferred state of the ribbon (see section 6.1.2) gives

$$\kappa_1^{(0)} = 0, \quad \kappa_2^{(0)} = \kappa_0, \quad \kappa_3^{(0)} = \tau_0 \quad (6.1.11)$$

Using eq. (6.1.4), we obtain a constant Frenet curvature and a constant Frenet torsion in the reference configuration, respectively equal to κ_0 and τ_0 . This, as expected, corresponds to a helical shape. Additionally we have $\zeta(s)^{(0)} = 0$ which leads to

$$\vec{d}_1^{(0)} = \vec{n}^{(0)}, \quad \vec{d}_2^{(0)} = \vec{b}^{(0)} \quad (6.1.12)$$

The reference configuration of the filament is hence a helix, characterized by its pitch p_0 and its radius R_0 . We define the reference helix pitch angle α_0 as the angle between a circumferential line and the filament centerline, such that $\tan \alpha_0 = p_0/2\pi R_0$. The position of the filament centerline is given by the following parametric equation:

$$\vec{x}^{(0)}(s) = \left\{ R_0 \cos\left(\frac{\cos \alpha_0}{R_0} s\right), \delta R_0 \sin\left(\frac{\cos \alpha_0}{R_0} s\right), s \sin \alpha_0 \right\} \quad (6.1.13)$$

expressed in the cartesian coordinate system $\{x, y, z\}$, where we have chosen (Oz) to be the helical axis. The chirality index δ denotes the chirality of the helix; $\delta = +1$ for right-handed helices and $\delta = -1$ for left-handed helices.

In the reference configuration, the tangent vector is given by

$$\vec{t}^{(0)} = (\vec{x}^{(0)})' = \left\{ -\cos \alpha_0 \sin\left(\frac{\cos \alpha_0}{R_0} s\right), \delta \cos \alpha_0 \cos\left(\frac{\cos \alpha_0}{R_0} s\right), \sin \alpha_0 \right\} \quad (6.1.14)$$

and we check that $\|\vec{t}^{(0)}\| = 1$. The rest of the reference Frenet triad is then simply expressed, still in the cartesian coordinate system, as well as the reference Frenet curvature and torsion

$$\kappa^{(0)} = \left\| \frac{\partial \vec{t}^{(0)}}{\partial s} \right\| = \frac{\cos^2 \alpha_0}{R_0} = \kappa_0 \quad (6.1.15)$$

$$\vec{n}^{(0)} = \frac{1}{\kappa^{(0)}} \frac{\partial \vec{t}^{(0)}}{\partial s} = \left\{ -\cos\left(\frac{\cos \alpha_0}{R_0} s\right), -\delta \sin\left(\frac{\cos \alpha_0}{R_0} s\right), 0 \right\} \quad (6.1.16)$$

$$\vec{b}^{(0)} = \vec{t}^{(0)} \wedge \vec{n}^{(0)} = \left\{ \delta \sin \alpha_0 \sin\left(\frac{\cos \alpha_0}{R_0} s\right), -\sin \alpha_0 \cos\left(\frac{\cos \alpha_0}{R_0} s\right), \delta \cos \alpha_0 \right\} \quad (6.1.17)$$

$$\tau^{(0)} = \frac{\partial \vec{n}^{(0)}}{\partial s} \cdot \vec{b}^{(0)} = \delta \frac{\sin \alpha_0 \cos \alpha_0}{R_0} = \tau_0 \quad (6.1.18)$$

6.2 Helices in Viscous Axial Flows: the Weak Flow Limit

The equations presented above are non-linear and strongly coupled. They usually do not exhibit analytic solutions. Analytic solution can however be obtained in weak flow limit. In this limit, we linearize the constitutive equations around the reference configuration. The validity range of this approximation is discussed later. We address the case of a viscous uniform axial flow and we seek the following explicit expansion (with $\epsilon \ll 1$)

$$\begin{aligned} \vec{U} &= \epsilon U \vec{e}_z \\ \vec{F} &= \epsilon F_1^{(1)} \vec{d}_1 + \epsilon F_2^{(1)} \vec{d}_2 + \epsilon F_3^{(1)} \vec{d}_3 \\ \kappa_1 &= \epsilon \kappa_1^{(1)} \\ \kappa_2 &= \kappa_0 + \epsilon \kappa_2^{(1)} \\ \kappa_3 &= \tau_0 + \epsilon \kappa_3^{(1)} \end{aligned}$$

As we have chosen $(s = 0)$ to be the free end, a positive flow $U > 0$ corresponds to a flow from the free end to the fixed end, we therefore expect compression of the helix. Reciprocally, we expect extension of the helix for $U < 0$.

6.2.1 Force and Stress Solutions

In this subsection, we drop the ⁽¹⁾ exponent for clarity. The linearized Kirchhoff equations, given by eqs. (6.1.5) and (6.1.6), are

$$\begin{aligned} A\kappa'_1 - B\tau_0\kappa_2 + C\kappa_0\kappa_3 - F_2 &= 0 \\ B\kappa'_2 + A\tau_0\kappa_1 + F_1 &= 0 \\ C\kappa'_3 - A\kappa_0\kappa_1 &= 0 \\ F'_1 - \tau_0F_2 + \kappa_0F_3 + f_1 &= 0 \\ F'_2 + \tau_0F_1 + f_2 &= 0 \\ F'_3 - \kappa_0F_1 + f_3 &= 0 \end{aligned}$$

which can be rearranged to

$$\kappa_3''' + (\kappa_0^2 + \tau_0^2)\kappa_3' = \frac{\kappa_0}{C}(2F_2' + f_2) \quad (6.2.1)$$

$$B\kappa_0\kappa_2' = \frac{\kappa_0}{\tau_0}(F_2' + f_2) - C\tau_0\kappa_3' \quad (6.2.2)$$

$$\kappa_1 = \frac{C\kappa_3'}{A\kappa_0} \quad (6.2.3)$$

$$F_1'' + (\kappa_0^2 + \tau_0^2)F_1 = \kappa_0f_3 - \tau_0f_2 - f_1' \quad (6.2.4)$$

$$F_2' = -\tau_0F_1 - f_2 \quad (6.2.5)$$

$$F_3' = \kappa_0F_1 - f_3 \quad (6.2.6)$$

The set of eqs. (6.2.1) to (6.2.6) provides a clear workflow for computing the elastic stress \vec{F} and the twist vector $\vec{\kappa}$ once the external forcing is known. Using eq. (6.1.8) in the weak flow limit writes

$$f_1 = \xi_1 U \vec{d}_1^{(0)} \cdot \vec{e}_z = 0 \quad (6.2.7)$$

$$f_2 = \xi_2 U \vec{d}_2^{(0)} \cdot \vec{e}_z = \delta \xi_2 U \cos \alpha_0 \quad (6.2.8)$$

$$f_3 = \xi_3 U \vec{d}_3^{(0)} \cdot \vec{e}_z = \xi_3 U \sin \alpha_0 \quad (6.2.9)$$

As f_1, f_2, f_3 are constant, the eqs. (6.2.1) to (6.2.6) are easily solved. The weak flow limit decouples the constitutive equations: the force equations are solved in the reference configuration of the filament. The deformed configuration of the filament is then actuated from the obtained elastic force and torque.

Solving eqs. (6.2.4) to (6.2.6) with boundary condition eq. (6.1.9) yields

$$F_1^{(1)}(s) = \frac{1}{k^2}(\kappa_0 f_3 - \tau_0 f_2)(1 - \cos ks) \quad (6.2.10)$$

$$F_2^{(1)}(s) = \frac{\tau_0}{k^3}(\kappa_0 f_3 - \tau_0 f_2) \sin ks - \frac{\kappa_0}{k^2}(\tau_0 f_3 + \kappa_0 f_2)s \quad (6.2.11)$$

$$F_3^{(1)}(s) = -\frac{\kappa_0}{k^3}(\kappa_0 f_3 - \tau_0 f_2) \sin ks - \frac{\tau_0}{k^2}(\tau_0 f_3 + \kappa_0 f_2)s \quad (6.2.12)$$

where we define k such that $k^2 = \tau_0^2 + \kappa_0^2 = \frac{\cos^2 \alpha_0}{R_0^2}$. We can then solve eqs. (6.2.1) to (6.2.3) with boundary condition eq. (6.1.10)

$$\begin{aligned} \kappa_3^{(1)}(s) = \frac{\kappa_0}{Ck^4} [-2\kappa_0\tau_0f_3 + (\tau_0^2 - \kappa_0^2)f_2]s + \frac{\kappa_0}{Ck^5} [3\kappa_0\tau_0f_3 + (\kappa_0^2 - 2\tau_0^2)f_2] \sin ks \\ + \frac{\kappa_0\tau_0}{Ck^4} (-\kappa_0f_3 + \tau_0f_2)s \cos ks \end{aligned} \quad (6.2.13)$$

$$\begin{aligned} \kappa_2^{(1)}(s) = \frac{\kappa_0}{Bk^4} [(\tau_0^2 - \kappa_0^2) f_3 + 2\kappa_0\tau_0 f_2] s + \frac{1}{Bk^5} [\kappa_0(\kappa_0^2 - 2\tau_0^2) f_3 + \tau_0(-2\kappa_0^2 + \tau_0^2) f_2] \sin ks \\ + \frac{\tau_0^2}{Bk^4} (\kappa_0 f_3 - \tau_0 f_2) s \cos ks \end{aligned} \quad (6.2.14)$$

$$\kappa_1^{(1)}(s) = \frac{1}{Ak^4} [2\kappa_0\tau_0 f_3 + (\kappa_0^2 - \tau_0^2) f_2] (\cos ks - 1) + \frac{\tau_0}{Ak^3} (\kappa_0 f_3 - \tau_0 f_2) s \sin ks \quad (6.2.15)$$

6.2.2 Actuation of the Filament Configuration

Similarly to the mechanical quantities, we seek a linear expansion for the Frenet curvature κ , the Frenet torsion τ and the excess twist ζ

$$\kappa = \kappa_0 + \epsilon \kappa^{(1)}$$

$$\tau = \tau_0 + \epsilon \tau^{(1)}$$

$$\zeta = \epsilon \zeta^{(1)}$$

Using eq. (6.1.4) we can simply write

$$\kappa^{(1)} = \kappa_2^{(1)} \quad (6.2.16)$$

$$\tau^{(1)} = \kappa_3^{(1)} - \frac{1}{\kappa_0} (\kappa_1^{(1)})' \quad (6.2.17)$$

$$\zeta^{(1)} = \frac{1}{\kappa_0} \kappa_1^{(1)} \quad (6.2.18)$$

which provides the full expressions in the deformed configuration of the filament.

We now have to solve the inverse problem, which consists in determining the parametric equation of the centerline \vec{x} knowing its Frenet curvature and torsion. The excess twist ζ encapsulates the twist of the material relative to the filament centerline and is therefore not a parameter of the centerline. To circumvent this difficult problem, and following our linearized approach, we prescribe a parametric near-helical shape for the deformed filament. The parameters of the shape are determined as to ensure equality with the Frenet curvature and torsion obtained above. We adopt the following parametrization of the filament centerline

$$\vec{x}(s) = \{R(s) \cos \psi(s), \delta R(s) \sin \psi(s), z(s)\} \quad (6.2.19)$$

where ψ is the arclength angle. The pitch angle $\alpha(s)$ is similarly defined as the local angle between a circumferential line and the centerline tangent. We therefore have (see fig. 6.1): $\cos \alpha = R\psi'$ and $\sin \alpha = z'$.

The filament centerline is hence fully characterized by two functions: the radius R and the pitch angle α , which matches the number of known quantities (the Frenet curvature and the Frenet torsion). We similarly seek a linear expansion around the reference configuration

$$R = R_0 + \epsilon R_1$$

$$\alpha = \alpha_0 + \epsilon \alpha_1$$

Finally we need to specify boundary conditions for these geometric quantities. We suppose that the fixed end is clamped so that

$$R_1(L) = 0, \quad R_1'(L) = 0 \quad (6.2.20)$$

$$\alpha_1(L) = 0, \quad \alpha_1'(L) = 0 \quad (6.2.21)$$

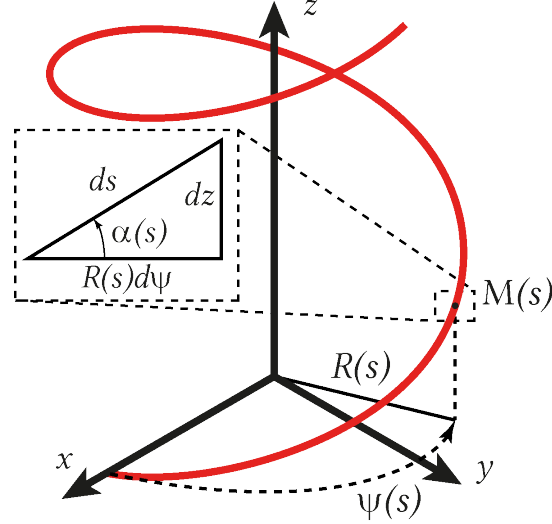


FIGURE 6.1 – Schematic of a right-handed helix and chosen parameters in the deformed configuration.

In the deformed configuration, the tangent vector and its norm are given by

$$\vec{t} = \vec{x}' = \{R' \cos \psi - \cos \alpha \sin \psi, \delta R' \sin \psi + \delta \cos \alpha \cos \psi, \sin \alpha\}$$

$$\|\vec{t}\| = \sqrt{1 + (R')^2} = \sqrt{1 + \epsilon^2 (R'_1)^2} \approx 1$$

which shows that the inextensibility of the filament is only verified in the linearized approximation. The proposed centerline parametrization is thus only valid within this limit. The perturbation of the Frenet curvature $\kappa^{(1)}$ and of the Frenet torsion $\tau^{(1)}$ are then expressed as a function of the two parameters R_1 and α_1

$$\kappa^{(1)} = -\frac{\kappa_0}{R_0} R_1 - R_1'' - 2\delta \tau_0 \alpha_1 \quad (6.2.22)$$

$$\tau^{(1)} = \delta \frac{1}{\kappa_0} (\kappa_0^2 - \tau_0^2) \alpha_1 + \delta \frac{1}{\kappa_0} \alpha_1'' - \frac{\tau_0}{R_0} R_1 - \frac{\tau_0}{\kappa_0} R_1'' \quad (6.2.23)$$

Equations (6.2.22) and (6.2.23) can be rearranged

$$\alpha_1 = -\frac{1}{2\delta \tau_0} \left(\kappa^{(1)} + \frac{\kappa_0}{R_0} R_1 + R_1'' \right) \quad (6.2.24)$$

$$R_1'''' + 2(\tau_0^2 + \kappa_0^2) R_1'' + \frac{\kappa_0^2}{R_0^2} R_1 = -(\kappa^{(1)})'' - (\kappa_0^2 - \tau_0^2) \kappa^{(1)} - 2\kappa_0 \tau_0 \tau^{(1)} \quad (6.2.25)$$

Using the results from eqs. (6.2.16) and (6.2.17), we obtain the following differential equation for R_1

$$R_1'''' + 2k^2 R_1'' + k^4 R_1 = a_1 s + a_2 k^{-1} \sin ks + a_3 s \cos ks \quad (6.2.26)$$

$$\text{with } \begin{cases} a_1 = \frac{2\kappa_0^2 \tau_0}{Ck^4} [2\kappa_0 \tau_0 f_3 + (\kappa_0^2 - \tau_0^2) f_2] + \frac{\kappa_0 (\kappa_0^2 - \tau_0^2)}{Bk^4} [(\kappa_0^2 - \tau_0^2) f_3 - 2\kappa_0 \tau_0 f_2] \\ a_2 = -\frac{2\kappa_0^2 \tau_0}{Ck^4} [3\kappa_0 \tau_0 f_3 + (\kappa_0^2 - 2\tau_0^2) f_2] + \frac{2\kappa_0 \tau_0^2}{Bk^4} [(2\kappa_0^2 - \tau_0^2) f_3 - 3\kappa_0 \tau_0 f_2] - \frac{2\kappa_0 \tau_0}{Ak^2} (\tau_0 f_3 + \kappa_0 f_2) \\ a_3 = \frac{2\tau_0^2}{k^4} \left(\frac{\kappa_0^2}{C} + \frac{\tau_0^2}{B} + \frac{k^2}{A} \right) (\kappa_0 f_3 - \tau_0 f_2) \end{cases}$$

The general solution is

$$R_1(s) = \frac{a_1 s}{k^4} + \left(C_1 + C_2 s - \frac{a_2 s^2}{8k^3} \right) \sin(ks) + \left(C_3 + C_4 s - \frac{a_3 s^2}{8k^2} \right) \cos(ks) \quad (6.2.27)$$

In a similar fashion, we rewrite eq. (6.2.16) using eq. (6.2.14)

$$\begin{aligned} \kappa^{(1)}(s) &= b_1 s + b_2 k^{-1} \sin ks + b_3 s \cos ks \quad (6.2.28) \\ \text{with } \begin{cases} b_1 = \frac{\kappa_0}{Bk^4} [(\tau_0^2 - \kappa_0^2) f_3 + 2\kappa_0 \tau_0 f_2] \\ b_2 = \frac{1}{Bk^5} [\kappa_0 (\kappa_0^2 - 2\tau_0^2) f_3 + \tau_0 (-2\kappa_0^2 + \tau_0^2) f_2] \\ b_3 = \frac{\tau_0^2}{Bk^4} (\kappa_0 f_3 - \tau_0 f_2) \end{cases} \end{aligned}$$

C_1, C_2, C_3 and C_4 are determined by solving the boundary conditions, which are given by eqs. (6.2.20) and (6.2.21). The full expressions as a function of $a_1, a_2, a_3, b_1, b_2, b_3$ are given in Appendix A. Using these two expressions in eq. (6.2.24), we easily express α_1

$$\begin{aligned} \delta\alpha_1(s) &= -\frac{1}{2\tau_0 k^2} (a_1 + b_1 k^2) s + \frac{1}{8\tau_0 k^3} (8C_4 k^4 + a_2 - 4b_2 k^2 - 2a_3 k^2 s) \sin ks \\ &\quad + \frac{1}{8\tau_0 k^2} [(a_3 - 8C_2 k^3) + (2a_2 - 4b_3 k^2) s] \cos ks \quad (6.2.29) \end{aligned}$$

6.2.3 Helical Axial Extension

During experiments, we characterize the deformed helices by measuring their axial length, defined as the projected length of the filament on the helical axis

$$H = \int_{s=0}^L dz = \int_{s=0}^L \sin \alpha(s) ds$$

In the reference configuration, we simply have $H_0 = L \sin \alpha_0$. In the deformed configuration, we have

$$H = H_0 + \epsilon \cos \alpha_0 \int_{s=0}^L \alpha_1(s) ds \quad (6.2.30)$$

The helical axial extension is defined as $\Delta H = H - H_0$. Within the weak flow limit, we have $\Delta H = \epsilon \cos \alpha_0 \int_{s=0}^L \alpha_1(s) ds$. We can already point out that, as α_1 does not diverge, we always have $\Delta H = 0$ when $\alpha_0 = \pi/2$. This is consistent, as this case corresponds to the limit case where the helix is a straight inextensible filament, which naturally cannot extend. In the general case, using eq. (6.2.29), the helical axial extension ΔH is given by

$$\begin{aligned} \Delta H &= -\frac{\cos \alpha_0}{8\delta\tau_0 k^4} [-8C_4 k^4 + 2L^2 a_1 k^2 + 2L^2 b_1 k^4 + a_2 + 4b_2 k^2 - 4b_3 k^2 \\ &\quad + (8C_2 k^4 - 2La_2 k + 4Lb_3 k^3 + a_3 k) \sin kL \\ &\quad + (8C_4 k^4 - 2La_3 k^2 - a_2 - 4b_2 k^2 + 4b_3 k^2) \cos kL] \quad (6.2.31) \end{aligned}$$

In our experimental conditions, we have $R_0 \ll L$ and hence $kL \gg 1$ as long as $\cos \alpha_0 \neq 0$. This approximation is called the long helix approximation. Therefore, we keep in the above expression only the terms scaling as L^2 , as it is the highest order term

$$\begin{aligned} \Delta H &= -\frac{\cos \alpha_0}{4\delta\tau_0} \left(b_1 + \frac{a_1}{k^2} \right) L^2 \quad (6.2.32) \\ &= -\frac{L^2 \kappa_0 \cos \alpha_0}{2 k^6} \left[\frac{\kappa_0}{C} (2\kappa_0 \tau_0 f_3 + (\kappa_0^2 - \tau_0^2) f_2) + \frac{\tau_0}{B} (2\kappa_0 \tau_0 f_2 - (\kappa_0^2 - \tau_0^2) f_3) \right] \end{aligned}$$

We rewrite the expression under the form

$$\Delta H = -\frac{R_0^2 L^2}{2} \frac{\xi_2 U}{C} f(\alpha_0) \quad (6.2.33)$$

where we have introduced the dimensionless helix extensibility f

$$f(\alpha_0) = \cos^4 \alpha_0 + \left(2\rho + 2\frac{C}{B} - 1 - \rho\frac{C}{B}\right) \cos^2 \alpha_0 \sin^2 \alpha_0 + \rho\frac{C}{B} \sin^4 \alpha_0 \quad (6.2.34)$$

with $\rho = \xi_3/\xi_2$ that denotes the drag anisotropy. The helix extensibility f encapsulates the influence of the reference pitch angle α_0 on the axial extension in flow.

Now that the axial extension has been derived, we address the validity of the weak flow approximation. Equations (6.2.13) and (6.2.14) provide scaling laws for the material stress: $\kappa_3^{(1)} \sim (U\eta/C)R_0L$ and $\kappa_2^{(1)} \sim (U\eta/B)R_0L$, as we have $\xi_2 \sim \xi_3 \sim \eta$ viscosity of the surrounding fluid. The weak flow limit is valid as long as $\kappa_3^{(1)} \ll \tau_0$ and $\kappa_2^{(1)} \ll \kappa_0$. As we have $B \sim C$, these two conditions both rewrite $(U\eta/B)R_0^2L \ll 1$, which is equivalent to $\Delta H \ll L$. **Hence the weak flow limit is valid as long as $\Delta H \ll L$.**

Our results come in contrast with previous derivations from the literature. The work of Kim et al. [8] and the work of Katsamba et al. [9] tackled the same problem using the same constitutive relations *i.e.* Kirchhoff rod equations and resistive-force theory. In both works, under the assumption that $A = B = C$, the axial extension ΔH was found to depend on the reference pitch angle α_0 only through the boundary conditions. This dependency was found to vanish in the limit of long helices ($kL \gg 1$), which is the case we have considered. The helix axial extension was hence found to be constant within this limit, the expression being

$$\Delta H = -\frac{R_0^2 L^2}{2} \frac{\xi_2 U}{C}$$

This was obtained with the assumptions that $A = B = C$ and $\rho = 1/2$. In our work, we find similarly a vanishing effect of the boundary conditions in the limit of long helices and we obtain a similar expression, but the dependency on the reference pitch angle remains. Indeed, even when considering $B = C$ and $\rho = 1/2$, we still have $f(\alpha_0) = \frac{1}{2} + \frac{\cos^2 \alpha_0}{2} \neq \text{cst.}$

6.3 RFT-Based Numerical Simulations

In order to confirm our methodology and our derivation, we implement numerical simulations based on the recent work of Walker et al. [12]. The simulation code is freely available online¹. These simulations rely on a coarse-grained implementation of Kirchhoff rod equations and RFT to simulate the behavior of slender filaments in viscous fluids. The constitutive equations are the same as our analytical modeling, with hence the same limitations, notably when modeling vanishingly thin ribbons. Both time and space parameters are coarse-grained, the space parameter being the filament length. The filament shape is hence approximated with N piecewise-linear segments, each of constant length L/N . The simulation framework was developed and optimized to tackle cylindrical filaments so most comparison with our analytical results is done in this case. But the framework can also tackle the case of flat triangular ribbon-like filaments, by simply adjusting the filament moduli A, B, C . The high efficiency and low computational cost of the method allows easy

1. <https://gitlab.com/bjwalker/3d-filaments>

parametric exploration. Typical simulations have indeed a runtime below a few minutes, on a standard lab computer.

6.3.1 Parametric Set-Up

We simulate the extension of a helically-shaped filament, clamped at one end, submitted to a uniform viscous axial flow. At $t = 0$, the helix is in its reference configuration and the flow is turned on. We follow the deformation dynamics by tracking the helical axial length $H(t)$. We focus on the influence of the reference pitch angle α_0 so we set the total length to a constant $L = 1$. We also set to a constant the number of turns $N_{\text{turn}} = 3$. As we have $kL = 2\pi N_{\text{turn}}$, this choice ensures that $kL \approx 19 \gg 1$: the long helix approximation is always verified. We vary the reference pitch angle α_0 in the widest possible range, from 0° to 80° . Above 80° , simulation instabilities are observed. We know however that we always have $\Delta H(\alpha_0 = 90^\circ) = 0$. This data point is hence added to the simulation results. As the total length and number of turns are constant, the choice of pitch angle sets the helical radius $R_0 = \frac{L \cos \alpha_0}{2\pi N_{\text{turn}}}$: as the pitch angle varies, so does the helical radius. These variations are accounted for when calculating the extensibility f .

The equation system is non-dimensionalized through the elasto-hydrodynamic number $E_h = \frac{8\pi\eta L^3 U_0}{B}$, with U_0 nominal flow velocity. This number compares the hydrodynamic viscous forcing to the restorative filament elasticity. The nominal flow velocity U_0 represents the typical flow velocity required to stretch the helix. For $U \ll U_0$ the helix is hardly stretched and remains in its reference configuration: the filament elasticity dominates. For $U \gg U_0$, the helix is completely stretched: viscous forces dominate. For simplicity we set $U_0 = 1$ and we set E_h to a value close to our experimental conditions, $E_h = 1000$. Typical flow velocities are taken so that $U \ll U_0$, to ensure that helix deformation happens within the linear regime. The typical helix response time is given by $t_0 \sim L/U_0 \sim 1$ so in order to observe the full stretching dynamic and equilibrium, we set the simulation time to $T = 5$ with 1000 time-steps. Finally we place ourselves in the limit of infinitely slender filaments so that $\rho = \xi_3/\xi_2 = 1/2$.

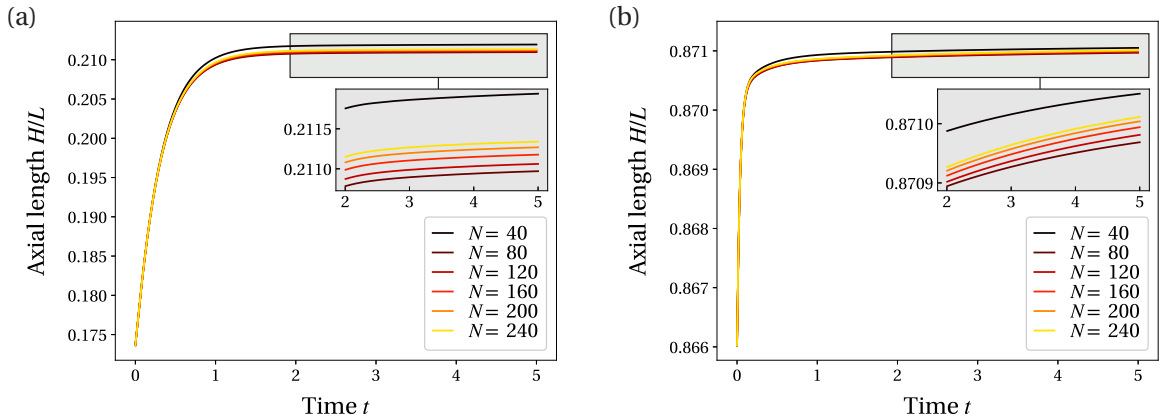


FIGURE 6.2 – Simulated dynamics of a helically-shaped cylindrical filament ($\nu = 0.5$) submitted to a uniform viscous axial flow, with varying N number of segments. The flow, with velocity $U = 0.1$, is turned on at $t = 0$. Inset zooms on the late part of the evolution ($t > 2$). The reference pitch angle is taken in (a) $\alpha_0 = 10^\circ$ and in (b) $\alpha_0 = 60^\circ$.

The number of segments N needs to be finely tuned. On the one hand, increasing the

number of segments improves precision but at the cost of exponentially increasing the computational time. On the other hand, simulation errors are observed for low values of N . In order to set the value, we conduct a series of simulations at fixed angle and velocity, while varying the number of segments. We show in fig. 6.2 the rescaled axial length H/L as a function of time, in the case of a cylindrical filament, for varying number of segments. In fig. 6.2 (a) we set $\alpha_0 = 10^\circ$ and $U = 0.1$ while in fig. 6.2 (b) we set $\alpha_0 = 60^\circ$ and again $U = 0.1$. We can thus check that the choice for N is relevant throughout the whole angle range. In both cases, we observe that numerical results converge to a unique curve as we increase the number of segments. For the highest number of segments, the differences are vanishing: for example less than 0.05% of difference between the results for $N = 200$ and $N = 240$. Meanwhile, the running time is more than 40% higher for $N = 240$ than for $N = 200$. Considering these observations, we set $N = 200$. This is in line with previous numerical works. As an example, the numerical work of Jawed et al. [13] used 173 segments to simulate a 4-turn helix.

We also observe in fig. 6.2 that an equilibrium state is never quite reached at long time, despite setting the simulation time much higher than the typical helix response time. The helix response is indeed observed within ~ 1 s, consistently with the estimation. The later evolution, evidenced by the insets in fig. 6.2, is hence likely to be simulation-related. In order to decouple the elasto-hydrodynamic response from this simulation-related drift, we fit the simulated results by a semi-phenomenological function. Similarly to the procedure adopted for the experimental results, we fit by the following function $H(t) = H_0 + \Delta H(1 - e^{-t/\tau}) + \mu t$, with 3 fitting parameters $\Delta H, \tau, \mu$. The fitted parameter ΔH is taken as the helix axial extension.

6.3.2 Simulation Results

Using this procedure, we obtain the helix axial extension ΔH as a function of the reference pitch angle α_0 and flow velocity U . We plot in fig. 6.3 (a) the rescaled axial extension $\Delta H/L$ as a function of reference pitch angle, for different flow velocities, in the case of a cylindrical filament (with $\nu = 0.5$). We plot in fig. 6.3 (b) the rescaled axial extension, normalized by the flow velocity U . We obtain a good collapse of the data for $U < 0.1$: in these cases deformation happens within the linear regime, consistently with the value of the nominal flow velocity $U_0 = 1$. For $U > 0.1$, non-linear effects are observed: $\Delta H/U$ decreases with increasing velocity. This corresponds to a stiffening of the helix at high speed, consistent with previous observations [14]. Good collapse is however observed for all velocities at high angle ($\alpha_0 > 60^\circ$). At high angle, the deformation verifies $\Delta H/L \ll 1$ for all velocities. It suggests, as we proposed in our analysis, that this criteria ultimately assesses the validity of the linear regime.

The extensibility f is computed from the simulation results by inverting eq. (6.2.33)

$$f = \frac{C}{\xi_2 U} \frac{2\Delta H}{R_0^2 L^2}$$

All quantities are known, either as parameters or as outputs of the simulation. We plot in fig. 6.3 (c) the extensibility f as a function of reference pitch angle for the same simulation results (cylindrical filament with $\nu = 0.5$). The analytical prediction for this case is plotted as the blue dashed line. Very good agreement is obtained between the simulation results and the analytical predictions, throughout the whole angle range.

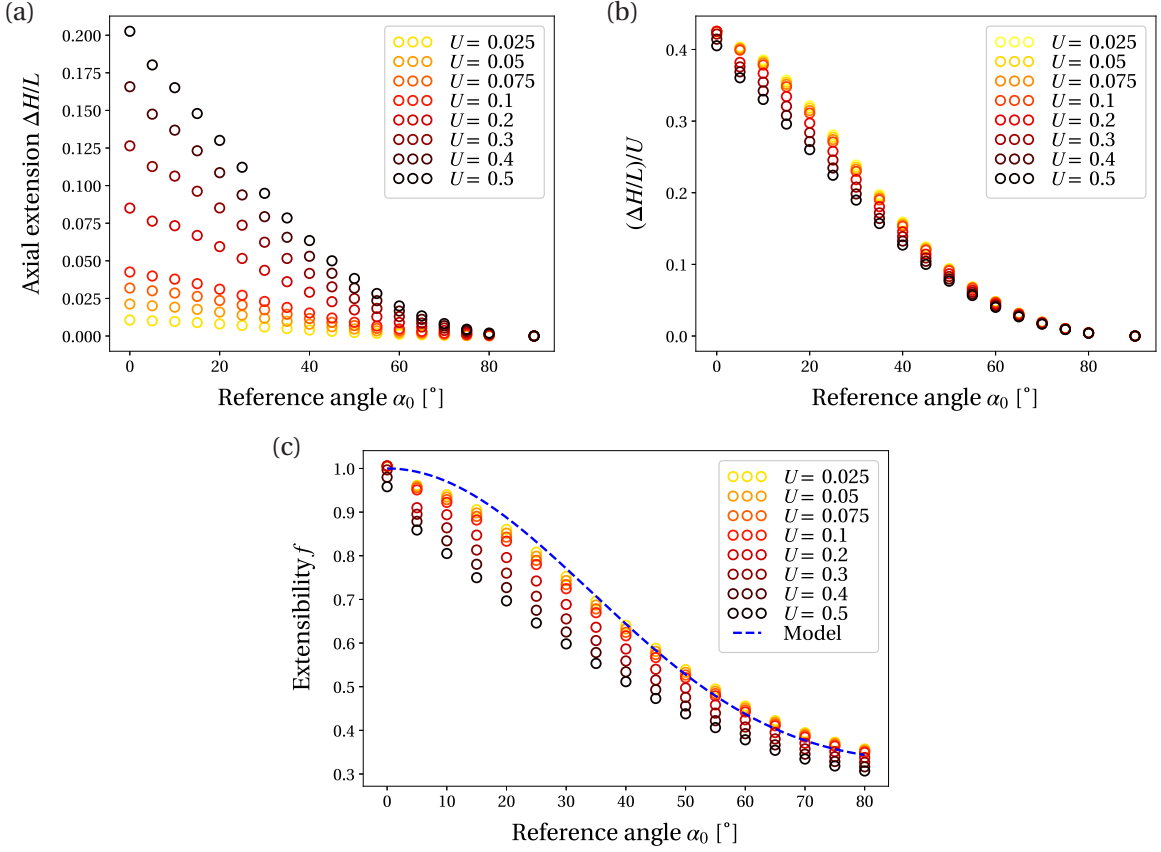


FIGURE 6.3 – Simulation results for a cylindrical filament with $\nu = 0.5$. (a) Rescaled axial extension $\Delta H/L$ as a function of reference pitch angle α_0 for different flow velocities. We recall that we have set the nominal flow velocity to $U_0 = 1$. (b) Rescaled axial extension, normalized by the flow velocity U . (c) Extensibility f compared with analytical predictions (blue dashed line) given by eq. (6.2.33) .

In order to further validate our derivation against the numerical results, we conduct the same investigation for a cylindrical filament for a different value of the Poisson's ratio: we set $\nu = 0$. This change has an influence on the moduli ratio C/B which is an important parameter of the model. We remain in the limit of infinitely slender filaments, so we still have $\rho = \xi_3/\xi_2 = 1/2$. Figure 6.4 (a) shows the simulated extensibility in this case for different flow velocities, along with the model prediction as the blue dashed line. This time we have only explored $U < 0.1$, the collapse of the different curves (corresponding to different flow velocities) is consistently better than previously. Again very good agreement with the model prediction is obtained. Finally we investigate the case of a ribbon-like filament with flat triangular cross-section and with $\nu = 0.5$. This changes the ratio C/B as well as the ratio A/B . For cylindrical filaments we indeed have $A = B$ while for ribbon-like filaments we have $B \ll A$. We again keep $\rho = 1/2$. Figure 6.4 (b) shows the simulation results for different flow velocities along with the model prediction. Once again very good agreement between simulation results and the model prediction is obtained. In short, the numerical simulations we have implemented fully validate our analytical methodology and derivation.

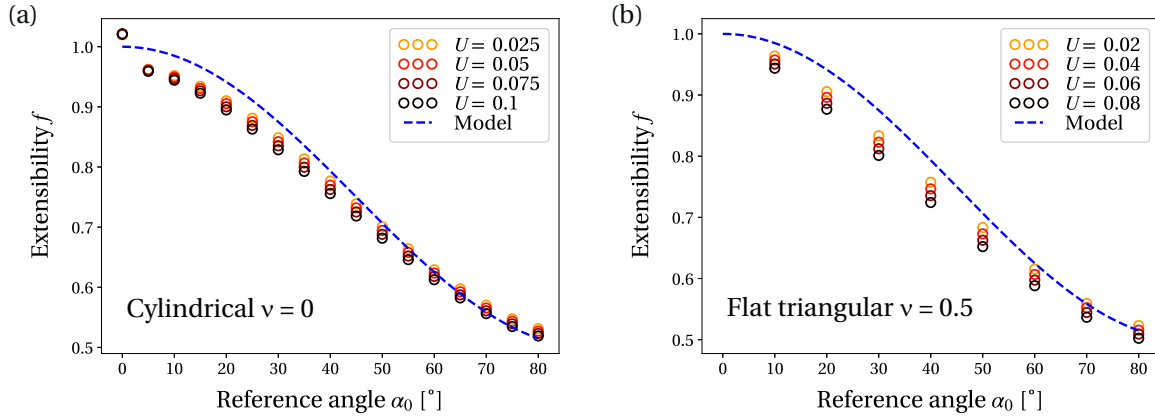


FIGURE 6.4 – Simulation results for (a) a cylindrical filament with $\nu = 0$; (b) a flat triangular ribbon-like filament with $\nu = 0.5$. In both cases we plot the extensibility as a function of reference pitch angle as well as the prediction given by eq. (6.2.33) (blue dashed line).

6.4 End-Loaded Helices

Finally, as to further test our framework, we investigate the deformation of an end-loaded helix. As this problem does not include the difficult question of modeling the viscous forces, much more literature is available on this topic, and in more details. The classical work of Love has established the deformation of a helically-shaped filament under a torque-free axial load [15]:

$$\Delta H_{\text{Love}} = \frac{F}{C} R_0^2 L \left(\cos^2 \alpha_0 + \frac{C}{B} \sin^2 \alpha_0 \right) \quad (6.4.1)$$

where F is the axial load. Love made use of Kirchhoff rod equations and assumed that the deformed helix remains a uniform helix (*i.e.* with uniform angle and radius along the filament length).

6.4.1 Helical Axial Extension

Contrary to the assumptions from the work of Love, we do not assume torque-free loading. We assume an axial load as well as clamped boundary conditions at both ends, as this corresponds more closely to our experimental conditions. We however assume that no torque is applied around the helical axis *i.e.* $\vec{F} \cdot \vec{M} = 0$ at both ends. Otherwise, rotation is not permitted around the filament axis, which prevents any change in the total filament torsion. We set the helix ends to correspond to $(s = -L/2)$ and $(s = L/2)$. The problem is hence symmetrical, which allows several simplifications in the derivation. Clamping at the helix ends determines the filament position and the filament tangent vector. As we have allowed rotation around the filament axis, we cannot determine the normal and bi-normal vector at the ends. The clamped boundary conditions are hence given by

$$R_1(L/2) = 0 \quad \alpha_1(L/2) = 0 \quad R_1'(L/2) = 0 \quad (6.4.2)$$

and similarly at $(s = -L/2)$.

Similarly to the weak flow limit, we place ourselves in the weak force limit

$$\vec{F}(s=0) = \epsilon F_0 \vec{e}_z \quad (6.4.3)$$

with $\epsilon \ll 1$. As there are no distributed forces, the force equilibrium given by eq. (6.1.5) is readily solved

$$F_1^{(1)} = \text{cst} = 0 \quad (6.4.4)$$

$$F_2^{(1)} = \text{cst} = F_0 \cos \alpha_0 = F_0 \frac{\kappa_0}{k} \quad (6.4.5)$$

$$F_3^{(1)} = \text{cst} = F_0 \sin \alpha_0 = F_0 \frac{\tau_0}{k} \quad (6.4.6)$$

We can then solve eqs. (6.2.1) to (6.2.3), and input the boundary condition $\vec{F} \cdot \vec{M}(s = L/2) = 0$. The solutions are

$$\kappa_1^{(1)} = -\frac{CD_1 k}{A\kappa_0} \sin ks \quad (6.4.7)$$

$$\kappa_2^{(1)} = -\frac{CD_1 \tau_0}{B\kappa_0} \cos ks - \frac{F_0 \kappa_0 \tau_0}{Bk^3} \quad (6.4.8)$$

$$\kappa_3^{(1)} = D_1 \cos ks + \frac{F_0 \kappa_0^2}{Ck^3} \quad (6.4.9)$$

As we have not specified full boundary conditions for the moment, one unknown constant D_1 remains at this point. One could expect that 2 unknowns would remain as we have specified only one scalar condition. But the symmetry of the system imposes a supplementary condition. Specifically, $\kappa_2^{(1)}$ and $\kappa_3^{(1)}$ must be even functions, while $\kappa_1^{(1)}$ must be an odd function.

The differential equation on R_1 given by eq. (6.2.25) writes as

$$R_1'''' + 2k^2 R_1'' + k^4 R_1 = a_1 + a_2 \cos ks \quad (6.4.10)$$

$$\text{with } \begin{cases} a_1 = \frac{F_0 \kappa_0 \tau_0}{Bk^3} (\kappa_0^2 - \tau_0^2) - \frac{2F_0 \kappa_0^3 \tau_0}{Ck^3} \\ a_2 = -2D_1 \frac{\tau_0}{\kappa_0} \left(\kappa_0^2 + \frac{C}{B} \tau_0^2 + \frac{C}{A} k^2 \right) \end{cases}$$

Using the symmetry of the system, R_1 must be an even function and the general solution is

$$R_1(s) = \frac{a_1}{k^4} + D_2 s \sin ks + \left(D_3 - \frac{a_2 s^2}{8k^2} \right) \cos ks \quad (6.4.11)$$

with D_2 and D_3 two additional unknown constants. Following the approach followed previously, we rewrite the solution for $\kappa_2^{(1)}$ as

$$\kappa_2^{(1)} = b_1 + b_2 \cos ks \quad (6.4.12)$$

$$\text{with } \begin{cases} b_1 = -\frac{F_0 \kappa_0 \tau_0}{Bk^3} \\ b_2 = -\frac{CD_1 \tau_0}{B\kappa_0} \end{cases}$$

We can then simply express α_1 as

$$\delta \alpha_1 = -\frac{1}{2\tau_0} \left(b_1 + \frac{a_1}{k^2} \right) + \frac{1}{\tau_0} \left(\frac{a_2}{8k^2} - \frac{b_2}{2} - D_2 k \right) \cos ks - \frac{a_2 s}{4\tau_0 k} \sin ks \quad (6.4.13)$$

D_1, D_2, D_3 are given by solving the clamped boundary conditions at $(s = L/2)$, given by eq. (6.4.2) We give in Appendix B the complete expressions. We then compute ΔH using

eq. (6.2.30) and place ourselves in the long helix approximation $kL \gg 1$. This time, the highest order terms scale as L , and thus only these terms are kept. ΔH is simply written as

$$\begin{aligned}\Delta H &= -\frac{L}{2\tau_0} \left(b_1 + \frac{a_1}{k^2} \right) \\ &= \frac{F_0}{C} R_0^2 L \left(\cos^2 \alpha_0 + \frac{C}{B} \sin^2 \alpha_0 \right)\end{aligned}\quad (6.4.14)$$

6.4.2 Discussion and Consequences for the Modeling of Helical Ribbons

We recover exactly the result from Love given in eq. (6.4.1). This again validates our analytical approach and the derivation. Interestingly, this result is recovered even as we have considered different boundary conditions. A similar effect was found when calculating the axial extension in flow: the influence of the boundary conditions (represented in this case by the value of D_1 , D_2 and D_3) vanishes in the limit of long helices. Again similarly to the case of deformations in flow, the axial extension is independent from the bending modulus A .

The work of Starostin et al. [7] has addressed specifically the case of end-loaded helical ribbons, without making use of Kirchhoff rod equations. The ribbon was rather modeled as an inextensible elastic strip. Under assumptions similar to the work of Love (axial load and uniformity of the deformed helix), the axial extension of end-loaded helical ribbons is expressed in the weak force limit as

$$\Delta H_{\text{Ribbon}} = \frac{F}{C} R_0^2 L \cos^2 \alpha_0 \left(\cos^2 \alpha_0 + \frac{C}{B} \sin^2 \alpha_0 \right) \quad (6.4.15)$$

The expression is very similar to the result of Love and to our results. However a additional multiplicative term ($\cos^2 \alpha_0$) is found. This term probably originates from the elastic strip model considered by Starostin et al. We recall that in chapter 4 very good agreement was obtained between these predictions and our experimental results. Conversely, the expression of Love or our predictions would badly fit our experimental results. This confirms once again, like previously stated in the literature [3], that the elastic strip model describes more accurately the mechanics of ribbon-like filaments than the classical Kirchhoff rod equations. Incorporating this approach in our analytical framework would hence greatly benefit the model but is beyond the scope of this work.

We can however speculate that in the case of helical ribbons submitted to viscous axial flows, a similar multiplicative term ($\cos^2 \alpha_0$) would result from considering an elastic strip model. We thus propose a corrected expression for the axial extension of helical ribbons submitted to viscous axial flows by adding this multiplicative term

$$\Delta H = -\frac{R_0^2 L^2}{2} \frac{\xi_2 U}{C} \cos^2 \alpha_0 f(\alpha_0) \quad (6.4.16)$$



In this chapter, we have implemented an analytical framework to model the deformation of helically-shaped filaments of arbitrary cross-section in viscous flows. The mechanics of filaments are described using Kirchhoff rod equations and viscous forces are approximated using resistive-force theory. We have specifically addressed the case of helices in

uniform axial flows. Under the assumption that the helix axial extension is small $\Delta H \ll L$, we found that the axial extension is expressed as

$$\Delta H = \frac{R_0^2 L^2}{2} \frac{\xi_2 U}{C} f(\alpha_0)$$

$$\text{with } f(\alpha_0) = \cos^4 \alpha_0 + \left(2\rho + 2\frac{C}{B} - 1 - \rho\frac{C}{B}\right) \cos^2 \alpha_0 \sin^2 \alpha_0 + \rho\frac{C}{B} \sin^4 \alpha_0$$

$\rho = \xi_3/\xi_2$ denotes the drag anisotropy specific to elongated objects. Our results come in contrast with previous analytical works, which found a vanishing influence of the pitch angle [8, 9] despite using the same elementary equations. We compared our results with numerical simulations based on the work of Walker et al. [12]. These simulations rely again on the same constitutive relations (Kirchhoff rod equations and RFT). We found excellent agreement between our analytical approach and simulation results, which validates our derivation. The discrepancies with previously published models remain unexplained.

We then adapted our framework to tackle the case of end-loaded helices. We recovered the classical result of Love [15], again validating our approach. In the specific case of helical ribbons, we compared our results to the work of Starostin et al. [7], which proposed a different model of the ribbon mechanics. Some differences were highlighted and we proposed a correction to the model in the case of helical ribbons. We speculated that addition of a multiplicative term $\cos^2 \alpha_0$ to our analytical results would account for the specific mechanics of ribbons.

6.5 References

- [1] Bruce Rodenborn, Chih-Hung Chen, Harry L Swinney, Bin Liu, and HP Zhang. Propulsion of microorganisms by a helical flagellum. *Proceedings of the National Academy of Sciences*, 110(5):E338–E347, 2013. [100](#)
- [2] Ellis Harold Dill. Kirchhoff’s theory of rods. *Archive for History of Exact Sciences*, pages 1–23, 1992. [100](#)
- [3] Basile Audoly and Keith A Seffen. Buckling of naturally curved elastic strips: the ribbon model makes a difference. In *The Mechanics of Ribbons and Möbius Bands*, pages 293–320. Springer, 2016. [100](#), [114](#)
- [4] Arun Kumar, Poornakanta Handral, CS Darshan Bhandari, Anindya Karmakar, and Ramsharan Rangarajan. An investigation of models for elastic ribbons: Simulations & experiments. *Journal of the Mechanics and Physics of Solids*, 143:104070, 2020. [100](#)
- [5] EL Starostin and GHM Van Der Heijden. The shape of a möbius strip. *Nature materials*, 6(8):563–567, 2007. [100](#)
- [6] Marcelo A Dias and Basile Audoly. “wunderlich, meet kirchhoff”: a general and unified description of elastic ribbons and thin rods. *Journal of Elasticity*, 119(1):49–66, 2015. [100](#)
- [7] EL Starostin and GHM van der Heijden. Tension-induced multistability in inextensible helical ribbons. *Physical review letters*, 101(8):084301, 2008. [100](#), [114](#), [115](#)

- [8] MunJu Kim and Thomas R Powers. Deformation of a helical filament by flow and electric or magnetic fields. *Physical Review E*, 71(2):021914, 2005. [100](#), [108](#), [115](#)
- [9] Panayiota Katsamba and Eric Lauga. Propulsion by stiff elastic filaments in viscous fluids. *Physical Review E*, 99(5):053107, 2019. [100](#), [108](#), [115](#)
- [10] Tyler McMillen, Alain Goriely, et al. Tendril perversion in intrinsically curved rods. *Journal of Nonlinear Science*, 12(3):241–281, 2002. [101](#)
- [11] Lyndon Koens and Eric Lauga. Slender-ribbon theory. *Physics of Fluids*, 28(1):013101, 2016. [102](#)
- [12] Benjamin J Walker, Kenta Ishimoto, and Eamonn A Gaffney. Efficient simulation of filament elastohydrodynamics in three dimensions. *Physical Review Fluids*, 5(12):123103, 2020. [108](#), [115](#)
- [13] Mohammad K Jawed and Pedro M Reis. Deformation of a soft helical filament in an axial flow at low reynolds number. *Soft matter*, 12(6):1898–1905, 2016. [110](#)
- [14] Jonathan T Pham, Alexander Morozov, Alfred J Crosby, Anke Lindner, and Olivia du Roure. Deformation and shape of flexible, microscale helices in viscous flow. *Physical Review E*, 92(1):011004, 2015. [110](#)
- [15] Augustus Edward Hough Love. *A treatise on the mathematical theory of elasticity*. Cambridge university press, 1944. [112](#), [115](#)

Appendix A

In the following, we give the full expression for C_1 , C_2 , C_3 and C_4 as defined in eq. (6.2.27). Please refer to eqs. (6.2.26) and (6.2.28) for the expression of $a_1, a_2, a_3, b_1, b_2, b_3$.

$$\begin{aligned}
 16k^5 C_1 &= (-2L^2 a_2 k^2 + 8L^2 b_3 k^4 - 4La_3 k^2 + 3a_2 - 4b_2 k^2 - 4b_3 k^2) + (2La_2 k - 3a_3 k) \sin 2kL \\
 &\quad + (-24La_1 k - 8Lb_1 k^3) \sin kL + (2La_3 k^2 + 3a_2 - 4b_2 k^2 - 4b_3 k^2) \cos 2kL \\
 &\quad + (8L^2 a_1 k^2 + 8L^2 b_1 k^4 - 24a_1 - 8b_1 k^2) \cos kL \\
 8k^4 C_2 &= (2La_2 k - 4Lb_3 k^3 + 2a_3 k) + (-a_2 + 2b_3 k^2) \sin 2kL + (4a_1 + 4b_1 k^2) \sin kL \\
 &\quad - a_3 k \cos 2kL + (-4La_1 k - 4Lb_1 k^3) \cos kL \\
 16k^5 C_3 &= (-2L^2 a_3 k^3 + 4La_2 k - 8Lb_2 k^3 - 8Lb_3 k^3 + 3a_3 k) \\
 &\quad + (-2La_3 k^2 - 3a_2 + 4b_2 k^2 + 4b_3 k^2) \sin 2kL \\
 &\quad + 8(-L^2 a_1 k^2 - L^2 b_1 k^4 + 3a_1 + b_1 k^2) \sin kL \\
 &\quad + k(2La_2 - 3a_3) \cos 2kL - 8k(3La_1 + Lb_1 k^2) \cos kL \\
 8k^4 C_4 &= (2La_3 k^2 - 2a_2 + 4b_2 k^2 + 2b_3 k^2) + a_3 k \sin 2kL + (4La_1 k + 4Lb_1 k^3) \sin kL \\
 &\quad + (-a_2 + 2b_3 k^2) \cos 2kL + (4a_1 + 4b_1 k^2) \cos kL
 \end{aligned}$$

Appendix B

In the following, we give the full expression for D_1 , D_2 and D_3 as defined in eq. (6.4.11). Please refer to eq. (6.4.10) for the expression of a_1 and a_2 .

$$\begin{aligned}
 D_3 &= \frac{\frac{1}{32} L^2 a_2 k^2 (Lk - \sin(Lk)) - a_1 \left(Lk \cos\left(\frac{Lk}{2}\right) + 2 \sin\left(\frac{Lk}{2}\right) \right)}{k^4 (Lk + \sin(Lk))} \\
 D_2 &= \frac{La_2 k \cos^2\left(\frac{Lk}{2}\right) - 8a_1 \sin\left(\frac{Lk}{2}\right)}{4k^3 (Lk + \sin(Lk))} \\
 2Ck^3 &\left[ABL^2 \kappa_0^2 k^2 \sin\left(\frac{Lk}{2}\right) + ABL\kappa_0^2 k \sin\left(\frac{Lk}{2}\right) \sin(Lk) + 2ABL\kappa_0^2 k \cos^3\left(\frac{Lk}{2}\right) \right. \\
 &\quad - ABL\kappa_0^2 k \cos\left(\frac{Lk}{2}\right) - AB\kappa_0^2 \sin(Lk) \cos\left(\frac{Lk}{2}\right) - ACL^2 \kappa_0^2 k^2 \sin\left(\frac{Lk}{2}\right) + ACL^2 k^4 \sin\left(\frac{Lk}{2}\right) \\
 &\quad - ACL\kappa_0^2 k \sin\left(\frac{Lk}{2}\right) \sin(Lk) - 2ACL\kappa_0^2 k \cos^3\left(\frac{Lk}{2}\right) + ACL\kappa_0^2 k \cos\left(\frac{Lk}{2}\right) + ACLk^3 \sin\left(\frac{Lk}{2}\right) \sin(Lk) \\
 &\quad + 2ACLk^3 \cos^3\left(\frac{Lk}{2}\right) + ACLk^3 \cos\left(\frac{Lk}{2}\right) + AC\kappa_0^2 \sin(Lk) \cos\left(\frac{Lk}{2}\right) + ACk^2 \sin(Lk) \cos\left(\frac{Lk}{2}\right) \\
 &\quad + BCL^2 k^4 \sin\left(\frac{Lk}{2}\right) + BCLk^3 \sin\left(\frac{Lk}{2}\right) \sin(Lk) + 2BCLk^3 \cos^3\left(\frac{Lk}{2}\right) - BCLk^3 \cos\left(\frac{Lk}{2}\right) \\
 &\quad \left. - BCk^2 \sin(Lk) \cos\left(\frac{Lk}{2}\right) \right] D_1 \\
 &= 8AF\kappa_0^2 (-BL\kappa_0^2 k + B\kappa_0^2 \sin(Lk) + CL\kappa_0^2 k - CLk^3 - C\kappa_0^2 \sin(Lk))
 \end{aligned}$$

Chapter 7

Discussion of the Experimental Results

Contents

7.1 RFT-Based Analytical Model	120
7.1.1 Discussion of the Analytical Results	120
7.1.2 Comparison with Experimental Results	121
7.1.3 Correcting the Ribbon Mechanics	123
7.2 Towards Slender-Body Theory	124
7.2.1 Proposed Approach	124
7.2.2 Computation of the SBT Drag Force	125
7.2.3 Drag Distribution along the Filament Length	126
7.2.4 Results of the Twice-Corrected Model	127
7.2.5 Predictions for Cylindrical Filaments	129
7.3 References	132

In chapter 5 we have presented experimental results for the axial extension of helical ribbons in uniform viscous axial flows. Experiments were conducted in water, with viscosity $\eta = 1 \times 10^{-3} \text{ Pa} \cdot \text{s}$. We have investigated the influence of the pitch angle, highlighting significant stiffening of the helical ribbons in flow as the resting pitch angle was increased. In chapter 6 we proposed a model based on resistive-force theory to model the hydrodynamic viscous forces and Kirchhoff rod equations to model the filament mechanics. Analytical predictions for the extension of helices in viscous axial flows were obtained. In this chapter, we compare model predictions to our experimental results. We thus assess validity of our model to describe the deformation of helical ribbons in flow and discuss the relevance of resistive-force theory to model the viscous forces acting on helices.

This chapter is organized as follows. In section 7.1 we compare our experimental results with the analytical model developed in chapter 6 and we highlight major discrepancies. Inspired by the results of Startostin et al., who investigated the deformation of end-loaded helical ribbons [1], we propose a correction to the model. The correction accounts for the specific mechanics of ribbons, which were evidenced in chapter 4. Addition of this correction into the model vastly improves the agreement with the experimental results, although some discrepancies are still observed. In section 7.2 we build upon the corrected model and incorporate slender-body theory to better estimate the hydrodynamic forcing. As discussed in section 1.3.1, the use of SBT to compute the viscous forces acting on helices has been validated several times [2–4]. Analytical results incorporating SBT are compared to our experimental data. Finally, we apply our findings to predict the extension of helices with cylindrical filaments in viscous flows.

7.1 RFT-Based Analytical Model

We recall that the model established in chapter 6 relies on Kirchhoff rod equations to model the ribbon mechanics coupled with RFT to model the hydrodynamic viscous drag. Within the weak flow regime, we obtained the following expression for the axial extension ΔH associated with a flow velocity U

$$\Delta H = \frac{R_0^2 L^2 \xi_2 U}{2 C} f(\alpha_0) \quad (7.1.1)$$

$$\text{with } f(\alpha_0) = \cos^4 \alpha_0 + \left(2 \frac{\xi_3}{\xi_2} + 2 \frac{C}{B} - 1 - \frac{\xi_3 C}{\xi_2 B} \right) \cos^2 \alpha_0 \sin^2 \alpha_0 + \frac{\xi_3 C}{\xi_2 B} \sin^4 \alpha_0 \quad (7.1.2)$$

We showed that the weak flow condition is equivalent to a small deformation condition given by $\Delta H \ll L$. During experiments, we observed at most $\Delta H/L \sim 0.1$. Considering furthermore the observed linearity of the deformations $\Delta H \propto U$, the weak flow assumption is verified within our experiments.

7.1.1 Discussion of the Analytical Results

The obtained analytical scaling is consistent with previous derivations *i.e.* $\Delta H \propto R^2 L^2 (\eta U / C)$. But as we mentioned, previous analytical studies found vanishing influence of the pitch angle α_0 [5, 6]. Within our model, this dependency results from two effects. The first is that, as the resting pitch angle varies from 0° to 90° (the helix going from a closed circle to a straight rod), the predominant drag force goes from perpendicular to the filament to tangential to the filament. The drag coefficients along these directions being

different, the helix extensibility varies. The second effect is that, as the resting pitch angle varies from 0° to 90° , the filament goes from being mostly twisted (C being the relevant modulus) to mostly bent (B being the relevant modulus). Both scale similarly $B \sim C \sim Ewt^3$ but have different values, which drives a change in the extensibility.

The two limits of the obtained expression eq. (7.1.1) are consistent with this analysis. For $\alpha_0 \rightarrow 0^\circ$, we obtain

$$\Delta H = \frac{R_0^2 L^2}{2} \frac{\xi_2 U}{C} \cos^4 \alpha_0$$

i.e. dominated by normal viscous forces and filament torsion, whereas when $\alpha_0 \rightarrow 90^\circ$, we obtain

$$\Delta H = \frac{R_0^2 L^2}{2} \frac{\xi_3 U}{B} \sin^4 \alpha_0$$

i.e. dominated by tangential viscous forces and filament bending. In the case of an isotropic drag force *i.e.* $\xi_3 = \xi_2$, the extensibility simplifies to $f = \cos^2 \alpha_0 + (C/B) \sin^2 \alpha_0$: only the effects of the torsion-to-bending transition remain. An isotropic drag force on a fiber is not a realistic description but the case of an isotropic distributed force corresponds to a vertically suspended helix deformed under its own weight. This case is simply recovered by substituting the drag per unit length ξU by the weight per unit length $\rho_r S g$, where S is the cross-sectional area and ρ_r density of the ribbon material. Conversely, if $B = C$, the extensibility simplifies to $f = \cos^2 \alpha_0 + \rho \sin^2 \alpha_0$: only the effects of the drag anisotropy remain. Finally if $C = B$ and $\rho = 1$, we obtain $f = \text{cst} = 1$: the influence of the resting pitch angle then vanishes.

7.1.2 Comparison with Experimental Results

We consider the case corresponding to our experimental conditions: a helically-shaped ribbon with flat triangular cross-section, of width w and thickness t with $t \ll w$. The relevant expressions for the moduli are $B = E(1/36)wt^3$ and $C = \mu(1/12)wt^3$ [7] and hence $C/B = 3/2(1 + \nu)$, where ν is the material Poisson's ratio. To estimate the drag coefficients, we consider the cross-section to be equivalent to a ellipsoidal section of width w and vanishing thickness. The work of Koens et al. [8] then provides an expression for the ratio of the drag coefficients

$$\rho_{\text{ribbon}} = \frac{\xi_3}{\xi_2} = \frac{1}{2} \frac{\ln(4L/w) + 1}{\ln(4L/w) - 1/2} \quad (7.1.3)$$

This expression for the drag coefficient ratio is very similar to the one obtained for cylindrical filaments:

$$\rho_{\text{cylinder}} = \frac{\xi_3}{\xi_2} = \frac{\xi_{\parallel}}{\xi_{\perp}} = \frac{1}{2} \frac{\ln(4L/d) + 1/2}{\ln(4L/d) - 1/2} \quad (7.1.4)$$

where $d = 2r$ is the filament diameter. As was already underlined in section 1.1.3, this suggests a very weak influence of the cross-sectional shape on the viscous forces and validates the approximation of the ribbon cross-section to a flat ellipse. In the high slender case *i.e.* $L \gg w$ or $L \gg d$, we recover the familiar result $\rho = 1/2$.

But these expressions were developed to compute the forces acting on straight filaments. Studying the case of helically-shaped cylindrical filaments, Lighthill suggested [9] that substituting the total length L by an effective length q yields better estimations of the viscous forces. Using a slender-body approximation, Lighthill proposed the following expression $q = 0.09\Lambda$ where $\Lambda = 2\pi R / \cos \alpha_0$ is the filament wavelength *i.e.* the filament

contour length corresponding to one helical loop. Considering the closeness of the coefficients' expression between cylinders and ribbons, we similarly substitute the total length L by the effective length q proposed by Lighthill in eq. (7.1.3). The drag coefficients for helical ribbons are thus given by

$$\xi_2 = \frac{8\pi\eta}{\ln(0.36\Lambda/w) + 1} \approx \frac{8\pi\eta}{\ln(2.26R_0/w \cos \alpha_0) + 1} \quad (7.1.5)$$

$$\xi_3 = \frac{4\pi\eta}{\ln(0.36\Lambda/w) - 1/2} \approx \frac{4\pi\eta}{\ln(2.26R_0/w \cos \alpha_0) - 1/2} \quad (7.1.6)$$

and the drag coefficient ratio by

$$\rho_{\text{ribbon}} = \frac{1}{2} \frac{\ln(0.36\Lambda/w) + 1}{\ln(0.36\Lambda/w) - 1/2} \approx \frac{1}{2} \frac{\ln(2.26R_0/w \cos \alpha_0) + 1}{\ln(2.26R_0/w \cos \alpha_0) - 1/2} \quad (7.1.7)$$

We notice that, because of Lighthill's correction, the drag coefficients ξ_2 and ξ_3 now depend on the resting pitch angle α_0 . As per eq. (7.1.1), the axial extension is proportional to $\xi_2 f$. Thus, influence of the resting pitch angle α_0 on the extension is not fully encapsulated by the extensibility function f . We thus correct f so that it fully captures the influence of the pitch angle

$$f^*(\alpha_0) = \frac{\xi_2}{\xi_2(\alpha_0 = 0^\circ)} f(\alpha_0) \quad (7.1.8)$$

We normalize by $\xi_2(\alpha_0 = 0^\circ)$ so that f^* verifies $f^*(\alpha_0 = 0^\circ) = 1$. We plot in fig. 7.1 (a) the corrected extensibility f^* as a function of resting pitch angle α_0 for different values of ν and R_0/w . In all cases, we also obtain a smooth decrease in the extensibility: similarly to what was observed experimentally, increasing the pitch angle effectively decreases the helix extension in flow.

We now compare the model predictions to our experimental results. For bulk PMMA, the Poisson's ratio is usually estimated within $\nu = 0.35 - 0.40$ so we take $\nu = 0.375$. In our experimental conditions, the helical radius varies within $R = 3 - 12 \mu\text{m}$. Precise measurements of the ribbon width are difficult to achieve, but we estimate $w \approx 0.5 - 1 \mu\text{m}$. The

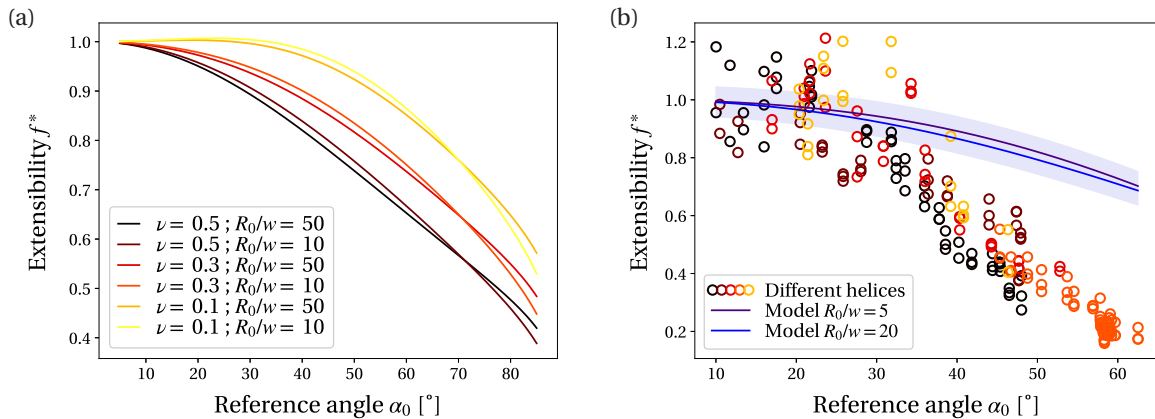


FIGURE 7.1 – (a) Model predictions for the helix dimensionless extensibility f^* in the case of flat triangular ribbon-like filaments, with ribbon width w and helical radius R_0 , for different values of the material Poisson's ratio ν and of R_0/w . (b) Comparison between model predictions and the experimental results obtained for five different PMMA helical ribbons. The Poisson's ratio is taken as $\nu = 0.375$ and two different values for R_0/w are considered. The purple shaded area represents a 5% deviation, which is typical in the experimental results.

ratio R_0/w therefore varies at most within $\sim 5 - 20$. But the variations in radius and width usually originate from the same factor, which is a change in the filament thickness. So we expect little variation in the ratio R_0/w , for which we take $R_0/w = 10$. Furthermore, the influence of this parameter is introduced through a logarithmic correction and is thus weak.

Figure 7.1 (b) shows the model predictions for these parameters along with the experimental results. Consistently with the definition of the extensibility, we have $f^*(\alpha_0 = 0^\circ) = 1$ and the model correctly predicts weak influence of the pitch angle at small angles. But for $\alpha_0 \gtrsim 30^\circ$, there is no qualitative or quantitative agreement between our experimental results and the model. The model does predict a stiffening but the magnitude of this effect is very small, at most a 25% change in extensibility, compared to the factor 5 observed experimentally. Moreover, the predicted change in extensibility happens smoothly over the whole angle range: no clear regime change is observed, in contrast to experimental findings. Finally, we verify that the influence of the parameter R_0/w is indeed negligible, the curves for $R_0/w = 5$ and $R_0/w = 20$ being very close.

This weakness in the predicted stiffening results from the fact that, for PMMA flat triangular ribbons, we have $C/B = 3/2(1 + \nu) = 3/2(1 + 0.375) \approx 1.1$. The torsion-to-bending transition thus plays a very weak role. Furthermore, we obtain $C > B$. So as the resting pitch angle increases, and that the mode of deformation changes from torsion to bending, the relevant filament modulus is actually decreased. The torsion-to-bending transition drives an *increase* in extensibility. Meanwhile, due to the drag anisotropy, we have $\rho < 1$ and the drag coefficient ξ_2 decreases with resting pitch angle. So the changes in the ribbon hydrodynamics drive a *decrease* in extensibility. These two competing effects partially cancel each other, leading to a weak predicted stiffening.

7.1.3 Correcting the Ribbon Mechanics

It is clear that this modeling, which relies on Kirchhoff rod equations and resistive-force theory, does not accurately describe the extension of helical ribbons in flow. As already discussed in section 6.4.2, several works [10, 11] already pointed out that Kirchhoff rod equations usually fail to describe accurately the mechanics of thin ribbons. Considering the results from Starostin et al. [1], we hypothesized that an accurate modeling of the ribbon mechanics would add a multiplicative term $\cos^2 \alpha_0$ to the expression of the extension. We thus propose a new corrected extensibility $f^*(\alpha_0) = \cos^2 \alpha_0 f^*(\alpha_0)$. f^* fully encapsulates the influence of the resting pitch angle and verifies again $f^*(\alpha_0 = 0^\circ) = 1$.

In fig. 7.2, we plot the corrected extensibility f^* as a function of resting pitch angle along with the experimental results. Strikingly, we find good agreement between the experimental data and the corrected model, especially in the high angle regime where stiffening is observed. The corrected model accurately predicts the overall stiffening. In the small angle regime however, agreement is not so good. Specifically, the corrected model predicts a smooth stiffening over the whole angle range whereas the actual stiffening evolves more sharply, with almost no change in extensibility until $\alpha_0 \sim 25 - 30^\circ$. But before we can draw conclusions on the mechanics of helical ribbons, and notably on the relevance of Kirchhoff rod equations, we must consider in more details the hydrodynamic forces.

So far, the viscous forces were modeled using resistive-force theory, which has been shown to inaccurately estimate the viscous forces acting on helical objects [2]. As RFT does not account for the hydrodynamic interactions between neighbors, we expect

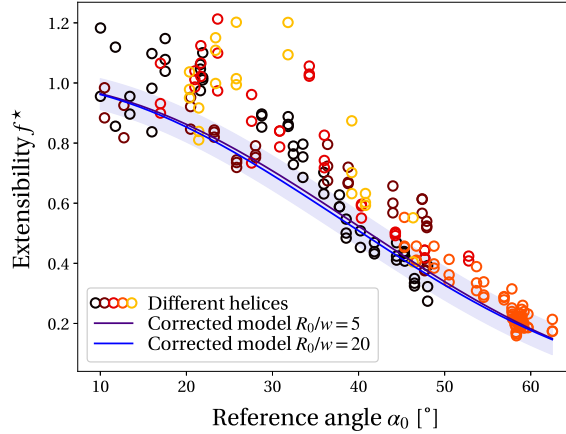


FIGURE 7.2 – Comparison between the model predictions, corrected to account for the specific mechanics of ribbons, and the experimental results obtained for five different PMMA helical ribbons. The Poisson's ratio is taken as $\nu = 0.375$ and two different values for R_0/w are considered. The purple shaded area represents a 5% deviation, which is typical in the experimental results.

RFT to especially fail for small angle helices, since the loops are closer together and thus hydrodynamic interactions are stronger. As it is precisely at small angles that agreement between the corrected model and data is not good, a more accurate modeling of the viscous forces may correct these discrepancies. Given the much better agreement between the corrected model and the experimental results, the corrective term $\cos^2 \alpha_0$ is kept.

7.2 Towards Slender-Body Theory

7.2.1 Proposed Approach

To model more accurately the viscous forces, a slender-body theory formulation is implemented, which takes into account the hydrodynamic interactions. In contrast to RFT, SBT does not exhibit an analytical formulation and thus cannot be incorporated into our analytical framework. But, in our experimental conditions *i.e.* PMMA flat triangular ribbons, we have $C/B \approx 1.1$ and so we approximate $C = B$. Given this approximation and considering the corrected analytical model (thus including the $\cos^2 \alpha_0$ term), the axial extension in flow is rewritten

$$\Delta H = \frac{R_0^2 L^2 U}{2 C} \cos^2 \alpha_0 (\xi_2 \cos^2 \alpha_0 + \xi_3 \sin^2 \alpha_0) = \frac{R_0^2 L}{2} \cos^2 \alpha_0 \frac{D_{\text{RFT}}}{C} \quad (7.2.1)$$

where we have recognized the total drag force $D_{\text{RFT}} = UL (\xi_2 \cos^2 \alpha_0 + \xi_3 \sin^2 \alpha_0)$ calculated using RFT. This expression corresponds to the drag force acting on the helix in its reference configuration, which is consistent with the linearized approach we have followed in chapter 6. We recall that the linearization decoupled calculation of the forces from actuation of the helix shape: the force equations were solved in the helix reference state and the helix shape was then actuated from the obtained forces. The drag force is calculated in the reference state, which is equivalent to the drag force acting on a rigid helix with identical geometrical parameters.

Given this equation, we propose to incorporate slender-body theory within our model by substituting the RFT drag force D_{RFT} by the drag force D_{SBT} calculated using slender-body theory. Similarly to the RFT drag force, the SBT drag force D_{SBT} is calculated in the

reference state of the helix, which is equivalent to the drag force acting on a rigid helix with identical geometrical parameters. This procedure assumes, beyond the assumption $B = C$, that the drag distribution along the filament length is the same for SBT and for RFT. Within RFT, the drag coefficients are constant along the filament length, the drag distribution is thus uniform. Validity of this assumption will be discussed later.

7.2.2 Computation of the SBT Drag Force

The work of Rodenborn et al. [2] provides a numerical implementation of SBT to calculate the viscous forces acting on helices with cylindrical filaments for various geometrical parameters. We are here interested in the drag force D , total drag force acting on a rigid helix immersed in a uniform axial flow. The simulation code is freely available online¹. Two different methods were implemented, Johnson slender-body theory [12] and Lighthill slender-body theory [9]. Johnson SBT was found to better describe experimental data, so this method is preferred. Koens et al. [8] performed a similar implementation for helical ribbons but the simulation code is not available. The authors kindly provided the calculated drag force on helical ribbons for some geometrical parameters.

We first compare these two approaches. In both cases, we set the helical radius to a constant and we chose for simplicity $R = 1$. Guided by the respective expression of the RFT drag coefficients (see eqs. (7.1.3) and (7.1.4) for the respective ratio), we hypothesize that the cylinder diameter and the ribbon width play an identical role. We set both to the same value $d = w = 0.1$ so that $R/d = 10$, which is representative of our experimental conditions. The total filament length varies significantly in experimental conditions, so we consider several values for this parameter.

We show in fig. 7.3 (a) the calculated SBT drag force D_{SBT} , as a function of resting pitch angle α_0 , for helical with cylindrical filaments and with ribbon-like filaments. The drag force is normalized by the scaling ηUL . We first notice that, in contrast to RFT, the SBT

1. mathworks.com/matlabcentral/fileexchange/39265-helical-swimming-simulator

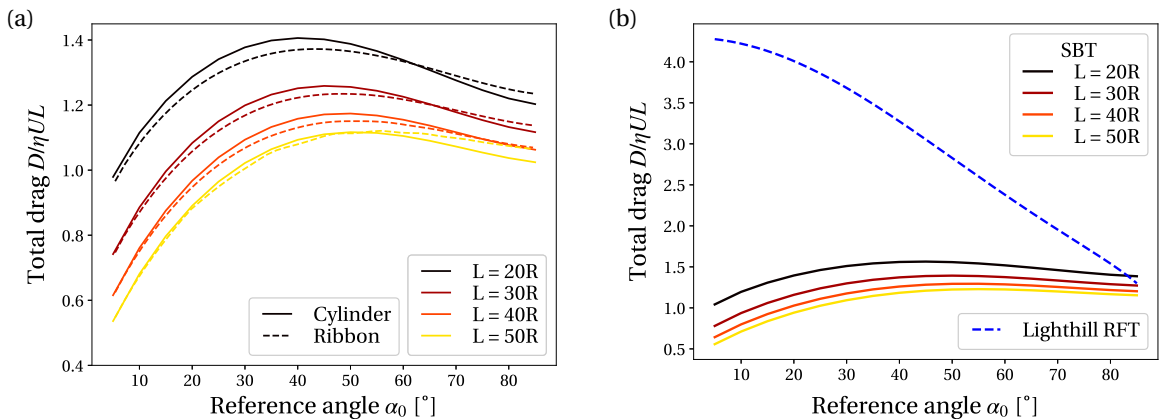


FIGURE 7.3 – (a) Rescaled total drag force $D/\eta UL$ acting on a rigid helix immersed in a uniform viscous axial flow, calculated using slender-body theory, as a function of pitch angle α_0 . The implementation of Rodenborn et al. for cylindrical filaments (set with cylinder diameter $d = 0.1 * R$) and the implementation of Koens et al. for ribbon-like filaments (set with ribbon width $w = 0.1 * R$) are compared. In both case we set the helical radius $R = 1$. (b) Rescaled drag force $D/\eta UL$ acting on a rigid helix with a cylindrical filament, estimated from SBT and from RFT with Lighthill’s correction, as a function of pitch angle. We again set the filament diameter $d = 0.1 * R$ and helical radius $R = 1$.

drag force does not scale linearly with the total filament length L . We find that results for cylindrical and ribbon-like filaments are very close throughout the whole angle range and for all tested lengths. This confirms that the cross-sectional shape has a very weak influence: the drag force is mainly set by the largest dimension of the cross-section (width for a ribbon, diameter for a cylinder). Considering these small differences in the results, we approximate the drag acting on our helical ribbons to the drag acting on helices with cylindrical filaments, with the filament diameter taken equal to the ribbon width. As the simulation code for cylindrical filaments is freely available, this allows easier access to SBT estimation and more flexibility.

We then compare the SBT results to the RFT approximation (with Lighthill's drag coefficients) for helices with cylindrical filaments. Figure 7.3 (b) shows the rescaled drag force $D/\eta UL$ as a function of resting pitch angle α_0 , for both methods. The settings are again $d = 0.1$ and $R = 1$. As shown, RFT estimations differ significantly from SBT results, for all angles and all filament lengths. As expected, discrepancies are especially high at small angles *i.e.* for tightly coiled helices. Specifically, RFT predicts very poorly the evolution of the drag force as the pitch angle varies. RFT predicts a smooth and sizable decrease in the drag force (roughly a factor 3.5 in decrease overall) as the pitch angle increases whereas the actual drag evolution is non-monotonic: the drag first increases with pitch angle, followed by a decrease. The overall variation in drag is at most $\sim 40\%$. This confirms previous findings of the literature [2, 13], which already pointed out that hydrodynamic interactions are crucial in determining the viscous forces acting on helical structures.

7.2.3 Drag Distribution along the Filament Length

As we mentioned, we propose to include SBT into our analytical model by substituting the SBT drag force to the RFT drag force. If we consider the corrected model (to account for the specific mechanics of ribbons) the extension therefore writes

$$\Delta H = \frac{R_0^2 L}{2} \cos^2 \alpha_0 \frac{D_{\text{SBT}}}{C} \quad (7.2.2)$$

This procedure assumes, as we mentioned, uniform drag distribution along the filament length. The implementation of Rodenborn et al., used to compute SBT viscous forces, does not explicitly provide the drag distribution. But this is recovered by adapting the simulation code. The filament is subdivided into N consecutive segments of equal length $\Delta s = L/N$ and we calculate the drag increment ΔD acting on each of these segments. Naturally the total drag is expressed as $D = \sum_N \Delta D$. The drag distribution is given by the differential $\Delta D/\Delta s$, the case of uniform drag corresponding to $\Delta D/\Delta s = D/L$ for all segments. For simplicity, we consider the rescaled differential $\frac{L}{D} \frac{\Delta D}{\Delta s}$. We set again $R = 1$ and $d = 0.1$ and we consider several values for the pitch angle α_0 and length L .

We show in fig. 7.4 the SBT drag force distribution along the filament length, for various resting pitch angles α_0 . Figure 7.4 (a) shows the distribution for $L = 30R$ while fig. 7.4 (b) shows the distribution for $L = 60R$. Firstly, we remark that the drag distribution is symmetrical with respect to the middle of the helix $s = L/2$. We indeed expect that, in the case of a rigid helix, reversing the flow direction *i.e.* changing the flow speed from U to $-U$ would yield the same drag distribution. Overall, the drag is rather uniformly distributed, variations being at most $\sim 20\%$ in most cases. We notice however that for $\alpha_0 \lesssim 20^\circ$, the non-uniformity is more pronounced and further increases with the filament length. For

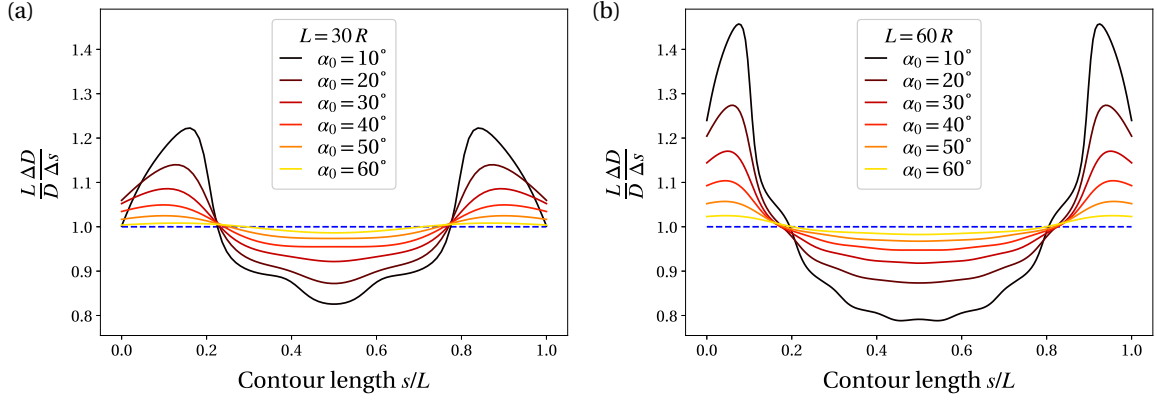


FIGURE 7.4 – Drag distribution for helices with cylindrical filaments, calculated from SBT, with $R = 1$, $d = 0.1$, various resting pitch angles and for (a) $L = 30R$ (b) $L = 60R$.

the highest length $L = 60R$ and for $\alpha_0 = 10^\circ$, variations in drag reach up to $\sim 70\%$. Hence, the proposed inclusion of SBT into our model is overall valid but we expect discrepancies at small angles. It is however difficult to predict the effects of this non-uniformity on the extension in flow. One could argue that a stronger local drag would increase the local deformation, thus potentially triggering non-linear effects, which would stiffen the local portion. But we have shown in section 5.3 that helix deformation is locally linear along the whole filament.

7.2.4 Results of the Twice-Corrected Model

The analytical model has now been twice corrected, firstly to account for the specific mechanics of ribbons and secondly to account for hydrodynamic interactions. The axial extension in flow is now expressed as

$$\Delta H = \frac{R_0^2 L}{2} \cos^2 \alpha_0 \frac{D}{C} = \frac{R^2 L^2 \eta U}{2} \cos^2 \alpha_0 \frac{D}{\eta UL} \quad (7.2.3)$$

with $D = D_{\text{SBT}}$ total drag force acting on the helix in its reference state, calculated using SBT. We now compare the twice-corrected model to our experimental results. We recall that experimental observations are quantified by the extensibility f , which encapsulates influence of the pitch angle. Within the corrected model, influence of the pitch angle is given by the quantity $\cos^2 \alpha_0 \frac{D}{\eta UL}$.

In our experimental conditions, the width-to-radius ratio w/R varies only slightly and the influence of this parameter is weak, we therefore set $w/R = 0.1$. The length-to-radius ratio L/S varies within 20 – 70 so we consider several values within this range. Figure 7.5 (a) shows the quantity $\cos^2 \alpha_0 \frac{D}{\eta UL}$ as a function of pitch angle, for various filament lengths. Evolution of this quantity with pitch angle is reminiscent of what is observed experimentally: little evolution at small angles, followed by a decrease at high angles. Transition between the two regimes happens for $\alpha_0 \sim 20 - 30^\circ$, depending on the filament length, which again is close to experimental findings. At small angles however, we do not observe a plateau but rather a slight increase, which contrasts with experimental results.

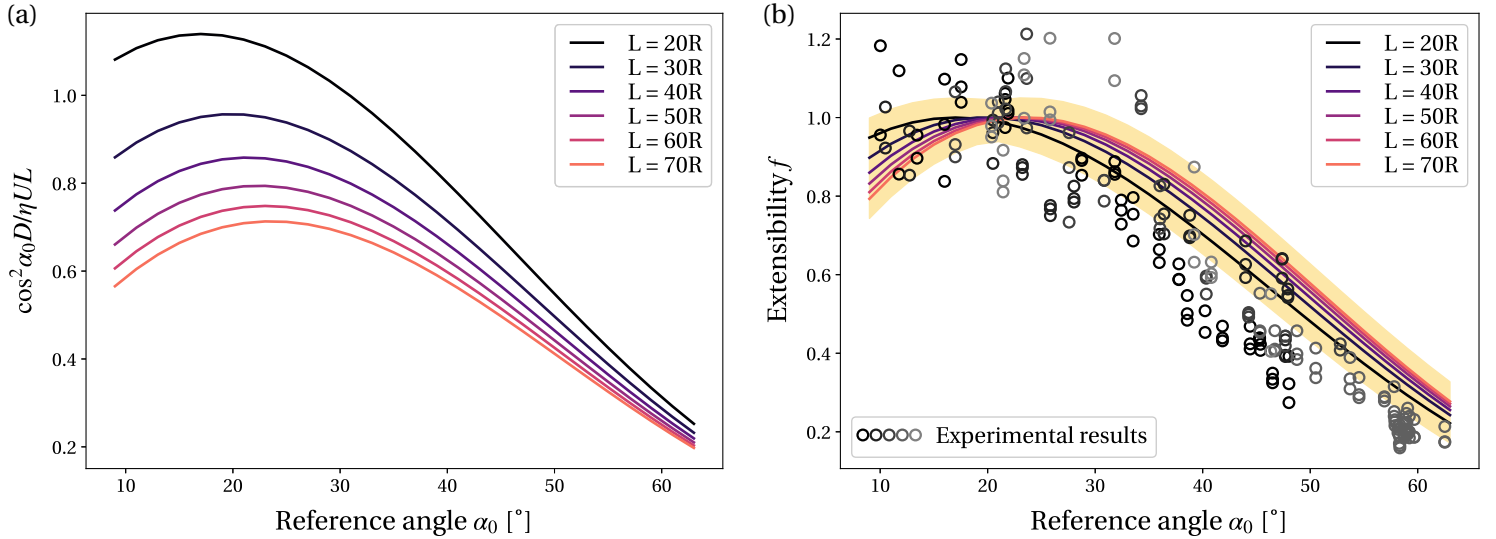


FIGURE 7.5 – (a) Quantity $\cos^2 \alpha_0 D / \eta UL$, calculated from the SBT simulations, as a function of pitch angle α_0 , for various filament lengths. The filament diameter is set to $d = 0.1R$ and the helical radius to $R = 1$. (b) Predicted extensibility, obtained by normalizing the quantity $\cos^2 \alpha_0 D / \eta UL$, for various filament lengths, along with the experimental results (in grey dots). The yellow shaded area represents a 5% deviation, which is typical in the experimental results.

To further compare the corrected model with the experimental results, we need to compute the predicted extensibility. We recall that for experimental results, the extensibility was obtained by normalizing the quantity $\Delta H / UR^2 L^2$ by the value of the plateau observed at small angles. As per eq. (7.2.3), the quantity $\cos^2 \alpha_0 D / \eta UL$ is directly proportional to $\Delta H / UR^2 L^2$. The extensibility can thus be obtained by normalizing $\cos^2 \alpha_0 D / \eta UL$. No plateau is observed for this quantity so we normalize by the maximum value over all pitch angles. Figure 7.5 (b) shows the predicted extensibility, calculated for various filament lengths, as a function of pitch angle along with the experimental results in grey dots. As expected from the evolution of $\cos^2 \alpha_0 D / \eta UL$ shown in fig. 7.5 (a), qualitative agreement with experimental data is very good. Both the small and the high angle regime are accurately described, and a sharp transition is obtained between the two regimes, consistent with experimental observations. Quantitative agreement is also good although the model slightly overestimates the extensibility in the high angle regime. Differences in extensibility between the different curves, each corresponding to a different filament length, are very small. Again this is consistent with experimental observations.

We conclude that the twice-corrected model accurately describes the evolution of the extensibility, which validates the expression proposed for the axial extension of helical ribbons in flow

$$\Delta H = \frac{R_0^2 L^2 \eta U}{2} \frac{1}{C} \cos^2 \alpha_0 \frac{D}{\eta UL}$$

The scaling $\Delta H \propto R^2 L^2 \eta U / C$ was already demonstrated but we have now established the dependency with the pitch angle. The exact value of the numerical factor, here 1/2, remains to be validated. The stiffening at high angles is mainly driven by the $\cos^2 \alpha_0$ term, as the drag force is roughly constant at high angles (see fig. 7.3 for more details). In the small angle regime, the plateau results from two competing effects. The total drag increases with pitch angle, thus increasing the extensibility, while the added term $\cos^2 \alpha_0$ drives a decrease

in extensibility. Overall, this results in little variation of the extensibility at small angles. Addition of the $\cos^2 \alpha_0$ term into the model, which accounts for the specific mechanics of ribbon-like filaments, is therefore validated. Analytical justification remains to be provided, but is beyond the scope of this work.

7.2.5 Predictions for Cylindrical Filaments

The twice-corrected model accurately describes the axial extension of helical ribbons in viscous axial flows. But in most applications, like bacterial flagella, filaments rather exhibit circular cross-sections, to which this model cannot apply. Indeed, for cylindrical filaments, the corrective term $\cos^2 \alpha_0$ is naturally not relevant. Furthermore, the ratio C/B is given by $C/B = 1/(1 + \nu) \approx 0.7$, as for most materials $\nu \sim 0.3 - 0.5$. The assumption $B = C$ does not hold true and we thus expect a much stronger influence of the torsion-to-bending transition. As a consequence, SBT can no longer be included into the model by simple substitution of the drag force: an interplay exists between changes in the drag force and the torsion-to-bending transition.

In the case of cylindrical filaments however, Zhang et al. [13] have proposed an analytical implementation of SBT. The authors suggested modifications to the RFT drag coefficients ξ_2 and ξ_3 so that the viscous forces computed from RFT match experimental and numerical measurements. The total drag force is thus still expressed as $D = UL(\xi_2 \cos^2 \alpha_0 + \xi_3 \sin^2 \alpha_0)$ but the drag coefficients are now given by

$$\xi_2 = S_{\text{drag}} C_n \frac{\ln(30)}{\ln(L/R)} \quad (7.2.4)$$

$$\xi_3 = S_{\text{drag}} C_t \frac{\ln(30)}{\ln(L/R)} \quad (7.2.5)$$

with

$$C_n = 4.05\pi\eta / \ln\left(\frac{0.271p}{r(\sin \alpha_0)^{3.1-6.23r/R}}\right) \quad (7.2.6)$$

$$C_t = 2.21\pi\eta / \ln\left(\frac{0.105p}{r(\sin \alpha_0)^{1.77}}\right) \quad (7.2.7)$$

$$S_{\text{drag}} = \left(0.359 - 1.252 \frac{r}{R}\right) \left(\frac{p}{R}\right)^{0.21+r/R} \quad (7.2.8)$$

with p helical pitch, R helical radius and r filament radius. Zhang et al. compared this approach to the experimental and numerical results obtained by Rodenborn et al. [2], finding very good agreement. Validity of this approach was verified for $\alpha_0 = 10 - 70^\circ$ and $r < R/10$. Discrepancies are expected outside of these ranges.

Therefore, in the case of helices with cylindrical filaments, we propose to include SBT into our analytical framework simply by adopting for the RFT drag coefficients the values proposed by Zhang et al. This procedure again assumes uniform drag distribution. We showed that this hypothesis is valid for $\alpha_0 \gtrsim 20^\circ$, so predictions at small angles may be inaccurate. No further modification of the model is needed and eq. (7.1.1) simply gives the axial extension in flow. Similarly to the Lighthill's correction, the drag coefficient ξ_2 now depends on the pitch angle α_0 . Expression of the extensibility f is thus again modified to fully encapsulate influence of the pitch angle. This time, the modified extensibility is taken as

$$f^*(\alpha_0) = \frac{\xi_2}{\eta} f(\alpha_0) \quad (7.2.9)$$

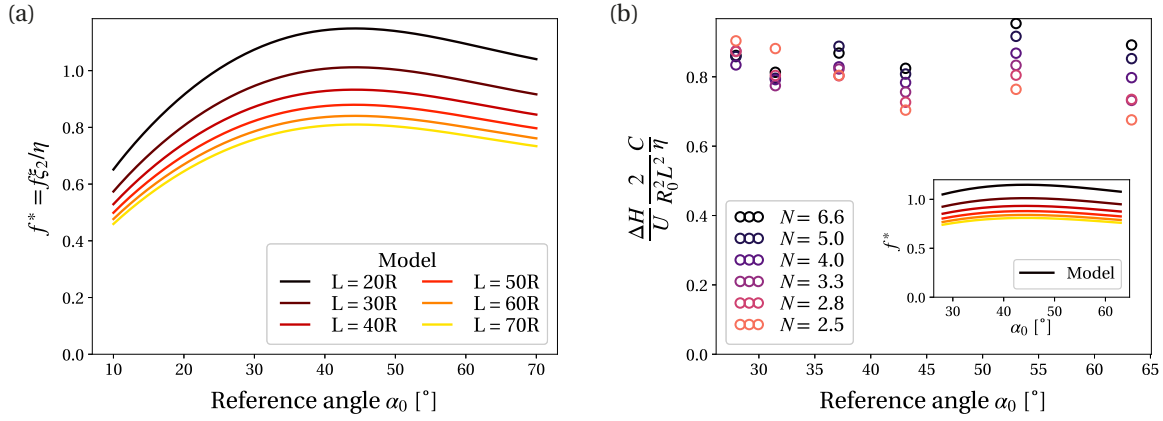


FIGURE 7.6 – (a) Predicted extensibility for helices with cylindrical filaments as a function of resting pitch angle α_0 , for various filament lengths. Results are obtained from the analytical model combined with the RFT drag coefficients proposed by Zhang et al. [13]. (b) Normalized extension as a function of resting pitch angle, extracted and adapted from the numerical results of Jawed et al. [14]. Each set of points corresponds to a different number of turns N . The inset shows the extensibility predicted by the analytical model for the same angle range. Colors correspond to the color code used in (a).

and thus the axial extension is expressed as

$$\Delta H = \frac{R_0^2 L^2}{2} \frac{\eta U}{C} f^*(\alpha_0) \quad (7.2.10)$$

As $\lim_{\alpha_0 \rightarrow 0^\circ} \xi_2 = 0$, the modified extensibility cannot verify $f^*(\alpha_0 = 0^\circ) = 1$. As we do not expect $\Delta H(\alpha_0 = 0^\circ) = 0$, this confirms that the expressions proposed by Zhang et al. are not valid at small angles.

The geometrical parameters are set with similar values as in the case of ribbon-like filaments: $r = d/2 = 0.05R$, $R = 1$ and several values are considered for the total filament length L . The pitch is given by the geometrical relation $p = 2\pi R \tan \alpha_0$. Figure 7.6 (a) shows the extensibility f^* as a function of pitch angle α_0 , for different filament lengths. The angle range is limited to $\alpha_0 = 10 - 70^\circ$ to ensure validity of the expressions proposed for the drag coefficients. Interestingly, evolution of the extensibility for helices with cylindrical filaments is inverse to what was found for ribbon-like filaments. At small angles, the extensibility increases with the pitch angle, followed by a slight decrease at high angles. The maximum is observed for $\alpha_0 \sim 45^\circ$. Qualitatively, at small angles, increasing the pitch angle effectively loosens the helix, while at high angles, influence of the pitch angle is weak.

As our experimental system consists of helical ribbons, experimental validation of the analytical model cannot be performed in the case of cylindrical filaments. But the extension of helices with cylindrical filaments in viscous axial flows was studied numerically by Jawed et al. [14]. The numerical method they used combines Lighthill SBT [9] to model the hydrodynamics forces and a discretized form of Kirchhoff rod equations [15] to simulate the filament mechanics. The deformation of helices was similarly characterized by the axial extension ΔH . A notable difference with our approach is that the flow velocity U was varied in a very wide range, including beyond the weak flow regime.

Jawed et al. [14] found that the $\Delta H(U)$ relationship is described by

$$\Delta H = H_0 C^* (1 - e^{-U/U_c}) \quad (7.2.11)$$

with C^* elongation parameter and U_c characteristic velocity, both obtained as fitting parameters. H_0 is again the resting axial length. In the weak flow regime, this equation

simply rewrites $\Delta H \approx H_0 C^* U / U_c$. We extract from the work of Jawed et al. the values obtained for C^* and U_c as the helix geometry was varied. The rescaled axial extension $\Delta H / U$ is thus obtained in the weak flow regime for various geometrical parameters. The resting axial length is kept constant for all simulations $H_0 = 0.2$ as well as the filament radius $r = H_0 / 126$. For each set of simulations, the number of turns N is fixed and the pitch angle is varied within the range $\sim 30 - 65^\circ$. As both H_0 and N are fixed while the pitch angle varies, the total filament length L and the helical radius R_0 vary for a given set of simulations. In order to correct these changes, and similarly to the procedure adopted in chapter 5 for the experimental data, we compute the quantity $\Delta H / UR^2 L^2$. Variations in this quantity only originate from changes in the resting pitch angle. Finally, guided by eq. (7.2.10), this quantity is multiplied by $2C / \eta$ for further normalization. The obtained quantity is called the normalized extension. Both C and η are known as they are parameters of the simulations.

Figure 7.6 (b) shows the adapted simulation results. For all conditions, we find weak influence of the resting pitch angle and very little difference is found between each set of simulations, each corresponding to a different number of turns N . The normalized extension is roughly constant, although small oscillatory variations are observed. Influence of the boundary conditions has been shown to create oscillatory variations on the axial extension [5, 6], but given the high length of the simulated helices ($L > 20R$), these effects are negligible. The origin of the oscillations remains unclear. The values found for the normalized extension are around 0.8, which confirms the validity of the scaling $\Delta H \sim R^2 L^2 (\eta U / C)$. Within the tested angle range, the analytical model correctly predicts a weak influence of the pitch angle, as shown in the inset of fig. 7.6 (b). Moreover, the values for the modified extensibility f^* are rather close to the ones obtained for the normalized extension, around 0.8. Further comparison with the numerical results is complex, since each set of simulations was computed with constant resting axial length H_0 while our analytical framework assumes constant filament length L . We conclude that within the tested angle range, good qualitative and quantitative agreement is obtained. But a wider angle range must be explored for stronger validation, especially in the regime where helix loosening is predicted. Furthermore, experimental validation would be beneficial. We conclude that for the tested angle range $\alpha_0 = 30 - 65^\circ$, eq. (7.2.10) constitutes a good approximation to compute the axial extension of helically-shaped cylindrical filaments in viscous axial flows.



In this chapter, we have compared our experimental results for the extension of helical ribbons in uniform viscous axial flows to the newly developed analytical model, which relies on Kirchhoff rod equations and resistive-force theory. We have demonstrated that neither Kirchhoff rod equations nor RFT are relevant in this situation.

As already underlined in the literature [10, 11], Kirchhoff rod equations do not accurately describe the mechanics of thin ribbons. We found in chapter 4 that an inextensible elastic strip model is preferable. We have hypothesized that inclusion of this approach within our model would add a multiplicative term $\cos^2 \alpha_0$ to the expression obtained for the axial extension. Analytical justification remains to be provided and would constitute a natural continuation of this work. Addition of this term vastly improved the agreement between the experimental data and the model, which validated its addition.

Guided by the work of Rodenborn et al. [2], we have again highlighted that RFT poorly approximates the viscous forces acting on helical ribbons. Slender-body theory is preferable as it takes into account the hydrodynamic interactions. We have shown that the viscous forces acting on a helical ribbon can be calculated as if the cross-section was circular, with a section diameter equal to the ribbon width. We have proposed an inclusion of SBT into our analytical model, at the cost of two reasonable approximations, namely that $B = C$ and that the drag force is uniformly distributed along the filament length. Overall the analytical model was twice corrected, firstly to account for the specific mechanics of ribbons and secondly to include SBT.

We have found very good agreement, both qualitative and quantitative, between the twice-corrected model and our experimental data. Overall, we have shown that, in the linear regime *i.e.* $\Delta H/L \lesssim 0.1$, the axial extension of a helical ribbon immersed in a uniform viscous axial flow is given by

$$\Delta H_{\text{ribbon}} = \frac{R^2 L}{2} \cos^2 \alpha_0 \frac{D}{C} \quad (7.2.12)$$

with D total drag force acting on the helix in its reference configuration. The value of the numerical constant (here $1/2$) remains to be validated.

Finally, leveraging our new understanding of the deformation of helical ribbons in flow, we have made predictions for the deformation of helices with cylindrical filaments in flow. Our predictions were compared to the numerical results of Jawed et al. [14], finding good agreement.

7.3 References

- [1] EL Starostin and GHM van der Heijden. Tension-induced multistability in inextensible helical ribbons. *Physical review letters*, 101(8):084301, 2008. [120](#), [123](#)
- [2] Bruce Rodenborn, Chih-Hung Chen, Harry L Swinney, Bin Liu, and HP Zhang. Propulsion of microorganisms by a helical flagellum. *Proceedings of the National Academy of Sciences*, 110(5):E338–E347, 2013. [120](#), [123](#), [125](#), [126](#), [129](#), [132](#)
- [3] Mohammad K Jawed, Noor K Khouri, Fang Da, Eitan Grinspun, and Pedro M Reis. Propulsion and instability of a flexible helical rod rotating in a viscous fluid. *Physical review letters*, 115(16):168101, 2015.
- [4] MK Jawed and Pedro M Reis. Dynamics of a flexible helical filament rotating in a viscous fluid near a rigid boundary. *Physical Review Fluids*, 2(3):034101, 2017. [120](#)
- [5] MunJu Kim and Thomas R Powers. Deformation of a helical filament by flow and electric or magnetic fields. *Physical Review E*, 71(2):021914, 2005. [120](#), [131](#)
- [6] Panayiota Katsamba and Eric Lauga. Propulsion by stiff elastic filaments in viscous fluids. *Physical Review E*, 99(5):053107, 2019. [120](#), [131](#)
- [7] N. A. Gloumakoff and Yi-Yuan Yu. Torsion of Bars With Isosceles Triangular and Diamond Sections. *Journal of Applied Mechanics*, 31(2):332–334, 06 1964. [121](#)
- [8] Lyndon Koens and Eric Lauga. Slender-ribbon theory. *Physics of Fluids*, 28(1):013101, 2016. [121](#), [125](#)

- [9] James Lighthill. Flagellar hydrodynamics. *SIAM review*, 18(2):161–230, 1976. [121](#), [125](#), [130](#)
- [10] Basile Audoly and Keith A Seffen. Buckling of naturally curved elastic strips: the ribbon model makes a difference. In *The Mechanics of Ribbons and Möbius Bands*, pages 293–320. Springer, 2016. [123](#), [131](#)
- [11] Arun Kumar, Poornakanta Handral, CS Darshan Bhandari, Anindya Karmakar, and Ramsharan Rangarajan. An investigation of models for elastic ribbons: Simulations & experiments. *Journal of the Mechanics and Physics of Solids*, 143:104070, 2020. [123](#), [131](#)
- [12] Robert E Johnson. An improved slender-body theory for stokes flow. *Journal of Fluid Mechanics*, 99(2):411–431, 1980. [125](#)
- [13] Zhang He-Peng, Liu Bin, Bruce Rodenborn, and Harry L Swinney. Propulsive matrix of a helical flagellum. *Chinese Physics B*, 23(11):114703, 2014. [126](#), [129](#), [130](#)
- [14] Mohammad K Jawed and Pedro M Reis. Deformation of a soft helical filament in an axial flow at low reynolds number. *Soft matter*, 12(6):1898–1905, 2016. [130](#), [132](#)
- [15] Miklós Bergou, Max Wardetzky, Stephen Robinson, Basile Audoly, and Eitan Grinspun. Discrete elastic rods. In *ACM SIGGRAPH 2008 papers*, pages 1–12. 2008. [130](#)

Chapter 8

Conclusion and Perspectives

Contents

8.1 General Conclusion	136
8.2 Future Works and Perspectives	137
8.2.1 Helices in Extensional Flows, Shear Flows and More	137
8.2.2 Multi-Component Assemblies	139
8.3 References	139

8.1 General Conclusion

In this work, we have developed a fully integrated experimental set-up to study the physics of flexible helices, from their mechanical properties to their interactions with viscous flows. We used micro-fabricated flexible helical ribbons as a model system, combined with cantilever force measurements and microfluidic techniques for flow control. Helical radii range within $R = 2 - 50 \mu\text{m}$ and typical filament length within $L = 0.1 - 2 \text{ mm}$.

The fabrication method builds upon the spontaneous coiling of flat triangular ribbons driven by surface tension, which results into helical ribbons of controllable radius but vanishing pitch [1]. We have demonstrated that the creep properties of materials can be leveraged to shape the helical ribbons into any desired geometry. Full shape control is thus achieved: the helical radius, the helical pitch and the total filament length can all be independently tuned. We have highlighted the importance of accurately controlling the helical pitch, since this parameter sets the magnitude of the chirality-induced effects (notably propulsion and lateral drift in shear flows). Furthermore, we have shown that material properties are not affected by creep deformations.

This fabrication method was validated for several materials: poly(methyl methacrylate), poly(dimethylaminoethyl methacrylate) and quantum dots, demonstrating its versatility. We found that each material is characterized by a typical creeping timescale, which denotes its susceptibility to creep deformations. PMMA helices were shown to exhibit the most favorable timescale whereas PDMAEMA helices and quantum dots helices were found to be too susceptible to creep. Subsequent experiments are thus conducted with PMMA helices.

We have then investigated the mechanical properties of helical ribbons by establishing the force-extension relationship. At a given geometry, a non-linear relationship is found: the force diverges as the helix approaches the fully uncoiled state. Leveraging the newly achieved control on the pitch angle, we quantified for the first time experimentally the influence of this parameter on the mechanical properties. We found that an increase in pitch angle is associated to an effective stiffening of the helical ribbons. Both the non-linearity of the force-extension relation and the effective stiffening are accurately described by the analytical model proposed by Starostin et al. [2]. Comparison with other established models [3] showed that the stiffening effect is specific to helical ribbons. We conclude that the tension force F associated to an axial extension ΔH is given by

$$F = \frac{C}{R^2} \frac{(\cos \alpha_0 \cos \alpha + \frac{C}{B} \sin \alpha_0 \sin \alpha) \sin(\alpha - \alpha_0)}{(\cos^2 \alpha + \frac{C}{B} \sin^2 \alpha)^2 \cos \alpha} \quad (8.1.1)$$

with C twisting modulus of the filament, B bending modulus, α_0 resting pitch angle and α pitch angle of the deformed helix. The axial extension verifies $\Delta H = L(\sin \alpha - \sin \alpha_0)$. Benefiting from this analytical expression, the twisting modulus of the helical ribbons was measured. The obtained values range within $C \sim 10^{-20} - 10^{-19} \text{ Pa} \cdot \text{m}^4$ for helical radii within $5 - 10 \mu\text{m}$, close to the typical stiffness of bacterial flagella.

Finally, we have investigated the deformation of clamped helical ribbons immersed in uniform viscous axial flows. For the first time experimentally, influence of the pitch angle on the extension in flow was studied. For small angle helical ribbons, the pitch angle was found to have a very weak influence. For high angle helical ribbons, we found that an increase in pitch angle is associated with a decrease in extension: the overall decrease

is significant, up to a factor 5 between $\alpha_0 = 10^\circ$ and $\alpha_0 = 60^\circ$. Transition between the two regimes happens for $\alpha_0 \sim 25 - 30^\circ$.

A new analytical framework was developed, relying on Kirchhoff rod equations and resistive-force theory. Comparison with experimental results highlighted that Kirchhoff rod equations do not accurately describe the mechanical behavior of thin ribbons, confirming the findings of previous studies [4, 5]. An inextensible elastic strip model, similar to the approach followed by Starostin et al. [2], is preferable. The model was corrected to account for the specific mechanics of ribbons, vastly improving its accuracy. Guided by the work of Rodenborn et al. [6], which showed that slender-body theory is preferable to estimate the viscous forces acting on helices, we proposed a second correction of the model to include SBT into the analytical framework. We showed that the viscous forces acting on a helical ribbon can be calculated as if the filament cross-section was circular, with section diameter equal to the ribbon width. Excellent agreement, both qualitative and quantitative, was found between the twice-corrected model and the experimental results. We conclude that, in the linear regime, the axial extension of a clamped helical ribbon immersed in a uniform viscous axial flow is given by

$$\Delta H = \frac{R^2 L}{2} \cos^2 \alpha_0 \frac{D}{C} \quad (8.1.2)$$

with D total drag force acting on the helical ribbon in its reference configuration. The linear regime approximation is valid for $\Delta H/L \lesssim 0.1$. The exact value of the numerical prefactor (here $1/2$) remains to be validated.

Overall, we have demonstrated fabrication of highly flexible micron-sized helical ribbons with controlled chirality and well-characterized flexibility. We have demonstrated that these micro-fabricated helical ribbons can be combined with microfluidic flow control techniques to carry out well-controlled and detailed experiments. These helical ribbons constitute an ideal model system to explore and study the behavior of flexible helices in viscous flows and notably the interplay between chirality and flexibility.

We have however pointed out that the properties of helical ribbons are significantly affected by the ribbon-like nature of the filament. The specific mechanical properties of ribbons drive significant stiffening effects as the pitch angle increases. Hence, care must be taken when applying our results to helically-shaped cylindrical filaments. Specifically, the relation between the helix flexibility and the geometrical parameters is different depending on the filament cross-section. But at a given flexibility and chirality, the exact shape of the cross-section should be of little importance.

8.2 Future Works and Perspectives

8.2.1 Helices in Extensional Flows, Shear Flows and More

The experimental set-up we have developed can naturally be leveraged to tackle more intricate fluid-structure interaction problems of flexible helices in viscous flows. Notable among them is the behavior of flexible helices in extensional/compressional flows or in shear flows. No studies have yet investigated the behavior of flexible helices in extensional/compressional flows and only the numerical work of Li et al. [7] has investigated the behavior of flexible helices in shear flows. Experimental study of these situations would thus be highly beneficial.

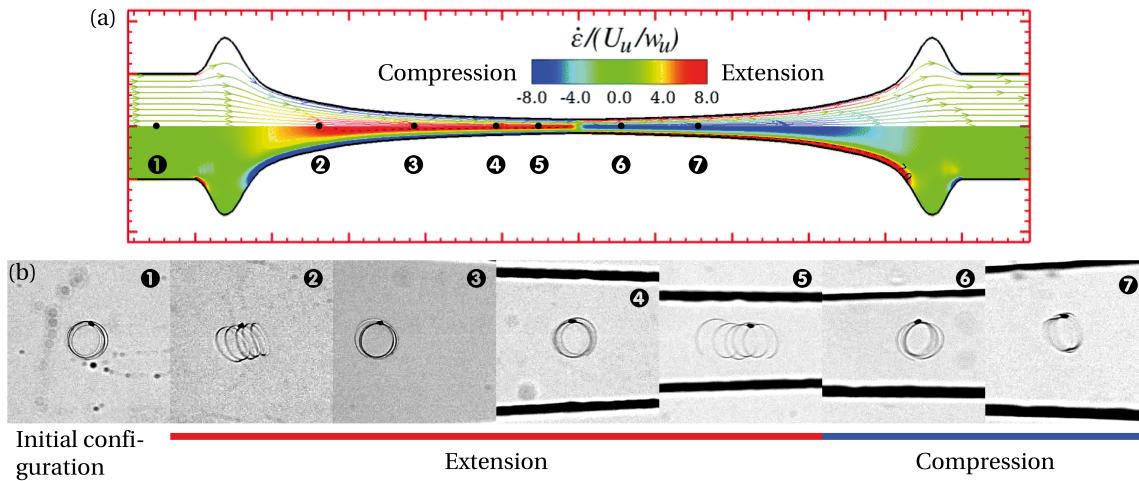


FIGURE 8.1 – (a) Geometry of an optimized hyperbolic channel, resulting in a constant extension rate $\dot{\epsilon}$ over a long distance, reproduced from Liu et al. [9]. (b) Series of bright-field images of a PMMA helical ribbon transported in such a hyperbolic channel, successively extended then compressed. The thick dark lines in images 4 to 7 are the channel walls.

The experimental study of flexible helical ribbons in extension/compressional flows has been initiated during this PhD and is being continued during the PhD of Andrea de la Sen. We use, in this case, hyperbolic microfluidic channels, optimized to obtain constant extension rates over long distances [8]. We show in fig. 8.1 (a) the geometry of a such an optimized channel with the computed extension rate $\dot{\epsilon}$, reproduced from Liu et al. [9]. As shown, the flow is purely extensional before the channel mid-point and then purely compressional. Combined with a tracking algorithm developed by Liu et al. [9], we can follow the transport and deformation of flexible helices in such flows.

We show in fig. 8.1 (b) preliminary observations of a PMMA helical ribbon transported in an extensional and then compressional flow. The helix starts in its initial equilibrium configuration (image 1). As the flow is started, the helix is transported towards the channel's constriction. As expected, in the first part of the flow (extensional), the helix is stretched with respect to its initial configuration (images 2 to 5). In the second part of the flow (after the mid-point *i.e.* compressional), the helix is compressed as expected (images 6 and 7). But we also observe that the helix seems to rotate about its vertical axis along the trajectory. The probable reason is that the helix is not perfectly centered in the channel and thus experiences a shear flow, which drives a rotation of the object. Several experimental hurdles, such as mitigating helix sedimentation and precise centering of the helix in the channel, have yet to be overcome for well-controlled experiments.

The experimental study of flexible helices in shear flows can also be conducted. A simple shear flow can be obtained by using a vertical Hele-Shaw cell *i.e.* a rectangular channel much higher than wide. The vertical flow profile (along the height) is then a plug flow while the horizontal flow profile (along the width) is parabolic. Provided the object size is much smaller than the channel width, the object experiences a simple shear in the horizontal plane. The shear plane then matches the observation plane (also horizontal) allowing observation of the rotational motion associated with shear flows. Such an approach was followed for example by Liu et al. to study experimentally the behavior of elastic filaments in shear flows [10].

In this study we have focused our attention on the effects of the flow on the structure

but the reciprocal disturbance in the flow field created by the structure has not been investigated. This topic remains unexplored in the literature. Continuation of our work could investigate in more detail the disturbed flow field, through the use of Particle Image Velocimetry (PIV) for example. Furthermore, a better understanding of the reciprocal flow disturbance may allow the study of the hydrodynamic interactions between neighboring helices in flow. Finally, the macroscopic properties of a suspension of flexible helices may be studied and eventually the link between the microscopic effects (at the size of the particle) and the macroscopic properties of the suspension might be elucidated.

8.2.2 Multi-Component Assemblies

Moving past the study of an isolated object, these helical ribbons can participate in the assembly of multi-component structures. Nature provides various examples of such assemblies, a notable one being a bacteria, which is the assembly of one or multiple helical flagella with a cellular body. The behavior of a bacteria in flow is determined by the coupling between the helical flagella and the vesicle-like body. A replication of such assemblies may allow fabrication of artificial bacteria, for the study of their behavior or for medical applications, such as targeted drug delivery [11].

Within this goal, we collaborated with Dylan M. Barber (D. M. B.), Zhefei Yang, Todd Emrick and Alfred J. Crosby (UMass, Amherst, USA) to produce assemblies of droplets with fibers and helices. Materials exhibiting pH response were designed by D.M.B., and used to fabricate helical ribbons whose three-dimensional shape and interfacial properties respond to pH. At high pH for example, the self-coiling phenomenon was suppressed. Moreover, ribbons with patterned properties were designed by D.M.B. to modulate the ribbon dimensions, mechanical properties or interfacial properties along the ribbon length. The assembly of the obtained helices and fibers with oil droplets was studied. We reproduce the published paper [12] in Appendix I and supporting information in Appendix II. We highlight the fabrication of oil droplets with arms (see Figure 1 and Figure 6 of the paper), which bear a strong resemblance with multi-flagellated bacteria. We contributed to the design of the experimental system, notably to produce oil droplets and to precisely manipulate the various objects involved. Furthermore, we conducted flow experiments to characterize the mechanical properties of the newly synthesized materials. Further progress in this direction may include achieving self-propulsion of the assemblies, by the rotation of helical ribbons for example.

8.3 References

- [1] Jonathan T Pham, Jimmy Lawrence, Dong Yun Lee, Gregory M Grason, Todd Emrick, and Alfred J Crosby. Highly stretchable nanoparticle helices through geometric asymmetry and surface forces. *Advanced Materials*, 25(46):6703–6708, 2013. [136](#)
- [2] EL Starostin and GHM van der Heijden. Tension-induced multistability in inextensible helical ribbons. *Physical review letters*, 101(8):084301, 2008. [136](#), [137](#)
- [3] Augustus Edward Hough Love. *A treatise on the mathematical theory of elasticity*. Cambridge university press, 1944. [136](#)

- [4] Basile Audoly and Keith A Seffen. Buckling of naturally curved elastic strips: the ribbon model makes a difference. In *The Mechanics of Ribbons and Möbius Bands*, pages 293–320. Springer, 2016. [137](#)
- [5] Arun Kumar, Poornakanta Handral, CS Darshan Bhandari, Anindya Karmakar, and Ramsharan Rangarajan. An investigation of models for elastic ribbons: Simulations & experiments. *Journal of the Mechanics and Physics of Solids*, 143:104070, 2020. [137](#)
- [6] Bruce Rodenborn, Chih-Hung Chen, Harry L Swinney, Bin Liu, and HP Zhang. Propulsion of microorganisms by a helical flagellum. *Proceedings of the National Academy of Sciences*, 110(5):E338–E347, 2013. [137](#)
- [7] Run Li, Gerhard Gompper, and Marisol Ripoll. Tumbling and vorticity drift of flexible helicoidal polymers in shear flow. *Macromolecules*, 54(2):812–823, 2021. [137](#)
- [8] K Zografos, F Pimenta, MA Alves, and MSN Oliveira. Microfluidic converging/diverging channels optimised for homogeneous extensional deformation. *Bio-microfluidics*, 10(4):043508, 2016. [138](#)
- [9] Yanan Liu, Konstantinos Zografos, Joana Fidalgo, Charles Duchêne, Clément Quintard, Thierry Darnige, Vasco Filipe, Sylvain Huille, Olivia du Roure, Mónica SN Oliveira, et al. Optimised hyperbolic microchannels for the mechanical characterisation of bio-particles. *Soft Matter*, 16(43):9844–9856, 2020. [138](#)
- [10] Yanan Liu, Brato Chakrabarti, David Saintillan, Anke Lindner, and Olivia Du Roure. Morphological transitions of elastic filaments in shear flow. *Proceedings of the National Academy of Sciences*, 115(38):9438–9443, 2018. [138](#)
- [11] Bradley J Nelson, Ioannis K Kaliakatsos, and Jake J Abbott. Microrobots for minimally invasive medicine. *Annual review of biomedical engineering*, 12:55–85, 2010. [139](#)
- [12] Dylan M Barber, Zhefei Yang, Lucas Prévost, Olivia Du Roure, Anke Lindner, Todd Emrick, and Alfred J Crosby. Programmed wrapping and assembly of droplets with mesoscale polymers. *Advanced Functional Materials*, 30(36):2002704, 2020. [139](#)

Chapter 9

Résumé Substantiel

9.1 Introduction

Les structures hélicoïdales jouent un rôle crucial dans de nombreux contextes chimiques, biologiques et mécaniques. La nature offre de nombreux exemples, couvrant plusieurs ordres de grandeur en longueur, y compris l'ADN double brin, les structures dites 'alpha-hélice' dans les protéines ou encore les vrilles des plantes. Les structures hélicoïdales revêtent une importance particulière pour la propulsion des micro-organismes, car nombre d'entre eux se propulsent par la rotation de flagelles flexibles hélicoïdales [1]. Enfin, de nombreuses technologies reposent sur des structures hélicoïdales, notamment des nano-ressorts métalliques pouvant servir d'actionneur ou de capteur de force [2, 3], des micro-nageurs artificiels [4], ou des micro-débitmètres [5, 6]. L'étude des propriétés mécaniques de telles structures hélicoïdales et de leurs interactions avec les écoulements est donc importante tant pour la science fondamentale que pour des applications technologiques.

Pour les hélices et plus généralement pour les objets chiraux en écoulement, un couplage existe entre les mouvements de translation et de rotation. Les particules chirales en écoulement dérivent donc à travers les lignes de courant dans une direction qui dépend de leur chiralité [7-9]. Ce phénomène a été utilisé pour séparer des objets de chiralité opposée, un processus crucial dans les industries alimentaires ou pharmaceutiques. L'influence de la chiralité a été étudiée dans diverses situations, telles que la sédimentation de particules [10] ou le transport de particules dans un flux de cisaillement [8, 11]. Les bactéries et les micro-nageurs artificiels sont typiquement constitués d'une ou plusieurs flagelles hélicoïdales attachées à un corps non chiral, et sont donc partiellement chiraux. Pour ces systèmes, la force de dérive induite par la chiralité crée un couple qui peut réorienter le nageur [12]. L'une des principales conclusions de ces études est que, pour les objets hélicoïdaux, l'ampleur des effets induits par la chiralité est principalement contrôlé par le pas de l'hélice, c'est-à-dire la distance entre deux boucles consécutives. Une hélice à pas nul correspond à un anneau, qui n'est pas chiral, et une hélice à pas infini à un filament droit, qui n'est pas non plus chiral. Par conséquent, les effets de chiralité sont maximisés pour un pas fini non nul.

Mais la plupart de ces études ne considèrent que des particules rigides, alors que la plupart des structures naturelles et artificielles qui les motivent sont très flexibles. Pour les hélices flexibles, des degrés de liberté supplémentaires sont ajoutés, tels que l'élongation/compression axiale ou le flambage. Un couplage très complexe est ainsi créé entre le

mouvement de translation, le mouvement de rotation et la déformation. Par exemple, la déformation peut faire varier le pas de l'hélice, ce qui modulera à son tour l'ampleur des effets de chiralité. Seul un petit nombre d'études ont examiné ce couplage entre la chiralité et la flexibilité, la plupart d'entre elles étant analytiques ou numériques [13–17].

Sur le plan expérimental, deux approches, à des échelles de longueur différentes, ont été explorées. D'une part, travailler à l'échelle macroscopique permet de fabriquer facilement des hélices flexibles aux propriétés contrôlées. Le contrôle des écoulements est cependant complexe et l'étude du transport des hélices par des écoulements est difficile, car une telle expérience nécessite que la longueur du canal soit beaucoup plus grande que la taille typique de l'hélice. Cette approche est donc particulièrement adaptée aux situations où le fluide est immobile [14, 15]. D'autre part, travailler à l'échelle microscopique permet de contrôler facilement l'écoulement grâce aux techniques de microfluidique et une taille de canal arbitraire peut être atteinte, permettant l'étude du transport. Mais la fabrication et la caractérisation d'hélices flexibles à l'échelle microscopique sont particulièrement compliquées. En effet, très peu de méthodes existent pour la fabrication d'hélices flexibles de taille micrométrique et de géométrie précisément contrôlée. En particulier, le contrôle du pas de l'hélice, qui est crucial pour déterminer l'ampleur des effets induits par la chiralité, est très rarement réalisé. Ces lacunes dans les méthodes expérimentales entravent les progrès dans l'étude du couplage entre la chiralité et la flexibilité.

Dans ce contexte, ce travail vise à développer un dispositif expérimental complet, de la fabrication d'hélices flexibles de taille micrométrique à la caractérisation de leurs propriétés mécaniques et à l'étude de leurs interactions avec des écoulements. L'accent est mis sur le contrôle de la forme de l'hélice et de ses propriétés mécaniques. La plate-forme développée s'appuie sur la formation spontanée de rubans hélicoïdaux microscopiques hautement flexibles mise en évidence par Crosby et al. [18–20]. Nos travaux ont été menés en étroite collaboration avec Dylan M. Barber et Alfred J. Crosby de l'Université du Massachusetts, Amherst, États-Unis. Anirban Jana et Andrea de la Sen ont contribué à ce travail pendant leur stage de recherche de Master. La plupart des travaux rapportés ici sont expérimentaux mais sont complétés par des approches analytiques et numériques, pour lesquelles nous avons été assistés par Lyndon Koens de l'Université Macquarie, Sidney, Australie.

9.2 Contenu

Dans le chapitre 2, nous avons présenté les différentes méthodes et techniques expérimentales que nous utilisons tout au long de ce travail, et le dispositif expérimental général a été décrit. Nous avons notamment détaillé le processus de fabrication des rubans hélicoïdaux flexibles de taille micrométrique. Nous avons mis en évidence que le rayon de l'hélice R est déterminé par l'épaisseur du ruban t et par la longueur élasto-capillaire du matériau γ/E

$$R = \frac{Et^2}{3\gamma} \quad (9.2.1)$$

Le contrôle de l'épaisseur du ruban est obtenu par gravure au plasma des échantillons avant les expériences, ce qui permet de contrôler le rayon de l'hélice. La longueur totale du filament L est réglée par simple découpe des échantillons. Le contrôle du pas de l'hélice est cependant absent, et les hélices présentent typiquement une géométrie étroitement

enroulée, avec donc une chiralité très faible. Plusieurs problèmes expérimentaux ont été observés, affectant de façon négative la fabrication des rubans et le phénomène d'auto-enroulement. Ces problèmes semblent être liés au vieillissement des composés chimiques, en particulier le polyméthacrylate de méthyle (PMMA) et le colorant fluorescent (Coumarin 153), par hydratation sous l'effet de l'humidité ambiante. Ces problèmes sont atténués par le stockage des composants sous vide avant leur utilisation. Enlever le colorant fluorescent participe également à l'atténuation de ces effets, au prix d'hélices non fluorescentes. Mais comme les hélices peuvent être visualisées par microscopie à contraste de phase en champ clair, la fluorescence n'est pas une caractéristique essentielle.

Dans le chapitre 3, nous avons présenté un ensemble de méthodes exécutées in-situ permettant de contrôler localement le pas de nos rubans hélicoïdaux. Le procédé consiste à créer une contrainte persistante dans le matériau en étirant l'hélice pendant une longue période de temps, généralement plusieurs minutes. Une fois la contrainte relâchée, une augmentation irréversible du pas de l'hélice est observée. Différents profils de contrainte peuvent être appliqués pour contrôler localement cette augmentation. Notamment, l'application d'une contrainte uniforme résulte en une augmentation uniforme du pas. Tous les paramètres géométriques de l'hélice sont maintenant contrôlables, le contrôle de la longueur et du rayon ayant déjà été réalisé. En outre, les paramètres géométriques peuvent être modifiés indépendamment les uns des autres. Aucun changement n'est attendu dans les propriétés mécaniques du matériau lors des traitements, mais une validation expérimentale serait bénéfique. Nous avons démontré que notre méthode exploite la susceptibilité accrue au fluage des matériaux confinés pour donner aux hélices la géométrie souhaitée. La susceptibilité de chaque matériau au fluage a été caractérisée par un coefficient $r/\Delta t$. Les hélices en PMMA présentent le rapport le plus favorable, ce qui valide l'utilisation de ce matériau lors des expériences futures. Les hélices en PDMAEMA et en boîtes quantiques se sont avérées trop sensibles au fluage.

Très peu de méthodes de fabrication aboutissent à des structures hélicoïdales flexibles avec un contrôle total de la forme et nous rapportons pour la première fois un contrôle *local* du pas. Les différentes méthodes de modification du pas ont été testées pour trois matériaux différents, démontrant la polyvalence du procédé : PMMA, polyméthacrylate de diméthylamino-éthyle (PDMAEMA) modifié et boîtes quantiques Cd-Se. Cette polyvalence contraste avec les méthodes précédentes pour lesquelles le choix du matériau est limité : nanotubes d'ADN pour les travaux de Maier et al. [21] ou composites métalliques pour les travaux de Li et al. [6].

Dans le chapitre 4, nous avons caractérisé expérimentalement les propriétés mécaniques des rubans hélicoïdaux en mesurant la relation force-extension $F(\Delta H)$. L'extension axiale est imposée, et la force correspondante est mesurée à l'aide d'une poutre cantilever. En profitant du contrôle nouvellement obtenu sur le pas de l'hélice, l'influence de ce paramètre a été étudiée. Pour une géométrie de référence donnée, la relation $F(\Delta H)$ s'est avérée non linéaire. Au fur et à mesure que l'angle de pas α_0 augmente, un raidissement des rubans hélicoïdaux est observé. Nous avons constaté que la non-linéarité de la relation force-extension et le raidissement effectif sont décrits avec précision par le modèle analytique proposé par Starostin et al. [22], obtenu en utilisant un modèle de bande élastique inextensible. Nos résultats fournissent donc une forte validation expérimentale de l'approche suivie par Starostin et al. La comparaison avec un modèle précédemment établi pour des hélices dont le filament est cylindrique [23] suggère que l'effet de raidissement

est spécifique aux rubans hélicoïdaux. A partir de la relation force-extension, le module de torsion du ruban C a été extrait. Nous avons suivi les changements potentiels de C alors que l'angle de pas varie. Aucun changement n'a été constaté, ce qui confirme que les propriétés mécaniques du matériau ne sont pas affectées par les déformations irréversibles déclenchées pendant le processus d'augmentation du pas. Nos mesures de C ont été comparées aux résultats antérieurs de Pham et al., qui ont utilisé le même système expérimental [24]. Un excellent accord a été trouvé, validant davantage nos résultats.

Dans le chapitre 5, nous avons présenté des résultats expérimentaux pour l'extension de rubans hélicoïdaux immergés dans des écoulements axiaux visqueux. En s'appuyant sur les méthodes nouvellement développées de contrôle du pas de l'hélice, nous avons étudié l'influence de ce paramètre sur l'extension en écoulement. Nous avons introduit la fonction d'extensibilité f , qui englobe l'influence de l'angle de pas α_0 sur l'extension. Nous rapportons une extensibilité constante aux petits angles (géométrie compacte) suivie d'une forte diminution aux angles élevés (vers une géométrie ouverte). Ainsi, aux petits angles, l'angle de pas n'a aucune influence sur la déformation alors qu'aux angles élevés, l'augmentation de l'angle de pas conduit à une diminution de l'extension. Le changement de régime se produit autour de $\alpha_0 \sim 25 - 30^\circ$. L'ampleur de cet effet de raidissement en écoulement est significatif : l'extensibilité diminue d'un facteur 5 entre $\alpha_0 = 10^\circ$ et $\alpha_0 = 60^\circ$. Les résultats analytiques précédemment rapportés pour la déformation d'une hélice en écoulement visqueux ne parviennent pas à décrire cet effet [13, 25].

Nous avons ensuite analysé la forme des hélices déformées par l'écoulement, mettant en évidence un changement du mode de déformation lorsque l'angle de pas augmente. Aux petits angles, le ruban est principalement sollicité en torsion (associée au module de torsion C) alors qu'aux angles élevés, le ruban est principalement sollicité en flexion (associée au module de flexion B). Cette transition dans le mode de déformation et l'effet de raidissement rappellent les observations faites dans le chapitre 4. Mais considérer uniquement l'influence de la mécanique du ruban ne permet pas de décrire précisément le comportement en écoulement. L'influence des forces visqueuses hydrodynamiques doit être prise en compte. Qualitativement, pour les hélices à petit angle, la géométrie est très compacte et le filament est orienté perpendiculairement à la direction de l'écoulement. Lorsque l'angle de pas augmente, la géométrie devient plus ouverte et le filament est orienté plus parallèlement à la direction de l'écoulement. Étant donné ces changements simultanés de compacité et d'orientation du filament, il est difficile d'estimer comment les forces visqueuses varient avec l'angle de pas.

Dans le chapitre 6, nous avons développé un cadre analytique pour modéliser la déformation d'une hélice flexible dont le filament est de section arbitraire, immergée dans un écoulement visqueux. Le comportement mécanique du filament est décrit à l'aide des équations de Kirchhoff et les forces visqueuses sont approximées à l'aide de la "resistive-force theory" (RFT). Nous avons spécifiquement détaillé le cas d'une hélice immergée dans un écoulement axial visqueux de vitesse uniforme U . En supposant que l'extension axiale de l'hélice est petite (soit $\Delta H \ll L$), une expression pour l'extension axiale a été obtenue

$$\Delta H = \frac{R_0^2 L^2}{2} \frac{\xi_2 U}{C} f(\alpha_0)$$

$$\text{où } f(\alpha_0) = \cos^4 \alpha_0 + \left(2\rho + 2\frac{C}{B} - 1 - \rho\frac{C}{B} \right) \cos^2 \alpha_0 \sin^2 \alpha_0 + \rho\frac{C}{B} \sin^4 \alpha_0$$

avec $\rho = \xi_3/\xi_2$ représentant l'anisotropie de traînée spécifique aux objets allongés. Nos

résultats contrastent avec les travaux analytiques précédents, qui ont trouvé une influence négligeable de l'angle de pas [13, 25] malgré l'utilisation des mêmes équations élémentaires. Nous avons comparé nos résultats avec des simulations numériques basées sur les travaux de Walker et al. [26]. Ces simulations reposent à nouveau sur les mêmes relations constitutives (équations de Kirchhoff et RFT). Nous avons trouvé un excellent accord entre notre approche analytique et les résultats de la simulation, ce qui valide notre dérivation. Les divergences avec les modèles précédemment publiés restent inexpliquées.

Nous avons ensuite adapté notre cadre pour traiter le cas d'une hélice chargée à son extrémité. Nous avons retrouvé le résultat classique de Love [23], validant à nouveau notre approche. Dans le cas spécifique des rubans hélicoïdaux, nous avons comparé nos résultats aux travaux de Starostin et al. [22], qui reposent sur une modélisation différente de la mécanique des rubans. Certaines différences ont été mises en évidence et nous avons proposé en conséquence une correction ad-hoc du modèle pour traiter le cas des rubans hélicoïdaux. Nous avons émis l'hypothèse que l'ajout d'un terme multiplicatif $\cos^2 \alpha_0$ à nos résultats analytiques rendrait compte de la mécanique spécifique des rubans. La justification analytique reste à fournir et constituerait une suite naturelle de ce travail.

Dans le chapitre 7, nous avons comparé nos résultats expérimentaux concernant l'extension de rubans hélicoïdaux immergés dans des écoulements axiaux visqueux à nos prédictions analytiques, obtenues en combinant les équations de Kirchhoff et la RFT. Nous avons démontré que ni les équations de Kirchhoff ni la RFT ne sont pertinentes dans cette situation. Comme déjà souligné dans la littérature [27, 28], les équations de Kirchhoff ne décrivent pas correctement la mécanique des rubans. Nous avons constaté dans chapter 4 qu'un modèle de bande élastique inextensible est préférable. L'ajout du terme multiplicatif ad-hoc $\cos^2 \alpha_0$ a grandement amélioré l'accord entre les données expérimentales et le modèle, ce qui a validé son ajout.

Guidés par les travaux de Rodenborn et al. [29], nous avons mis en évidence que la RFT approxime mal les forces visqueuses agissant sur les rubans hélicoïdaux. La "slender-body theory" (SBT) est préférable car elle prend en compte les interactions hydrodynamiques. Nous avons montré que les forces visqueuses agissant sur un ruban hélicoïdal peuvent être calculées comme si la section était circulaire, avec un diamètre égal à la largeur du ruban. Nous avons proposé une inclusion de la SBT dans notre modèle analytique, au prix de deux approximations raisonnables, à savoir que $B = C$ et que la force de traînée est uniformément distribuée le long du ruban. Le modèle analytique a donc été corrigé deux fois, d'abord pour tenir compte de la mécanique spécifique des rubans et ensuite pour inclure la SBT. Nous avons constaté un très bon accord, tant qualitatif que quantitatif, entre le modèle doublement corrigé et nos données expérimentales. Nous avons conclu que, dans le régime linéaire *i.e.* $\Delta H/L \lesssim 0.1$, l'extension axiale d'un ruban hélicoïdal immergé dans un écoulement axial visqueux est donnée par

$$\Delta H_{\text{ribbon}} = \frac{R^2 L}{2} \cos^2 \alpha_0 \frac{D}{C} \quad (9.2.2)$$

avec D la force de traînée totale agissant sur l'hélice dans sa configuration de référence. La valeur de la constante numérique (ici $1/2$) reste à valider.

9.3 Conclusion

En conclusion, nous avons démontré la fabrication de rubans hélicoïdaux de taille micrométrique hautement flexibles avec une chiralité contrôlée et une flexibilité bien caractérisée. Nous avons démontré que ces rubans hélicoïdaux micro-fabriqués peuvent être combinés avec des techniques de microfluidique pour réaliser des expériences détaillées. Ces rubans hélicoïdaux constituent un système modèle idéal pour explorer et étudier le comportement des hélices flexibles en écoulement visqueux et notamment l'interaction entre chiralité et flexibilité. Nous avons cependant souligné que les propriétés des rubans hélicoïdaux sont significativement affectées par la mécanique spécifique des rubans. Ces propriétés mécaniques entraînent notamment des effets de raidissement importants lorsque l'angle de pas augmente. Les résultats obtenus dans le cas de rubans hélicoïdaux ne peuvent donc pas s'appliquer directement à des hélices dont le filament est de section différente. Notamment, la relation entre la flexibilité de l'hélice et les grandeurs géométriques (rayon, pas et longueur) est différente selon la section du filament. Mais à une flexibilité et une chiralité données, la forme exacte de la section devrait être de peu d'importance.

9.4 Références

- [1] Eric Lauga and Thomas R Powers. The hydrodynamics of swimming microorganisms. *Reports on Progress in Physics*, 72(9) :096601, 2009. [141](#)
- [2] Gaoshan Huang and Yongfeng Mei. Helices in micro-world : Materials, properties, and applications. *Journal of Materiomics*, 1(4) :296–306, 2015. [141](#)
- [3] Lichun Liu, Liqiu Zhang, Sang Min Kim, and Sungho Park. Helical metallic micro- and nanostructures : fabrication and application. *Nanoscale*, 6(16) :9355–9365, 2014. [141](#)
- [4] Bradley J Nelson, Ioannis K Kaliakatsos, and Jake J Abbott. Microrobots for minimally invasive medicine. *Annual review of biomedical engineering*, 12 :55–85, 2010. [141](#)
- [5] Rafaele Attia, Daniel C Pregibon, Patrick S Doyle, Jean-Louis Viovy, and Denis Bartolo. Soft microflow sensors. *Lab on a Chip*, 9(9) :1213–1218, 2009. [141](#)
- [6] Weiming Li, Gaoshan Huang, Jiao Wang, Ying Yu, Xiaojing Wu, Xugao Cui, and Yongfeng Mei. Superelastic metal microsprints as fluidic sensors and actuators. *Lab on a Chip*, 12(13) :2322–2328, 2012. [141](#), [143](#)
- [7] Masato Makino and Masao Doi. Migration of twisted ribbon-like particles in simple shear flow. *Physics of Fluids*, 17(10) :103605, 2005. [141](#)
- [8] Marcos, Henry C Fu, Thomas R Powers, Roman Stocker, et al. Separation of microscale chiral objects by shear flow. *Physical review letters*, 102(15) :158103, 2009. [141](#)
- [9] Marcin Kostur, Michael Schindler, Peter Talkner, and Peter Hänggi. Chiral separation in microflows. *Physical review letters*, 96(1) :014502, 2006. [141](#)
- [10] Martina Palusa, Joost De Graaf, Aidan Brown, and Alexander Morozov. Sedimentation of a rigid helix in viscous media. *Physical Review Fluids*, 3(12) :124301, 2018. [141](#)

- [11] Qi-Yi Zhang. Chirality-specific lift forces of helix under shear flows : Helix perpendicular to shear plane. *Chirality*, 29(2) :97–102, 2017. [141](#)
- [12] Arnold JTM Mathijssen, Nuris Figueroa-Morales, Gaspard Junot, Éric Clément, Anke Lindner, and Andreas Zöttl. Oscillatory surface rheotaxis of swimming e. coli bacteria. *Nature communications*, 10(1) :1–12, 2019. [141](#)
- [13] MunJu Kim and Thomas R Powers. Deformation of a helical filament by flow and electric or magnetic fields. *Physical Review E*, 71(2) :021914, 2005. [142](#), [144](#), [145](#)
- [14] Mohammad K Jawed, Noor K Khouri, Fang Da, Eitan Grinspun, and Pedro M Reis. Propulsion and instability of a flexible helical rod rotating in a viscous fluid. *Physical review letters*, 115(16) :168101, 2015. [142](#)
- [15] Mohammad K Jawed and Pedro M Reis. Deformation of a soft helical filament in an axial flow at low reynolds number. *Soft matter*, 12(6) :1898–1905, 2016. [142](#)
- [16] MK Jawed and Pedro M Reis. Dynamics of a flexible helical filament rotating in a viscous fluid near a rigid boundary. *Physical Review Fluids*, 2(3) :034101, 2017.
- [17] Run Li, Gerhard Gompper, and Marisol Ripoll. Tumbling and vorticity drift of flexible helicoidal polymers in shear flow. *Macromolecules*, 54(2) :812–823, 2021. [142](#)
- [18] Hyun Suk Kim, Cheol Hee Lee, PK Sudeep, Todd Emrick, and Alfred J Crosby. Nanoparticle stripes, grids, and ribbons produced by flow coating. *Advanced Materials*, 22(41) :4600–4604, 2010. [142](#)
- [19] Dong Yun Lee, Jonathan T Pham, Jimmy Lawrence, Cheol Hee Lee, Cassandra Parkos, Todd Emrick, and Alfred J Crosby. Macroscopic nanoparticle ribbons and fabrics. *Advanced materials*, 25(9) :1248–1253, 2013.
- [20] Jonathan T Pham, Jimmy Lawrence, Dong Yun Lee, Gregory M Grason, Todd Emrick, and Alfred J Crosby. Highly stretchable nanoparticle helices through geometric asymmetry and surface forces. *Advanced Materials*, 25(46) :6703–6708, 2013. [142](#)
- [21] Alexander Mario Maier, Wooli Bae, Daniel Schiffels, Johannes Friedrich Emmerig, Maximilian Schiff, and Tim Liedl. Self-assembled dna tubes forming helices of controlled diameter and chirality. *ACS nano*, 11(2) :1301–1306, 2017. [143](#)
- [22] EL Starostin and GHM van der Heijden. Tension-induced multistability in inextensible helical ribbons. *Physical review letters*, 101(8) :084301, 2008. [143](#), [145](#)
- [23] Augustus Edward Hough Love. *A treatise on the mathematical theory of elasticity*. Cambridge university press, 1944. [143](#), [145](#)
- [24] Jonathan T Pham, Alexander Morozov, Alfred J Crosby, Anke Lindner, and Olivia du Roure. Deformation and shape of flexible, microscale helices in viscous flow. *Physical Review E*, 92(1) :011004, 2015. [144](#)
- [25] Panayiota Katsamba and Eric Lauga. Propulsion by stiff elastic filaments in viscous fluids. *Physical Review E*, 99(5) :053107, 2019. [144](#), [145](#)

- [26] Benjamin J Walker, Kenta Ishimoto, and Eamonn A Gaffney. Efficient simulation of filament elasto-hydrodynamics in three dimensions. *Physical Review Fluids*, 5(12) : 123103, 2020. [145](#)
- [27] Basile Audoly and Keith A Seffen. Buckling of naturally curved elastic strips : the ribbon model makes a difference. In *The Mechanics of Ribbons and Möbius Bands*, pages 293–320. Springer, 2016. [145](#)
- [28] Arun Kumar, Poornakanta Handral, CS Darshan Bhandari, Anindya Karmakar, and Ramsharan Rangarajan. An investigation of models for elastic ribbons : Simulations & experiments. *Journal of the Mechanics and Physics of Solids*, 143 :104070, 2020. [145](#)
- [29] Bruce Rodenborn, Chih-Hung Chen, Harry L Swinney, Bin Liu, and HP Zhang. Propulsion of microorganisms by a helical flagellum. *Proceedings of the National Academy of Sciences*, 110(5) :E338–E347, 2013. [145](#)

List of Figures

1.1	Velocity field for shear flows and planar extension flows	17
1.2	Examples of microscopic helices for locomotion	21
1.3	Various micro-fabricated flexible helices	27
2.1	Description of the self-coiling phenomenon	39
2.2	The coffee-ring effect and the flow-coating method for ribbon fabrication .	41
2.3	Various examples of helical ribbons, coiled from PMMA or PDMAEMA ribbons	43
2.4	Examples of unsuccessfully coiled PMMA ribbons	47
2.5	Experimental set-up	49
2.6	Cantilever tip deflection δ as a function of dragging speed ν	50
3.1	Previous observations of irreversible deformations in helical ribbons	54
3.2	Helix fabrication workflow including the pitch tuning method	55
3.3	The two modes of ribbon bending	56
3.4	The stretching treatment: methods and observations	58
3.5	Characterization of the stretching treatment for PMMA helices	59
3.6	Stretching treatments applied to other materials: quantum dots and PDMAEMA	60
3.7	Fabrication of a double-helix	61
3.8	The flow treatment: methods and observations	63
3.9	Shear viscosity of bulk PMMA as a function of temperature	65
3.10	Simple torsion of a flat triangular straight ribbon	66
4.1	Experimental workflow for the mechanical characterization of helical ribbons	75
4.2	Typical measurements made to establish the force-extension curve	75
4.3	Force-extension curves for a PMMA helix under axial end-loading	79
4.4	Force-extension curves for another PMMA helix under axial end-loading . .	79
4.5	Measurements of the twisting modulus as the pitch angle is varied and com- parison with previously published data	81
5.1	Experimental workflow for studying the deformation of clamped helical ribbons in viscous axial flows	87
5.2	A typical flow cycle imposed upon a PMMA helical ribbon and the correspon- ding axial length	88
5.3	Experimental results for the extension in flow of PMMA helical ribbons . . .	90
5.4	Extensibility f as a function of pitch angle α_0 for five different PMMA helical ribbons	91
5.5	Successive image analysis steps to extract the two-dimensional filament shape	92
5.6	Detailed decomposition of the filament two-dimensional shape	92

5.7	Distribution of the flow-induced deformations for a small-angle PMMA helical ribbon	94
5.8	Distribution of the flow-induced deformations on a high-angle PMMA helical ribbon	94
5.9	Torsion change $\Delta\tau$ and curvature change $\Delta\kappa$ as the resting pitch angle α_0 is varied	95
6.1	Parametrization of the deformed helix	106
6.2	Simulated extension dynamics with various number of segments N	109
6.3	Simulations results and comparison with the model for a cylindrical filament ($\nu = 0.5$)	111
6.4	Simulations results and comparison with the model for a cylindrical filament ($\nu = 0$) and for a ribbon-like filament ($\nu = 0.5$)	112
7.1	Analytical predictions for the extensibility of helical ribbons and comparison with experimental results	122
7.2	Comparison between the corrected model and experimental results	124
7.3	Comparison of the drag estimations between slender-body theory and resistive-force theory	125
7.4	Drag distribution for helices with cylindrical filaments, calculated from SBT	127
7.5	Comparison of the twice-corrected model with experimental results	128
7.6	Analytical predictions for the extensibility of helices with cylindrical filaments	130
8.1	Preliminary experiments of flexible helical ribbons in extensional/compressional flows	138

List of Tables

1.1	Synthesis of the available fabrication methods for micron-sized flexible helices	27
2.1	Critical exposure time to oxygen plasma treatment for varying sacrificial layer thickness	46
2.2	Experimental results for the calibration of the cantilever stiffness	50

Programmed Wrapping and Assembly of Droplets with Mesoscale Polymers

Dylan M. Barber, Zhefei Yang, Lucas Prévost, Olivia du Roure, Anke Lindner, Todd Emrick,* and Alfred J. Crosby*

Nature is remarkably adept at using interfaces to build structures, encapsulate reagents, and regulate biological processes. Inspired by nature, flexible polymer-based ribbons, termed “mesoscale polymers” (MSPs), are described to modulate interfacial interactions with liquid droplets. This produces unprecedented hybrid assemblies in the forms of flagellum-like structures and MSP-wrapped droplets. Successful preparation of these hybrid structures hinges on interfacial interactions and tailored MSP compositions, such as MSPs with domains possessing distinctly different affinity for fluid–fluid interfaces as well as mechanical properties. In situ measurements of MSP–droplet interactions confirm that MSPs possess a negligible bending stiffness, allowing interfacial energy to drive mesoscale assembly. By exploiting these interfacial driving forces, mesoscale polymers are demonstrated as a powerful platform that underpins the preparation of sophisticated hybrid structures in fluids.

damage-preventing mechanisms activated upon impact-driven disassembly and reassembly. Another example is the integration of flagella and fimbriae with the membrane of bacteria. These long, flexible mesostructures couple with the vesicle-like core to modulate interfacial interactions with their surroundings.^[4–11] These examples illustrate how assemblies of fibers and spheroids with well-controlled interactions and length scales give rise to advantageous properties and performance. While some synthetic systems demonstrate isolated principles of such natural phenomena,^[12,13] a robust platform with material-, interfacial-, and geometry-enabled tuning of fiber-spheroid assemblies has yet to be realized.

1. Introduction

Nature provides striking examples of mesoscale assemblies featuring properties and architectures that inspire synthetic replication. Some naturally occurring structures take the form of long, fibrous building blocks that act in concert with spheroids, such as droplets, colloidal particles, or live cells. For example, fiber-in-droplet packing is exemplified by spooling observed in spider capture silk,^[1–3] in which a fiber is periodically wetted with aqueous droplets and winds into an internally spooled configuration. The balance between interfacial energy and fiber bending energy drives such assembly, as well as the dissipative,

Figure 1a describes our use of polymer ribbons, termed mesoscale polymers (MSPs), at the interface of oil-in-water droplets, in which three modes of interaction were identified: nonadhesion, adhesion without wrapping, and spontaneous wrapping. These interactions are dictated by the critical strain energy release rate, $G_c = \gamma_{ow} + \gamma_{pw} - \gamma_{op}$ (comprising the oil–water, polymer–water, and oil–polymer interfacial tensions), and the critical elastoadhesive length, $R_c = \sqrt{Et^3/G_c}$, a droplet radius defined by MSP mechanics (Young’s modulus E), interfacial strength (G_c), and geometry (thickness t), above which an adhesive MSP spontaneously wraps droplets.^[12,13] A pH-responsive trigger embedded in the MSPs controls the observed assembly mode. Figure 1b describes MSPs with segments of alternating compositions, termed mesoscale block copolymers (MSBCPs), such that G_c and R_c are partitioned along the ribbon length. When brought into contact with a droplet of radius R , selective wrapping is designed to afford droplets with one or many pendent arms. In this paper, we realize the vision in Figure 1, starting from monomer and copolymer synthesis, fabrication of MS(BC)Ps (thickness $t \approx 100$ – 600 nm, width $w \approx 10$ – 35 μm , and length 2 – 4 mm), and MS(BC)P contact with emulsion droplets (radius $R = 6$ – 350 μm). Key structures were derived from different ribbon interactions with droplets, including weak adhesion (Figure 1c, far left), spontaneous wrapping (Figure 1c, center left), and selective wrapping by specific MSBCP segments to afford structures with one (Figure 1c center right) or many (Figure 1c far right) arms extending into the surrounding fluid, or a mesoscale micelle. By embedding responsive chemistry into MSPs, we modulate the resulting

D. M. Barber, Dr. Z. Yang, Prof. T. Emrick, Prof. A. J. Crosby
Polymer Science and Engineering Department
University of Massachusetts Amherst
Amherst, MA 01003–9263, USA
E-mail: tsemrick@mail.pse.umass.edu; crosby@mail.pse.umass.edu
L. Prévost, Dr. O. du Roure, Prof. A. Lindner
PMMH
ESPCI Paris
PSL Research University
CNRS
Université de Paris
Sorbonne Université
Paris 75005, France

The ORCID identification number(s) for the author(s) of this article can be found under <https://doi.org/10.1002/adfm.202002704>.

DOI: 10.1002/adfm.202002704

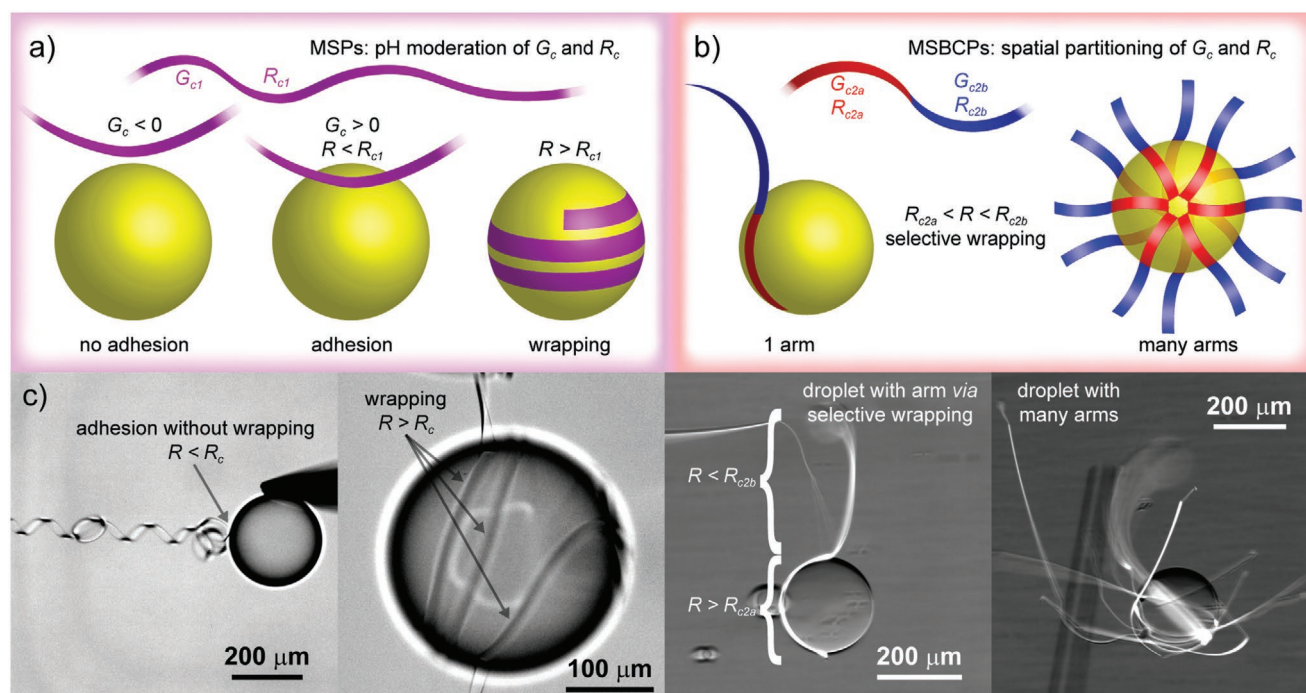


Figure 1. System design. MS(BC)P–droplet interactions are dictated by controlling material properties (G_c , E) and geometry (t , R) via pH and spatial partitioning: a) MSPs adopt nonadhesive (left), adhesive (center), and wrapped (right) interaction modes, stemming from the pH-dependent work of adhesion (G_c) and the relative size of the droplet radius R and critical elasto-adhesive length R_c ; b) MSBCPs, with segments of alternating composition, G_c and R_c , enable selective wrapping for all droplet radii $R_{c2a} < R < R_{c2b}$, affording droplets with 1 (left) or many (right) arms; c) micrographs (left to right) of MSPs in adhesive ($R < R_{c1}$) and wrapped ($R > R_{c1}$) modes, and MSBCPs in selectively wrapped ($R_{c2a} < R < R_{c2b}$) modes with one or many arms.

ribbon/droplet architecture and in turn produce a new materials toolbox of hybrid structures. Moreover, by providing access to a broad array of structures from mesoscale ribbons and droplets, we build a platform of increasingly sophisticated soft materials that begin to emulate the exquisite examples found in Nature.

2. Materials Preparation

The MSPs described in this work were prepared with reactive and functional polymers using flow-coating methods we described previously.^[14–16] The polymers were designed to exhibit pH response (polymer 1) and amenability to photopatterning (polymer 2), as shown in Figure 2a. Polymer 1 ($M_n = 38$ kDa, $\bar{D} = 2.7$) was prepared by free radical copolymerization of dimethylaminoethyl methacrylate (DMAEMA) with 5 mol% of benzophenone methacrylate (BPMA) and 1 mol% of fluorescein-*o*-methacrylate (FMA). The tertiary amines enable pH response by transitioning from charge neutral to cationic with increasing acidity,^[17–20] while BPMA imparts a crosslinking mechanism and FMA contributes fluorescence to aid visualization. Copolymer 2 ($M_n = 21$ kDa, $\bar{D} = 2.2$) was prepared by free radical polymerization of *t*-butyl methacrylate (TBMA) with 2 mol% of glycidyl methacrylate (GMA), 4 mol% of triphenylsulfonium 4-vinylbenzenesulfonate (TPS4VBS), and 0.2 mol% of rhodamine B methacrylate (RBMA). In polymer 2, the aromatic sulfonium sulfonate comonomer functions as

a photoacid generator upon UV exposure to trigger acid-catalyzed deprotection of the *t*-butyl esters and crosslinking via the glycidyl ethers, affording MSPs with segments of alternating composition, termed MSBCPs.^[21]

To prepare the MSPs, a clean glass slide (24 mm × 40 mm × 170 μm) was coated with an ≈50 nm layer of poly(styrene sulfonate) (PSS, sodium salt) at 2 or 4 mm intervals to afford stripes of bare glass ≈100 μm wide, over which was flow-coated a toluene solution of polymer 1 or 2 (Figure 2b left).^[14–16] The substrate was translated in 1 mm intervals at 3 mm s^{−1}, with a 1.1–1.5 s delay between steps to deposit the MSPs. The ribbons were then irradiated i) at $\lambda = 365$ nm (3300 mJ cm^{−2}) (copolymer 1) to afford a crosslinked polyDMAEMA network (schematic Figure 2b, purple) or at ii) $\lambda = 254$ nm (200–695 mJ cm^{−2}) through a photomask, then heated to 150 °C for 60 s (copolymer 2), to afford MSBCPs with alternating segments of hydrophobic, glassy poly(*t*-butyl methacrylate) (PTBMA) and hydrophilic, crosslinked poly(methacrylic acid) (PMAA, Figure 2b, red and blue, Figure S1, Supporting Information). The ribbons were cut into 2–4 mm long segments with a CO₂ laser engraver ($\lambda = 10.6$ μm) and subjected to reactive ion etching with O₂ plasma for 30 s to remove any residual polymer film between the MSPs. The MSPs were released from the substrate by submerging the sample in an aqueous solution to dissolve the underlying PSS layer, then brought into contact with oil-in-water droplets; the resulting assemblies were studied as a function of their interfacial activity (G_c) and critical elasto-adhesive length (R_c).

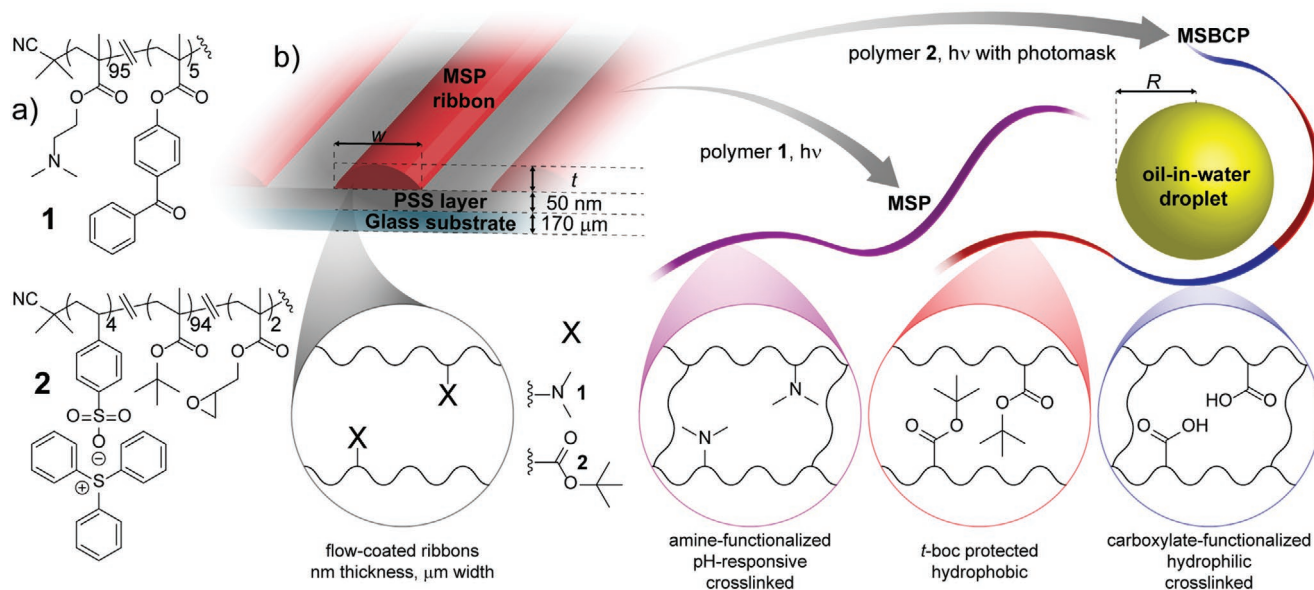


Figure 2. Experimental design. a) Structure of PDMAEMA copolymer 1 and PTBMA copolymer 2 used to prepare ribbons; b) copolymers were flow-coated onto a PSS-coated glass slide to afford ribbons of thickness t and width w , with functionality determined by copolymer selection, then irradiated to afford MSPs or MSBCPs (structural representations simplified for clarity).

3. Controlling Ribbon–Droplet Architectures with pH

Experiments with MSPs prepared from copolymer 1 were performed in pH 1–10 buffer solutions using individual perfluorodecalin (PFD) droplets ($R = 6\text{--}350\ \mu\text{m}$) to avoid coalescence. Pendant drop tensiometry revealed the oil–water surface tension γ_{ow} to be roughly constant ($\approx 50\ \text{mN m}^{-1}$) across this pH range. Droplet-to-MSP contact was achieved using a glass microcapillary fixed to a hand-controlled micromanipulator (Figure 3a,b). Droplets were introduced by inflation at the microcapillary tip or by emulsification and injection via pipette. The optical micrograph in Figure 3b features an MSP adhered end-on to the surface of a PFD droplet, alongside the microcapillary tip. The schematics in Figure 3c illustrate a typical experimental setup. The microcapillary tube and translating stage are used to probe MSP/droplet interactions by moving droplets through the fluid phase; pH-dependent assembly spans weak adhesion, possibly mediated by nonuniformities on the MSP surface, to spontaneous wrapping. We note that MSPs were observed to spontaneously curve into wavy structures or well-defined helices, especially in aqueous environments from pH 1–6; the observed curvature, a function of MSP mechanical properties and interfacial interactions with the surrounding aqueous phase, was used to estimate a pH-independent copolymer modulus of $\approx 200\ \text{MPa}$ by helix extension in viscous flow (details in the Supporting Information).^[15,22,23]

3.1. Weak Adhesion Modes: Ribbon Stretching and Flagellum-Like Assemblies

From pH 1–6, MSPs and droplets were observed to slide past one another upon contact, with adhesion occurring randomly along the MSP. Figure 3d (left) shows sequential frames from Video S1

in the Supporting Information, in which a coiled MSP (helix radius = $38\ \mu\text{m}$) is suspended between the substrate and an adhered droplet ($R = 132\ \mu\text{m}$). By translating the substrate, the helix transitions from unstretched (top) to extended (center), to fully detach from the droplet (bottom), recoiling like a stretched spring. This adhesion is too weak to macroscopically deform the droplet before detachment. Video S2 in the Supporting Information illustrates similar adhesion at pH 4, while Video S3 in the Supporting Information displays an example of interfacial slip along a smooth MSP helix at pH 6. At pH 8, the adhesion occurred at the MSP ends (Figure 3c,d center) to afford flagellum-like structures. Video S4 in the Supporting Information shows a droplet attached to an MSP segment (length $\approx 400\ \mu\text{m}$) that is pushed through the fluid with the capillary tip to demonstrate i) adhesion between the droplet and MSP end and ii) a lack of adhesion along the MSP face. This flagellum-like assembly was maintained while the MSP was stretched (Figure 3d center; Video S4, Supporting Information), but when the droplet was brought into contact with the MSP face (time $T \approx 0.4\text{--}0.8\ \text{s}$) the two faces slid past one another without adhering. We speculate that these distinct adhesion modes may result from laser cutting (CO_2 laser, $\lambda = 10.6\ \mu\text{m}$) of the MSPs after flow-coating, which heats the material^[24] and potentially alters its surface composition (i.e., via oxidation), G_c , and roughness.^[25,26] We note that MSPs that were stored under ambient conditions for ≈ 3 weeks before release into pH 8 buffer qualitatively exhibited a decrease in selectivity for adhesion at the end.

3.2. Capillary Wrapping

At pH 10, the MSPs were observed to spontaneously wrap the droplets upon contact between the ribbon face and fluid–fluid interface, suggesting both large G_c and $R > R_c$. This wrapping

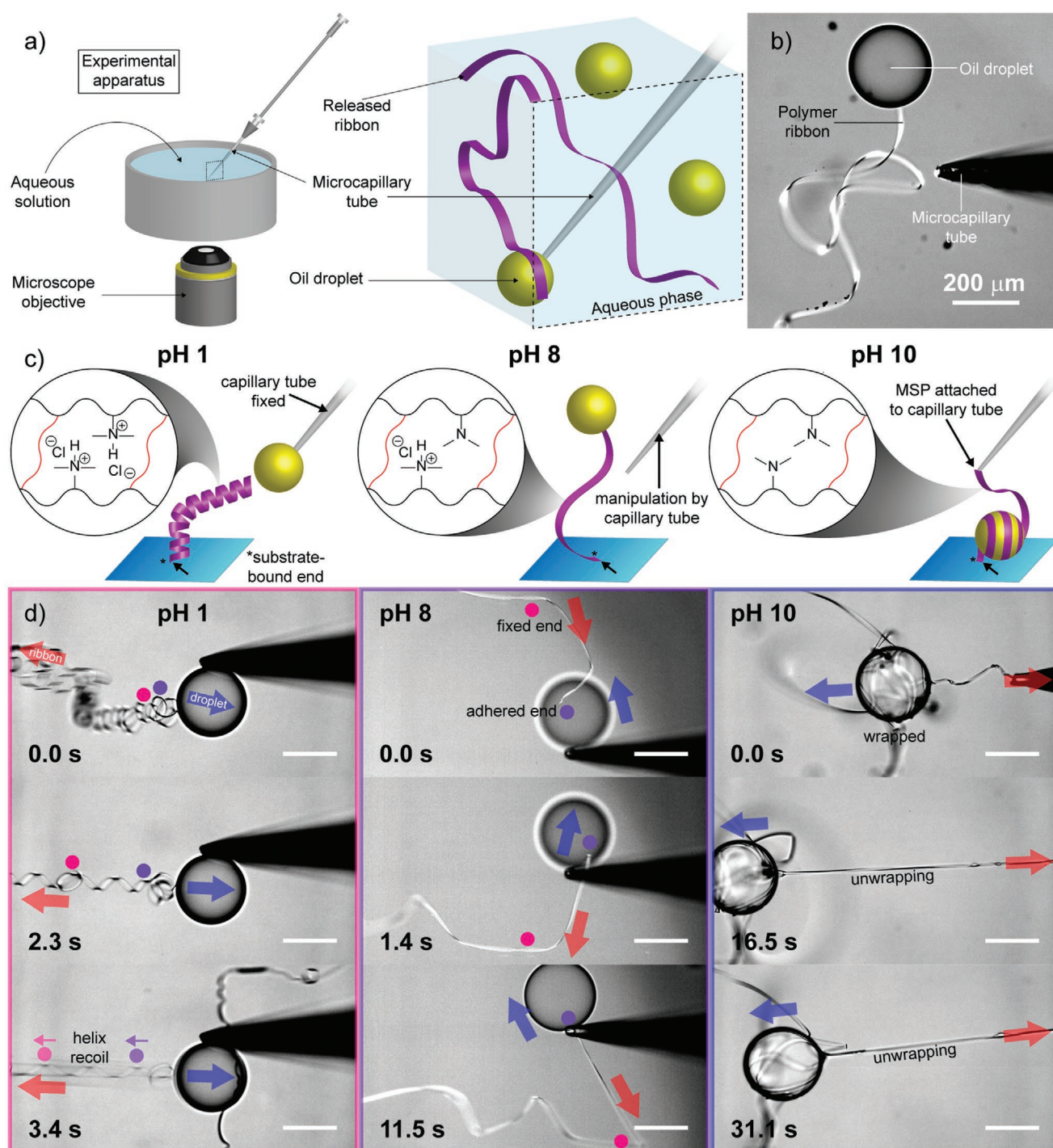


Figure 3. pH-Dependent MSP interfacial activity. a) Schematic of experimental apparatus: a submerged microcapillary tube was fixed to a micromanipulator and used to move MSPs and droplets through the solution; b) a frame of data featuring a flagellum-like MSP–droplet assembly; c) schematics of experimental design: at pH 1–6 (left), the droplet was fixed to the microcapillary tube and the MSP manipulated via translation of the substrate-adhered end; flagellum-like assemblies at pH 8 (center) and spooled assemblies (right) were manipulated by translation of the microcapillary tube and the substrate; d) sequential frames of MSP–droplet assemblies: (left, pH 1) weak, defect-mediated adhesion ($R < R_c$) that detached without macroscopic droplet deformation; (center, pH 8) flagellum-like assembly, and (right, pH 10) unwrapping an assembly where $R > R_c$. Red and blue arrows indicate relative motion of the droplet and the MSP fixed end. Scale bars 200 μm .

event is in stark contrast to the weak adhesion observed at lower pH and marks a transition from polycation (in acidic solution) to neutral polymer (in basic solution, Figure 3c inset

structures),^[17–20] while a pH-independent E and γ_{ow} implicate the polymer surface chemistry as the driving force for wrapping. Wrapping continued until terminated by one of several

mechanisms, including: i) onset of tension in the MSP, supplied by MSP adhesion to the substrate or microcapillary tip; ii) wrapping over an existing coil rather than available oil–water interface; or iii) consumption of the entire MSP length, to afford droplets with partial interfacial coverage. The wrapped droplets were subsequently unwrapped by withdrawing the MSP via the microcapillary tube (Video S5, Supporting Information). Figure 3c (right) schematically depicts the experimental design, while Figure 3d (right) displays frames from Video S5 in the Supporting Information that show clean unwinding of millimeters of an MSP while it maintains its structural integrity. The unwound MSPs then wrap the droplets again when tension is released and the wrapping/unwrapping cycles were repeated up to three times, without noticeable change, for a given MSP–droplet pair. Videos S6 and S7 in the Supporting Information demonstrate cases of partial rewrapping to create assemblies in which droplets are decorated with arms that extend into the continuous phase. Because wrapping stops when the MSP wraps upon itself, we infer that it is confined to the oil–water interface, and further, that the wrapping mechanism requires an uninterrupted 3-phase contact line at the wrapping edge.

From a mechanics standpoint, the MSP-wrapped droplets can be described by a thin, wide elastic beam confined to a curved oil–water interface.^[12] The components of a wrapped assembly of contact length L_c include bending ($U_b = EI_{yy}L_c/2R^2$) and adhesion ($U_\gamma = G_c w L_c$) energies, where E is the elastic modulus, I_{yy} is the second moment of inertia for axial wrapping, and G_c is critical strain energy release rate. When $R = R_c$, the wrapped and unwrapped states are energetically equivalent, affording $R_c = \sqrt{\frac{EI_{yy}}{2G_c w}} \sim \sqrt{\frac{Et^3}{G_c}}$. Thus, for $R < R_c$ we expect adhesion without wrapping, while for $R > R_c$ we expect spontaneous wrapping. This relationship was studied as a function of droplet radius R in the experiments shown in Figure 4. In Figure 4a (and Video S8, Supporting Information), the

microcapillary tip was positioned adjacent to an MSP and used to introduce a droplet, which grew until it contacted the MSP. Figure 4a (left) shows the system at $T = 0.4$ s, immediately before contact and wrapping. To the left, the MSP is fixed to the glass substrate, and to the right, it is unconstrained and free to wrap the droplet. At $T = 11$ s (Figure 4a, center), wrapping had nearly advanced one turn around the droplet, and the two wrapping edges passed by one another at $T = 1.4$ s. Approximating wrapping at the droplet circumference, each wrapping edge advanced at $\approx 350 \mu\text{m s}^{-1}$. After $T = 1.6$ s, the free MSP end was completely wrapped, while the slack between the droplet and the fixed end was pulled tight at $T = 7.6$ s (Figure 4a (right) and final frames of Video S8, Supporting Information).

To examine the impact of droplet size on wrapping, a ribbon-wrapped droplet with radius $R = 279 \mu\text{m}$ was pierced with the microcapillary tip and oil was continuously withdrawn to reduce the droplet radius (Figure 4b). At $R = 136 \mu\text{m}$, deflation stopped as applied force from the tip translated the droplet without piercing the surface. Despite the decrease in droplet dimensions, the droplet remained wrapped, with an appearance of more substantial interfacial coverage. Even in the presence of small droplets ($R \approx 6\text{--}30 \mu\text{m}$) prepared by emulsification via pipette, wrapping occurred such that MSPs effectively connected multiple droplets in series. For example, Figure 4c shows brightfield (left) and fluorescence (right) micrographs of an MSP ($w = 14 \mu\text{m}$) wrapped around 13 droplets as small as $R = 6 \mu\text{m}$ (droplet 7). For even smaller droplets, where $R < w$, we anticipate edgewise wrapping dictated by a lateral moment of inertia I_{xx} , which becomes infinitesimally small as MSP thickness tapers toward the edges (Figure S2, Supporting Information). Accordingly, we expect wrapping even in cases where the thickness t of the MSP central axis might otherwise prohibit lengthwise wrapping.

3.3. Evaluating MSP–Droplet Interactions

The energy landscape of elastoadhesive MSP wrapping, as described by G_c , in pH 10 buffer was probed by measuring the peel force, F_c , required to separate a wrapped MSP from the fluid–fluid interface. As described in Figure 5, these measurements utilized deflection of a single carbon fiber fixed to the end of a glass capillary tube that was dipped into a cyanoacrylate glue and cured to afford a cantilever with a hydrophobic, adhesive bead near the tip. A sample of MSPs was released into the buffer and PFD droplets were introduced by pipette. The cantilever was brought into contact with a PFD droplet via a micromanipulator, which adhered to the cured poly(cyanoacrylate) bead, then the cantilever-bound droplet was brought into contact with an MSP to initiate spontaneous wrapping (Figure 5a). For ribbons with one end fixed to the substrate, the MSP–droplet assembly was loaded by substrate translation, enabling direct quantification of the applied force by measuring cantilever deflection. The applied force increased linearly as the MSP stretched and the droplet deformed, as shown by the 3-phase contact line meniscus (Figure 5b), until unwrapping began at a critical force, F_c . Figure 5c,d and Video S9 in the Supporting Information follow the progress of an experiment with droplet radius $R = 88 \mu\text{m}$ through two

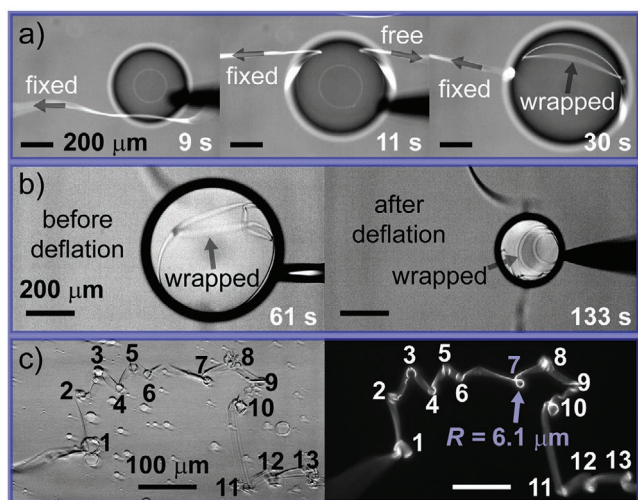


Figure 4. Critical elastoadhesive dimension R_c . a) Time points of a droplet inflated until (left) ribbon contact, (center) during wrapping, and (right) pulled tight against the substrate-adhered end; b) deflating a wrapped droplet to $R = 136 \mu\text{m}$ without any unwrapping; c) bright-field (left) and fluorescence (right) micrographs showing complete wrapping of droplets with diameter $\leq w = 14 \mu\text{m}$.

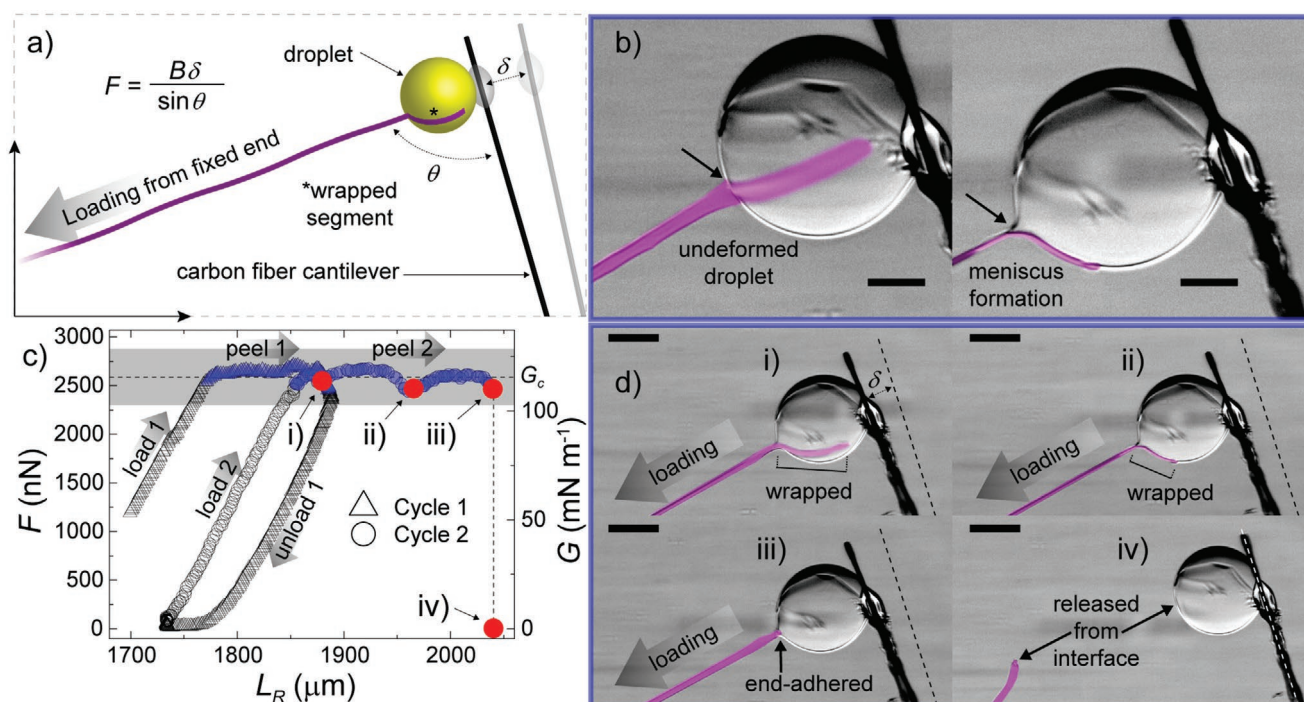


Figure 5. Measuring MSP peel force and G_c by cantilever deflection. a) Schematic of experimental apparatus: a droplet is adhered to the tip of a carbon fiber cantilever and partially wrapped by an MSP of suspended length L_R . The assembly is loaded by substrate translation to deflect the cantilever by distance δ ; b) false color micrographs of the system at low load (left, no MSP–droplet meniscus) and while peeling (right, meniscus formation); c) force– L_R plot of a typical experiment, in which the sample is cycled through two load–peel events, then peeled until rupture. Blue data points denote a visible meniscus and correspond to F_c and G_c ; cycle averages were combined to estimate peel force and G_c (dashed reference line with 95% confidence in gray); red points i–iv) correspond to frames di–iv); d) sequential frames from the same peel experiment. The MSP unwraps i,ii) from the droplet surface until only the end adheres iii), then is released from the interface iv). False coloration highlights the MSP. Scale bars b) 50 μm and d) 100 μm .

complete loading cycles, with an unloading step in between the cycles. Force (Figure 5c, left) and the applied energy release rate G (right, describing the energetics of separating the interface) are plotted as a function ribbon length (L_R) between its fixed end and the droplet contact point; on the second cycle, the MSP was unwrapped until detachment, when the ribbon contact length was exhausted. The loading curve exhibited two distinct regimes: linear loading, in which the force increased monotonically with the droplet-to-fixed-end MSP length (L_R), followed by a plateau of sustained peel at constant force (F_c , blue data points) of 2.6 μN . The initial loading slope was consistent from cycle to cycle, as was F_c . During unloading, the linear force– L_R curve matched the slope of the loading curve, suggesting elastic recovery in the stretched MSP. At $F = 0$, $\approx 50 \mu\text{m}$ of visible slack spontaneously rewrapped the droplet.

The second load cycle followed a similar stretch–plateau shape and loading continued until the MSP detached completely from the fluid–fluid interface and dispersed in water. Figure 5d corresponds to red data points in Figure 5c during the second loading cycle, with wrapped lengths of i) $\approx 140 \mu\text{m}$, ii) $\approx 85 \mu\text{m}$, and iii) $\approx 0 \mu\text{m}$ (end-adhered), iv) marking continuous unwrapping before detachment. The critical force for unwrapping is divided by w ($\approx 22 \mu\text{m}$, measured from video frames) to define a critical energy release rate, $G_c = 116 \text{ mN m}^{-1}$ for the copolymer 1-PFD interface in this solution (Figure 5c, reference line). For an MSP of thickness $t = 300 \text{ nm}$ and

modulus 200 MPa, the critical elastoadhesive dimension for axial wrapping (bending in I_{yy}) $R_c \approx 7 \mu\text{m}$. We note that R_c is readily decreased by reducing t , which is accomplished easily during ribbon fabrication by flow-coating.^[14–16]

4. Building Droplets with Arms by Photopatterning Ribbons

Photopatterned ribbons prepared from copolymer 2 were used to study additional MSP–droplet assembly modes. Here, composition, geometry, and interfacial chemistry are partitioned to afford MSBCPs, reflecting spatial control of R_c such that only predetermined segments wrap the droplets. Remarkably, only the hydrophobic segments (composed of PTBMA) were observed to wrap PFD droplets, while the hydrophilic PMAA segments exhibited no wrapping tendency, suggesting that for droplet radii $R \approx 60\text{--}150 \mu\text{m}$, $R_{c,PTBMA} < R < R_{c,PMAA}$.

Droplet–ribbon assemblies with appendages extended into the aqueous phase were realized by photochemically programmed wrapping with specific MSP segments, enabled by controlling domain size via the photomask and the number of segments via laser engraving. Figure 6a describes MSBCP assembly consisting of 1 segment each of deprotected PMAA and protected PTBMA (block length 500 μm) with a PFD droplet ($R \approx 110 \mu\text{m}$) in water; false color (frame 1) highlights the

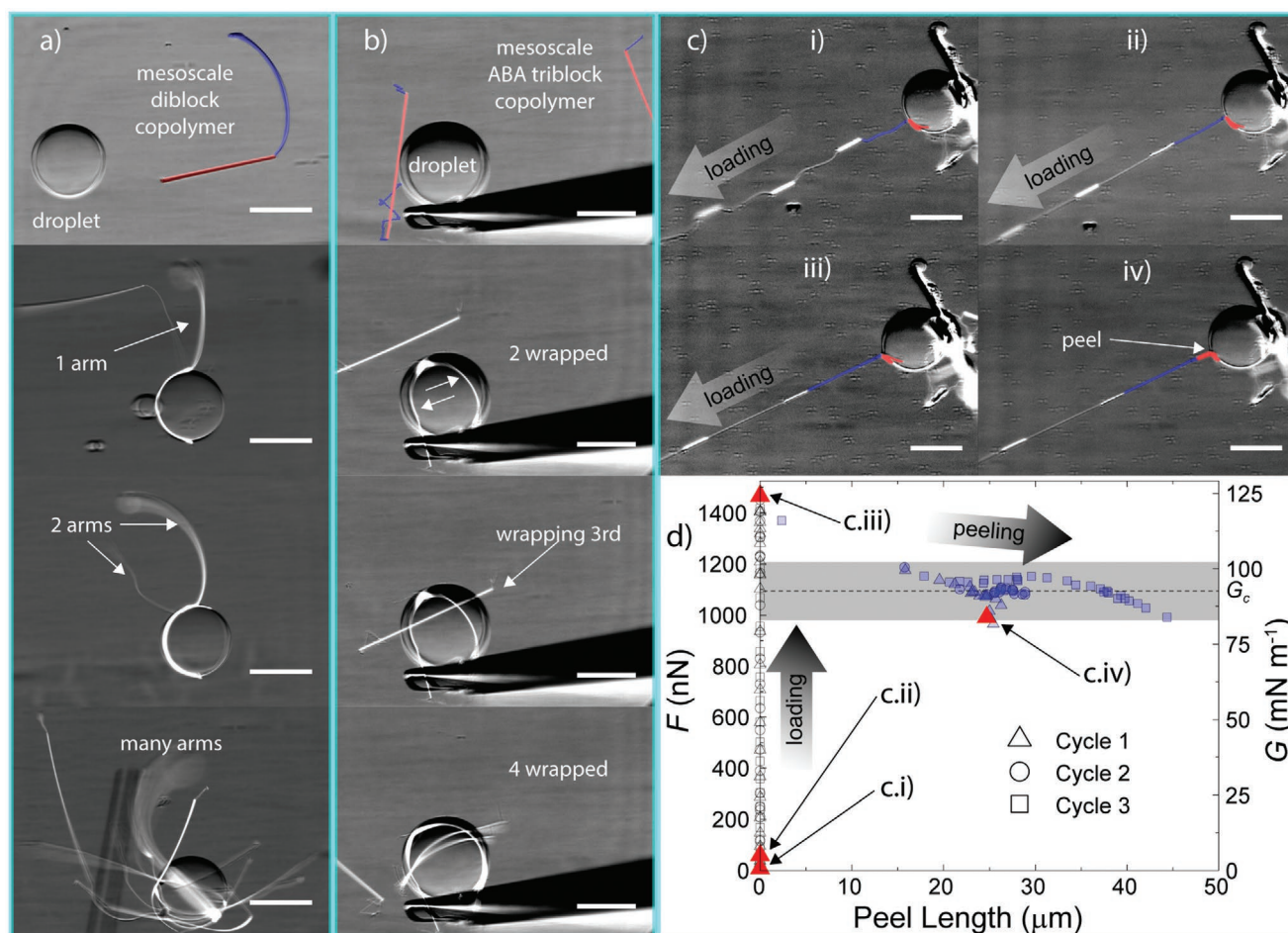


Figure 6. Droplet–MSBCP assemblies. Assembly of droplets with a) “diblock” MSP in reverse osmosis water and b) “triblock” MSP in $500 \times 10^{-3} \text{ M}$ NaOH: a) The droplet and ribbon (false color, top, red = hydrophobic; blue = hydrophilic) are brought into contact; selective wrapping affords a droplet with an arm (frame 2); subsequent ribbon addition allows installation of 2 (frame 3) or many (frame 4) arms; b) assembly of MSBCPs (false color, top) enables shorter arms driven to coil in basic solution; c) cantilever deflection of an MSBCP with one wrapped segment to quantify peel force; d) plot of measured force F (left axis) and G (right axis) as a function of peel length of an adhered MSBCP subjected to three load-peel cycles. Red data points correspond to frames ci–iv); blue data points denote peeling (F_c, G_c); cycle averages were combined to calculate peel force and G_c (dashed reference line with 95% confidence in gray). Scale bars a,b) $200 \mu\text{m}$ and c) $100 \mu\text{m}$.

distinct blocks. Upon contact, the hydrophobic PTBMA block wrapped the droplet until reaching the junction point, affording a droplet with a single PMAA arm (Figure 6a frame 2 and Video S10, Supporting Information). We note that this mechanism of pendent arm formation is distinct from the pH-dependent methods used to prepare extended structures from MSPs of copolymer 1. Subsequent contact with additional MSBCPs decorated the droplet with a second arm (Figure 6a frame 3 and Video S11, Supporting Information), and up to ten arms using mixed assembly modes spanning i) selective wrapping, ii) weak adhesion of PMAA domains, and iii) end-on adhesion (Figure 6a, frame 4 and Video S12, Supporting Information).

Related structures were obtained by using PMAA–PTBMA–PMAA triblock MSBCPs, decorating droplets with two pendent arms per wrapping step. Figure 6b and Video S13 in the Supporting Information describe the use of a droplet of $R \approx 150 \mu\text{m}$ to pick up the ribbons, which are resting on a substrate in $500 \times 10^{-3} \text{ M}$ NaOH solution. The central PTBMA block was

$500 \mu\text{m}$ in length, with shorter blocks of approximate length $\approx 250 \mu\text{m}$ in PMAA domains. Here, the crosslinked PMAA domains coiled tightly into helices of $R \approx 3.5 \mu\text{m}$ upon release into solution, suggesting swelling-dependent coiling consistent with MSBCP architectures reported previously.^[21] In contrast, the hydrophobic PTBMA domains remained straight until contact with a droplet initiated bending. False coloration in frame 1 of Figure 6b highlights the coiled helical end blocks (blue) and rigid core block (red) of an MSBCP immediately before droplet contact and wrapping. Frames 2–4 represent subsequent frames from Video S13 in the Supporting Information as the droplet is used to remove additional ribbons from the substrate surface by selective wrapping. Wrapping of additional MSBCPs advances until overlap with those present already. Notably, this does not stop the wrapping events as observed for longer, substrate-adhered PDMAEMA MSPs at pH 10; rather, wrapping was seen to continue by pushing the previously wrapped segments across the interface ($T \approx 7.2\text{--}14.0 \text{ s}$).

4.1. Quantifying MSBCP Segment–Droplet Interactions

The peel force of PTBMA segments at the PFD–water interface was measured by cantilever deflection. MSBCPs of alternating 50 μm blocks were prepared with one end fixed to the substrate surface, released into pH 10 buffer solution, then brought into contact with a cantilever-bound droplet ($R \approx 60 \mu\text{m}$). Measurements were made by translating the substrate with the adhered MSBCP end, pulling on the droplet, and measuring the deflection of the attached cantilever. The system was taken through two complete load–unload cycles, then loaded until detaching completely from the droplet surface (Video S14, Supporting Information). Figure 6c represents successive frames from the first cycle in this experiment, including: i) an unstretched MSBCP; ii) loading until slack is removed; iii) hydrogel segment stretching and droplet deformation; and iv) peeling (false coloration highlights the hydrophobic (red) and hydrogel (blue) domains). The measured force is shown in Figure 6d, revealing continued loading, without peeling, until a critical load of ≈ 1460 nN is reached, when the system transitions to a partially peeled state. For each cycle, the average peel force F_c is taken from blue data points, with a typical value of ≈ 1100 nN. Four data points are highlighted as red triangles, corresponding to Figure 6c–iv, revealing the load at each stage of the measurement. ii) The initially curved PMAA domains (i) straighten under relatively little force (≈ 60 nN, ii), then stretch from ≈ 115 microns (low load) to ≈ 160 microns as the load increases to 1470 nN (iii). The load decreases to 990 nN immediately after peel (iv) and the gel domains elastically recover during unloading, consistent with expectations for a crosslinked hydrogel. Notably, this strain concentration within hydrophilic PMAA gel domains enabled direct measurement of gel modulus $E_{\text{PMAA}} \approx 2$ MPa by tracking the segmental junction points between PMAA and PTBMA domains. By contrast, we estimated E_{PTBMA} on the order of 1 GPa based on the known $T_{g,\text{PTBMA}}$ of 116–118 $^{\circ}\text{C}$,^[27,28] a 500-fold modulus difference achieved simply by photopattern-mediated swelling.

The measured F_c represents the energy per unit length required to unwrap ribbons from the curved oil–water interface. Having demonstrated that capillary interactions dominate bending stiffness at the selected length scales in PDMAEMA MSPs of modulus 200 MPa ($G_c = 116 \text{ mN m}^{-1}$, $R_c = 7 \mu\text{m}$ for $t = 300$ nm), we applied the same assumption when measuring MSBCP segments. Dividing F_c by segment width $w = 12 \mu\text{m}$ (measured via optical profilometry before release), $G_c \approx 93 \text{ mN m}^{-1}$ (Figure 6d reference line) was calculated. Thus, for a hydrophobic MSBCP segment with $t = 300$ nm, $R_c = 17 \mu\text{m}$, while smaller values are readily accessible by printing thinner MSBCPs. Notably, G_c for MSPs ($\approx 116 \text{ mN m}^{-1}$) and hydrophobic MSBCP segments ($\approx 93 \text{ mN m}^{-1}$) are comparable to the oil–water interfacial tension $\gamma_{\text{ow}} = 51 \text{ mN m}^{-1}$ measured by pendent drop tensiometry; moreover, MSBCP adhesion at the oil–water interface ceased upon the addition of a polymer surfactant, further connecting the high energy oil–water and polymer–water interfaces to adhesion and wrapping phenomena. Together, our measurements of G_c and γ_{ow} combined with loss of adhesion in the presence of surfactant implicate the oil–water and polymer–water interfaces as a primary driving force for large scale assembly of mesoscale ribbons. Notably, despite a modulus approximately three orders of magnitude

smaller than the glassy PTBMA domains, the PMAA gel segments adhered to droplets without wrapping, suggesting an equally dramatic change in G_c from segment to segment. Thus, MSBCPs possess partitioned domains of alternating physical and mechanical properties, including a 500-fold difference in elastic modulus, and dramatic differences in G_c and R_c that enable selective wrapping and assembly upon contact with oil-in-water droplets.

5. Conclusion

In summary, we described the use of compliant, surface-active, mesoscale polymer ribbons to build assemblies with liquid droplets via the fluid–fluid interface of the droplets. We adapted a model of cylindrical filaments at droplet surfaces to describe the uniquely flat geometry of MSPs in contact with an oil-in-water droplet, spanning wrapping and nonwrapping interaction modes as a function of a modulus-, geometry-, and G_c -dependent elasto-adhesive dimension R_c . Using photocrosslinked MSPs derived from copolymer 1, we mapped pH-dependent interactions, ranging from i) weak adhesion ($R_c > R$) from pH 1–8, including flagellum-like architectures formed by selective adhesion at the MSP tip, to ii) spontaneous wrapping at pH 10, producing spools amenable to unwrapping, rewinding, and addition of pendent arms. We employed the “built-in” photoacid generators in copolymer 2 to effect chemically amplified deprotection and crosslinking, using a photomask to partition distinct properties into segments along the ribbon length. Within the resulting MSBCP structures, hydrophobic PTBMA segments were observed to selectively wrap oil-in-water droplets independent of pH, enabling the construction of droplets with 1, 2, or many arms extended into solution. Moreover, quantification of G_c and thickness-dependent R_c confirms that the bending compliance and strong interfacial activity of MSPs and MSBCPs affords elasto-adhesive lengths of microns or smaller. Together, these pH-, light-, and spatially programmable structures provide a robust platform to transform simple soft materials building blocks and interaction modes into sophisticated meso-to-macroscale bio-inspired assemblies.

Supporting Information

Supporting Information is available from the Wiley Online Library or from the author.

Acknowledgements

This project was supported by the Department of Energy, Office of Basic Energy Sciences, Division of Materials Science and Engineering under award number DE-SC0008876 and a National Defense Science and Engineering Graduate (NDSEG) Fellowship awarded to D.M.B. A.L., L.P., and D.M.B. acknowledge funding from the ERC Consolidator Grant PaDyFlow (Grant Agreement no. 682367).

Conflict of Interest

The authors declare no conflict of interest.

Keywords

bioinspired architectures, capillary assemblies, mesoscale, photopatterning, responsive materials

Received: March 25, 2020

Revised: May 17, 2020

Published online:

-
- [1] F. Vollrath, D. T. Edmonds, *Nature* **1989**, 340, 305.
[2] H. Elettro, S. Neukirch, A. Antkowiak, F. Vollrath, *Science Nat.* **2015**, 102, 41.
[3] H. Elettro, S. Neukirch, F. Vollrath, A. Antkowiak, *Proc. Natl. Acad. Sci. USA* **2016**, 113, 6143.
[4] S. M. King, W. S. Sale, *Mol. Biol. Cell* **2018**, 29, 698.
[5] G. L. Takei, M. Fujinoki, K. Yoshida, S. Ishijima, *MHR: Basic Sci. Reprod. Med.* **2017**, 23, 817.
[6] D. M. Woolley, G. G. Vernon, *J. Exp. Biol.* **2001**, 204, 1333.
[7] T. C. Adhyapak, H. Stark, *Soft Matter* **2016**, 12, 5621.
[8] M. Jabbarzadeh, H. C. Fu, *Phys. Rev. E* **2018**, 97, 012402.
[9] T. Rehman, L. Yin, M. B. Latif, J. Chen, K. Wang, Y. Geng, X. Huang, M. Abaidullah, H. Guo, P. Ouyang, *Microb. Pathog.* **2019**, 137, 103748.
[10] V. M. Suchanek, M. Esteban-López, R. Colin, O. Besharova, K. Fritz, V. Sourjik, *Mol. Microbiol.* **2019**, 113, 728.
[11] P. Horváth, T. Kato, T. Miyata, K. Namba, *Biomolecules* **2019**, 9, 462.
[12] R. D. Schulman, A. Porat, K. Charlesworth, A. Fortais, T. Salez, E. Raphaël, K. Dalnoki-Veress, *Soft Matter* **2017**, 13, 720.
[13] B. Roman, J. Bico, *J. Phys.: Condens. Matter* **2010**, 22, 493101.
[14] H. S. Kim, C. H. Lee, P. K. Sudeep, T. Emrick, A. J. Crosby, *Adv. Mater.* **2010**, 22, 4600.
[15] J. T. Pham, J. Lawrence, D. Y. Lee, G. M. Grason, T. Emrick, A. J. Crosby, *Adv. Mater.* **2013**, 25, 6703.
[16] D. Y. Lee, J. T. Pham, J. Lawrence, C. H. Lee, C. Parkos, T. Emrick, A. J. Crosby, *Adv. Mater.* **2013**, 25, 1248.
[17] C.-A. Ghiorghita, F. Bucatariu, E. S. Dragan, *Int. J. Biol. Macromol.* **2018**, 107, 1584.
[18] P. Van De Wetering, E. E. Moret, N. M. E. Schuurmans-Nieuwenb roek, M. J. Van Steenberg, W. E. Hennink, *Bioconjugate Chem.* **1999**, 10, 589.
[19] Z. Guo, X. Chen, J. Xin, D. Wu, J. Li, C. Xu, *Macromolecules* **2010**, 43, 9087.
[20] S. B. Abbott, W. M. de Vos, L. L. E. Mears, M. Skoda, R. Dalglish, S. Edmondson, R. M. Richardson, S. W. Prescott, *Macromolecules* **2016**, 49, 4349.
[21] D. M. Barber, A. J. Crosby, T. Emrick, *Adv. Mater.* **2018**, 30, 1706118.
[22] J. T. Pham, J. Lawrence, G. M. Grason, T. Emrick, A. J. Crosby, *Phys. Chem. Chem. Phys.* **2014**, 16, 10261.
[23] J. T. Pham, A. Morozov, A. J. Crosby, A. Lindner, O. du Roure, *Phys. Rev. E* **2015**, 92, 011004.
[24] D. Fried, S. F. Borzillary, S. M. McCormack, R. E. Glens, J. D. B. Featherstone, W. D. Seka, *Proc. SPIE* **1994**, 2128, 319.
[25] D. G. Waugh, J. Lawrence, C. D. Walton, R. B. Zakaria, *Opt. Laser Technol.* **2010**, 42, 347.
[26] S. Prakash, S. Kumar, *Precis. Eng.* **2017**, 49, 220.
[27] J. M. Yu, P. Dubois, R. Jérôme, *Macromolecules* **1996**, 29, 8362.
[28] S. Watanabe, T. Ohmura, K. Ueno, M. Murata, Y. Masuda, *Polym. J.* **2008**, 40, 743.

Supporting Information

Programmed Wrapping and Assembly of Droplets with Mesoscale Polymers

Dylan M. Barber, Zhefei Yang, Lucas Prévost, Olivia du Roure, Anke Lindner, Todd Emrick, and Alfred J. Crosby**

Methods

Chemicals. Methacryloyl chloride, rhodamine B, 4-dimethylaminopyridine (DMAP), N,N'-dicyclohexylcarbodiimide (DCC), 2-hydroxyethyl methacrylate (HEMA), triphenylsulfonium chloride (TPSCI), fluorescein-*O*-methacrylate (FOMA), toluene, perfluorodecalin (PFD), buffer solutions, basic alumina, lithium chloride (LiCl), poly(sodium 4-styrenesulfonate) (PSS, MW 70 kDa, Aldrich), 4-hydroxybenzophenone (4HBP, TCI America), methanol (MeOH), dimethylformamide (DMF), hexanes, isopropanol (IPA, Fisher Scientific), sodium 4-vinylbenzenesulfonate (Na4VBS, Alfa Aesar), and silica gel (Sorbent Technologies) were used as received without further purification. Triethylamine (TEA, Aldrich) and dichloromethane (DCM, Fisher Scientific) were dried over calcium hydride and distilled. 2.1% aqueous ammonium hydroxide solution was prepared by diluting 28 wt% ammonium hydroxide solution (Aldrich) into stirring RO water. 100 mM HCl solution was prepared by dropwise addition of 12.1 N HCl (Fisher Scientific) to a beaker of stirring RO water. 2-(Dimethylamino)ethyl methacrylate (DMAEMA), *tert*-butyl methacrylate (TBMA), and glycidyl methacrylate (GMA, Aldrich) were purified by passage through a plug of basic alumina. 2,2'-Azobisisobutyronitrile (AIBN, Aldrich) was recrystallized from MeOH. Tetrahydrofuran (THF, Fisher Scientific) was dried over sodium benzophenone ketyl, then distilled. N₂ gas was dried by passing through Drierite (W.A. Hammond Drierite Company).

Instrumentation. ^1H NMR (500 MHz) spectroscopic data was collected using a Bruker Ascend TM500 spectrometer with a Prodigy cryoprobe. Copolymer molecular weight was estimated against PMMA standards by gel permeation chromatography (GPC), eluting in a mobile phase of 0.01 M LiCl in DMF at 1 mL min^{-1} flow rate (Agilent 1260 Infinity isocratic pump) through a $50 \times 7.5\text{ mm}$ PL gel mixed guard column, a $300 \times 7.5\text{ mm}$ PL gel $5\text{ }\mu\text{m}$ mixed C column, and a $300 \times 7.5\text{ mm}$ PL gel $5\text{ }\mu\text{m}$ mixed D column at $50\text{ }^\circ\text{C}$. Solute was detected using an Agilent 1260 Infinity refractive index detector. UV-ozone (UVO) surface treatment was conducted with a Jelight Company, Inc. Model 342 UVO-Cleaner®. Laser engraving was carried out using a Universal Laser Systems VLS3.50 laser engraver equipped with a 30W CO_2 ($10.6\text{ }\mu\text{m}$) laser with 0.005“ z-axis offset, 2% power, 40% speed, and 1000 ppi pulse rate. Flow-coating was carried out using a SmarAct, Inc SLC-1780s linear actuator. 365 nm UV-irradiation was performed on a Newport 97435 lamp housing with a Newport 69910 power supply and Newport 6285 Mercury arc lamp or a Suss Micro Tec MA6 Mask Aligner. An OAI Instruments 1000 Watt DUV Exposure System equipped with a DUV 1000 lamp (Advanced Radiation Corporation) was used for all 254 nm UV irradiation. Reactive Ion Etch (RIE) experiments employed an Advanced Vacuum Vision 320 MkII Reactive Ion Etch System with 50 sccm $\text{O}_2(\text{g})$ flow rate, 50 mTorr chamber pressure, 100 W RF power, and 13.56 MHz RF frequency. Microscopy was conducted on an Axio Observer 7 Materials microscope equipped with a Hamamatsu C11440 Orca-Flash4.0 Digital Camera, 2 Eppendorf TransferMan 4r micromanipulators, an X-Cite 120LED (Excelitas Technologies), and Zeiss filter set 38 HE (green fluorescence, copolymer **1**) or 45 (red fluorescence, copolymer **2**). Fourier-transform Infrared (FT-IR) data were collected in attenuated total reflectance mode using a PerkinElmer Spectrum One FT-IR Spectrometer equipped with a Universal ATR Sampling Accessory. Optical profilometry data was collected using a Zygo NewView 7300 Optical Surface Profiler (Amherst) or a Veeco Instruments Wyko NT9100 (Paris). Microcapillary tubes were prepared by drawing glass capillary tubes (ChemGlass, 1.0-1.1 mm

O.D.) in a P-1000 Flaming/BrownTM Micropipette Puller System (Sutter Instrument) and the melted ends were opened using an MF-830 Microforge (Narishige International).

Synthesis of benzophenone methacrylate (BPMA) monomer. BPMA synthesis was adapted from a reported procedure.^[1] In brief, a 500 mL round-bottom flask with a stir bar was flame-dried and purged with dry nitrogen, then 4-hydroxybenzophenone (5.1 g, 25.7 mmol, 1 equivalent) was added against a positive flow of dry N₂(g). The flask was sealed with a septum. Dry TEA (8 mL, 57.4 mmol, 2 equivalents) and dry DCM (75 mL) were added by syringe against positive N₂(g) pressure; the solution was stirred until homogeneous then cooled to 0 °C. Methacryloyl chloride (4.8 mL, 49.6 mmol, 1.93 equivalents) in dry DCM (25 mL) was added dropwise while stirring. The solution was allowed to return to 20 °C where it was stirred for 15.5 h, then concentrated under vacuum, redissolved in ether, and washed with 2.1% aqueous ammonium hydroxide solution. The product was purified by column chromatography (basic alumina as stationary phase, 90:10 hexanes:ethyl acetate as eluent) to afford the desired product as white crystals (4.0 g, 58% yield). ¹H NMR (500 MHz, CDCl₃, δ) 7.82-7.77 (m, 2H, aromatic), 7.75-7.70 (d, 2H, aromatic, J = 7.02 Hz), 7.54-7.49 (t, 1H, aromatic, J = 7.43 Hz), 7.45-7.38 (t, 2H, aromatic, J = 7.68 Hz), 7.21-7.15 (m, 2H, aromatic), 6.34-6.29 (s, 1H, vinyl), 5.75-5.71 (t, 1H, vinyl J = 1.39 Hz), 2.03-1.99 (s, 3H, CCH₃).

Synthesis of rhodamine B methacrylate (RBMA) monomer. The RBMA synthesis was also adapted from a reported procedure.^[2,3] In brief, a 2-neck, 250 mL round-bottom flask with stir bar was flame-dried and purged with dry nitrogen gas, then rhodamine B (10 g, 20.9 mmol, 1 equivalent), DMAP (150 mg, 1.23 mmol, 0.06 equivalents), and DCC (5.2 g, 25.2 mmol, 1.21 equivalents) were added against positive flow of dry N₂(g). The flask was sealed with a septum, then dry DCM (105 mL) and HEMA (3.1 mL, 25 mmol, 1.20 equivalents) were

added by syringe. The solution was stirred at 20 °C for 25 h, then concentrated under reduced pressure and purified by column chromatography (silica gel stationary phase, 90:10

DCM:MeOH eluent) and dried under high vacuum to afford a dark purple powder (6.15 g, 50% yield). ¹H NMR (500 MHz, CDCl₃, δ) 8.33-8.26 (d, 1H, aromatic, J = 7.90 Hz), 7.88-7.81 (t, 1H, aromatic, J = 7.45 Hz), 7.79-7.72 (t, 1H, J = 7.68 Hz), 7.35-7.30 (d, 1H, J = 7.50 Hz), 7.10-7.03 (d, 2H, J = 9.45), 6.97-6.90 (dd, 2H, J₁ = 9.45 Hz, J₂ = 2.25 Hz), 6.82-6.77 (d, 2H, J = 2.20 Hz), 6.05-5.98 (s, 1H, vinyl), 5.58-5.52 (s, 1H, vinyl), 4.33-4.28 (t, OCH₂CH₂O, J = 4.95 Hz), 4.21-4.16 (t, 2H OCH₂CH₂O, J = 4.68 Hz), 3.70-3.63 (8H, q, NCH₂CH₃, J = 7.20 Hz), 1.90-1.85 (s, 3H, methacrylate CCH₃), 1.37-1.29 (t, 12H, NCH₂CH₃, J = 7.05 Hz)

Synthesis of triphenylsulfonium 4-vinylbenzenesulfonate (TPS-4-VBS) monomer. TPS-4-VBS was synthesized by adapting a procedure from a literature report.^[4] In brief, 94% TPSCl (1.06 g, 3.33 mmol, 1 equivalent) and 90% Na₄VBS (767 mg, 3.35 mmol, 1 equivalent) were combined and shaken with 3.3 mL RO water in a 20 mL scintillation vial to afford a brown emulsion. The brown organic phase was removed, and the aqueous phase extracted with 6 x 1 mL DCM. The combined organic phase was diluted to 12 mL, washed with 4 x 1 mL RO water, filtered to remove residual brown solid, concentrated, then diluted with hexanes (1 mL) to induce crystallization. Residual solvent was removed under reduced pressure to afford the desired product as white crystals (1.24 g, 83 % yield). ¹H NMR: (500 MHz, CDCl₃, δ): 7.86-7.81 (d, 2H, 4-vinylbenzenesulfonate aromatic, J = 8.23 Hz), 7.76-7.72 (d, 6H, S⁺(C₆H₅)₃, J = 7.51 Hz), 7.70-7.66 (t, 3H, S⁺(C₆H₅)₃, J = 7.42 Hz), 7.64-7.59 (t, 6H, S⁺(C₆H₅)₃, J = 7.62 Hz), 7.30-7.27 (d, 2H, 4-vinylbenzenesulfonate aromatic, J = 8.20 Hz), 6.70-6.60 (dd, 1H, 4-vinylbenzenesulfonate vinyl, J = 10.89, 17.61 Hz), 5.74-5.65 (d, 1H, 4-vinylbenzenesulfonate vinyl, J = 17.61 Hz), 5.24-5.17 (d, 1H, 4-vinylbenzenesulfonate vinyl, J = 10.97 Hz).

Synthesis of copolymer 1. DMAEMA (3.2 mL, 19 mmol, 197 equivalents), BPMA (289 mg, 1.1 mmol, 11 equivalents), FOMA (83 mg, 0.21 mmol, 2 equivalents), and AIBN (15.8 mg, 0.10 mmol, 1 equivalent) were dissolved in a mixture of THF (9 mL) and DMF (1 mL) in a 20 mL scintillation vial containing a stir bar. The vial was sealed with a rubber septum, then degassed with dry N₂(g) for 30 minutes while stirring at 20 °C. After removing needles, the septum was covered with a piece of electrical tape and the vial transferred to an aluminum heating block, where the mixture was stirred for 22 hours at 60 °C. The reaction mixture was then precipitated three times in stirring hexanes at 20 °C and dried under vacuum at 60 °C for 18 h to afford the desired product (1.22 g, 36 % yield). ¹H NMR: (500.13 MHz, CDCl₃, δ): 8.07-7.97 (br s, aromatic), 7.89-7.70 (br m, 4H, BPMA aromatic), 7.63-7.54 (br m, 1H, BPMA aromatic), 7.52-7.41 (br m, 2H, BPMA aromatic), 7.30-7.16 (br m, 2H, BPMA aromatic), 6.85-6.42 (br m, FOMA aromatic), 4.25-3.85 (br m, 2H, DMAEMA OCH₂CH₂N), 2.70-2.45 (br m, 2H, DMAEMA OCH₂CH₂N), 2.44-2.11 (br m, 6H, N(CH₃)₂), 2.11-0.73 (br m, aliphatic backbone, CH₂CCH₃). ¹³C NMR: (125.76 MHz, CDCl₃, δ): 195.85-195.12 (s, 1C, BPMA ketone), 178.63-173.61 (br m, ester carbonyl), 154.45-153.66 (m, 1C, BPMA aromatic), 137.86-137.22 (m, 1C, BPMA aromatic), 135.43-134.83 (m, 1C, BPMA aromatic), 132.81-132.43 (m, 1C, BPMA aromatic), 131.98-131.46 (m, 2C, BPMA aromatic), 130.26-129.85 (s, 2C, BPMA aromatic), 128.69-128.28 (s, 2C, BPMA aromatic), 121.57-121.00 (m, 2C, BPMA aromatic), 63.77-62.55 (m, 1C, DMAEMA OCH₂), 57.63-56.98 (m, 1C, DMAEMA CH₂N), 55.40-51.52 (br m, 1C, backbone methylene), 46.30-45.47 (s, 2C, DMAEMA N(CH₃)₂), 45.47-44.49 (br m, 1C, backbone quaternary), 19.42-15.94 (br m, 1C, backbone CH₃). GPC: (DMF with 10 mM LiBr, PMMA standards): M_n = 38 kDa, M_w = 104 kDa, Đ = 2.70.

Synthesis of copolymer 2. TBMA (2.3 mL, 14 mmol, 89 equivalents), TPS-4-VBS (200 mg, 0.45 mmol, 2.8 equivalents), GMA (39 μ L, 0.29 mmol, 1.9 equivalents), RBMA (20 mg, 34 μ mol, 0.2 equivalents), and AIBN (26 mg, 0.16 mmol, 1 equivalent) were dissolved in DMF (5 mL) in a 20 mL scintillation vial equipped with a stir bar, then degassed by bubbling for 30 minutes with dry N₂(g) while stirring at 20 °C. After degassing, the septum was covered with a piece of electrical tape and the vial was transferred to an aluminum block, where the mixture was stirred at 80 °C for 22 h. The reaction was stopped by cooling to -20 °C, then purified by precipitating into 65:35 water:MeOH, re-dissolving in THF, precipitating three times in stirring hexanes, and finally drying under high vacuum at 20 °C for 18 h to yield the desired product. (1.03 g, 45%). ¹H NMR: (500.13 MHz, CDCl₃, δ): 7.88-7.80 (d, 6H, S⁺(C₆H₅)₃, J = 7.69 Hz), 7.79-7.71 (br s, 2H, 4-vinylbenzene aromatic), 7.74-7.69 (t, 3H, S⁺(C₆H₅)₃, J = 7.39 Hz), 7.69-7.61 (t, 6H, S⁺(C₆H₅)₃, J = 7.64 Hz), 7.10-6.93 (br s, 2H, 4-vinylbenzene aromatic), 4.37-4.03 (br m, overlapping (1H, GMA COOCH $\underline{\underline{H}}$)^[5] and (4H, RBMA OCH₂CH₂O), 3.97-3.78 (br s, 1H, GMA COOCH $\underline{\underline{H}}$), ^[5] 3.70-3.57 (br m, 8H, RBMA (N(CH $\underline{\underline{2}}$ CH₃)₂)₂), 3.27-3.13 (br s, 1H, GMA COOCH₂CH $\underline{\underline{O}}$ CH $\underline{\underline{H}}$), ^[5] 2.91-0.14 (br m, aliphatic backbone), 2.86-2.77 (br s, 1H, GMA COOCH₂CH $\underline{\underline{O}}$ CH $\underline{\underline{H}}$), ^[5] 2.69-2.57 (br s, 1H, GMA COOCH₂CH $\underline{\underline{O}}$ CH $\underline{\underline{H}}$), ^[5] 1.50-1.35 (br m, 9H, TBMA C(CH₃)₃). GPC: (DMF with 10 mM LiBr, PMMA standards): M_n = 21 kDa, M_w = 46 kDa, Đ = 2.16.

Characterization of copolymer photoactivity. Copolymer **1** was dissolved to 10 mg mL⁻¹ in MeOH, then drop-cast onto a glass slide heated to 60 °C to afford a polymer film on the slide surface. The film was irradiated (3000 mJ cm⁻², λ = 365 nm) then placed in a beaker containing a 100 mM HCl solution. Upon contact with the aqueous solution, the colorless film became yellow then colorless as pendent fluorescein moieties were protonated. The film swelled and delaminated from the glass substrate surface within ~2 minutes of contact with

the acid solution and remained fully intact in solution for at least 25 hours after delamination. Copolymer **2** was dissolved to 100 mg mL⁻¹ in toluene, and drop-cast (5 μL) onto glass slides and allowed to dry without heating. Then, the films were characterized by ATR IR i) without further processing, ii) after heating to 150 °C for 60 s; and iii) after irradiating at $\lambda = 254$ nm for a dose of 900 mJ cm⁻², then heating to 150 °C for 60 s. The change in thickness resulting from cleavage of *t*-butyl esters during photopatterning was quantified by optical profilometry after irradiation ($\lambda = 254$ nm) at doses of 12, 25, 50, 100, 200, 450, and 900 mJ cm⁻² and heating to 150 °C for 60 s.

Substrate preparation, flow-coating, release, and droplet experiments. Glass slides (24 x 40 x 0.17 mm³, Fisher Scientific) were cleaned by sonication for 15 minutes each in soapy water, reverse osmosis water, and isopropanol, followed by 15 minutes of surface treatment by UV-ozone to render the surface hydrophilic. Immediately afterwards, a solution of PSS in RO water (20 mg mL⁻¹) was applied by spin-coating onto the hydrophilized glass surface (10 s at 500 RPM, then 40 s at 2000 RPM). Samples were partitioned into 2 groups: 1) for experiments with substrate-adhered MS(BC)Ps (Figure 3d, 4, 5, 6c, and S1), PSS-coated slides were laser engraved (2% power, 40% speed, 1000 PPI) at 2-4 mm intervals to afford stripes of bare glass to which MS(BC)Ps would adhere upon flow-coating and release; 2) for experiments with free-floating ribbons (MSDCPs and MSTCPs in Figure 6a-b), the substrate was not laser-engraved. Then, the substrates were fixed to a translating stage, and a razor blade bolted to a stationary mount was lowered to a height of ~ 200 μm above the substrate surface. A polymer-in-toluene solution (5-15 μL of 16 mg mL⁻¹ **1** or 4 μL of 4 mg mL⁻¹ **2**) was injected between the blade and substrate to afford a capillary bridge 24-36 mm in length. The substrate was translated in 1 mm intervals at 3 mm s⁻¹, with a 1.1-1.5 s delay between steps to deposit the MSPs, which were irradiated at i) 3300 mJ cm⁻² at $\lambda = 365$ nm (copolymer

1) to afford a crosslinked PDMAEMA network, or ii) 200-695 mJ cm⁻² at $\lambda = 254$ nm through a photomask, then heated to 150 °C for 60 s (copolymer 2), to afford an MSBCP with alternating segments of hydrophobic PTBMA and hydrophilic PMAA. MS(BC)Ps were then cut into 1-4 mm segments *via* laser engraver and subjected to reactive ion etching with O₂ plasma for 30 s to remove any residual inter-MS(BC)P polymer film. To release MS(BC)Ps, an aqueous solution was prepared by filling a polystyrene Petri dish (Fisher Scientific, 60 mm diameter, 15 mm depth) with 10 mL of pH buffer solution or RO water. Then, a coated substrate was gently floated on top of the solution and quickly submerged using tweezers. Upon submersion, the underlying PSS layer dissolved to release the MS(BC)Ps. In the case of samples in which the PSS layer was cut before flow-coating, MS(BC)Ps were adhered at one end to the glass surface but were otherwise free to twist, bend, and stretch; for those not subjected to laser cuts, MS(BC)P movement was completely unrestricted. Drawn glass microcapillary tubes were inserted into a Capillary Holder 4 (Eppendorf), which was mounted in a TransferMan 4r micromanipulator (Eppendorf) and connected to a syringe loaded with PFD for injection and withdrawal of the oil phase. Thus equipped, the microcapillary tip was lowered into the aqueous solution to enable hand-controlled manipulation of MS(BC)Ps and droplets. Droplets were introduced by either i) emulsifying a mixture of PFD and the chosen aqueous continuous phase in a 7 mL scintillation vial by ~5 cycles of rapid injection and withdrawal of both liquids (~1 mL aqueous and ~100 μ L PFD) through a Pasteur pipette, then quickly injecting the mixture into the Petri dish with released MS(BC)Ps, or ii) directly injecting oil *via* the microcapillary tube.

Force measurements using a carbon fiber cantilever. An individual carbon fiber was cut to ~5 mm length, then glued to the end of a capillary tube using Loctite superglue. The cantilever was cut to ~1 mm in length, and the tip dipped into a drop of Loctite superglue then withdrawn to leave a liquid bead attached near the fiber tip. This was cured for a minimum of

12 h, then the capillary tube with affixed cantilever was inserted into a holder, clamped into the hand-controlled micromanipulator, rotated until parallel with the focal plane of the microscope objective, and deflected by bringing it into contact with a glass slide to verify that tip displacement was due exclusively to cantilever deflection. Then, the capillary tube was rotated until the cantilever orientation was out of the objective focal plane and lowered into an aqueous solution reservoir containing MS(BC)Ps and droplets. The superglue bead at the cantilever tip was brought into contact with i) a PFD droplet, then ii) an MS(BC)P that spontaneously wrapped the droplet. The substrate (with attached MS(BC)P end) was translated to load the ribbon-droplet-cantilever assembly and deflect the cantilever, with video data collected at 30 fps. Individual frames were saved in .tif format. Videos were converted to .avi file format using ImageJ image processing software, and the pixel (x,y) positions of key features, including cantilever tip, droplet-cantilever attachment point, MS(BC)P fixed end, and MSBCP inter-segment boundaries were tracked frame-by-frame using Tracker Video Analysis and Modeling Tool. The ribbon vector $\vec{R} = \langle R_x, R_y, 0 \rangle$ was calculated by subtracting the point of ribbon-droplet contact (for MSPs) or an arbitrary inter-segment junction point (for MSBCPs) from the point of cantilever-droplet contact, with assumed 0 z-component because the entire visible ribbon length was within the focal plane. The x- and y-components of the cantilever vector $\vec{C} = \langle C_x, C_y, C_z \rangle$ were calculated by subtracting the position of the cantilever tip from the superglue bead center point, while the z-component was calculated using the Pythagorean theorem $C_x^2 + C_y^2 + C_z^2 = L_{tip}^2$, where L_{tip} is the actual length between bead and tip, measured when the cantilever was parallel to the objective focal plane. The applied force angle θ was then calculated using the dot product $\vec{R} \cdot \vec{C} = |\vec{R}| |\vec{C}| \cos \theta$. Cantilever displacement was measured from the point of cantilever-droplet contact, with 0 deflection defined by the average (x,y) position before MS(BC)P attachment, after MS(BC)P detachment, and/or during periods of slack in the MS(BC)P. The y position was plotted as a function of x position for

every frame, and a line of best fit crossing the origin was calculated. The data was then rotated about the origin *via* the rotation matrix with $-\phi$ the angle between the best-fit line and the x axis to afford

$$\begin{bmatrix} \cos \phi & -\sin \phi \\ \sin \phi & \cos \phi \end{bmatrix} \begin{bmatrix} x_0 \\ y_0 \end{bmatrix} = \begin{bmatrix} \delta \\ y_\phi \end{bmatrix},$$

where δ describes cantilever deflection in the equation

$$F = \frac{3 \delta E I}{L^3 \sin \theta}$$

with cantilever modulus $E = 230$ GPa, moment of inertia for circular cross-section $I = \frac{\pi c^4}{4}$, radius $r_c = 3.5 \mu\text{m}$,¹⁵ and cantilever length L measured as the distance between the cantilever fixed end and the center of droplet attachment (approximated as a point load). In this way, force was calculated for every video frame. Suspended ribbon length (L_R , MSPs) was calculated as the distance between the MSP fixed end and the point of ribbon-droplet attachment. Peel length (MSBCPs) was calculated as the distance between the end of the wrapped segment and the point of segment-droplet contact. Moduli of deprotected PMAA MSBCP gel domains were measured from cycle 1 of the same video used for peel force measurements (Video S14) by tracking the (x,y) pixel locations of the segment junction points between PTBMA and PMAA domains; uniaxial swelling ratio was determined by dividing the PMAA segment length (defined as the measured length when cantilever deflection began) by the initial mask feature size ($50 \mu\text{m}$), while cross-sectional area was determined by multiplying the cross-sectional area (estimated by optical profilometry) by the square of the uniaxial swelling ratio.

Modulus estimate of copolymer 1

i. Experimental design. The Young's modulus, E , for copolymer **1** MSPs was estimated by examining the deformation of coiled helical MSPs under viscous flow, inspired by a general

strategy reported previously.^[7] For each selected pH (1, 4, 6, 8, and 10) helical MSPs were subjected to a series of flow steps at increasing flow rate. The helical axial elongation, H , was measured as a function of flow velocity (**Figure S4**). We characterized the obtained velocity-extension curves by the slope of the linear regime. The measured slope was combined with an estimated drag coefficient $\xi_{//}$ and several geometrical parameters in a theoretical model to estimate MSP bending modulus B that was then used with measured values of t and w to estimate E .^[7,8]

ii. Apparatus. Helical extension measurements were conducted in PDMS channels (Sylgard 184, DOW Corning) printed using standard soft lithography methods. The channels were coated with a 10% bovine serum albumin (Sigma Aldrich) solution for 15 minutes in order to avoid adsorption on the channel walls. Glass capillaries were similarly coated with a 2% bovine serum albumin solution for 15 minutes. MSPs were released in a pool of the selected buffer solution and displaced using an open glass capillary controlled by a micro-manipulator. The glass capillary was connected to a syringe to catch MSPs by withdrawing and released by expelling liquid. MSPs were captured at one end, then placed in a microfluidic channel connected to the pool. A flow rate Q of the buffer solution was applied to the channel and the resultant helix deformation was tracked by measuring H via fluorescence microscopy. The flow velocity V adopted a parabolic distribution in the channel, but as typical helix radii are small compared to the channel size, we estimate a locally uniform flow near the helix. For a given helical MSP, V was taken as the average of the flow field velocity over all the positions occupied by the MSP. The flow field in the channel was computed from the channel dimensions using a derivation from White,^[9] and the position of the MSP was measured from captured micrographs.

iii. Axial elongation measurements. As seen in Figure S4a, the H does not reach an equilibrium state over the duration of one flow step (usually 30 seconds to 1 minute), verified by immersing helical MSPs in flow for over 1 hour. Moreover, we observed that the helical

MSP do not recover the initial length after a flow step (Figure S4a) and that the resting length evolves considerably over the duration of a multi-cycle experiment (Figure S4c). These observations are likely due to creeping of the material under stress induced by the viscous forces. In order to quantify the elastic contribution that is controlled by E , we implemented an analysis that decouples the viscous and elastic components of axial extension.

During a single flow step, the deformation has two components: the elastic deformation of the material and the creeping-induced deformation. Assuming constant pulling force and friction, the elastic component is expressed under the form $H_{elastic} (1 - \exp(-t/\tau))$, where $H_{elastic}$ corresponds to the amplitude of the elastic deformation and τ to the timescale of the helix recovery. We also add a phenomenological term, μt , where μ denotes the susceptibility of the material to creeping. The extension curve $H(t)$ is hence fitted by the following semi-phenomenological function: $H(t) - H_0 = H_{elastic} (1 - \exp(-t/\tau)) + \mu t$. H_0 is the resting axial length, which is measured and thus not a fitting parameter. Experimentally we find the timescale τ (typically under 1 s) to be significantly smaller than the typical creeping time H_0/μ (typically above 100 s). This allows us to clearly separate the elastic regime and the creeping regime. As seen in Figure S4b, agreement with experimental data is good. With this fitting method we recover the elastic extension $\Delta H = H_{elastic} - H_0$ as a function of the flow velocity V . The elastic extension, ΔH , as a function of V for 6 different helical MSPs at the same pH is plotted in **Figure S5a**. To characterize the flow-extension curve, we used the heuristic expression proposed by Jawed *et al.*,^[10] based on the simulation of flexible helices in uniform flow: $\Delta H = \Delta H_{lim} (1 - \exp(-V/V_c))$. Here, the parameter ΔH_{lim} is the maximum elongation, and the parameter V_c is the characteristic flow speed separating the linear and non-linear regime. As seen in Figure S5a, this expression provides a good description of the helical MSP extension, particularly at low speed. The discrepancies at high speed are likely

due to creeping effects. Using this fitting method, we estimated the slope in the small deformation limit as $\Delta H_{lim} / V_c$.

iv. Modeling. For a flexible helix immersed in a uniform flow of velocity V , the helix elastic axial extension ΔH can be expressed^[7,8] in the small deformation limit as $\Delta H = R^2 L^2 (\xi_{||} / B) V$ where $\xi_{||}$ is the drag coefficient along the tangential direction, B is the bending modulus, R is the helix radius, and L is the total length along the curvilinear abscissa. The MSP cross section is a very shallow triangle with width $w \gg$ thickness t . The general form for B of a triangular cross section is $B = (1/36) E w t^3$. $\xi_{||}$ was estimated by approximating the cross section as a rectangle of negligible thickness, giving $\xi_{||} = 4\pi\eta / (2 \ln(8L/w) - 1)$,^[11] where η is the fluid viscosity. The Young's modulus was calculated as

$$E = \frac{144 p}{2 \ln\left(\frac{8L}{w} - 1\right)} \eta \frac{R^2 L^2}{w t^3} \left(\frac{V_c}{\Delta H_{lim}} \right).$$

v. MSP width and thickness measurements. The t and w in the above expressions correspond to the immersed state of the material. w (typically $\sim 20 \mu\text{m}$) was measured optically *in situ*. However, t (typically 100-400 nm) is below the optical resolution limit and was determined by applying a pH-dependent swelling ratio^[12,13] to the dry thickness, measured by optical profilometry.

vi. Results. The measured values of E are presented in Figure S5b. Overall, E for copolymer **1** in the immersed state is approximately constant at 100-350 MPa across the pH 1-10 range.

Supplementary Figures

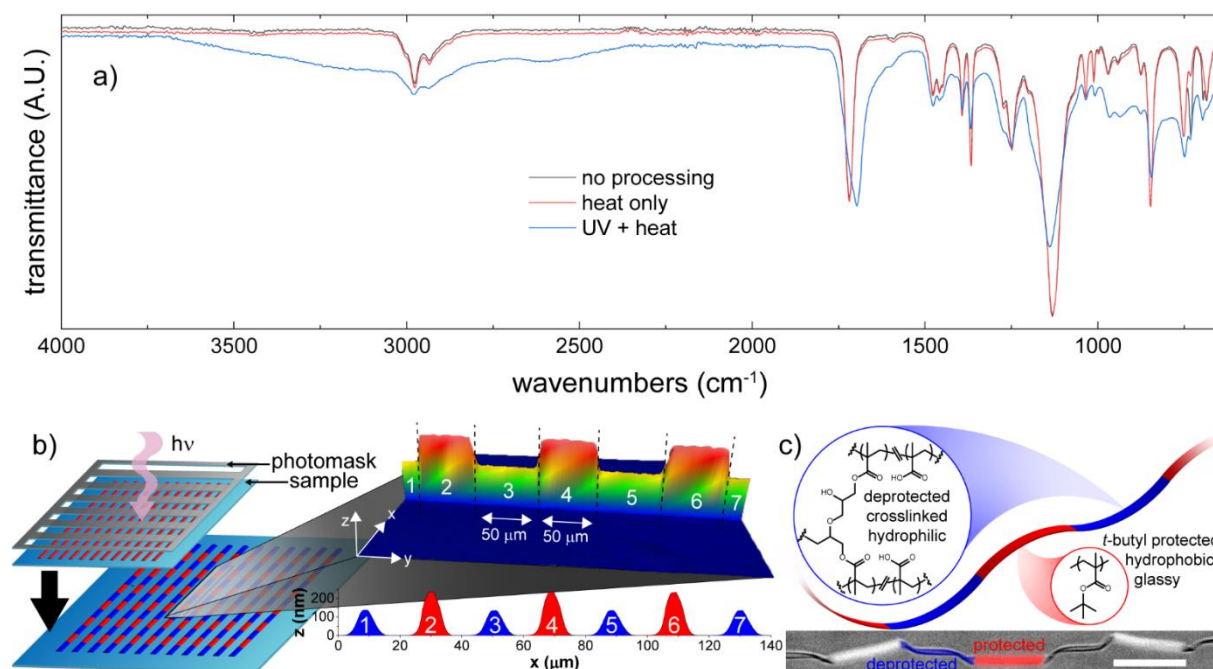


Figure S1. Copolymer 2 photoactivity and MSBCP characterization. a) Drop-cast thick films of copolymer **2** were characterized by ATR IR spectroscopy before any treatment (black line), after heating to 150 °C for 60 s (red line), and after irradiating at a dose of 900 mJ cm⁻² ($\lambda = 254$ nm) and then heating to 150 °C for 60 s, revealing carboxylate evolution after irradiation and heating. MSBCPs are prepared by b) irradiating an array of copolymer **2** ribbons through a photomask to afford segments of alternating thickness, shown in 3D (top) and 2D cross-section slices (bottom); c) irradiated domains (blue) are composed of crosslinked poly(methacrylic acid), while masked domains (red) are composed of PTBMA; the false color micrograph represents a typical MSBCP of 50 μ m segment length in RO water, with alternating twisted, compliant hydrogel and rigid, brightly fluorescent, hydrophobic domains; scale bar 50 μ m.

Photoactivity of copolymer **2** was verified by ATR IR spectroscopy in drop-cast films (**Figure S1a**). A 100 mg mL⁻¹ solution of **2** in toluene was drop-cast in 5 μ L drops onto glass slides, then characterized i) without further treatment (black spectrum), ii) after heating to 150 °C for 60 s (red spectrum), and iii) after irradiating with $\lambda = 254$ nm for a dose of 900 mJ cm⁻², then heating to 150 °C for 60 s (blue spectrum). The carbonyl peaks were normalized to 20 % absorbance at λ_{max} , then converted to % transmittance and offset by 1%. The untreated and heat only samples were identical, with no carboxylic acid -OH signal and a maximum carbonyl signal of 1719 cm⁻¹, while a carboxylic acid stretch (3700-2400 cm⁻¹) evolved and the carbonyl maximum shifted to 1697 cm⁻¹ after irradiation and heating, confirming successful deprotection of *t*-butyl esters. Moreover, ribbons were observed to undergo a change in thickness upon irradiation and heating. In Figure S1b-c, irradiated domains are

schematically depicted in blue, while masked domains are shown in red. Optical profilometry (Figure S1b) reveals a thickness loss of up to 0.45x in irradiated segments (labelled 1, 3, 5, and 7) at UV doses of 200 mJ cm⁻² or larger, while masked domains (labelled 2,4, and 6) retained the original ribbon thickness, consistent with other chemically amplified ribbon and photoresist compositions.^[2,14,15] The 3D optical profile data (Figure S1b top) reveals the structure of a typical MSBCP patterned in alternating segments of 50 μm, while the 2D cross section data of each segment (Figure S1b bottom) shows the uniformity in thickness in masked versus irradiated domains. Figure S1c describes a released MSBCP, with schematic structure and inset structure (top) and a micrograph of a typical MSBCP in RO water, including false coloration of a compliant, photobleached, and deprotected hydrogel segment (blue), and a stiff, brightly fluorescent masked segment (red). Crosslinking of pendent epoxides after irradiation and heating was verified by analysis of deprotected domains, which begin to bear load at length ~93 μm in pH 10 buffer solution, an approximate 86% uniaxial strain due to swelling from the original patterned length of 50 μm. This suggests a water volume fraction $\phi_{H_2O} \sim 0.85$ while cyclically bearing the loads required to unwrap an adjacent hydrophobic segment from a PFD droplet.

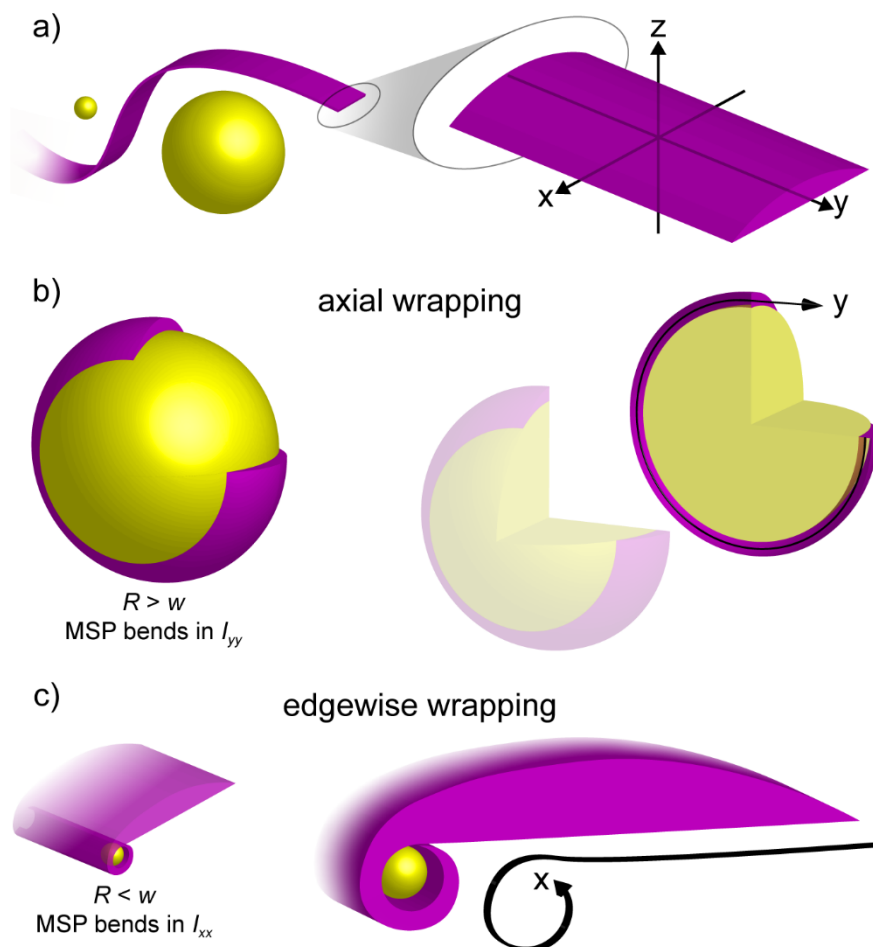


Figure S2. Axial and edgewise wrapping. The MSP wrapping axis is expected to depend on the relative size of R and w : a) an MSP with a small (left, $R < w$) and large (right $R > w$) droplet. The magnified segment shows the directions of the y - and x -axis relative to the MSP long axis; b) axial wrapping where $R > w$: bending occurs along the y -axis as described by I_{yy} ; c) edgewise wrapping where $R < w$: bending is anticipated along the x -axis as described by I_{xx} , which decreases with t toward the tapered edges of the MSP.

Figure S2 describes the R - and w -dependent wrapping modes accessible through moments of inertia I_{xx} and I_{yy} . In the case where $R > w$, MSP wrapping depends on the thickness t at the MSP center, and wrapping is observed to proceed along the long ribbon axis, defined as y in Figure S2a. This axial wrapping phenomenon is shown schematically in Figure S2b; because $R > w$, the entire width of the MSP is in contact with the droplet and wrapping proceeds by consuming MSP length and is dependent on bending moment I_{yy} . In contrast, we anticipate edgewise wrapping in the case of a droplet with radius $R < w$ (Figure S2c) In this case, MSP bending stiffness becomes vanishingly small toward the MSP edges as t decreases, so droplet contact is predicted to elicit wrapping *via* a rolled-in edge.

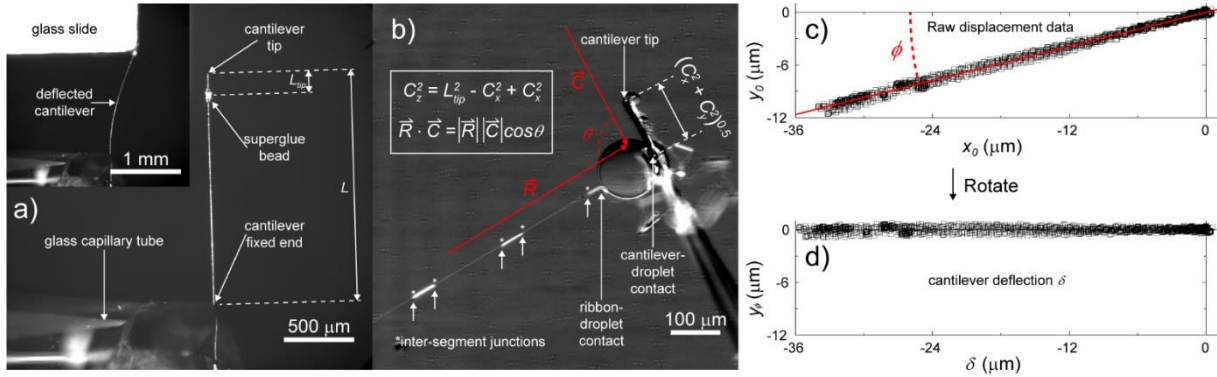


Figure S3. Cantilever video data acquisition and frame-by-frame processing to determine θ and δ . a) The total length L and bead-to-tip length L_{tip} were imaged and measured, then the cantilever was deflected (inset) using a glass slide on a translating stage; b) video data of an MSBCP-droplet-cantilever system under applied load. (x, y) pixel locations of key features, including cantilever tip, cantilever-droplet contact point, ribbon-droplet contact point, and MSBCP inter-segment junctions were tracked frame-by-frame. The force angle θ was calculated *via* the dot product of the cantilever and ribbon vectors \vec{R} and \vec{C} in each frame, while cantilever deflection δ was determined from the raw (x, y) displacement data of the cantilever-droplet contact point by rotating about the origin to lie on the x -axis.

Before measurement of cantilever deflection, a test deflection was carried out at low magnification (**Figure S3a**) by bringing into contact with a glass slide on a translating stage (**Figure S3a** inset). Frames from this experiment were used to ensure that the cantilever fixed end remained stationary during deflection and to measure the full cantilever length L and the distance from the superglue bead to the cantilever tip L_{tip} . Accurate force measurement required quantification of cantilever deflection δ and applied force angle θ . The ribbon vector \vec{R} (**Figure S3b**) was assumed to have negligible z -component because the ribbon was in the focal plane of the lens, while the x - and y - components were tracked frame-by-frame (see **Methods**). The cantilever vector \vec{C} had a significant z -component that was determined using $C_x^2 + C_y^2 + C_z^2 = L_{tip}^2$, where $C_y^2 + C_z^2$ was determined visually frame by frame by tracking the bead center and cantilever tip, and L_{tip} was a constant as measured in **Figure S3a**. θ was calculated *via* the dot product of \vec{R} and \vec{C} (see **Methods**). Similarly, cantilever deflection was determined by tracking the (x, y) pixel location of the point of cantilever-droplet contact (in the case of **Figure 6**, **Figure S3**, and **Video S14**, this was taken to be the center of the superglue bead) against an origin defined by the average position in the absence of load. This raw data was converted to microns (**Figure S3c** top), then rotated about the origin such that the line of best

fit was $y = 0$; δ was defined for each frame as the rotated x displacement data (Figure S3c bottom).

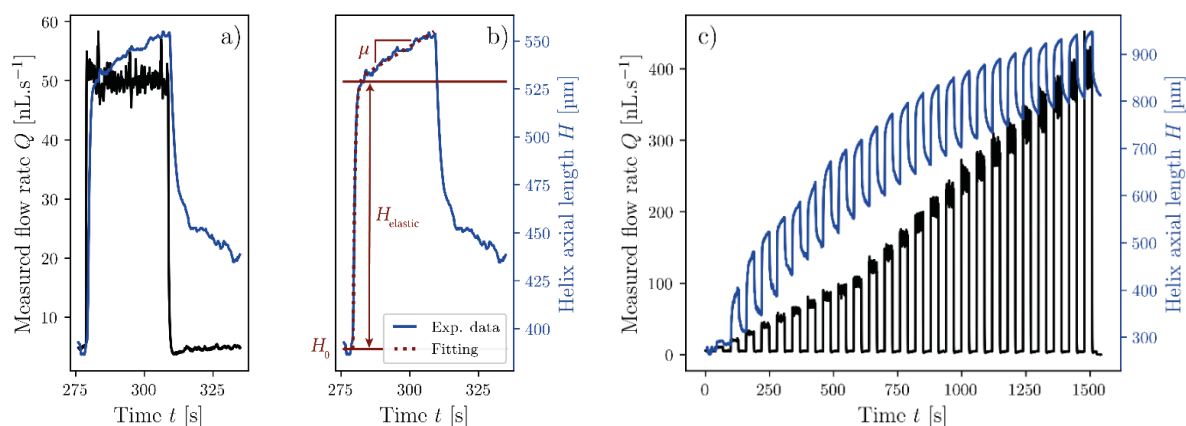


Figure S4. Helix extension under axial flow. a) Typical applied flow step and following relaxation: the measured buffer solution flow rate (black) and measured helical axial length (blue) are plotted as a function of time. The flow is not completely stopped during the relaxation phase, keeping instead a vanishing value $Q = 2$ nL/s. The syringe pump responds more quickly when changing the flow rate than when starting the flow. The viscosity of the buffer solution is always 1.0 mPa.s. For all experiments, the channel width is 250 μm and height is 650 μm . b) Fitting of the previous helix extension curve using a semi phenomenological function (3 fitting parameters). c) Typical full flow cycle applied; Figure S4a is extracted from this curve.

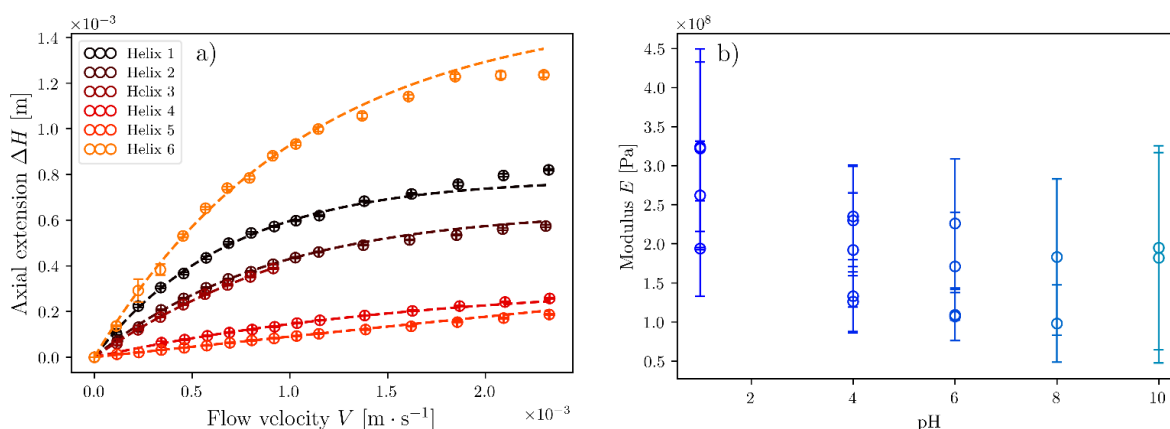


Figure S5. a) Flow-extension curves for 6 different copolymer **1** helical MSPs immersed in a pH 4 buffer solution with heuristic fitting. b) Measured values for the Young's modulus E across the 1-10 pH range.

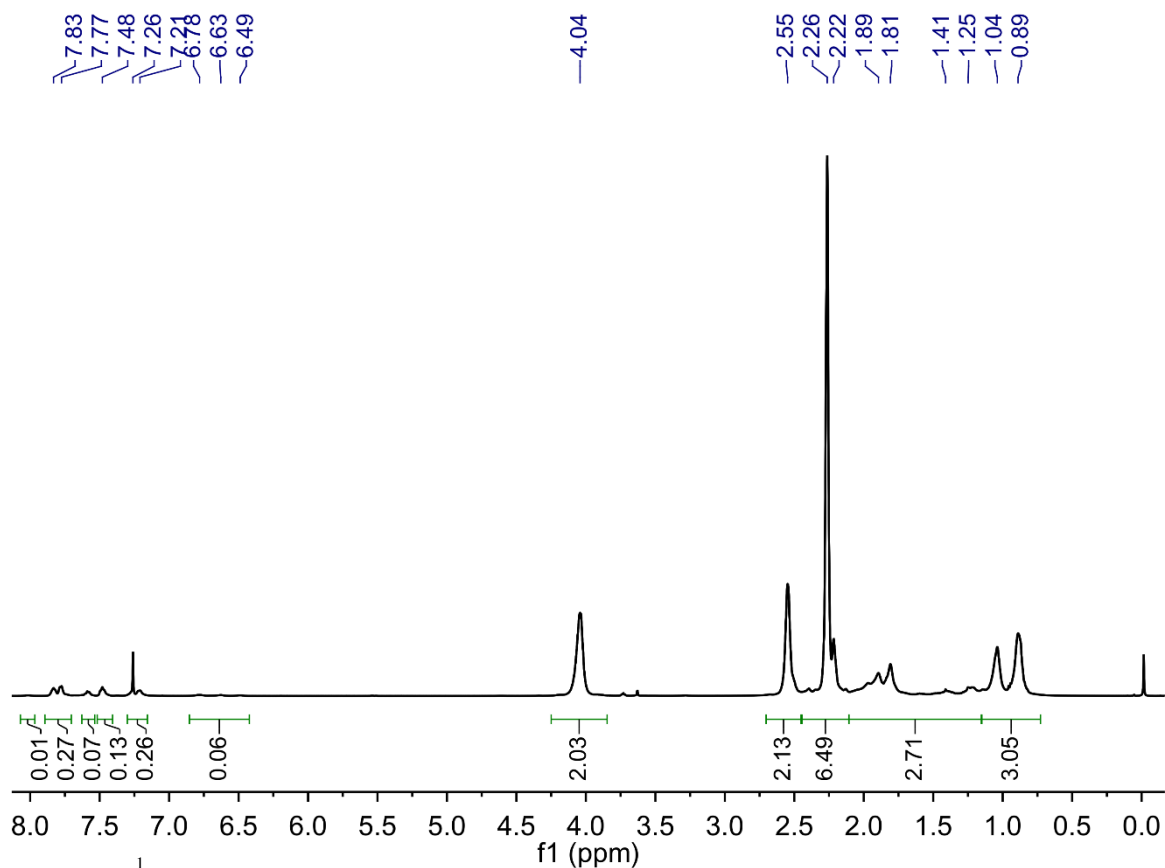


Figure S6. ¹H NMR spectrum of copolymer **1**

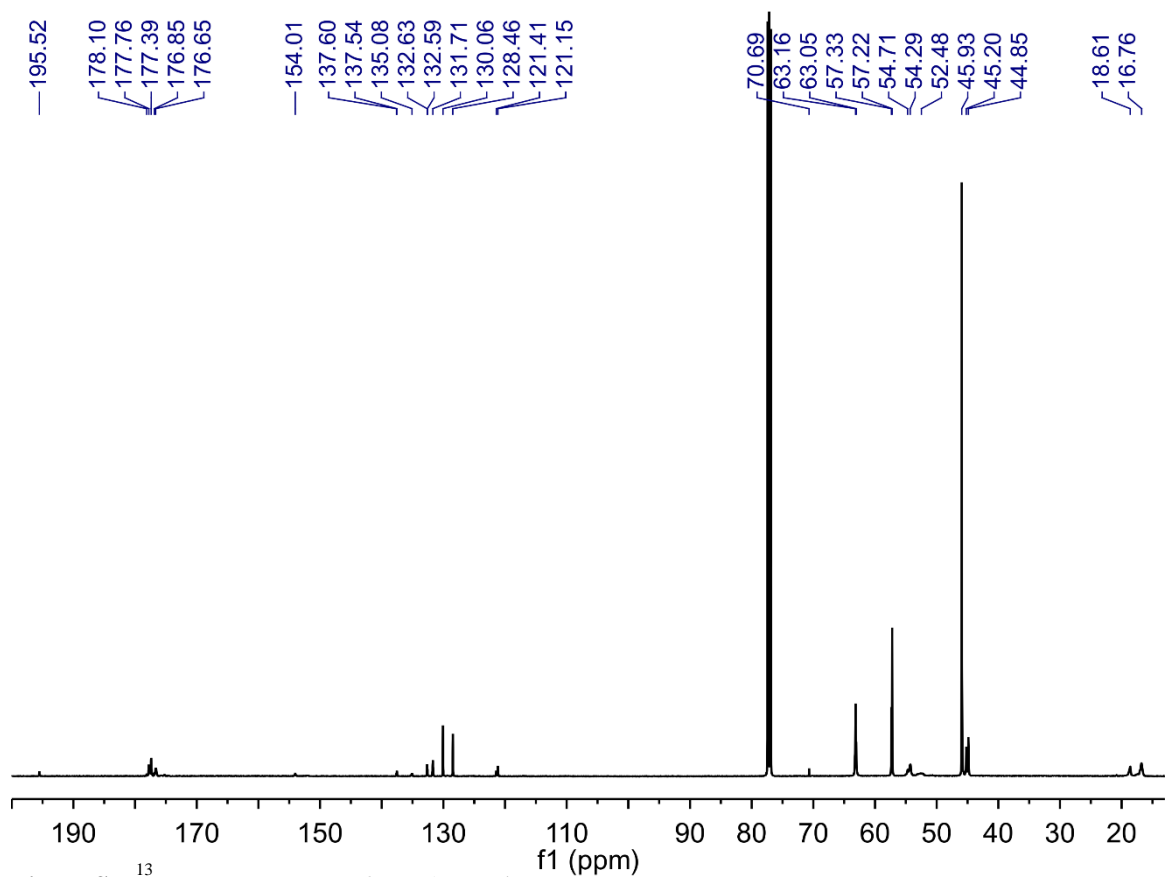


Figure S7. ¹³C NMR spectrum of copolymer **1**

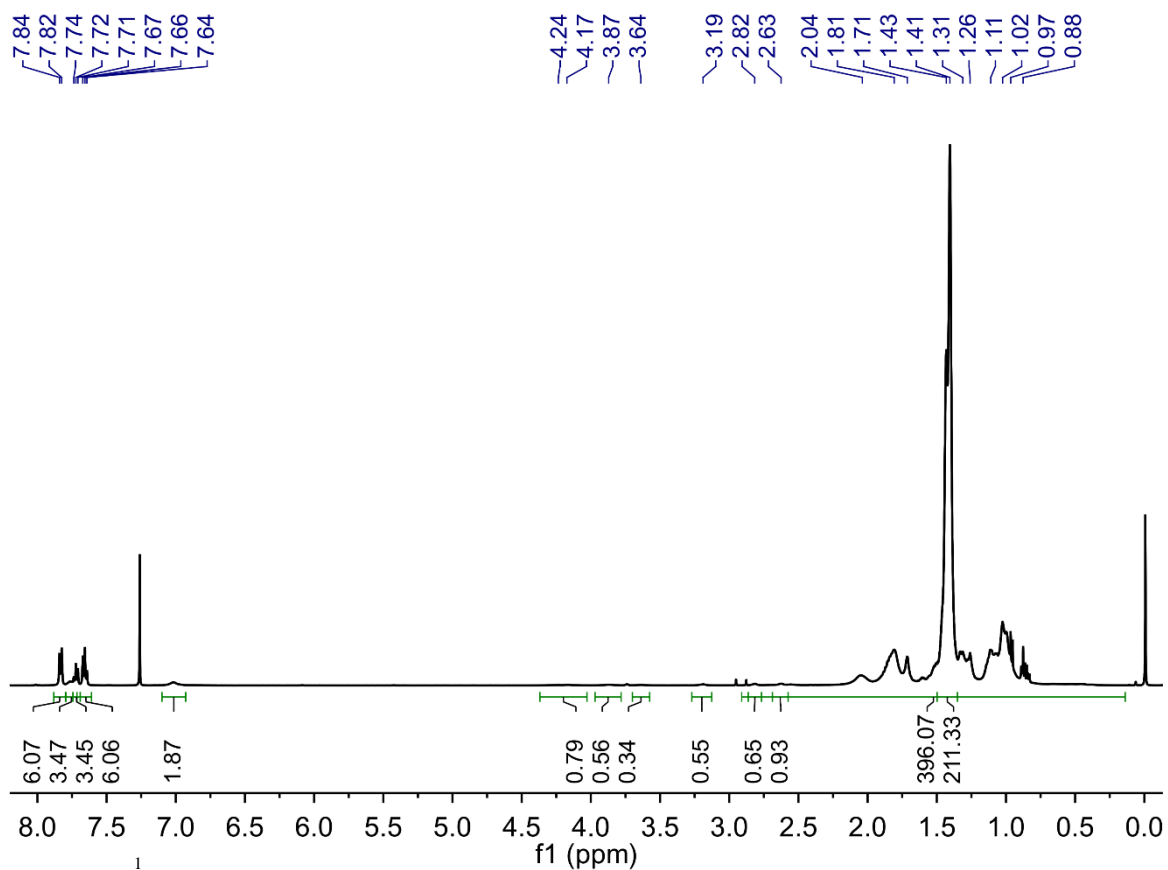


Figure S8. ¹H NMR spectrum of copolymer 2

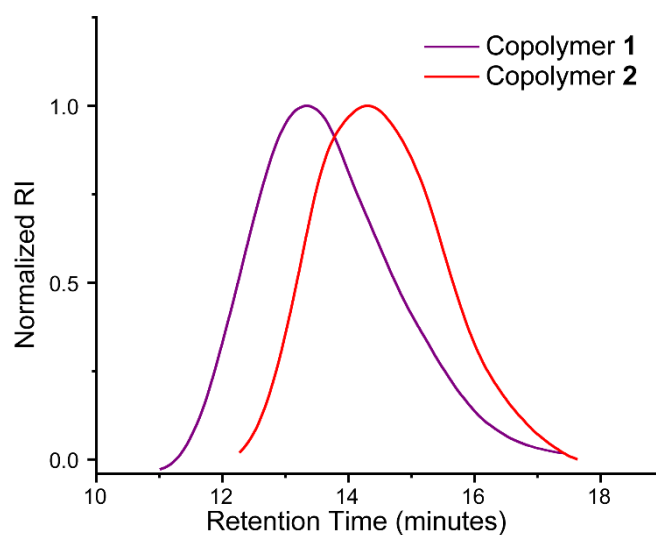


Figure S8. GPC traces of copolymers 1 and 2.

Supplementary Videos

Video S1. A helical MSP (copolymer **1**, helix radius $r = 38 \mu\text{m}$) in pH 1 buffer solution with one end fixed to the substrate surface in contact with a PFD droplet ($R = 132 \mu\text{m}$). As the substrate with adhered MSP end is translated to the left, the coiled helical MSP stretches until it detaches from the droplet surface and recoils through the solution.

Video S2. A helical MSP (copolymer **1**, helix radius $r = 55 \mu\text{m}$) in pH 4 buffer solution with one end fixed to the substrate surface in contact with a PFD droplet ($R = 335 \mu\text{m}$). As the substrate with adhered MSP end is translated to the left, the coiled helical MSP stretches until 4 coils detach from the droplet surface (time $T \sim 2.3 \text{ s}$). Upon further stretching, the droplet is pulled from the microcapillary tip by the adhered MSP spring.

Video S3. A helical MSP (copolymer **1**) in pH 6 buffer solution. The left end of the helix is attached to the substrate, while the right end became fixed to the substrate after release, affording a structure with 2 fixed ends. As a PFD droplet is brought into contact with the helical ribbon, the two bodies slide past each other without apparent adhesion.

Video S4. A short MSP segment (copolymer **1**, length $\sim 400 \mu\text{m}$) in pH 8 buffer solution is adhered at one end to the surface of a droplet and at the far end to the substrate. Ribbon and droplet are manipulated through the solution *via* microcapillary tip and translating stage, revealing selective adhesion at the ribbon tip.

Video S5. MSPs (copolymer **1**) in pH 10 buffer solution wrapped around a droplet. The droplet is anchored in place by the fixed end of a wrapped ribbon, while the microcapillary tube and translating stage are used to “unwrap” the droplet.

Video S6. An MSP (copolymer **1**) is held in tension by the microcapillary tip to control wrapping in pH 10 buffer solution. As slack is added to the system by bringing the MSP end toward the wrapped droplet, the MSP continues to wrap until it overlaps an existing coil, arresting the wrapping event.

Video S7. A droplet is inflated next to an MSP (copolymer **1**) in pH 10 buffer solution. To the left (out of frame), the MSP is fixed to the substrate surface; to the right it floats freely. When the droplet touches the MSP, spontaneous wrapping occurs until a defect in the ribbon causes self-overlap, stopping the wrapping event before the ribbon length is consumed and creating a droplet with a pendent arm. To the left, wrapping continues until the ribbon is pulled tight against the substrate-adhered end.

Video S8. A droplet is inflated until it comes into contact with an MSP (copolymer **1**) in pH 10 buffer solution. The ribbon is fixed to the substrate to the left (out of frame) and floats freely to the right. Upon contact, the ribbon spontaneously wraps the droplet until the free end is consumed and the ribbon is pulled tight against the substrate-bound end to the left, final droplet radius $R = 360 \mu\text{m}$.

Video S9. An MSP (copolymer **1**) in pH 10 buffer with one end adhered to the substrate surface (left, out of frame) is partially wrapped around a droplet ($R = 88 \mu\text{m}$) that is adhered to a superglue bead near the end of a carbon fiber cantilever. The ribbon-droplet and cantilever-droplet interfaces are loaded by translating the substrate to the left to pull on the ribbon. Cantilever deflection is used to quantify the applied loads as the system is loaded, unloaded, and then loaded until detachment of the ribbon from the droplet surface.

Video S10. Copolymer **2** MSBCP with $500 \mu\text{m}$ block length has selectively wrapped a droplet ($R = 110 \mu\text{m}$) in pH 10 buffer solution to afford a droplet with a single arm extended into solution.

Video S11. An MSBCP in pH 10 buffer solution attached to the same droplet as in **Video S11** *via* selective wrapping to add a second arm.

Video S12. More MSBCPs in pH 10 buffer solution adhered to and selectively wrapped around the same droplet as in Videos S10 and S11. In this case, we observe mixed assembly

modes, including end-on adhesion, adhesion of the hydrophilic segment without wrapping ($R < R_c$), and selective segmental wrapping of the hydrophobic block ($R > R_c$).

Video S13. MSBCPs are picked up from the substrate using a PFD droplet ($R = 150 \mu\text{m}$) adhered to the microcapillary tip in 500 mM NaOH solution.

Video S14. Cantilever deflection of an MSBCP (patterned segment length $50 \mu\text{m}$) with one end adhered to the substrate surface, and a far segment adhered to a cantilever-bound droplet ($R = 60 \mu\text{m}$). The system is twice subjected to a full cycle of loading until peel initiation and unloading until re-wrap. On the third cycle, peel is initiated, then propagated until complete detachment of the adhered segment.

References for Supplementary Information

- [1] Z. Zhang, F. Torok, J. Li, M. Bouchard, J. Victor, Photoactivatable Fouling-Resistant Copolymers **2017**.
- [2] D. M. Barber, A. J. Crosby, T. Emrick, *Adv. Mater.* **2018**, *30*, 1706118.
- [3] W. Lin, G. Ma, F. Ji, J. Zhang, L. Wang, H. Sun, S. Chen, *J. Mater. Chem. B* **2015**, *3*, 440.
- [4] K. Masunaga, A. Tanaka, D. Domon, S. Watanabe, Y. Ohsawa, M. Ohashi, Chemically amplified positive photoresist composition and pattern forming process **2010**.
- [5] M. H. Espinosa, P. J. O. del Toro, D. Z. Silva, In *Polymer*; 2001; Vol. 42, pp. 3393–3397.
- [6] J. T. Pham, J. Lawrence, D. Y. Lee, G. M. Grason, T. Emrick, A. J. Crosby, *Adv. Mater.* **2013**, *25*, 6703.
- [7] J. T. Pham, A. Morozov, A. J. Crosby, A. Lindner, O. du Roure, *Phys. Rev. E* **2015**, *92*, 011004.
- [8] M. Kim, T. R. Powers, *Phys. Rev. E* **2005**, *71*, 021914.

- [9] F. M. White, I. Corfield, *Viscous Fluid Flow*; 3rd ed.; McGraw-Hill: New York, 2006.
- [10] M. K. Jawed, P. M. Reis, *Soft Matter* **2016**, *12*, 1898.
- [11] L. Koens, E. Lauga, *Phys. Fluids* **2016**, *28*, 013101.
- [12] A. Emileh, E. Vasheghani-Farahani, M. Imani, *Eur. Polym. J.* **2007**, *43*, 1986.
- [13] N. Orakdogan, *J. Polym. Res.* **2012**, *19*, 9914.
- [14] L. Pain, C. Le Cornec, C. Rosilio, P. J. Paniez, *Microelectron. Eng.* **1996**, *30*, 271.
- [15] C. Liu, M. Cheng, *J. Micro/Nanolithography, MEMS, MOEMS* **2005**, *4*, 033001.